uOttawa

L'Université canadienne
Canada's university

FACULTÉ DES ÉTUDES SUPÉRIEURES ET POSTDOCTORALES

uOttawa

L'Université canadienne
Canada's university

FACULTY OF GRADUATE AND POSTDOCTORAL STUDIES

Khalid Al-Qadi

AUTEUR DE LA THÈSE / AUTHOR OF THESIS

Ph.D. (Physics)

GRADE / DEGREE

Department of Physics

FACULTÉ, ÉCOLE, DÉPARTEMENT / FACULTY, SCHOOL, DEPARTMENT

Magnetic Properties of the Icosahedral Quasicrystals $Ag_{50}In_{36}Gd_{14}$ and $Zn_{77}Fe_7Sc_{16}$, and the 1/1 Approximant $Ag_{50}In_{36}Gd_{14}$

TITRE DE LA THÈSE / TITLE OF THESIS

Z. Stadnik

DIRECTEUR (DIRECTRICE) DE LA THÈSE / THESIS SUPERVISOR

CO-DIRECTEUR (CO-DIRECTRICE) DE LA THÈSE / THESIS CO-SUPERVISOR

EXAMINATEURS (EXAMINATRICES) DE LA THÈSE / THESIS EXAMINERS

B. Joós

R. Varin

G. Lamarche

H. Logan

Gary W. Slater

Le Doyen de la Faculté des études supérieures et postdoctorales / Dean of the Faculty of Graduate and Postdoctoral Studies

Magnetic Properties of the Icosahedral Quasicrystals $Ag_{50}In_{36}Gd_{14}$ and $Zn_{77}Fe_7Sc_{16}$, and the 1/1 Approximant $Ag_{50}In_{36}Gd_{14}$

BY
Khalid Al-Qadi

Thesis submitted to the
Faculty of Graduate and Postdoctoral Studies
In partial fulfillment of the requirements
For the PhD degree in Physics

Department of Physics
Faculty of Science
University Of Ottawa

Your file Votre référence
ISBN: 978-0-494-59477-3
Our file Notre référence
ISBN: 978-0-494-59477-3

TABLE OF CONTENTS

List of tables..... VI

List of figures..... VII

Abstract..... XV

Acknowledgments..... XVIII

1. Introduction..... 1-1

1.1. Quasicrystals..... 1-1

1.2. Icosahedral quasicrystals 1-2

1.2.1. Fibonacci chain..... 1-4

1.2.2. Tiling 1-4

1.3. Roadmap of the thesis..... 1-6

2. Magnetic Theory and Background..... 2-1

2.1. Introduction..... 2-1

2.2. Non-Magnetic materials..... 2-2

2.2.1. Diamagnetism..... 2-2

2.2.2. Paramagnetism..... 2-3

2.3. Ordered Magnets..... 2-6

2.3.1. Ferromagnetism..... 2-6

2.3.2. Antiferromagnetism..... 2-9

2.3.3. Ferrimagnetism 2-13

2.4. Spin Glasses..... 2-14

2.4.1. Introduction..... 2-14

2.4.2. Mean-Field Theory..... 2-16
2.4.3. Phenomenological Models..... 2-28
2.4.3.1. Droplet model..... 2-28
2.4.3.2. Fractal cluster model..... 2-30
2.4.4. Dynamics in the Ising model..... 2-34
2.4.4.1. Glauber model..... 2-35
2.4.4.2. Soft-spin model..... 2-36
2.5. Possibility of long-range magnetic order in quasicrystals 2-40
2.5.1. The geometrical model..... 2-40
2.5.2. The Ising model..... 2-40
2.5.3. The XY model..... 2-41
2.5.4. The Heisenberg and Hubbard models..... 2-42
3. Experimental Techniques..... 3-1
3.1. Introduction..... 3-1
3.2. Sample preparation..... 3-1
3.2.1. Introduction..... 3-1
3.2.2. Ingot preparation..... 3-2
3.2.2.1. Introduction..... 3-2
3.2.2.2. Arc melting..... 3-4
3.2.2.3. Radio frequency melting..... 3-6
3.2.2.3.1. Radio frequency generator..... 3-7
3.2.2.3.2. Induction coil..... 3-7
3.2.2.3.3. The sample chamber..... 3-8

3.2.2.3.4. The melting process..... 3-8

3.2.2.4. Furnace melting..... 3-8

3.2.2.4.1. Sample container preparation..... 3-11

3.2.2.4.2. Quartz tube sealing..... 3-12

3.2.2.5. Ribbon preparation..... 3-14

3.3. Experimental setups..... 3-18

3.3.1. Introduction..... 3-18

3.3.2. Powder X-ray diffraction..... 3-18

3.3.2.1.X-ray diffractometer..... 3-18

3.3.2.2.Rietveld analysis..... 3-21

3.3.3. Mössbauer spectroscopy..... 3-22

3.3.3.1.Mössbauer effect theory..... 3-24

3.3.3.1.1. Isomer shift..... 3-25

3.3.3.1.2. Quadrupole splitting..... 3-27

3.3.3.1.3. Magnetic splitting..... 3-27

3.3.3.2.^{57}Fe Mössbauer spectroscopy setup..... 3-29

3.3.3.3.^{155}Gd Mössbauer spectroscopy setup..... 3-31

3.3.4. dc magnetometry 3-31

3.3.5. ac magnetometry 3-35

4. Icosahedral quasicrystal $Ag_{50}In_{36}Gd_{14}$..... 4-1

4.1. Introduction 4-1

4.2. Experimental procedure 4-1

4.3. Results and discussion 4-2

4.3.1. Structural characterization..... 4-2

4.3.2. Magnetic measurements..... 4-5

4.3.2.1. dc magnetic susceptibility..... 4-5

4.3.2.2. ac magnetic susceptibility..... 4-9

4.3.3. Mössbauer spectroscopy..... 4-14

4.3.4. Conclusions..... 4-19

5. Icosahedral quasicrystal $Zn_{77}Fe_7Sc_{16}$..... 5-1

5.1. Introduction 5-1

5.2. Experimental procedure 5-1

5.3. Results and discussion 5-2

5.3.1. Structural characterization..... 5-2

5.3.2. Magnetic measurements..... 5-3

5.3.2.1. dc magnetic susceptibility..... 5-3

5.3.2.2.Relaxation effects in the dc magnetization..... 5-8

5.3.2.3. ac magnetic susceptibility..... 5-15

5.3.3. Mössbauer spectroscopy..... 5-20

5.3.4. Conclusions..... 5-29

6. 1/1 APPROXIMANT $Ag_{50}In_{36}Gd_{14}$ 6-1

6.1. Introduction 6-1

6.2. Experimental procedure 6-1

6.3. Results and discussion 6-2

6.3.1. Structural characterization..... 6-2

6.3.2. Magnetic measurements..... 6-2

6.3.2.1. dc magnetic susceptibility..... 6-2

6.3.2.2. ac magnetic susceptibility..... 6-7

6.3.3. Mössbauer spectroscopy..... 6-14

6.3.4. Conclusions..... 6-16

7. Conclusions..... 7-1

References..... 7-4

LIST OF TABLES

Table Page

(2-1) A summary of some of the symbols used in the chapter and their definitions..... 2-44

(4-1) Positions in terms of $2\theta_1$ (in degrees) corresponding to Cu $K\alpha_1$ radiation and Q_{exp} (in $Å^{-1}$), full width at half maximum Γ_Q (in $Å^{-1}$), and relative intensity INT normalized to 100.0 of all detected icosahedral Bragg peaks, which are labeled with consecutive integers in column 1, as obtained from the fit [23]. The integers correspond to the vertical lines in figure 1. Q_{cal} (in $Å^{-1}$) is the calculated Q value by taking the position of the second line with the $I1$ index 18/29 as the reference line. $I1$ and $I2$ are the indices (N/M) and (h/h',k/k',l/l') based on the indexing scheme of Cahn *et al* [24], whereas $I3$ and $I4$ are the indices corresponding, respectively, to the indexing schemes of Elser [25] and Bancel *et al* [26].....4-4

(4-2) Hyperfine interaction parameters derived from the fits to the ^{151}Gd Mössbauer spectra of the icosahedral $Ag_{50}In_{36}Gd_{14}$ at various temperatures.....4-17

(5-1) Positions in terms of $2\theta_1$ (in degrees) corresponding to Cu $K\alpha_1$ radiation and Q_{exp} (in $Å^{-1}$), full width at half maximum Γ_Q (in $Å^{-1}$), and relative area A normalized to 100.0 of all detected icosahedral Bragg peaks. Q_{cal} (in $Å^{-1}$) is the calculated Q value by taking the position of the ninth line with the $I1$ index 18/29 as the reference line. $I1$ and $I2$ are the indices (N/M) and (h/h',k/k',l/l') based on the indexing scheme of Cahn *et al* [21], whereas $I3$ and $I4$ are the indices corresponding, respectively, to the indexing schemes of Elser [22] and Bancel *et al* [23].....5-4

(5-2) Results of a fit to equation (2) of ZFC magnetization decays at T = 4.8 K and H = 20 Oe for different waiting times t_w.....5-10

(6-1) Atomic positions for the $Ag_{50}In_{36}Gd_{14}$ alloy obtained through Rietveld analysis..... 6-3

(7-1) Comparison between experimental values obtained of the two different structures of $Ag_{50}In_{36}Gd_{14}$ alloy..... 7-3

LIST OF FIGURES

Chapter	Figure		Page
(1)	(1)	Photograph of a single-grain of icosahedral Ho-Mg-Zn quasicrystal. It is shown on a mm scale, the edges are 2.2 mm long.....	1-2
	(2)	Photograph of a wall of octagonal tomb tower built in the 12^{th} century.....	1-3
	(3)	To the left a photograph of a fivefold flower nearby Rocca Calascio (Abruzzo, central Italy). To the right five fivefold delicate pink flowers.....	1-4
	(4)	The Penrose pattern constructed from two different blocks..	1-5
	(5)	At the bottom, experimental electron diffraction pattern of the icosahedral quasicrystal Al-Mn for (a) fivefold axis, (b) twofold axis, and (c) threefold axis. At the top is the calculated Fourier transform of the three dimensions Penrose tiling.....	1-6

LIST OF FIGURES

Chapter	Figure		Page
(2)	(1)	Spin-orbit interaction between the angular momenta $\vec{L}$ and $\vec{S}$. $\vec{\mu}_L = -\mu_B \vec{L}$, $\vec{\mu}_S = -g_e \mu_B \vec{S}$, $\vec{\mu}_{total} = \vec{\mu}_L + \vec{\mu}_S$, and $\vec{\mu} = \vec{\mu}_{total} \cos\theta$.	2-2
	(2)	Energy levels splitting for one electron in a magnetic field directed along the positive z-axis.....	2-4
	(3)	Schematic of the temperature dependence of the reciprocal magnetic susceptibility of a paramagnet.....	2-5
	(4)	The reduced magnetization versus the reduced temperature calculated by equation (16) for several values of *J*. Included are Fe experimental data (x) and Ni experimental data (o) [1].....	2-8
	(5)	Schematic of the temperature dependence of the magnetization M, and the reciprocal magnetic susceptibility of a ferromagnet.	2-8
	(6)	Two simple antiferromagnetic spin arrangements for (a) body-center cubic lattice and (b) simple cubic lattice.....	2-10
	(7)	Simple antiferromagnetic spin arrangements in the unit cell of YMn_2Ge_2 below its Néel temperature T_N = 395 K. Yellow circles represent the Y atoms, the green circles represent Ge atoms, and the blue circles represents the magnetic Mn atoms.....	2-10
	(8)	Schematic of the temperature dependence of the magnetization M, and the reciprocal magnetic susceptibility of an antiferromagnet.....	2-11
	(9)	The perpendicular applied magnetic field to the easy magnetic direction of a single crystal antiferromagnet and the two sublattices moments.....	2-12
	(10)	Ferrimagnetic magnetic moments arrangements of the GdCo5 unit cell. The green circles are Co atoms and the yellow are Gd atoms.....	2-13
	(11)	Schematic of the temperature dependence of the magnetization M, and the reciprocal magnetic susceptibility of a ferrimagnet..	2-14
	(12)	The zero-field cooled (ZFC) (green circles) and field-cooled (FC) (red circles) susceptibility curves of the CdCr1.7In0.3S4 thiospinel spin-glass.....	2-15
	(13)	ZF susceptibility χ' as a function of temperature for (Cu-0.94 at.% Mn, powder). Measuring frequencies: red squares 1330 Hz;	

green circles 234 Hz; black crosses 10.4 Hz; and blue triangles 2.6 Hz. 2-16

(14) The calculated (a) magnetic susceptibility and (b) the specific heat versus the reduced temperature using the EA model for two spin values, the red line is $S = \frac{1}{2}$ and the green line $S = \infty$. 2-19

(15) The magnetic phase diagram for Ising spins predicted by the SK model..... 2-21

(16) Phase diagrams showing the instability of the SK model (a) in the absence of a magnetic field and (b) in the presence of the magnetic field. 2-22

(17) The hierarchical organization of the metastable states in a spin glass. The coarse-grained free-energy surface is represented at each level corresponding to a given temperature. When the temperature is decreased ($T_2 < T_1 < T_f$), each valley subdivides into others. Ageing refers to jumping of the system over ever increasing energy barriers during the waiting time t_w. 2-24

(18) Tree representation of the Parisi replica symmetry breaking scheme. 2-25

(19) Schematic picture of the droplet model. 2-29

(20) Schematic picture of the fractal cluster. 2-31

(21) Multi-valley 'landscape' for the free energy of an Ising spin glass according to the replica breaking symmetry..... 2-40

Chapter	Figure		Page
(3)	(1)	Last column of table (1) is plotted to visualize the difference between the calculated and measured weights. The blue squares are Zn/Sc differences, the red circles are Zn/Fe differences, and the green triangles are the Sc/Fe differences.....	3-3
	(2)	The arc melting setup.	3-5
	(3)	The horizontal RF sample chamber.	3-10
	(4)	The vertical RF sample chamber.	3-11
	(5)	Steps to prepare the sample container from a sheet of metal. .	3-14
	(6)	The modified water-cooled copper hearth.	3-16
	(7)	The steps for sealing the sample. First, as shown in (B), the quartz tube is sealed from one end. Then the sample container is inserted in it, as shown in (C). Next, in an area in the quartz tube that is close enough to the sample container, a small-diameter neck of the order of 2–3 cm long and 3–4 mm thick with a tiny opening is prepared, as shown in (D). The neck is necessary to make the final sealing process easier. Once the neck is prepared, the quartz tube is evacuated to high vacuum of 10-5 Torr for about an hour. Then the quartz tube is filled with argon gas with a pressure of 300 Torr and the neck is heated and sealed (E)...	3-17
	(8)	The melt spinning technique.....	3-18
	(9)	The Bragg–Brentano geometry diffractometer.	3-20
	(10)	A typical Mössbauer spectrometer block diagram.	3-24
	(11)	The zero shift (A) and the isomer shift (B).	3-27
	(12)	The quadrapole splitting for 57Fe nucleus with spin I =3/2 in the excited state.....	3-29
	(13)	For 57Fe the ground state split into two sublevels. The excited state split into 4 sublevels.	3-31
	(14)	The inner components of the MPMS.	3-33
	(15)	A simple SQUID consists of two superconducting identical semi-circles joint together with Josephson junctions.	3-35
	(16)	PPMS insert and coil set.....	3-37

Chapter	Figure		Page
(4)	(1)	The XRD spectrum of an Ag50In36Gd14 alloy at 298 K. The vertical lines labeled with integers above all detected i Bragg peaks correspond to the positions calculated for the Cu Kα1 radiation, as explained in the text. The position, full width at half maximum, and relative intensity of each detected i peak are given in table 1 together with the corresponding index. The symbol ▼ indicates the peak positions corresponding to an unidentified second phase.....	4-2
	(2)	(a) The temperature dependence of the magnetic susceptibility of the icosahedral $Ag_{50}In_{36}Gd_{14}$ quasicrystal, measured in an external magnetic field of 30 Oe. The solid line is the fit to equation (1) in the temperature range 50 – 300 K as explained in the text. (b) The inverse magnetic susceptibility corrected for the contribution $\chi 0$, $(\chi - \chi_0)^{-1}$ versus temperature T of the icosahedral $Ag_{50}In_{36}Gd_{14}$ quasicrystal. The solid line is the fit to equation (1).....	4-6
	(3)	The temperature dependence of the zero-field (ZFC) and field-cooled (FC) magnetic susceptibility of the icosahedral $Ag_{50}In_{36}Gd_{14}$ quasicrystal, measured in an external magnetic field of 30 Oe.....	4-8
	(4)	The temperature dependence of the in-phase magnetic susceptibility χ' (a) and out-of-phase magnetic susceptibility χ'' (b) measured for different applied frequencies from 20 Hz to 10 kHz for the icosahedral $Ag_{50}In_{36}Gd_{14}$ quasicrystal.....	4-10
	(5)	The frequency dependence of the freezing temperature T_f for the icosahedral $Ag_{50}In_{36}Gd_{14}$ quasicrystal. The solid line is the best linear fit to the T_f data.....	4-11
	(6)	The frequency dependence of the freezing temperature T_f for the icosahedral $Ag_{50}In_{36}Gd_{14}$ quasicrystal. The solid line is the best fit to equation (3).....	4-12
	(7)	The frequency dependence of the freezing temperature T_f for the icosahedral $Ag_{50}In_{36}Gd_{14}$ quasicrystal. The solid line is the best fit to equation (4).....	4-13
	(8)	The ^{155}Gd Mössbauer spectrum of the icosahedral $Ag_{50}In_{36}Gd_{14}$ at 10.4 K fitted (solid line) with (a) one quadrupole pattern and (b) a distribution of quadrupole patterns. The zero-velocity scale is relative to the source.....	4-15
	(9)	^{155}Gd Mössbauer spectra of the icosahedral $Ag_{50}In_{36}Gd_{14}$ at various temperatures. Solid lines are fits, as described in the text. The zero-velocity scale is relative to the source.....	4-17

Chapter	Figure		Page
(5)	(1)	The XRD spectrum of the $Zn_{77}Fe_7Sc_{16}$ quasicrystal at 298 K corrected for the $CuK\alpha_2$ lines. The vertical lines labeled with integers above all detected i Bragg peaks correspond to the positions calculated for the Cu $K\alpha_1$ radiation, as explained in the text. The position, full width at half maximum, and relative intensity of each detected i peak are given in table (1) together with the corresponding index. The symbol ▾ indicates the peak positions corresponding to an unidentified second phase.....	5-4
	(2)	(a) The temperature dependence of the magnetic susceptibility of the icosahedral $Zn_{77}Fe_7Sc_{16}$ quasicrystal, measured in an external magnetic field of 50 Oe. The solid line is the fit to equation (1) in the temperature range 40 – 300 K, as explained in the text. (b) The inverse magnetic susceptibility corrected for the contribution χ_0, $(\chi - \chi_0)^{-1}$ versus temperature T of the icosahedral $Zn_{77}Fe_7Sc_{16}$ quasicrystal. The solid line is the fit to equation (1).	5-6
	(3)	The temperature dependence of the zero-field-cooled (ZFC) and field-cooled (FC) magnetic susceptibility of the icosahedral $Zn_{77}Fe_7Sc_{16}$ quasicrystal, measured in an external magnetic field of 50 Oe.....	5-7
	(4)	The time dependence the ZFC magnetization for an applied magnetic field of 20 Oe at 4.8 K for different waiting times t_w of the icosahedral $Zn_{77}Fe_7Sc_{16}$ quasicrystal. The solid lines are the fits to equation (2).....	5-9
	(5)	The TRM time decays at H = 50 Oe for the different waiting times t_w at (a) 4.8 K and (b) 6.0 K of the icosahedral $Zn_{77}Fe_7Sc_{16}$ quasicrystal. The solid lines are guides for the eye.....	5-11
	(6)	The TRM time decays for t_w = 3600 s at (a) 4.8 K and (b) 6.0 K for different cooling fields H of the icosahedral $Zn_{77}Fe_7Sc_{16}$ quasicrystal. The solid lines are guides for the eye.....	5-14
	(7)	The temperature dependence of the in-phase magnetic susceptibility χ' (a) and out-of-phase magnetic susceptibility χ'' (b) measured for different applied frequencies from 20 Hz to 10 kHz for the icosahedral $Zn_{77}Fe_7Sc_{16}$ quasicrystal.....	5-16
	(8)	The frequency dependence of the freezing temperature T_f for the icosahedral $Zn_{77}Fe_7Sc_{16}$ quasicrystal. The solid line is the best linear fit to the T_f data.....	5-17

(9) The frequency dependence of the freezing temperature T_f for the icosahedral $Zn_{77}Fe_7Sc_{16}$ quasicrystal. The solid line is the best fit to equation (4)..... 5-18

(10) The frequency dependence of the freezing temperature T_f for the icosahedral $Zn_{77}Fe_7Sc_{16}$ quasicrystal. The solid line is the best fit to equation (5)..... 5-20

(11) The ^{57}Fe Mössbauer spectra of the icosahedral $Zn_{77}Fe_7Sc_{16}$ quasicrystal.obtained at the indicated temperatures fitted (solid lines) with the quadrupole splitting distributions $P(\Delta)$ shown in figure (13). The residuals are shown above each spectrum. The zero-velocity origin is relative to α-Fe at room temperature..... 5-21

(12) The quadrupole splitting distributions $P(\Delta)$ which fit the best the ^{57}Fe Mössbauer spectra in figure (12)..... 5-23

(13) The temperature dependence of the average quadrupole splitting of the icosahedral icosahedral $Zn_{77}Fe_7Sc_{16}$ quasicrystal. The solid line is the fit to equation (7)..... 5-24

(14) The ^{57}Fe Mössbauer spectra of the icosahedral $Zn_{77}Fe_7Sc_{16}$ quasicrystal obtained at the indicated temperatures fitted (solid lines) with the hyperfine magnetic field distributions $P(H_{hf})$ shown in figure (16). The residuals are shown above each spectrum. The zero-velocity origin is relative to α-Fe at room temperature..... 5-25

(15) The hyperfine magnetic field distributions $P(H_{hf})$ which fit the best the ^{57}Fe Mössbauer spectra in figure (15)..... 5-26

(16) The temperature dependence of the average hyperfine magnetic field of the icosahedral $Zn_{77}Fe_7Sc_{16}$ quasicrystal. The solid line is a guide for the eye..... 5-27

(17) The temperature dependence of the average center shift of the icosahedral $Zn_{77}Fe_7Sc_{16}$ quasicrystal. The solid line is the fit to equation (8), as explained in the text..... 5-28

Chapter	Figure		Page
(6)	(1)	The x-ray diffraction spectrum of an $Ag_{50}In_{36}Gd_{14}$ alloy at 298 K. The experimental data are denoted by open circles, while the line through the circles represents the results of the Rietveld refinement. The vertical bars represent the Bragg peak positions corresponding to the $Ag_{50}In_{36}Gd_{14}$ phase. The lower solid line represents the difference curve between experimental and calculated spectra.....	6-3
	(2)	(a) The temperature dependence of the magnetic susceptibility of the $Ag_{50}In_{36}Gd_{14}$ alloy measured in an external magnetic field of 50 Oe. The solid line is the fit to equation (1) in the temperature range 70–300 K, as explained in the text. (b) The inverse magnetic susceptibility corrected for the contribution χ_0, $(\chi-\chi_0)^{-1}$ versus temperature T of the $Ag_{50}In_{36}Gd_{14}$ alloy. The solid line is the fit to equation (2).....	6-5
	(3)	The temperature dependence of the zero-field-cooled (ZFC) and field-cooled (FC) magnetic susceptibility of the $Ag_{50}In_{36}Gd_{14}$ alloy measured in an external magnetic field of 50 Oe.....	6-6
	(4)	The temperature dependence of the in-phase magnetic susceptibility χ' measured for different frequencies from 300 Hz to 10 kHz for the $Ag_{50}In_{36}Gd_{14}$ alloy. The inset shows a magnification of the low-temperature region.....	6-7
	(5)	The temperature dependence of the out-of-phase magnetic susceptibility χ'' measured for different frequencies from 300 Hz to 10 kHz for the $Ag_{50}In_{36}Gd_{14}$ alloy. The insets show a magnification of the low-temperature region.....	6-8
	(6)	The frequency dependence of the freezing temperatures (a) T_{f_1} and (b) T_{f_2} for the $Ag_{50}In_{36}Gd_{14}$ alloy. The solid lines are the best linear fits to the data.....	6-9
	(7)	The frequency dependence of the freezing temperatures (a) T_{f_1} and (b) T_{f_2} for the $Ag_{50}In_{36}Gd_{14}$ alloy. The solid line is the best fit to equation (4).....	6-11
	(8)	The frequency dependence of the freezing temperatures (a) T_{f_1} and (b) T_{f_2} for the $Ag_{50}In_{36}Gd_{14}$ alloy. The solid line is the best fit to equation (5).....	6-13
	(9)	The ^{155}Gd Mössbauer spectrum of the $Ag_{50}In_{36}Gd_{14}$ alloy at 4.6 K fitted (solid line) with an electric quadrupole hyperfine interaction. The zero-velocity origin is relative to the source.....	6-14

(10) ^{155}Gd Mössbauer spectrum of the $Ag_{50}In_{36}Gd_{14}$ at 1.5 K fitted (solid line) with a combined magnetic dipole and electric quadrupole hyperfine interactions. The zero-velocity origin is relative to the source..... 6-16

ABSTRACT

This thesis is a study of magnetic properties of new icosahedral quasicrystals $Ag_{50}In_{36}Gd_{14}$, $Zn_{77}Fe_7Sc_{16}$ and a 1/1 crystalline approximant $Ag_{50}In_{36}Gd_{14}$. The $Ag_{50}In_{36}Gd_{14}$ and $Zn_{77}Fe_7Sc_{16}$ quasicrystals are shown to have a primitive six-dimensional Bravais lattice with a six-dimensional hypercubic lattice constant of, respectively, 7.805(2) and 7.087(1) Å. The crystal structure of the approximant $Ag_{50}In_{36}Gd_{14}$ is found to be of the $YbCd_6$ type (space group $Im\bar{3}$) with a lattice constant of 15.202(1) Å. No evidence is found for a transition to a ground state with long-range magnetic order in the temperature range 2–300 K for all three alloys.

These three alloys are shown to be spin glasses. The spin freezing temperature of the $Ag_{50}In_{36}Gd_{14}$ and $Zn_{77}Fe_7Sc_{16}$ quasicrystals is, respectively, 4.25(5) and 7.75(2) K. The unusual spin freezing in the approximant is found to occur in two stages: at ~3.6 K spins develop short-range correlations but they continue to fluctuate at low frequencies, and then long-range freezing is achieved upon further cooling to below ~2.4 K. The $Ag_{50}In_{36}Gd_{14}$ quasicrystal and its 1/1 approximant are shown to belong to a category of strongly geometrically frustrated magnets.

The frequency dependence of the freezing temperature in all three alloys is shown to be equally well accounted for by the Vogel-Fulcher law and the power law. Analysis of the ageing effects observed in the $Zn_{77}Fe_7Sc_{16}$ quasicrystal leads to a major discovery that the nature of the spin-glass state in this quasicrystal is fundamentally different from that of a canonical spin glass.

The effective magnetic moment at Gd atoms in the $Ag_{50}In_{36}Gd_{14}$ quasicrystal and its

1/1 approximant is found to be close to that of a Gd^{+3} ion. The effective magnetic moment at Fe atoms in the $Zn_{77}Fe_7Sc_{16}$ quasicrystal is the largest ever found in an Fe-containing quasicrystal.

The hyperfine magnetic fields at ^{155}Gd and ^{57}Fe nuclei in the $Ag_{50}In_{36}Gd_{14}$ and $Zn_{77}Fe_7Sc_{16}$ quasicrystals are shown to set in at temperatures larger than the corresponding freezing temperatures. The presence of the distribution of the electric quadrupole splitting in the ^{155}Gd Mössbauer spectra of the $Ag_{50}In_{36}Gd_{14}$ quasicrystal indicates the existence of the multiplicity of Gd sites. The binomial distribution of the electric quadrupole splitting and the hyperfine magnetic field derived from the ^{57}Fe Mössbauer spectra $Zn_{77}Fe_7Sc_{16}$ quasicrystal indicates the existence of two classes of Fe sites. The Debye temperatures of the quasicrystals $Ag_{50}In_{36}Gd_{14}$, $Zn_{77}Fe_7Sc_{16}$, and the approximant $Ag_{50}In_{36}Gd_{14}$ determined from the Mössbauer spectra are, respectively, 199(2), 443(8), and 199(1) K.

In the memory of my beloved parents

whom I could not see before they died

ACKNOWLEDGEMENT

I would like to acknowledge the support of my thesis supervisor Dr. Z.M. Stadnik. I will always be grateful for his tremendous support and inspiration for this project. I would also like to acknowledge Dr. G. Lamarche for his invaluable advice and contribution to the experimental part of this work.

Many thanks for my friend and research colleague Pu Wang for his valuable help. Many heartfelt thanks go to Ms. H. Lacasse who has been extremely helpful and generous to me over the past years. Also many thanks to my colleague at work S. Robineau who is truly a supporting person. I would also like to thank the kind staff in the machine and electronic workshops.

Finally, a deep and most loving acknowledgement to my family. I thank my parents, who both are deceased now, for their continuous support and affection. Father: If I can, I will fulfill your wish… '*Son when you finish your PhD come and stand before my grave and tell me so*'. I thank my wife who has most patiently endured and has done a wonderful job in raising our beautiful children.

1) INTRODUCTION

1.1) Quasicrystals

Solids are traditionally divided into two groups: crystalline and amorphous. The dramatic discovery of an icosahedral (i) Al-Mn alloy by Shechtman *et al* [1] extended this dichotomous division by introducing the notion of quasicrystals (QCs). These are materials that possess a new type of long-range translational order, *quasiperiodicity*, and a noncrystallographic orientational order associated with the classically forbidden fivefold, eightfold, tenfold, and twelvefold symmetry axes [2, 3]. A main problem in condensed matter physics is determining whether quasiperiodicity leads to physical properties which are significantly different from those of crystalline and amorphous materials of the same/similar compositions.

One of the central questions in the physics of QCs is that of the possibility of the existence of long-range magnetic order in these alloys. The initial intuition suggests that quasiperiodicity necessarily leads to geometrical frustration and is therefore incompatible with long-range magnetic order. However, various theoretical models dealing with magnetism in QCs indicate the possibility of existence of long-range magnetic order in QCs. These models are geometrical models [4–7] and the physical ones, such as the Ising model [8–15], the *XY* model [16–18], the Heisenberg model [19–25], and the Hubbard model [26, 27]. A short review for those models will be given in the next chapter.

On the experimental side, all known QCs are either diamagnets, paramagnets or spin glasses [28, 29]. The recent claim [30] of the existence of long-range magnetic order in icosahedral (i) R-Mg-Zn (R = rare earth) QCs was shown [31–33] to result from the

presence of magnetic impurities in the studied samples. Recent extensive neutron diffraction studies [34–38] of i R-Mg-Zn and i R-Mg-Cd QCs, which are of very high structural quality and which can be produced in a single-grain form, revealed the presence of short-range spin correlations at low temperatures and the absence of long-range magnetic order; these QCs are spin glasses. Figure (1-1) shows a photograph of a single-grain of i Ho-Mg-Zn [39].

Approximants to quasicrystals are complex crystalline alloys close in composition and with a structural similarity to quasicrystals [40]. In this thesis magnetic properties of the 1/1 approximant $Ag_{50}In_{36}Gd_{14}$ are investigated and compared with those of the icosahedral quasicrystal $Ag_{50}In_{36}Gd_{14}$.

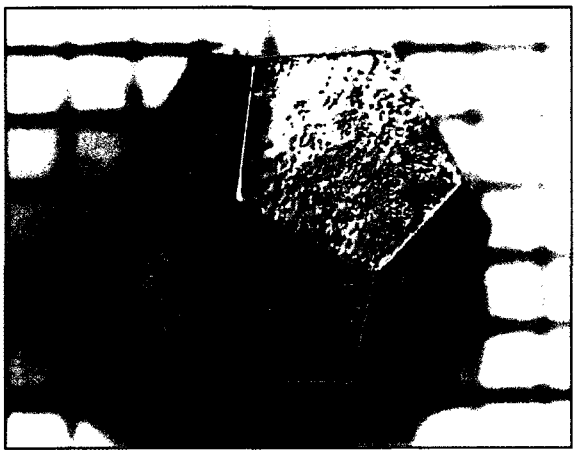

Figure (1-1) Photograph of a single-grain of icosahedral Ho-Mg-Zn quasicrystal. It is shown on a mm scale, the edges are 2.2 mm long [39].

1.2) Icosahedral quasicrystals

Quasicrystals can be classified as icosahedral (i-), octagonal (o-), decagonal (d-) or dodecagonal (dd-) phases [41]. Of special interest in this research are the icosahedral quasicrystals. Understanding the structure of quasicrystals is necessary when trying to explain how the structure affects the physical properties. According to crystallography rules the quasicrystal symmetry is forbidden. However, more than 100 years ago some

mathematicians had introduced a family of quasi-periodic and almost periodic functions which had a dense set of sharp peaks in the Fourier space [42]. Moreover, decagonal and quasicrystalline tilings were known to Islamic architecture in the 12^{th} century, as shown in figure (1-2) [43]. Finally, nature is full of fascinating beauty built with the *forbidden* fivefold symmetry, as can be seen in figure (1-3) [44, 45].

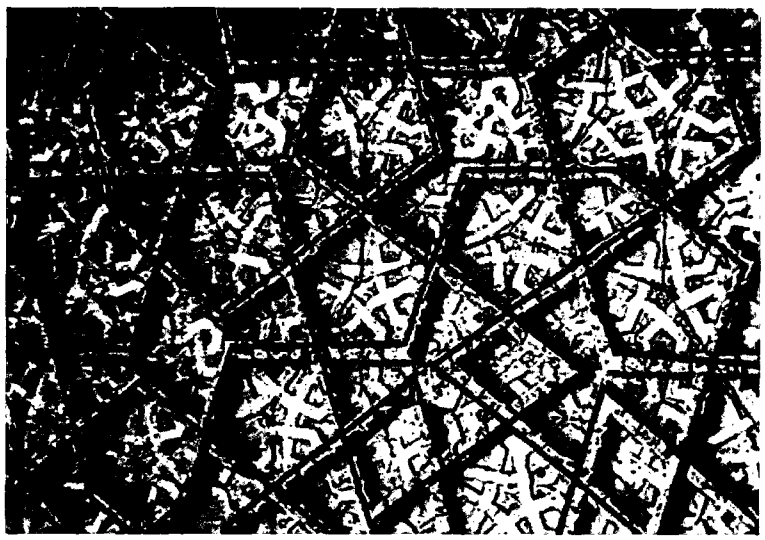

Figure (1-2) Photograph of a wall of octagonal tomb tower built in the 12^{th} century [43].

Figure (1-3) Left: photograph of a fivefold flower by Grata di Silenzio [44].
Right: photograph of another fivefold delicate violet flower by Aleksey Golyko [45].

1.2.1) Fibonacci chain

An important number that always will show in the calculations of quasicrystal

structure is the golden mean τ. It is an irrational number that can be defined as $\tau = 2\cos 36^o = \left(1+\sqrt{5}\right)/2$. The ratio of distances, center to vertex and center to mid-edge, in a pentagon is equal to $\tau/2$ [42]. The successive powers of the golden mean follow the Fibonacci series. A Fibonacci series or chain, also called the musical sequence, can be generated from two segments short (*S*) and long (*L*). Each *S* is replaced by *L* and each *L* is replaced by *L-S*. For example, we start by *S-L* then by applying the above rule we have *L-L-S*. Then applying the rule again on *L-L-S*, one has *L-S-L-S-L*. Appling this rule again leads to the chain *L-S-L-L-S-L-L-S*.... The chain can grow with a perfectly determined scheme but without periodicity. If one counts the number of times *L* is repeated, N_L, over the number of times *S* is repeated, N_S, in an long enough chain, the result will be the golden mean $\tau = \lim_{N_L+N_S\to\infty}\left(\frac{N_L}{N_S}\right)$.

1.2.2) Tiling

Penrose [46] showed that one can fill a two dimensional space using two different blocks by following simple rules (figure (1-4)). The two blocks are two rhombohedra, the first one with angles 72° and 108° and the second with angles 36° and 144°. The blocks are put beside each other in a way that the side arrows match for both blocks. The result is a perfect lattice without the need of periodicity.

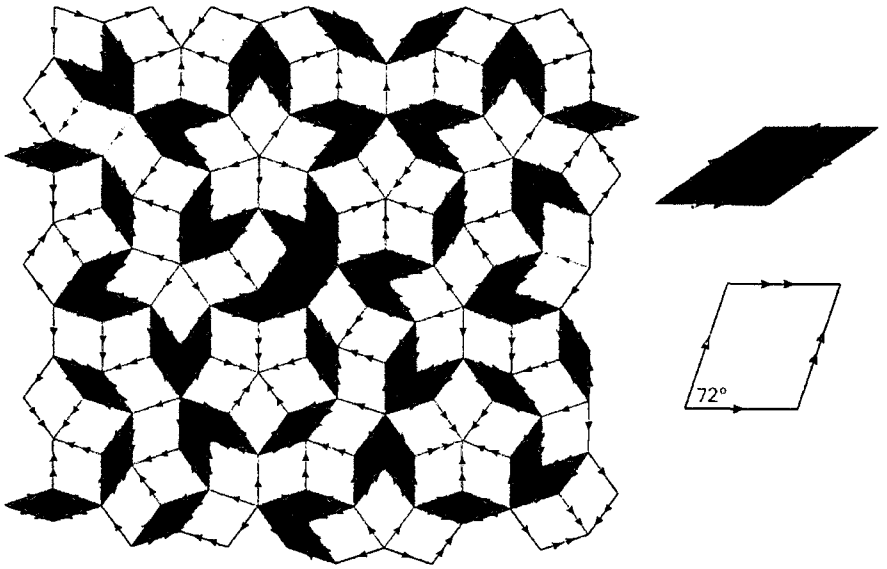

Figure (1-4) The Penrose pattern constructed from two different blocks [46].

In crystallography a crystal can be described in the reciprocal space using three Miller indices (*h, k, l*). In one dimension quasicrystals in the form of Fibonacci chain, one needs two independent variables to construct the chain. In three dimensions the number of independent reciprocal lattice vectors is more than the spatial dimension. Therefore, a hyperspace with six dimensions is needed to describe an icosahedral quasicrystal. The reciprocal lattice vector for an icosahedral quasicrystal can be written as:

$$G = (h + h'\tau)b_1 + (k + k'\tau)b_2 + (l + l'\tau)b_3, \qquad (1\text{-}1)$$

where b_1, b_2, b_3, are reciprocal lattice unit vectors. Using six Miller indices (h, h', k, k', l, l') one can describe the structure similarly to the classic crystal description.

The Fourier transform of the three-dimensional Penrose pattern matches well the experimental electron diffraction pattern. Figure (1-5) shows both the calculated and the experimental pattern for Al-Mn [47]. This suggests that the structure of an icosahedral is closely related to the three-dimensional Penrose pattern.

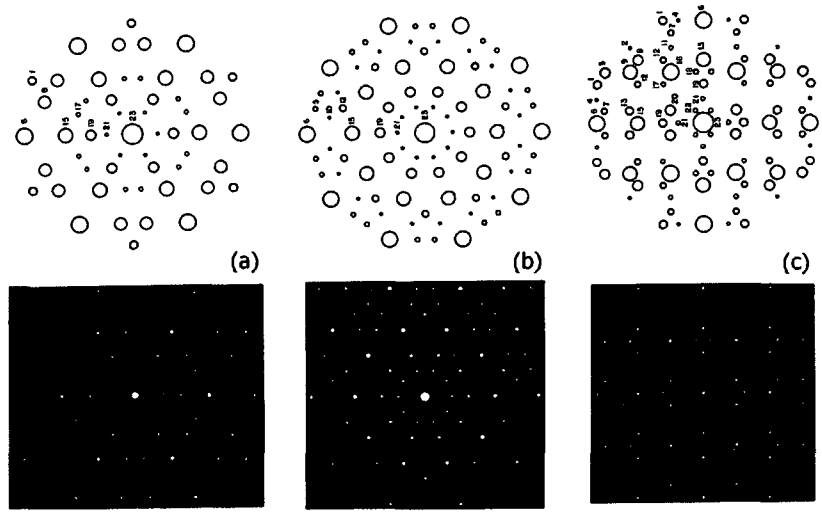

Figure (1-5) Bottom: experimental electron diffraction pattern of the icosahedral quasicrystal Al-Mn for (a) fivefold axis, (b) twofold axis, and (c) threefold axis. Top: the calculated Fourier transform of the three-dimensional Penrose tiling [47].

1.3) Roadmap of the thesis

An attempt is made in this thesis to search for such a long-range magnetic order in the recently discovered $Ag_{50}In_{36}Gd_{14}$ and $Zn_{77}Fe_7Sc_{16}$ icosahedral quasicrystals which contain the possible magnetic-moment carrying elements Gd and Fe.

Despite the fact that both icosahedral quasicrystals were found not to have such long-range magnetic order, they open the doors to a new direction of research. Hopefully, more researchers will be inspired by the fact that the nature of the spin-glass state in the icosahedral quasicrystal $Zn_{77}Fe_7Sc_{16}$ is fundamentally different from that of a canonical spin glass. Does this occur only for the icosahedral quasicrystal $Zn_{77}Fe_7Sc_{16}$ or is it a characteristic of all icosahedral quasicrystals?

This thesis is organized in the following manner. In chapter (2) a review of quasicrystals, types of magnetic ordering in solids, and spin glasses is presented. Chapter (3) describes the synthesis of the studied quasicrystals and the approximant and the experimental techniques used to investigate their structural and magnetic properties. In

chapter (4) the results of the structural and magnetic studies of the icosahedral quasicrystal $Ag_{50}In_{36}Gd_{14}$ are presented and discussed. Chapter (5) is devoted to the structural and magnetic studies of the icosahedral quasicrystal $Zn_{77}Fe_7Sc_{16}$. The results of the structural and magnetic studies of the 1/1 approximant $Ag_{50}In_{36}Gd_{14}$ are presented and discussed in chapter (6). Chapter (7) summarizes the results of this thesis and proposes further direction for research.

2) MAGNETIC THEORY AND BACKGROUND

2.1) Introduction

To understand the source of magnetism in a free atom, one needs to consider the orbital and spin motion of electrons in that atom and the interaction between them. The total orbital angular momentum for a given atom or ion is:

$$\vec{L} = \sum_i \vec{L}_i \,, \tag{2-1}$$

where the summation is over all the electrons, and the total spin angular momentum is [48]:

$$\vec{S} = \sum_i \vec{S}_i \,. \tag{2-2}$$

Each of the above two summations is equal to zero over a complete electron shell. The $\vec{L}$ and $\vec{S}$ are coupled through the Russell-Saunders coupling which is a spin-orbit interaction to form the total angular momentum $\vec{J} = \vec{L} + \vec{S}$. J can have multiplet values ranging from $J = (L-S), (L-S+1),$ to $(L+S-1), (L+S)$. The angular momenta $\vec{L}$ and $\vec{S}$ exert a torque on each other which force them to move around the constant vector $\vec{J}$, as can be seen in figure (2-1). The magnetic moment of that atom is [48]:

$$\vec{\mu} = -g\,\mu_B J, \tag{2-3}$$

where $g = \left[1 + \dfrac{J(J+1) + S(S+1) - L(L+1)}{2J(J+1)}\right]$ is called the Landé spectroscopic g-factor and $\mu_B = e\hbar/2mc$ is the Bohr magneton.

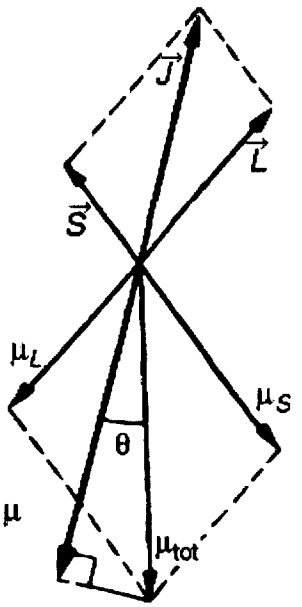

Figure (2-1) Spin-orbit interaction between the angular momenta $\vec{L}$ and $\vec{S}$. $\vec{\mu}_L = -\mu_B \vec{L}$, $\vec{\mu}_S = -g_e \mu_B \vec{S}$, $\vec{\mu}_{total} = \vec{\mu}_L + \vec{\mu}_S$, and $\vec{\mu} = \vec{\mu}_{total} \cos\theta$ [48].

2.2) Non-magnetic materials

2.2.1) Diamagnetism

When an atom or an ion has all the electronic shells filled the total orbital angular moment of each electron pair will sum to zero, as mentioned above, and no net magnetic moment will appear on the atom. Once such atom is placed in a magnetic field *B*, the field will interact with each electron spin. The field-induced energy shift in the ground-state energy due to this interaction is [49, 50]:

$$\Delta E_o = \frac{e^2}{12mc^2} B^2 Z \langle r^2 \rangle, \tag{2-4}$$

where Z is the total number of electrons in the atom and $\langle r^2 \rangle$ is the mean square distance of the electrons from the nucleus. The susceptibility of a solid composed of N such atoms or ions can be calculated, using the Larmor diamagnetic susceptibility or Langevin

susceptibility, as [49, 50]:

$$\chi = -\frac{N}{V}\frac{\partial^2 \Delta E_o}{\partial B^2} = -\frac{N}{V}\frac{e^2 Z}{6mc^2}\langle r^2 \rangle, \tag{2-5}$$

where V is the volume of the N atoms. One can conclude several facts from equation (2-5). First, the diamagnetic susceptibility values are negative which means that the induced moment in such atoms is in the opposite direction of the applied magnetic field. Second, diamagnetic susceptibility values are independent of temperature. Third, diamagnetic magnetization $M = \chi B_A$ values are small compared to the applied magnetic field B_A; they are of the order of 10^{-5}. The molar susceptibility can be defined as $\chi_m = \chi(N_A(V/N))$, where N_A is Avogadro's number. Molar susceptibility typical values are of the order of -10^{-4} to -10^{-6} cm^3/mol [50]. These small values of diamagnetic susceptibility can be neglected in non electron-closed-shell systems at low temperatures.

2.2.2) Paramagnetism

In contrast to the negative susceptibility contribution of diamagnetic atoms or ions, paramagnetism contribution to susceptibility is positive. When a free atom or ion has an odd number of electrons, or the inner electron shell is partially filled, and $\vec{J} \neq 0$, then that atom will have a net permanent magnetic moment μ which is described in equation (2-3). This free atom or ion will have a paramagnetic susceptibility.

The energy levels for such an atom when placed in a magnetic field B is [49]:

$$U = -m_J g \mu_B B, \tag{2-6}$$

where m_J is the magnetic quantum number that describes the component of $\vec{J}$ along the particle direction and has the values of J, J-1, . . . , -J. For example, the energy levels for

one electron, with a single spin and zero orbital spin in a magnetic field directed along the positive z-axis, are $U = \pm(\frac{1}{2})(2)\mu_B B$ and the total energy split is $2\mu_B B$, as can be seen in figure (2-2) [49]. In the low-energy state, the magnetic moment is parallel to the magnetic field.

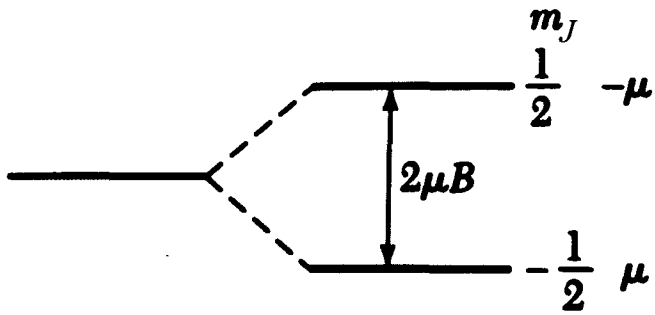

Figure (2-2) Energy levels splitting for one electron in a magnetic field directed along the positive z-axis [49].

In the general case where the orbital spin is not equal to zero, the atom has $2J+1$ equally spaced energy levels. The magnetization of N atoms is [49, 50]:

$$M = NgJ\mu_B B_J\left[\frac{gJ\mu_B}{k_B T}\right], \tag{2-7}$$

where B_J is called the Brillouin function and is defined as:

$$B_J[x] = \frac{2J+1}{2J}ctnh\left\{\frac{(2J+1)x}{2J}\right\} - \frac{1}{2J}ctnh\left\{\frac{x}{2J}\right\}. \tag{2-8}$$

In the limit of $\mu B/k_B T \langle\langle 1$ the susceptibility can be calculated as [49, 50]:

$$\chi_C \cong \frac{N p^2 \mu_B^2}{3k_B T} = \frac{C_C}{T}, \tag{2-9}$$

where p is called the effective number of Bohr magnetons and $p = g\sqrt{(J(J+1))}$. Equation

(2-9) is the Curie law, and C_C is the Curie constant. Figure (3-2) shows the schematic of the temperature dependence of the reciprocal magnetic susceptibility of a paramagnet [48]. The paramagnetic susceptibility of equation (2-9) is 500 times larger than the diamagnetic susceptibility of equation (2-5) at room temperature [50]. Consequently, in such an atom or ion, the positive contribution is much larger than the temperature-independent negative contribution to the total magnetic susceptibility and the diamagnetic contribution can be calculated and subtracted from the total susceptibility or neglected [51].

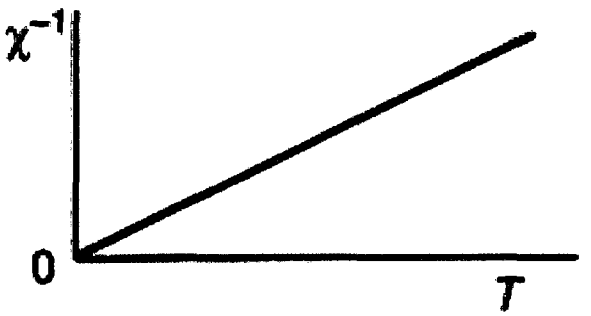

Figure (3-2) Schematic of the temperature dependence of the reciprocal magnetic susceptibility of a paramagnet [48].

For rare earth atoms or ions, where the $4f$ shell responsible for paramagnetism lies inside the atom or the ion, J is a good total quantum number and $p = g\sqrt{(J(J+1))}$. The calculated p and the experimental p are in good agreement. However, for transition metals $p = g\sqrt{(S(S+1))}$ [49, 51]. This is due to the fact that the $3d$ shell responsible for paramagnetism is in the outermost shell and subject to the strong influence of the inhomogeneous electric field (crystal field) produced by other ions in the crystal. This crystal field will destroy the spin-orbit interaction and split the degenerate $2L+1$ sublevels. This splitting will cancel the contribution of the orbital motion to J and quench the orbital moment [49, 51].

2.3) Ordered magnets

2.3.1) Ferromagnetism

If a material is composed of atoms or ions with permanent magnetic moments and has a spontaneous magnetic moment below some critical temperature T_C even in zero external magnetic field, then the material is ferromagnetic. Above T_C the thermal vibrations of the atoms or ions destroy the spin order and the material becomes paramagnetic. The spontaneous magnetic moment is due to some internal interaction field that tends to align the magnetic moments parallel to each other. This internal interaction field was suggested first by P. Weiss when he put forth his theory of ferromagnetism, called the Weiss field, or the exchange field B_E. This magnetic exchange field is not real in a sense that there is no current density associated with it. The magnitude of B_E is much larger than the magnitude of the real magnetic field that is induced by the magnetic ions in the crystal [49]. In his approach, each magnetic atom or ion in the solid experience a Weiss field that is proportional to the magnetization [48, 49]:

$$B_E = \lambda M, \tag{2-10}$$

where λ is the Weiss constant and it is independent of temperature.

To find the effect of B_E on the total susceptibility with the presence of an applied field B_A we can use [48]:

$$M = \chi_C (B_E + B_A) \tag{2-11}$$

Since we define the ferromagnet material as paramagnetic above T_C, then we can use equation (2-9) for χ_C and $\chi = (M/B)$, then equation (2-11) becomes:

$$M = \frac{C}{T}(\lambda M + B_A), \tag{2-12}$$

and the susceptibility is [48, 49]:

$$\chi_{C-W} = \frac{C}{T - T_C}; \quad T_C = \lambda C. \tag{2-13}$$

Equation (2-13) is the Curie-Weiss law and T_C is the Curie temperature. The physical meaning of the singularity of equation (2-13) when $T = T_C$ is that at T_C or below there exists a spontaneous magnetization. The Curie-Weiss constant can be determined from the experimental value of T_C as [48, 49]:

$$\lambda = \frac{3k_B T_C}{Ng^2 S(S+1)\mu_B^2}. \tag{2-14}$$

Equation (2-13) adds a correction to the predicted susceptibility values by the Curie law of ideal paramagnet in equation (2-9). This correction agrees with the experimental results at high temperatures for three-dimension ferromagnets. However, measured values of susceptibility near the T_C does not agree well with the predicted values by the Curie-Weiss law [50].

In the region between $T = 0$ and $T = T_C$ the magnetization of a ferromagnet follows the equation [48]:

$$M(T) = Ng\mu_B J\left[\frac{gJ\mu_B \lambda M(T)}{k_B T}\right][B_J], \tag{2-15}$$

and the reduced magnetization with the reduced temperature equation is [48]:

$$\frac{M(T)}{M(0)} = \left[\frac{3J}{J+1}\cdot\frac{T_C}{T}\cdot\frac{M(T)}{M(0)}\right][B_J]. \tag{2-16}$$

Equation (2-16) suggests that for a certain J value the change of the reduced magnetization with the reduced temperature depends solely on the Brillouin function defined in equation (2-8). Moreover, the magnetization of all ferromagnets which have the same J states should

follow the same unique curve that is generated by equation (2-16), which is independent on T_C or N. Figure (2-4) shows two ferromagnets, Fe and Ni, with the same J value, $J = \frac{1}{2}$, but with different T_C values; Fe (T_C = 1044 K) and Ni (T_C = 627 K) [48]. Figure (2-5) shows the schematic of the temperature dependence of the magnetization M, and the reciprocal magnetic susceptibility of a ferromagnet [48].

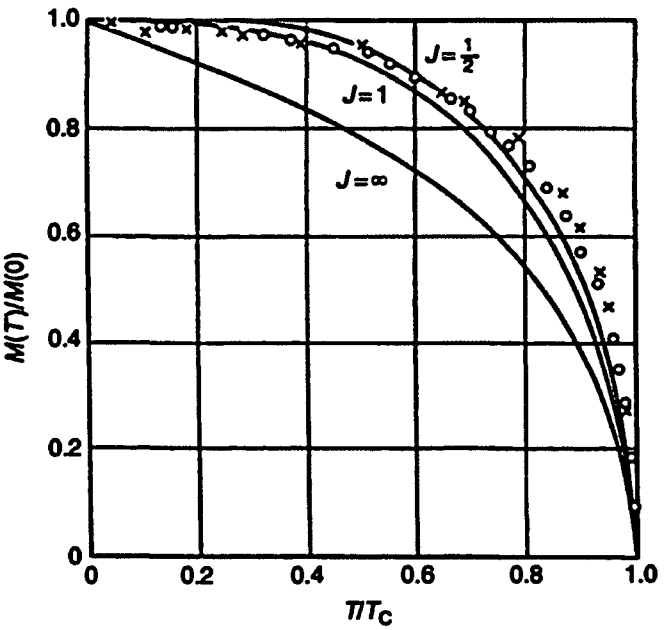

Figure (2-4) The reduced magnetization versus the reduced temperature calculated by equation (2-16) for several values of J. Included are Fe experimental data (x) and Ni experimental data (o) [48].

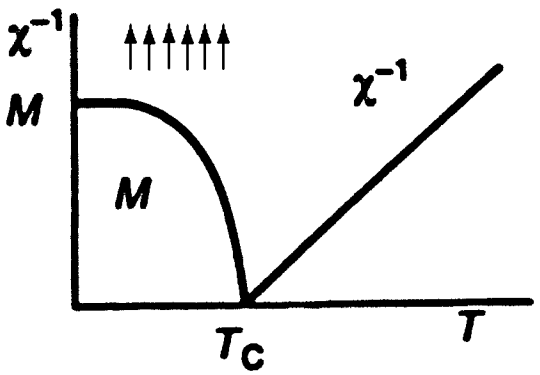

Figure (2-5) Schematic of the temperature dependence of the magnetization M, and the reciprocal magnetic susceptibility of a ferromagnet [48].

2.3.2) Antiferromagnetism

In a simple antiferromagnet all the local moments have the same magnitude but they belong to two different magnetic sublattices (X and Y) of the same magnetic structure. In the magnetically ordered state below certain temperature and within each sublattice the moments are parallel, but the net moments of the two sublattices are oppositely oriented. Examples of such magnetic sublattices are: simple cubic sublattice, which can be seen as two interpenetrating face-centered cubic lattices, and body-center cubic lattice, which can be seen as two interpenetrating simple cubic lattices, as can be seen in figure (2-6) [50]. Another example shown in figure (2-7) is the magnetic moments arrangement in the unit cell of the antiferromagnet YMn_2Ge_2 in the magnetically ordered state [48]. Due to this equal-opposite moments magnetic structure, the total magnetization of such simple antiferromagnets is zero.

In order to study the effect of the two sublattices on susceptibility we need to analyze the magnetic fields induced by both sublattices. The total field experienced by sublattice X by the moments of the sublattices is [48]:

$$\vec{B}_X = \vec{B}_A + N_{XX}\vec{M}_X + N_{XY}\vec{M}_Y \tag{2-17}$$

and total field experienced by sublattice Y by the moments of the sublattices is:

$$\vec{B}_Y = \vec{B}_A + N_{YY}\vec{M}_Y + N_{YX}\vec{M}_X, \tag{2-18}$$

where the sublattice moments have the same absolute value as $\left|\vec{M}_X\right| = \left|\vec{M}_Y\right| = \frac{1}{2}NgJ\mu_B$ and the intra-sublattice molecular field constant $N_{XX} = N_{YY} = N_1$ is different in magnitude and sign of the inter-sublattice molecular field constant $N_{XY} = N_{YX} = N_2$. Following the same

argument of deriving equation (2-13) but for two sublattices, the susceptibility of a simple antiferromagnet above the magnetic ordering temperature (Néel temperature) is [48]:

$$\chi_P = \frac{C}{T-\theta}; \quad \theta = \tfrac{1}{2}C(N_1 + N_2), \tag{2-19}$$

and the Néel temperature is $T_N = \frac{1}{2}C(N_1 - N_2)$. The paramagnetic Curie temperature does not equal to the Néel temperature. In fact $T_N > \theta$ because N_2 is negative. In many types of antiferromagnets the absolute value of the inter-sublattice molecular field constant is larger

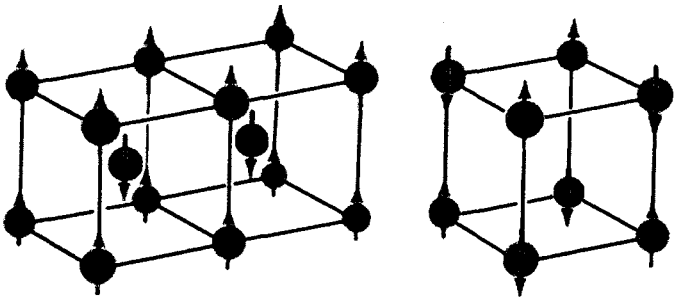

Figure (2-6) Two simple antiferromagnetic spin arrangements for (a) body-center cubic lattice and (b) simple cubic lattice [50].

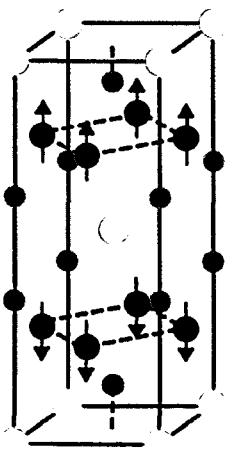

Figure (2-7) Simple antiferromagnetic spin arrangements in the unit cell of YMn_2Ge_2 below its Néel temperature T_N = 395 K. Yellow circles represent the Y atoms, the green circles represent Ge atoms, and the blue circles represents the magnetic Mn atoms [48].

than the absolute value of the intra-sublattice molecular field constant which will lead to a

negative θ. Figure (2-8) shows the schematic of the temperature dependence of the magnetization M, and the reciprocal magnetic susceptibility of an antiferromagnet [48].

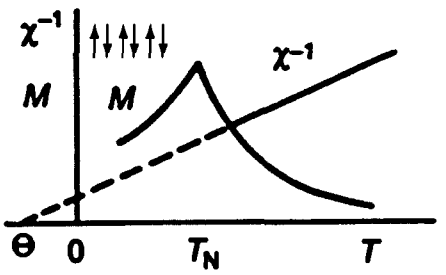

Figure (2-8) Schematic of the temperature dependence of the magnetization M, and the reciprocal magnetic susceptibility of an antiferromagnet [48].

Below the Néel temperature, the temperature depends of the magnetization and the susceptibility depends on the direction of the applied magnetic field (parallel or perpendicular) with respect to a chosen magnetic direction of an antiferromagnet crystal. In a single crystal antiferromagnet, when an applied field is perpendicular to the easy magnetization direction for example, the perpendicular net magnetization from the two sublattices in the direction of the applied field is [48, 49]:

$$M_{\perp} = 2M \sin\varphi, \tag{2-20}$$

where 2φ is the angle between the two spins moments $\vec{M}_X$ and $\vec{M}_Y$, as shown in figure (2-9) and $\sin\varphi = -\frac{B_A}{2MN_2}$. The perpendicular susceptibility is then [48]:

$$\chi_{\perp} = \frac{1}{|N_2|}. \tag{2-21}$$

As can be seen from equation (2-21), the perpendicular susceptibility for an antiferromagnet below the Néel temperature is independent of temperature and can be used to determine the absolute value of the inter-sublattice molecular field constant experimentally.

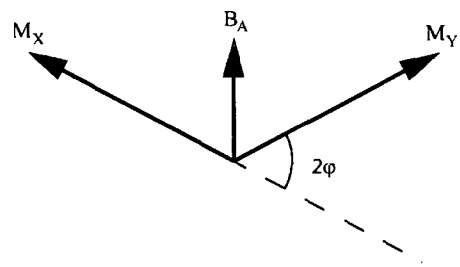

Figure (2-9) The perpendicular applied magnetic field to the easy magnetization direction of a single crystal antiferromagnet and the two sublattices moments [48].

In the absence of any field (parallel or perpendicular) the exchange field will lead to the splitting of the *2J+1* ground-state in both sublattices. As a result, in the two sublattices the statistical average value of $\langle \mu_z \rangle$ is the same but has opposite direction. The magnetization of each sublattice is proportional to $\langle \mu_Z \rangle$ by the relation $M = \frac{1}{2} N \langle \mu_Z \rangle$. When a parallel magnetic field is applied to the easy magnetization direction the parallel susceptibility can be written as [48]:

$$\chi_{\parallel} = \frac{\Delta M_X + \Delta M_Y}{B_A}. \qquad (2\text{-}22)$$

At T = 0 K, there will be no change in the magnetization since for each sublattice only the lowest level is occupied and we have $\Delta M_X = \Delta M_Y = 0$. As a result, the parallel susceptibility (equation (2-22)) will be equal to zero.

As the temperature is increased from the absolute zero, *2J+1* levels will start to be occupied. The applied parallel magnetic field will make the total splitting for the two sublattices different, and the level occupations will be different for both sublattices. When temperature is increased more, the difference in the level occupations becomes bigger. As a consequence to this, the difference between $\langle \mu_Z \rangle$ of the sublattices becomes stronger and the parallel susceptibility will increase until the ordering temperature is reached [48, 49].

In the case of polycrystalline antiferromagnetic samples the polycrystalline susceptibility (χ_{poly}) can be shown to be [48]:

$$\chi_{poly} = \tfrac{1}{3}\chi_{\parallel} + \tfrac{2}{3}\chi_{\perp},\ 0 < T < T_N, \tag{2-23}$$

$$\chi_{poly} = \chi_{\parallel} = \chi_{\perp},\quad T = T_N, \text{ and} \tag{2-24}$$

$$\chi_{poly} = \tfrac{2}{3}\chi_{\perp},\quad T = 0. \tag{2-25}$$

Once the temperature is above the ordering temperature, the magnetic ordering in the system will be destroyed by the thermal vibrations in the lattice and the system becomes paramagnetic.

2.3.3) Ferrimagnetism

A ferrimagnet has two dissimilar magnetic sublattices (X and Y) of different magnetic structures or different magnetic moments. Within each magnetic sublattice the magnetic moments are aligned parallel to each other. However, between the magnetic sublattice X and sublattice Y the alignment of the moments is antiparallel. Figure (2-10) shows an example of such magnetic arrangements for $GdCo_5$. Figure (2-11) shows a schematic of the temperature dependence of the magnetization M, and the reciprocal magnetic susceptibility of a ferrimagnet.

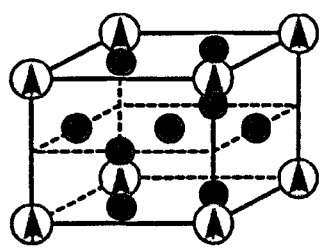

Figure (2-10) Ferrimagnetic magnetic moments arrangements of the $GdCo_5$ unit cell. The green circles are Co atoms and the yellow are Gd atoms [48].

Following a similar argument of deriving equation (2-19), but with the differences: the

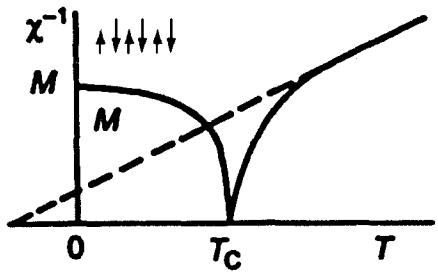

Figure (2-11) Schematic of the temperature dependence of the magnetization M, and the reciprocal magnetic susceptibility of a ferrimagnet [48].

two sublattices do not have the same magnetic structure and the two moments are not equal, one can find the relation of the ferrimagnetic susceptibility above the ferrimagnetic Curie temperature as [48, 49]:

$$\chi_P = \frac{M_X + M_Y}{B_A} = \frac{T(C_X + C_Y) - 2\mu C_X C_Y}{T^2 - (\mu^2 C_X C_Y)}, \tag{2-26}$$

where $M_X = \frac{C_X(B_A - \mu M_Y)}{T}$, $M_Y = \frac{C_Y(B_A - \mu M_X)}{T}$, and the ferrimagnetic Curie temperature is $T_C = \sqrt{\mu^2 C_X C_Y}$.

2.4) Spin glasses

2.4.1) Introduction

A spin glass can be defined as a disordered and frustrated system with random interacting magnetic moments on the lattice, characterized by a random freezing of the magnetic moments without a long-range order at a well defined temperature, T_f [52, 53]. Below T_f the spin glass condition state is $\sum_i S_i = 0$, where the sum is over all the spin states and the time correlation function $\langle S_i(t) S_i(0) \rangle$ remains finite as $t \to \infty$. Far above T_f the spin glass is a paramagnetic system [51].

Experimentally, spin glasses show interesting magnetic properties such as:

- There is a clear distinction between the zero-field-cooled (ZFC) and field cooled (FC) magnetic susceptibility curves, as shown in figure (2-12) [52]. The point where the two curves meet is T_f [51, 52].
- There exist a remanence and a magnetic relaxation effect below T_f when the applied magnetic field changes [54].
- The freezing temperature is dependent on the time scale of the measurement. For ac magnetic susceptibility measurements as shown in figure (2-13) [55] or Mössbauer spectroscopy measurements [56], T_f will shift towards a higher temperatures as the frequency of the measurement increases.
- Neutron diffraction studies show no Bragg peaks below T_f, demonstrating that there is no long-range magnetic interaction [51, 54].

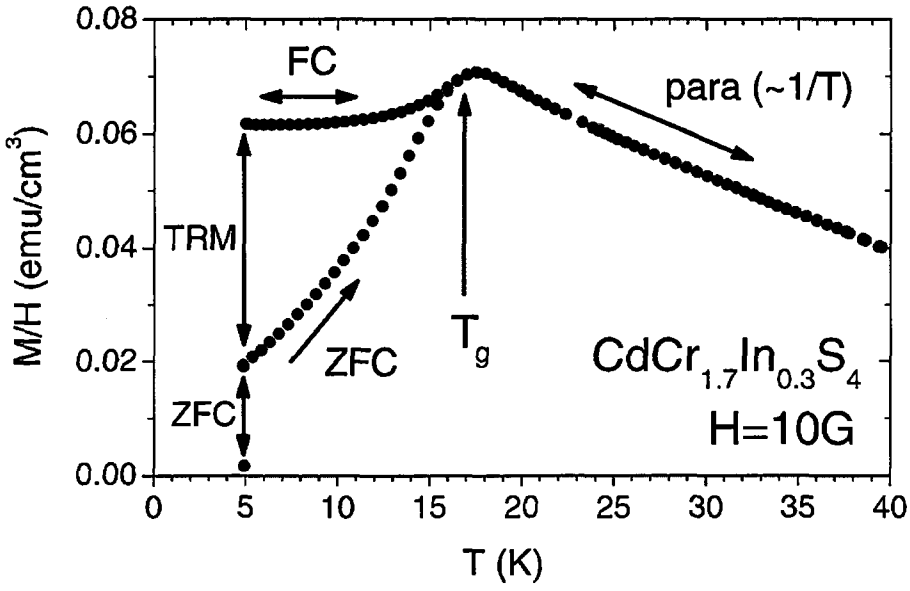

Figure (2-12) The zero-field cooled (ZFC) (green circles) and field-cooled (FC) (red circles) susceptibility curves of the $CdCr_{1.7}In_{0.3}S_4$ thiospinel spin-glass. TRM is the thermoremanent magnetization, T_g is the glass temperature, and para is the paramagnet region [52].

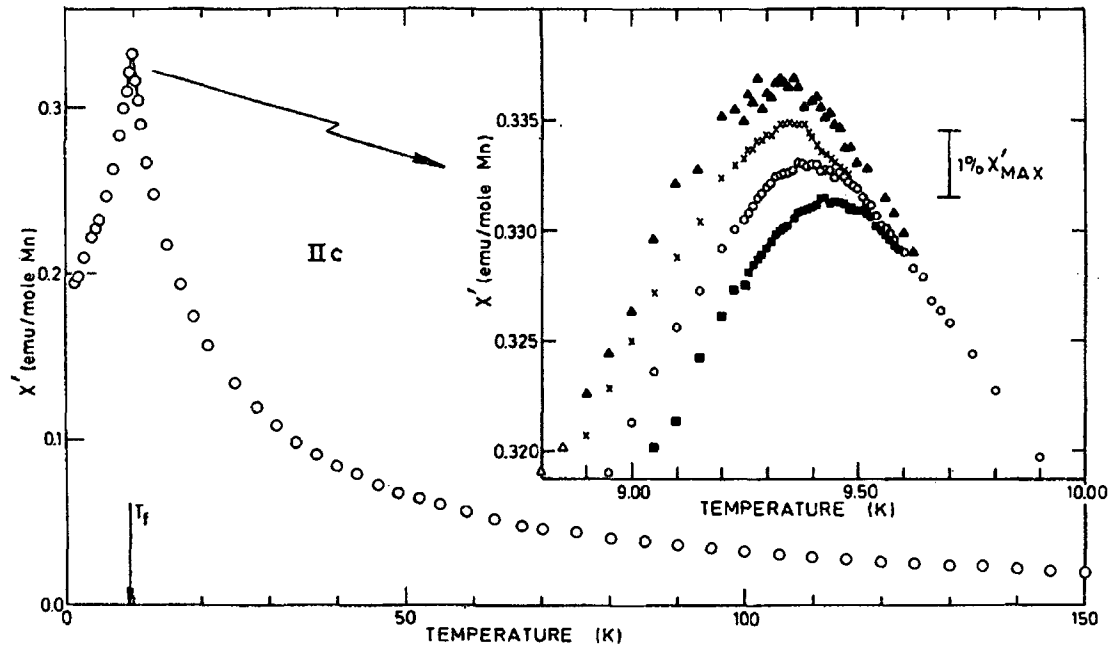

Figure (2-13) Zero field (ZF) ac real susceptibility χ' as a function of temperature for (Cu-0.94 at.% Mn, powder). Measuring frequencies: red squares 1330 Hz; green circles 234 Hz; black crosses 10.4 Hz; and blue triangles 2.6 Hz [55].

To achieve the randomness condition experimentally, one can dilute magnetic ions such as Mn, Gd, Fe, etc, in small concentrations, in non magnetic noble metals such as Au, Ag, Cu, etc. These dilute magnetic alloys are often called canonical spin glasses [51, 52]. Recent experimental work by several research groups has been devoted towards creating such spin glass systems with the two conditions of frustration and randomness using icosahedral quasicrystals [57–65]. Since the discovery of spin glasses in 1930, a lot of theories have been suggested to explain the physics of those alloys. Among those, two main different approaches have been utilized, the mean field approach and the phenomenological models.

2.4.2) Mean-field theory

Edward and Anderson (EA) laid down the foundations of the mean-field theory for

spin glasses [66]. In a spin glass, the transition of each spin from paramagnetic interaction above T_f, to a locked or frozen preferred direction based on random orientation over the whole distribution of sites in the solid below T_f, requires a type of order parameter. EA suggested that if a specific spin S_i at site i is frozen into its ground state, then the probability, q, of finding the same specific spin pointing in the same direction after a long time later, does not equal to zero [66]:

$$q = \left\langle S_i^{(1)} \cdot S_i^{(2)} \right\rangle \neq 0 , \tag{2-27}$$

where $S_i^{(1)}$ is the spin observation at t_1, $S_i^{(2)}$ is the same spin observation at long time later t_2, and $\langle ... \rangle$ is the random average. One expects that $q = 1$ at $T = 0$ and $q \to 0$ as $T \to T_f$.

Assuming random magnetic bonds in a three dimension square lattice the EA model uses a standard hamiltonian [51]:

$$\mathrm{H} = -\sum_{ij} J_{ij} S_i \cdot S_j . \tag{2-28}$$

The classical spins on sites i and j interact through the exchange couplings J_{ij} which are randomly chosen using a gaussian distribution [51, 66]:

$$P(J_{ij}) = \frac{1}{\sqrt{2\pi\Delta_{ij}^{\,2}}} \exp\left(-\frac{J_{ij}^2}{2\Delta_{ij}^2} \right), \tag{2-29}$$

where Δ_{ij} depends on the lattice separation between the sites i and j. The free energy is then given by the partition function Z [51, 66]:

$$F = -k_B T \ln Z = -k_B T \, Tr\left(\exp \frac{-\mathrm{H}}{k_B T} \right). \tag{2-30}$$

The function $\ln Z$ must be averaged over the distribution $P(J_{ij})$ which is cumbersome.

However, a replica trick can be used and one can write $\ln Z$ as [51, 66]:

$$\ln Z = \lim_{n\to 0}\left[\frac{1}{n}\left(Z^n - 1\right)\right], \tag{2-31}$$

where n is an integer. EA showed [66] that once the order parameter is known, the magnetic susceptibility and the specific heat can be determined. We have [51, 66]:

$$q\left(T \to T_f\right) = -\frac{1}{2}\left[1 - \left(\frac{T_f}{T}\right)^2\right] \tag{2-32}$$

and

$$q\left(T \to 0\right) = 1 - \sqrt{\frac{2}{3\pi}}\frac{T}{T_f}. \tag{2-33}$$

Then we can write the magnetic susceptibility as [51, 66]:

$$\chi\left(T \le T_f\right) = \frac{\left(g\mu_B\right)^2}{3k_B T} - O\left(T_f - T\right)^2, \tag{2-34}$$

and

$$\chi\left(T \to 0\right) = \frac{\left(g\mu_B\right)^2}{3k_B T}\frac{T}{T_f}\sqrt{\tfrac{2}{3}\pi} = \text{constant}. \tag{2-35}$$

The specific heat is [66]:

$$C_V\left(T \le T_f\right) = +\lambda\left(1 - q^2\right) - 4\lambda^2 q\frac{\partial q}{\partial \lambda}, \tag{2-36}$$

and

$$\frac{C_V\left(T \to 0\right)}{k_B} = \lambda\left[-\frac{\left(1-q\right)^3 + \frac{\left(1+3q^2\right)}{2\lambda q}}{3q - 1 + \frac{1}{2\lambda q}}\right] = \text{constant}. \tag{2-37}$$

Fischer [67] extended the EA model and used a quantum spins $\frac{1}{2}$ instead of classical spins. His results of the calculated magnetic susceptibility and the specific heat are shown in figure

(2-14).

While the EA model magnetic susceptibility prediction in figure (2-14) agrees well with the experiments, it is clear that the cusp in specific heat predicted by the EA model does not exist experimentally and that the EA mean-field approximation assumption needs improvement.

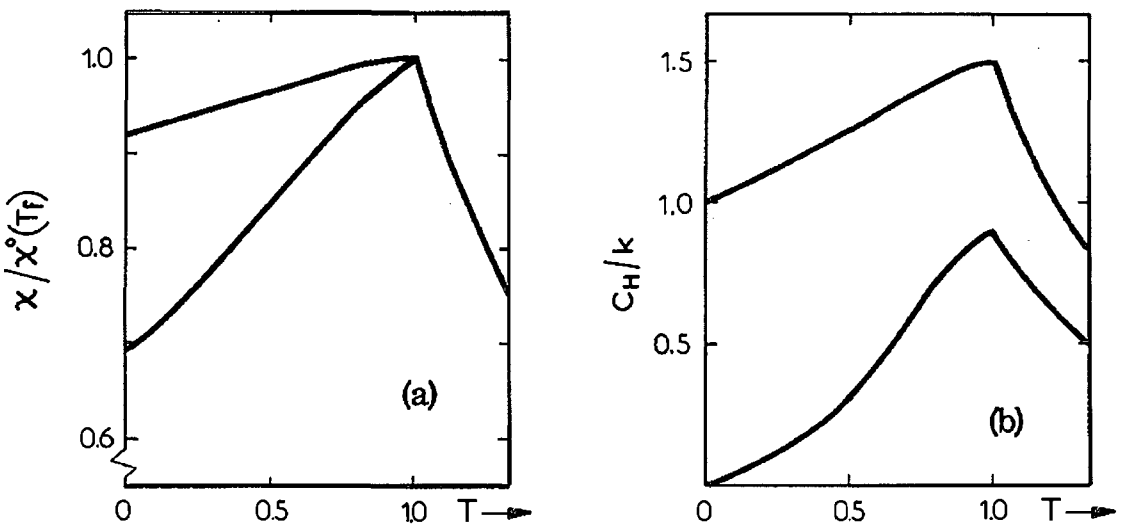

Figure (2-14) The calculated (a) magnetic susceptibility and (b) the specific heat versus the reduced temperature using the EA model for two spin values. The red lines are for $S = \frac{1}{2}$ and the green lines are for $S = \infty$ [67].

To overcome this problem in the EA model, Sherrington and Kirkpatrick (SK) [68] suggested that the assumption made in $P(J_{ij})$, equation (2-29), is physically wrong. Instead, they proposed that $P(J_{ij})$ should be of the form [4, 21]:

$$P(J_{ij}) = \frac{1}{\sqrt{2\pi\Delta'^2_{ij}}} \exp\left(-\frac{(J_{ij} - J'_o)^2}{2\Delta'^2_{ij}} \right), \tag{2-38}$$

where a mean, J'_o, has been added for the possibility of ferromagnetism in the Gaussian function. Because the infinite-range interactions require the scaling of both J'_o and Δ' as

$J_o^{'} = J_o/N$ and $\Delta' = \Delta/\sqrt{N}$, then equation (2-38) becomes [51, 68]:

$$P(J_{ij}) = \sqrt{\frac{N}{2\pi}}\frac{1}{\Delta_{ij}}\exp\left(-\frac{N\left(J_{ij}-\frac{J_o}{N}\right)^2}{2\Delta^2{}_{ij}}\right). \tag{2-39}$$

In their long mathematical calculations they repeat the same replica trick as in equation (2-31) and take the thermodynamic limit $N \to \infty$ and then the replica limit $n \to 0$. They use what is called the replica-symmetry solution by assuming all the various replicas to be the same. SK showed that the spin-glass order parameter is [51, 68]:

$$q = q_{\alpha\beta} = \left\langle \left\langle S^{\alpha} S_{\beta} \right\rangle_T \right\rangle_C, \tag{2-40}$$

and the ferromagnetic parameter is:

$$m = m_{\alpha} = \left\langle \left\langle S^{\alpha} \right\rangle_T \right\rangle_C. \tag{2-41}$$

The SK results for the simultaneous equations for q and m are [51, 68]:

$$q = \frac{1}{\sqrt{2\pi}}\int \exp\left(\frac{-z^2}{2}\right)\tanh^2\left[\frac{\Delta q^{\frac{1}{2}}}{k_B T^z} + \frac{J_o m}{k_B T}\right]dz, \tag{2-42}$$

$$m = \frac{1}{\sqrt{2\pi}}\int \exp\left(\frac{-z^2}{2}\right)\tanh\left[\frac{\Delta q^{\frac{1}{2}}}{k_B T^z} + \frac{J_o m}{k_B T}\right]dz. \tag{2-43}$$

The SK magnetic susceptibility and specific heat are:

$$\chi(T) = \frac{[1-q(T)]}{k_B T - J_o[1-q(T)]} \tag{2-44}$$

$$C = \frac{N k_B \Delta^2}{(2k_B T)^2}. \tag{2-45}$$

For a given ratios of J_o/Δ, one can calculate both $q(T)$ and $m(T)$ and create a magnetic

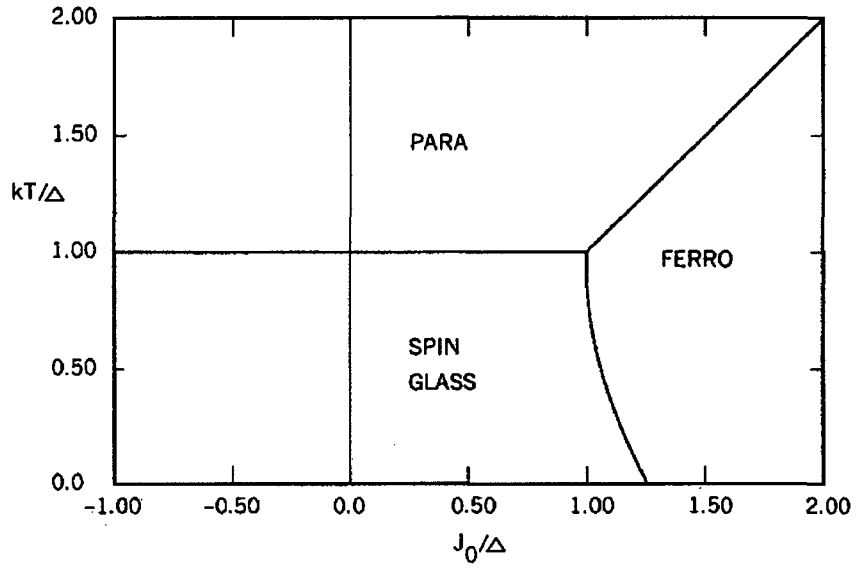

Figure (2-15) The magnetic phase diagram for Ising spins predicted by the SK model [68].

phase diagram as in figure (2-15) [68]. Figure (2-15) shows kT/Δ versus J_o/Δ plot for Ising spins centered at J_o with width Δ. Although the prediction of the SK model for the magnetic susceptibility agrees with the experimental results, and the model is accurate to predict a possible paramagnetic $\rightarrow$ ferromagnetic $\rightarrow$ spin glass phase transition, the model prediction of a cusp in the specific heat was wrong. Also SK pointed out to their theory shortcomings when they were referring to the unphysical negative entropy result predicted by their model *"but it leads to unacceptable consequences as* $T \rightarrow 0$*; for example if* $H = 0$, $m = 0$, *the* $T \rightarrow 0$ *limit of (2.28) is* $-k_B/2\pi$ *"* [68].

The SK model was carefully analyzed by de Almeida and Thouless (AT) [69]. AT showed that the SK solution was unstable for both the spin glass and the ferromagnetic phases at low temperatures, as shown in figure (2-16)(a) where the solution becomes unstable below certain AT line [69]. Also, the SK solution can be unstable in the presence of a magnetic field H at low temperatures. An example of this is when $H \neq 0$ and $J_o = 0$, as

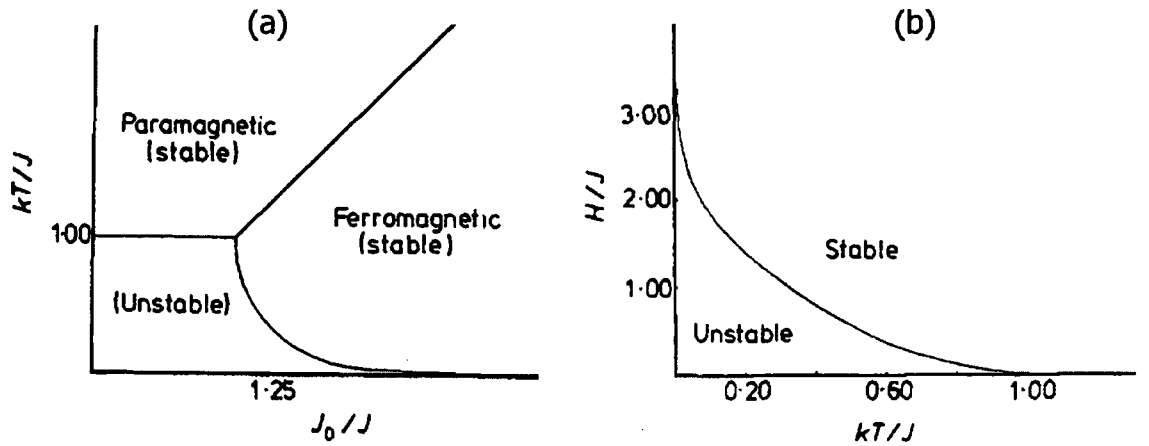

Figure (2-16) Phase diagrams showing the instability of the SK model (a) in the absence of a magnetic field and (b) in the presence of the magnetic field [69].

can be seen in figure (2-16)(b) [69]. Moreover, according to the SK solution, the spin glass magnetic susceptibility appears negative which is physically incorrect in the case of spin glasses [51, 69]. The reason for this instability is the SK assumption that all the replicas are the same, and all the states are symmetrical.

Thouless, Anderson, and Palmer (TAP) suggested adding a reaction field to the mean-field equations to avoid using the replica method completely when solving them [70]. If a spin $\langle S_i \rangle_T$ exists at site i, then it produces $J_{ij}\langle S_i \rangle_T$ field and induces $J_{ij}\langle S_i \rangle_T \chi_{ij}$ moment at site j. The moment at site j produces a reaction field back at site i as [51, 70]:

$$J_{ij} \cdot J_{ij}\langle S_i \rangle_T \chi_{ij} = J_{ij}^2 \langle S_i \rangle_T \frac{1}{k_B T}\left[1 - \langle S_j \rangle_T^2\right]. \tag{2-46}$$

The original mean-field equation can be modified by the reaction field (equation (2-46)) and then we have [51, 70]:

$$\langle S_i \rangle = \tanh\left[\frac{1}{k_B T}\sum_i J_{ij}\langle S_i \rangle_T - \left(\frac{1}{k_B T}\right)^2 \sum_i J_{ij}^2 \left(1 - \langle S_j \rangle_T^2\right)\langle S_i \rangle_T\right], \tag{2-47}$$

where $i = 1, 2, ..., N$. The resulting free energy from the TAP method is given by [4, 23]:

$$F_{TAP} = -\left\{\sum_{ij} J_{ij}\langle S_i\rangle_T\langle S_j\rangle_T - \frac{1}{2k_BT}\sum_{ij} J_{ij}^2\left(1-\langle S_i\rangle_T^2\right)\left(1-\langle S_j\rangle_T^2\right)\right\}$$

$$+\frac{1}{2k_BT}\sum_i\left[\left(1+\langle S_i\rangle_T\right)\ln\left(1+\langle S_i\rangle_T\right)\right.$$

$$\left.+\left(1-\langle S_i\rangle_T\right)\ln\left(1-\langle S_i\rangle_T\right)\right]. \qquad (2\text{-}48)$$

The first term in equation (2-48) represents the energy of the frozen spin glass. The second term corrects the paramagnetic energy correlation result by subtracting the term $\left(1-\langle S_i\rangle_T^2\right)$ from it. And the last term represents the entropy of N Ising spins.

The TAP model predicts several solutions of the mean-field theory which are physically possible and stable below the AT-line. Several stable solutions could mean that those different states can have different locally stable thermodynamics, even though the local minimum is not a global minimum [51, 70]. Although the TAP model is successful in its prediction of positive entropy, in contrary to the previous SK model, it predicts like previous mean-field theory models a cusp in the specific heat. It is clear from all the above trials that the mean-field theory for spin glasses needs a new theoretical treatment and an unconventional order parameter.

Parisi suggests an infinite number of order parameters when dealing with the mean-field theory for spin glasses, which leads to breaking the replica symmetry [71–74]. The metastable states of the mean-field theory spin glass system have a kind of ultrametric topology where the states can be represented as a hierarchical tree-like organization, as shown in figure (2-17) [75]. As the temperature is lowered from, say, T_1 to T_2 ($T_2 < T_1 < T_f$), a given metastable state α at T_1 gives 'birth' to N_α new states at T_2. Another illustration for the method of breaking the replica symmetry is shown in figure (2-18) [51], where α is

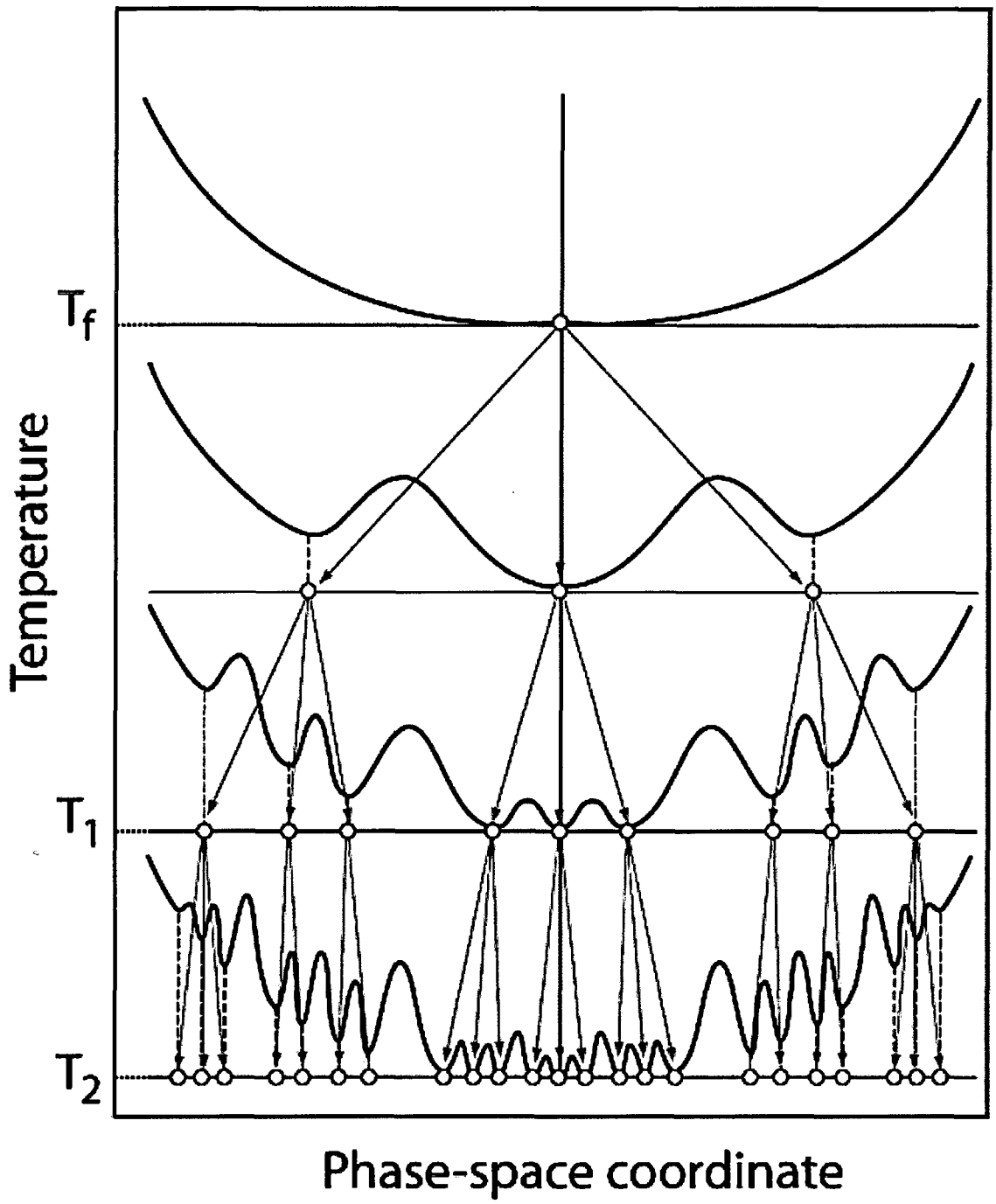

Figure (2-17) The hierarchical organization of the metastable states in a spin glass. The coarse-grained free-energy surface is represented at each level corresponding to a given temperature. When the temperature is decreased ($T_2 < T_1 < T_f$), each valley subdivides into others. Ageing refers to jumping of the system over ever increasing energy barriers during the waiting time t_w [75].

replica 1 and β is replica 4. Also, q_{12}, q_{34}, q_{56}, q_{78}, all have the value of q_{12} and all of them overlap, however, those replicas do not overlap with replicas 1 and 7, represented by q_{17}.

In mathematics, the replica overlap problem was known long time before it was

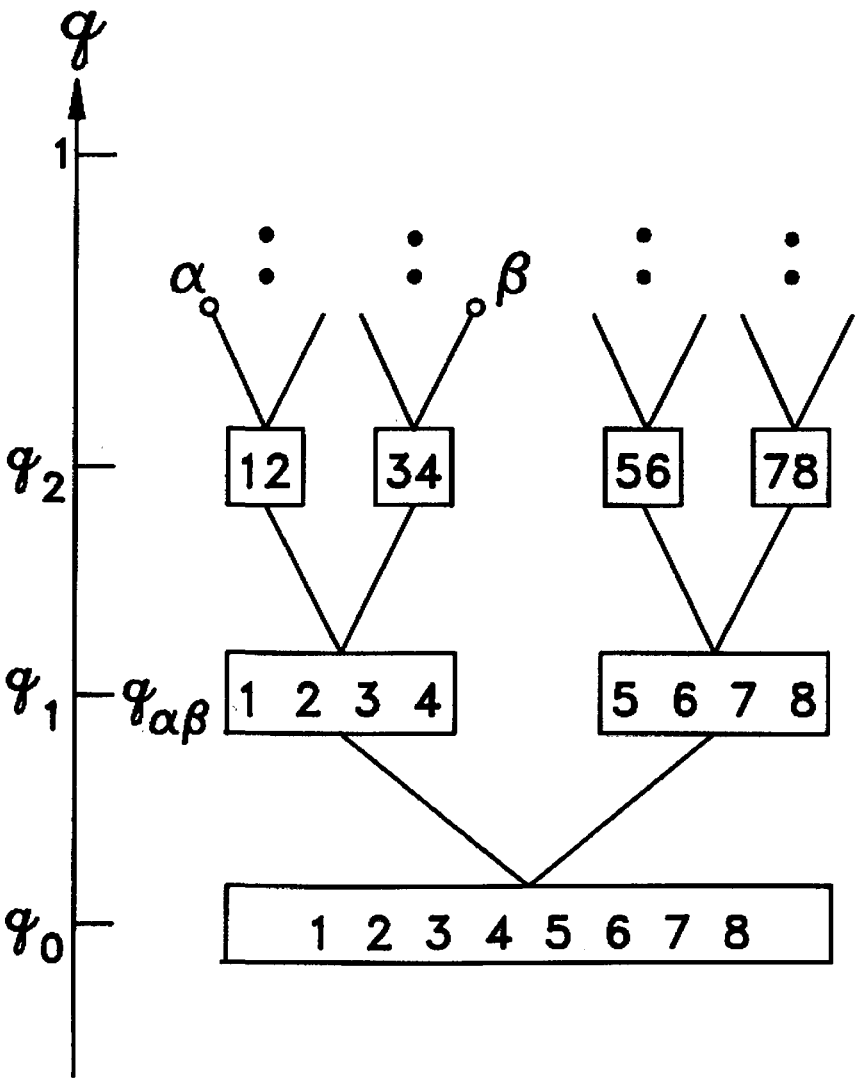

Figure (2-18) Tree representation of the Parisi replica symmetry breaking scheme [51].

introduced to the mean-field theory and already was treated in [76]. Ultrametricity can be defined in mathematics as "A metric space is a space endowed with a distance. A distance, in general, obeys the triangular inequity

$$d(A,C) \le d(A,B) + d(B,C), \tag{2-49}$$

where A,B,C are any three points of the space. The ultrametric inequity is a stronger inequality:

$$d(A,C) \le \max\{d(A,B) + d(B,C)\}. \tag{2-50}$$

A distance that satisfies the ultrametric inequality is called an ultrametric distance. A space endowed with an ultrametric distance is called an ultrametric space" [76].

In a spin glass, the overlap is equivalent to the ultrametric distance. In the Parisi treatment of the replicas the overlap between two Ising spins configurations or replicas is [51, 71–74]:

$$q^{\alpha\beta} = \frac{1}{N}\sum_{i=1}^{N} S_i^{\alpha} S_i^{\beta}. \tag{2-51}$$

The ultrametric inequality then becomes:

$$q^{\alpha\beta} \ge \min\left\{q^{\alpha\beta}, q^{\beta\gamma}\right\}. \tag{2-52}$$

Equation (2-52) states that for any three states α, β, and γ having mutual overlaps $q^{\alpha\beta}$, $q^{\alpha\gamma}$, and $q^{\beta\gamma}$, at least two of the overlaps are equal and the third is larger than or equal to the other two. The Parisi order parameter $q(x)$ can be defined as [51, 74]:

$$-\lim_{n\to 0}\frac{1}{n}\sum_{\alpha\beta} q_{\alpha\beta} = \int_0^1 q(x)dx. \tag{2-53}$$

When the temperature of a spin glass is lowered below the freezing temperature, the direction of different spins is aligned in many different ways such that all spins

arrangements have the same multi-degenerate free energy. Among those energy states, if an energy state has lower free energy then this energy state is pure equilibrium state, whereas it is a metastable state if the free energy is higher. For an equilibrium state α, it has a weighting probability [51]:

$$w_\alpha \propto \exp\left[\frac{1}{k_B T} F_\alpha\right], \tag{2-54}$$

where F_α is the free energy of α. One can differentiate equilibrium state α from another equilibrium state β, by defining a distance $d_{\alpha\beta}^2$ between the two states as [51]:

$$d_{\alpha\beta}^2 = \sum_i \frac{\left(\langle S_i \rangle_\alpha - \langle S_i \rangle_\beta\right)^2}{N}. \tag{2-55}$$

The original EA order parameter q_{EA} represents states that overlap with themselves, so $q_{EA} = q_{\alpha\alpha} = q_{\beta\beta}$. Then equation (2-54) can be written as [51]:

$$d_{\alpha\beta}^2 = 2\left[q_{EA} - q_{\alpha\beta}\right], \tag{2-56}$$

which is a simple relation between distance and overlap. The probability distribution $P(q)$ of the overlap between pure equilibrium states can be written as [51, 74]:

$$P(q) = \sum_{\alpha\beta} w_\alpha w_\beta \delta\left(q_{\alpha\beta} - q\right). \tag{2-57}$$

Equation (2-57) indicates that $P(q)$ is the probability of finding two states with an overlap q after weighting each state with its ensemble probability. The Parisi model susceptibility is defined as [51, 74]:

$$\chi = \frac{1}{k_B T} \int_0^1 \left(1 - q(x)\right) dx, \tag{2-58}$$

and the internal energy as:

$$U = -\frac{1}{2k_B T}\int_0^1 \left(1 - q^2(x)\right)dx \,. \tag{2-59}$$

By evaluating the integral in equation (2-53), one can find the value of $q(x)$ and hence evaluate the magnetic susceptibility and the entropy. In this model there is no cusp in the specific heat and the entropy is zero at 0 K, which marks the best model of the mean-field theory for spin glasses. However, Newman and Stein argue that Parisi model for spin glasses is not valid in any dimension and at any temperature [77]. They suggest also applying other models such as the droplet model, for Ising spin glasses [78, 79]. Many other papers [80–105] state that the slow dynamics in spin glasses can be explained using the analysis of phenomenological models like fractal cluster or droplet models, which are based on short-range interactions rather than the infinite-range interactions adopted in the mean-field theory for spin glasses.

2.4.3) Phenomenological models

2.4.3.1) Droplet model

Fisher and Huse presented a phenomenological scaling theory of droplet excitations for Ising spin glass in short-range interactions. They named it the droplet model [93, 100, 101]. In their model they define a droplet of length scale L containing site j (figure (2-19)) in its ground state and consider this state as the lowest energy excitation [101]. Due to randomness, the droplets can have complicated shapes and topologies. Outside the droplet the spins are aligned in the ground state Γ. Inside the droplet the spins are aligned opposite to the outside spins in the ground state $\overline{\Gamma}$. They also assume that the surface of the droplet is fractal. Those ground states cannot be lowered by flipping any finite collection of spins. The

model assumes a phase transition of the spin glass where the spin-reversal symmetry is broken. This phase transition occurs below T_f and it has only two pure-equilibrium states related to

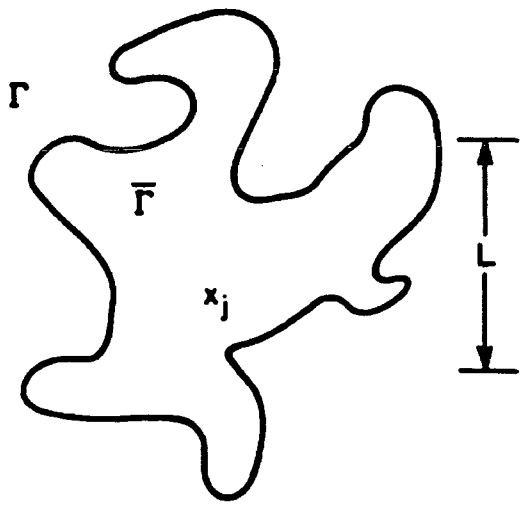

Figure (2-19) Schematic picture of the droplet model [101].

the global broken symmetry [51, 101].

The droplets have a broad distribution of free energy which can be described as [93, 100, 101]:

$$F_L \sim \mathrm{Y}(T) L^{\theta} \tag{2-60}$$

where $\mathrm{Y}(T)$ is the stiffness constant and θ is some exponent related to the dimension of the system d as:

$$\theta \le \frac{d-1}{2}. \tag{2-61}$$

The droplet scaling distribution of free energies for large L can be of the form [101]:

$$\rho_L(F_L) \approx \frac{1}{\mathrm{Y}L^{\theta}} \tilde{\rho}\left(\frac{F_L}{\mathrm{Y}L^{\theta}}\right), \tag{2-62}$$

where $\tilde{\rho}(x) = 2\left(e^{-x} - e^{-2x}\right)$. According to the model, the Ising spin glass state will be

destroyed when a constant magnetic field is applied on it by breaking the global spin-flip symmetry. When the system becomes unstable and is out of equilibrium due to any applied field, then the susceptibility is finite.

According to the droplet model, a droplet can be created and destroyed. To create a droplet, it is necessary to go over some free energy barrier $B \sim L^{\psi}$ which is larger than F_L, where ψ is a new independent exponent $\theta \leq \psi \leq d-1$. This creation or growth of the droplet to scale length L has a characteristic time which is needed to overcome the energy barrier. When a droplet of length L is created it will last for [51, 101]:

$$\tau = \tau_o \exp\left(\frac{B}{k_B T}\right). \tag{2-63}$$

The autocorrelation function (equation (2-63)) derived above has an extremely slow logarithmic decay of temporal correlations as:

$$C(t) \sim (\ln t)^{-\theta/\psi}. \tag{2-64}$$

The creation and destruction of the droplets determine the equilibrium low-frequency dynamics of the ordered phase. The real part of the magnetic susceptibility of the droplet model scales as [51, 101]:

$$\chi'(\omega) \sim |\ln \omega|^{-(\theta/\omega)}, \tag{2-65}$$

and the imaginary magnetic susceptibility part:

$$\chi''(\omega) \sim |\ln \omega|^{-1+(\theta/\omega)}. \tag{2-66}$$

2.4.3.2) Fractal cluster model

Another model based on the cluster scaling of spin glasses, which could be more applicable for real spin glasses, is the fractal cluster model. Malozemoff and Barbra [81, 90]

proposed a scaling theory for spin glasses based on previous work on percolation of infinite clusters [54, 84, 85–87]. The spin glass system is considered as a set of clusters of correlation length ξ which diverge as $\left[\left(T-T_f\right)/T_f\right]^{-\nu}$. The fractal clusters are assumed highly irregular, branched, and can have complicated shapes and topologies (figure (2-20)) [90]. The polarization of clusters is ignored because of the shape of the cluster. The interactions between clusters are also ignored due to the fact that those interactions are taken into account through the critical growth of the clusters. The fractal dimension is D, its correlation length is ξ, its volume is ξ^D, and its size is s_ξ. All the physical properties in the model depend on the cluster size. The magnetization of the cluster can have two values: $m_\xi = \mu_o s^{\frac{1}{2}}$ for random distribution of spins in the cluster and $m_\xi = \mu_o s$ for ferromagnetic distributions [51, 81, 90].

The cluster scale size distribution can be defined according to the percolation-scaling theory as [86, 90]:

$$n_s = s^{-\tau_\delta} f_s\left(\frac{s}{s_\xi}\right), \qquad \tau_\delta = 2+\frac{1}{\delta}, \tag{2-68}$$

where τ_δ is a critical exponent, $f_s(x)$ is a scaling function defined as $f_s(x)\to 0, \quad x>1$, and $f_s(x)=const., \quad x\to 0$. When there is no applied magnetic field we have [86, 90]:

$$\xi \propto \left|\left(\frac{T-T_f}{T_f}\right)\right|^{-\nu}, \tag{2-69}$$

$$s_\xi \propto \left|\left(\frac{T-T_f}{T_f}\right)\right|^{-\nu D}. \tag{2-70}$$

ξ_D/ξ_d is the equivalent order parameter to the mean-field theory for spin glasses, where d is

equal to the spatial dimension of the system. The model also defines a relaxation time of a cluster as [89]:

$$\frac{\tau}{\tau_o} = \left| \frac{T - T_f}{T_f} \right|^{-\nu z} , \tag{2-71}$$

where z is dynamical exponent.

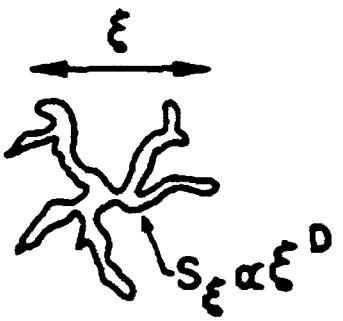

Figure (2-20) Schematic picture of the fractal cluster of the correlation length ξ, the volume ξ^D, and the size s_ξ [90].

Above T_f the fractal cluster model assume the spin glass as a superparamagnet. This is a direct result of the assumption that the clusters are rigid and do not interact with each other. When a magnetic field is applied to a spin glass above T_f then the only freedom for the clusters is either to rotate or change their size. The superparamagnetic susceptibility is [90]:

$$\chi = \frac{N}{B_A} \int n_s \mu_o s^\gamma \Omega \frac{\mu_o s^\gamma B_A}{k_B T} ds , \tag{2-72}$$

where N is the number density of spins, Ω is the Langevin function, and n_s is the number of clusters with spin s. The dynamic susceptibility for an Ising spin glass assuming Debye relaxation is [94]:

$$\chi(\omega) \propto \frac{1}{B_A} \int_0^{\infty} n_s s^{\frac{1}{2}} \frac{\tanh\left(\frac{s^{\frac{1}{2}} B_A}{k_B T}\right)}{1 + i\omega t}. \tag{2-73}$$

From the above equation one can get the real and imaginary parts of the magnetic susceptibility as [94]:

$$\chi'(\omega) \propto \frac{1}{T} (\omega t_o)^{\beta/\nu z} g_2(\omega t_o), \tag{2-74}$$

$$\chi''(\omega) \propto \frac{1}{T} \left[1 - (\omega t_o)^{\beta/\nu z} g_1(\omega t_o)\right]. \tag{2-75}$$

The scaling of the magnetic susceptibility in the fractal cluster model occurs for ω in contrast to the droplet model where the scaling occurs for $\ln \omega$. The net magnetization is given by [98]:

$$M \propto n_s m_\xi B_J \left(\frac{m_\xi B_A}{k_B T}\right). \tag{2-76}$$

When $m_\xi B_A \approx k_B T$ the system has a crossover permitting the clusters to align along the field. In analogy to the AT line, one can defined the crossover $B_A T$ line as [98]:

$$B_A \left[\frac{T - T_f}{T_f}\right]^{-[\phi/2]} = \text{const}, \tag{2-77}$$

where the crossover exponent $\phi = \nu D$.

Below T_f, one can imagine the picture of spin glass clusters as follows. The correlated clusters were rotating freely above the T_f, but now they are seeing the internal energy barriers of a frozen matrix. A frozen matrix is an infinite percolating cluster that forms at T_f. The barriers heights are fixed and independent of temperature. The energy barriers can slowdown or hinder the clusters rotation. However, those barriers can be

overcome via thermal activation. When the temperature is lowered more, the clusters size grows or becomes part of the frozen matrix [51]. Using the fractal cluster model for an Ising spin glass can lead to [51, 90]:

$$M \propto \int_0^\infty n_s s^{\frac{1}{2}} \tanh\left(\frac{\mu_o s^{\frac{1}{2}} B_A}{k_B T}\right) ds \,. \tag{2-78}$$

where n_s is the cluster-size distribution.

One can calculate the time decay of the magnetization below T_f that is predicted by the fractal cluster model assuming a weak field so as to use the B_J small-argument limit. When the field is turned off at $t = 0$ the reduced magnetization can be given as [98]:

$$\frac{M(t)}{M(t=0)} = \frac{\int_0^\infty s^{\frac{1}{2}-\tau} f\left(\frac{s}{s_\xi}\right)\left[\frac{\mu_o s^{\frac{1}{2}} B_A}{k_B T}\right] \exp\left(\frac{-t}{t'}\right) ds}{\int_0^\infty s^{\frac{1}{2}-\tau} f\left(\frac{s}{s_\xi}\right)\left[\frac{\mu_o s^{\frac{1}{2}} B_A}{k_B T}\right] ds}, \tag{2-79}$$

where the relaxation time t is exponential (which represents an average relaxation time for the clusters) and $\tanh(x) \cong x$. On can simplify the above equation using $t' = t_o s^x$, $t_o = t_{oo} \exp(E_B / k_B T)$, and $f\left(\frac{s}{s_\xi}\right) \approx \exp\left[\left(-\frac{s}{s_\xi}\right)^v\right]$. This will lead to [51, 88, 91]:

$$M(t) \propto \exp\left[\left(-\frac{t}{t_1}\right)^{1-n}\right], \tag{2-80}$$

where $n = x/(x+v)$ and $t_1 \propto s_\xi^x$. This is the common stretched exponential which is used to describe the slow relaxation of real spin glasses.

2.4.4) Dynamics in the Ising model

Since the mean-field model neglects the natural intrinsic dynamics in the original hamiltonian (equation (2-28)), it is necessary to introduce such time dependence separately via some equations of motion that couple spins to other degrees of freedom. This can be achieved through kinetic Ising model of Glauber [54, 106] or the soft-spin model [51, 54, 107].

2.4.4.1) Glauber model

Glauber introduced a time-dependent statics for the Ising model. Glauber considered a set on N individual spins interacting in a heat reservoir which causes them to change their spins randomly with time. Those individual spins are coupled among themselves via the assumption that the transition probability for any specific spin depends on the spin values of the surrounding spins.

Assuming there is no magnetic field, each spin is allowed to switch between spin states ($\sigma = +1$ and $\sigma = -1$). Then the probability $p(\sigma,t)$ that the spin takes on the value σ at a time t is [106]:

$$\frac{d}{dt}p(\sigma,t) = -\tfrac{1}{2}\alpha\, p(\sigma,t) + \tfrac{1}{2}\alpha\, p(-\sigma,t), \tag{2-81}$$

where $\frac{1}{2}\alpha$ is the rate for the spin to make a transition from one state to another per unit time. The mean spin then will decay exponentially with a relaxation time α^{-1} from any initial time as:

$$q(t) = q(0)\exp(-\alpha t). \tag{2-82}$$

The transition probability for an Ising spin can be written as:

$$w_i(\sigma_i) = \tfrac{1}{2}\alpha\{1 - \tfrac{1}{2}\lambda\sigma_i(\sigma_{i-1} + \sigma_{i+1})\}, \tag{2-83}$$

where $w_i(\sigma_i) = \frac{1}{2}\alpha(1-\lambda)$, $\frac{1}{2}\alpha$, $\frac{1}{2}\alpha(1+\lambda)$. The positive values of λ indicate that the coupling between individual spins is ferromagnetic whereas an antiferromagnetic coupling exists if λ is negative. The physical meaning of λ is that it describes the tendency of spins toward alignment. Its absolute value is less or equal to one. Glauber evaluated explicitly the frequency dependence of the magnetic susceptibility in the weak field limit for several situations. For example, the magnetic susceptibility for an Ising spin glass in a magnetic field is [106]:

$$\chi(\omega) = \frac{\mu^2 N}{k_B T}\frac{1+\eta}{1-\eta}\frac{\alpha(1-\lambda)}{\alpha(1-\lambda) - i\omega}, \tag{2-84}$$

and in the low frequency limit it is:

$$\chi(0) = \frac{\mu^2 N}{k_B T}\frac{1+\eta}{1-\eta} = \frac{\mu^2 N}{k_B T}\exp\left(\frac{2J}{k_B T}\right), \tag{2-85}$$

where $\eta = \tanh(J/k_B T)$.

2.4.4.2) Soft-spin model

In this model the autocorrelation function is defined as [51, 54, 107]:

$$q(t) = \left\langle \langle S_i(0) S_i(t) \rangle_T \right\rangle_C, \tag{2-86}$$

where $\langle ... \rangle_T$ is the thermal average and $\langle ... \rangle_C$ is the random average. The autocorrelation function is defined also in the dynamical scaling theory as:

$$q(t) \propto t^{-\gamma} Q_{\pm}\left(\frac{t}{\tau}\right), \tag{2-87}$$

where $Q_{\pm}(x)$ are universal scaling functions, γ is a critical exponent, and τ is the

characteristic time. The characteristic time and length ξ_{SG} are related by:

$$\tau \propto \xi_{SG}^{z} \propto \left(\frac{T - T_f}{T_f} \right)^{-z\nu}, \tag{2-88}$$

where ν is the critical exponent and z is a dynamical exponent. One can take the limit of $t \to \infty$ for $q(t)$:

$$\lim_{t\to\infty} q(t) = q_{EA} \propto \left(\frac{T - T_f}{T_f} \right)^{\beta}, \tag{2-89}$$

where $\beta = \gamma z \nu$ is the order parameter exponent.

Above the AT line where the SK model is valid, for $B_A = 0$ one gets [51, 54, 107]:

$$q(t) \propto t^{-\frac{1}{2}} Q_{+}\left(t \left(\frac{T - T_f}{T_f} \right)^{2} \right). \tag{2-90}$$

With a proper scaling function one can apply $Q_{+}(x) \propto \exp(-x)$ for $T > T_f$ and $t \to \infty$, then equation (2-90) becomes:

$$q(t) \propto \frac{t^{-\frac{3}{2}}}{\left(\frac{T - T_f}{T_f} \right)^{2}} \exp\left(-t \left(\frac{T - T_f}{T_f} \right)^{2} \right). \tag{2-91}$$

At $T = T_f$ equation (2-91) reduces to:

$$q(t) \propto \frac{1}{\sqrt{t}}. \tag{2-92}$$

When $B_A \neq 0$, the dynamical scaling holds assuming ($\beta = 1, \nu = \frac{1}{2}$). The autocorrelation function will have the form:

$$q(t) \propto t^{-\beta/z\nu}\,\tilde{q} + \left(t\left[\frac{T - T_{AT}(B_A)}{T_{AT}(B_A)} \right]^{z\nu} \right). \tag{2-93}$$

Below the AT line the SK model is not stable due to the fact that the kinetic coefficient becomes negative. This will cause the correlations to diverge exponentially with time. One can start the soft-spin model calculations by taking the order parameter to be [51, 54, 107]:

$$q(t) = \left\langle \left\langle S_i(0) S_i(\tau_x) \right\rangle_T \right\rangle_C \quad 0 \le x \le 1, \tag{2-94}$$

where τ_x is the relaxation time. When $x_2 > x_1$ then we have $\tau_{x_1} >> \tau_{x_2}$, so when $x \to 0$ then the relaxation time is very long. Then the statistical-mechanics order parameter after very long time, which is necessary to achieve equilibrium, is:

$$q = q(0) = \lim_{N\to\infty} \lim_{t\to\infty} q(t), \tag{2-95}$$

Equation (2-95) indicates that after a long enough time, when the magnetic field is set to zero, all the correlations have decayed away, i.e., the system reached equilibrium. On the other hand, when $x \to 1$ then we have the EA model order parameter

$$q_{EA} = q(1) = \lim_{t\to\infty} \lim_{N\to\infty} q(t). \tag{2-96}$$

When equations (2-95) and (2-96) are compared one realizes that the order parameter is determined depending on which limit comes first.

The dynamical magnetic susceptibility measured at frequency $\omega_x = 1/\tau_x$ is:

$$k_B T \int_0^{\tau_x} \chi_{ii}(t)\,dt = 1 - q_{EA} + \nabla(x). \tag{2-97}$$

The above equation is valid at short times $x \to 1$, whereas at $x = 1$ $\nabla(1) = 0$ and equation (2-97) reduces to the EA-form. The stability condition for the above equation, using

$M = \tanh\left(\tilde{B}_A / k_B T\right)$ is:

$$\frac{J^2}{(k_B T)^2}\left[1 - 2q(1) + \langle M^4 \rangle\right] = 1, \tag{2-98}$$

where $\tilde{B}_A$ is the local field which will freeze at a time scale τ_x and J is the width of the Gaussian-distribution of the exchange interactions.

When the applied magnetic field goes to zero the only stable solution is the one at equilibrium susceptibility $\chi = \chi_{ii}$

$$k_B T_\chi = 1 - q(1) + \nabla(0). \tag{2-99}$$

In the limit of $x \to 0$, $\nabla(x) = q(1) - 1 + k_B T/J$ which leads to $\chi = 1/J$. Ac susceptibility (the short time limit) is given by:

$$\chi_{ac} = \frac{1}{k_B T}(1 - q_{EA}), \tag{2-100}$$

and the true equilibrium susceptibility which is far beyond an experimental time, is

$$\chi_{\text{true equilibrium}} = \frac{1}{k_B T}(1 - q_{EA} + \nabla(0)). \tag{2-101}$$

One can describe the dynamics of an Ising spin glass below T_f using figure (2-21) [98]. There are two main dynamical processes: firstly, non-exponential-relaxation processes that are confined to an individual valley; and secondly the hopping processes between one valley to another. The second processes appear on much longer time scales and they diverge with the size of the system as $\log \tau \propto N^{\frac{1}{4}}$.

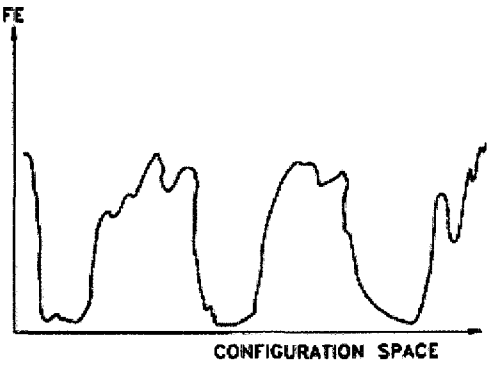

Figure (2-21) Multi-valley 'landscape' for the free energy of an Ising spin glass according to the replica breaking symmetry [98].

2.5) Possibility of long-range magnetic order in quasicrystals

2.5.1) The geometrical model

The geometrical model [4–7] predicts antiferromagnetic (AF) long-range interaction for a body centered (BC) magnetic lattice in two-dimensional (2-d) and three-dimensional (3-d) octagonal quasicrystals. However, according to the same model calculations, face center (FC) quasicrystals do not allow such long-range AF interaction. Moreover, the geometrical model does not include any calculations for other known long-range magnetic interactions, such as ferromagnetic or ferrimagnetic interactions.

2.5.2) The Ising model

Several attempts have been carried out using the Ising model, where two states of spin are allowed, spin up and down, to predict the long-rage magnetic interactions in quasicrystals. Godreche *et al* [8] apply the Ising model on a 2-d Penrose tiling. Their model follows the inflation rules of the tiling. Although their model starts with a quasi 2-d lattice, it ends up with a prediction of a ferromagnetic phase transition that is similar to the one in a 2-

d periodic lattice.

Bhattacharjee *et al* [9] also applied the Ising model on a 2-d Penrose titling using a Monte Carlo simulation of finite lattice. They estimated the critical transition temperature as 2.4 K. However, their simulation leads to a result that is similar to a 2-d periodic Bravais lattice. Okabe *et al* [10] applied the same Monte Carlo simulation but to a larger number of spin sites (439204). Unfortunately, their result turned out to be identical to the results obtained for a 2-d periodic lattice.

Monte Carlo simulation of a 3-d quasicrystal structure was adopted by Matsuo *et al* [12–15]. In their 2-d and 3-d model they assume a Ruderman–Kittel–Kasuya–Yosida (RKKY)-like alternating magnetic exchange interaction between neighboring spins. The shortest magnetic exchange interaction is assumed to be antiferromagnetic. The remaining magnetic interactions are assumed to be sign-alternating. In the 2-d model they include up to the second neighbor spin interaction, while in the 3-d they expand the simulation to include the interactions to the four nearest neighbors for 12524 and 67896 Ising spins sites. The simulations resulted in predicting antiferromagnetic long-range order interaction.

2.5.3) The XY model

In the XY model the spins of a system are considered to be classic spins that are confined in a 2-d lattice. The classical spins are unit vectors that have U(1) symmetry. This model is applied to a quasiperiodic lattice [16-18]. Monte Carlo numerical simulations are carried out on a 2-d Penrose tiling of some limited sites, 570 sites in one simulation [16], and assuming free boundary conditions. In the simulation, the magnetic interactions between spins only consider three neighboring spins and the next neighboring spin interaction is set

to be antiferromagnetic. In this method, the magnetic energy is minimized by adjusting the orientations of the spins to set the whole system into magnetic ground. During the Monte Carlo simulations thousands of iterations are needed to calculate the magnetic ground state for each temperature. The results of such a lengthy procedure are mostly identical with the original XY periodic lattice model in 2-d and 3-d which indicates that the XY model has universal characteristics that are not changed when applying them to a quasiperiodic lattice.

2.5.4) The Heisenberg and Hubbard models

Attempts have been made [19-25] to apply the Heisenberg antiferromagnet spin ½ model Monte Carlo simulations to octagonal quasicrystal structures in 2-d and 3-d. The models predict a long-range AF interaction in octagonal quasicrystals. The models exclude the icosahedral structure from their simulations due to the degree of difficulty to apply the same model to icosahedral quasicrystals.

The Hubbard model, which is a highly over-simplified model [50], was applied in 2-d octagonal quasiperiodic tiling [26] and in one-dimensional (1-d) Fibonacci Hubbard chain [27]. The 1-d model behaves as a uniform Heisenberg antiferromagnet chain whereas the 2-d octagonal quasiperiodic model results in an antiferromagnetic state.

The icosahedral quasicrystal structure was not included among all the above models except for one of the geometrical models [5], where the model predicts that icosahedral quasicrystal structure prevents any antiferromagnet long-range interaction. Although the 3-d Penrose tiling is close to describing the icosahedral quasicrystal structure, the icosahedral quasicrystal structure is not a 3-d Penrose. Due to the fact that the icosahedral quasicrystal structure is very complicated and mostly unknown, very little information is available for researchers to build a sound model to predict such long-range magnetic interaction.

Table (2-1) A summary of some of the symbols used in the chapter and their definitions.

Name	Symbol
The total orbital angular momentum	L
The total spin angular momentum	S
Total angular momentum	J
Magnetic moment of an atom	μ
Landé spectroscopic g-factor	g
Bohr magneton	μ_B
Brillouin function	B_J
Effective number of Bohr magnetons	p
Curie constant	C_C
Exchange field	B_E
Applied magnetic field	B_A
Curie temperature	T_C
Curie-Weiss constant	C
Néel temperature	T_N
Magnetic sublattice	X
Different magnetic sublattice	Y
Curie-Weiss constant of sublattice X	C_X
Curie-Weiss constant of sublattice Y	C_Y
Random average	$\langle \dots \rangle_c$
Thermal average	$\langle \dots \rangle_T$
Lattice separation between two spins	Δ
Free energy barrier	B
Real part of the ac susceptibility	χ'
Imaginary part of the ac susceptibility	χ''
Real exponent	ν
Ac susceptibility frequency	ω
The fractal cluster dimension (fc)	D
The correlation length of the fc	ξ
The volume of fc	ξ^D
The size of the fc	s_ξ
The spin of the fc	s
Spatial dimension of the system	d
Standard critical exponent	δ
Dynamical critical exponent	y

3) EXPERIMENTAL TECHNIQUES

3.1) Introduction.

Many experimental techniques, methods, and procedures were followed in this research. This review can be divided into three major parts: the sample preparation, the experimental setups, and the descriptions of the different measurement techniques.

3.2) Sample preparation.

3.2.1) Introduction.

The synthesis of quasicrystals is a very challenging and lengthy process. The synthesis of a typical sample requires at least two weeks of very careful work. Some samples require a month or more of annealing. I explored different methods and experimental techniques in order to master the art of quasicrystalline synthesis. During this research more than 70 trials have been made to prepare the required alloys. Those trials resulted in producing several single-phase, high-purity quasicrystalline and crystalline alloys.

In this research, I produced two types of alloys: crystalline and quasicrystalline. For a given crystalline alloy, it can have a simple unit cell structure or an approximant structure. The approximant is an alloy that has a very close chemical composition to the quasicrystal alloy, but it has a complicated crystalline structure. $Cd_{17}Ca_3$ quasicrystal and $Cd_{18}Ca_3$ approximant is a good example. The alloys prepared in this research are ternary alloys. The different preparation procedures generally result in ingots of the wanted alloys. In some

cases, quenched ribbons are produced. As a rule of thumb, there is no one experimental technique that can be followed to prepare all kinds of alloys.

3.2.2) Ingot preparation.

3.2.2.1) Introduction.

In this research three major techniques were followed in the preparation of the ingots: arc melting, radio-frequency melting, and melting or annealing using an electrical furnace. The weight of the elements is computed according to the desired alloy composition. The elements of the desired alloy are weighed using a digital analytical balance with accuracy of 0.1 mg. The accuracy of the analytical balance is limited to four significant numbers. The process of rounding the calculated weight to four significant numbers will produce errors. I invented a simple method to minimize this rounding error. Table (3-1) shows an example of this error. The second column in the table is the starting measured value of the first element, Zn in this example. The third column is the calculated weight value based on the chemical composition $Zn_{77}Fe_7Sc_{16}$. The fourth column is the value rounded to 4 digits after the decimal to match the accuracy of the balance. The rounding will cause a difference between the actual values and the experimental values that one can measure with the balance. The fifth column is the number of atoms ratio of each element with respect to the other. The last column is the difference between the rounded ratios to the calculated ratios. The last column is plotted in figure (3-1) to visualize the difference. The graphical presentation allows visual assistance in choosing the possible weights with minimum difference between the calculated and the measured values for the three elements simultaneously. In this example the most accurate weights will be the weights in row

Table (1) Example of the error produced by the process of rounding the calculated weight to four significant digits.

	Measured	Calculated		Rounding the calculated values to 4 digit		Ratio of the number of atoms resulted from the measured weights			Difference between the theoretical and the measured values		
	Zn (g)	Sc (g)	Fe (g)	Sc (g)	Fe (g)	Zn/Sc	Zn/Fe	Sc/Fe	Zn/Sc	Zn/Fe	
1	0.9990	0.1426729	0.0775387	0.1427	0.0775	4.8116	11.0055	2.2873	0.00092	-0.00549	
2	0.9991	0.1426871	0.0775465	0.1427	0.0775	4.8121	11.0066	2.2873	0.00043	-0.00659	
3	0.9992	0.1427014	0.0775542	0.1427	0.0776	4.8125	10.9935	2.2843	-0.00005	0.00649	
4	0.9993	0.1427157	0.0775620	0.1427	0.0776	4.8130	10.9946	2.2843	-0.00053	0.00539	
5	0.9994	0.1427300	0.0775697	0.1427	0.0776	4.8135	10.9957	2.2843	-0.00101	0.00429	
6	0.9995	0.1427443	0.0775775	0.1427	0.0776	4.8125	10.9968	2.2851	0.00000	0.00319	
7	0.9996	0.1427586	0.0775853	0.1428	0.0776	4.8111	10.9979	2.2859	0.00140	0.00209	
8	0.9997	0.1427728	0.0775930	0.1428	0.0776	4.8116	10.9990	2.2859	0.00092	0.00099	
9	0.9998	0.1427871	0.0776008	0.1428	0.0776	4.8121	11.0001	2.2859	0.00043	-0.00011	
10	0.9999	0.1428014	0.0776085	0.1428	0.0776	4.8125	11.0012	2.2859	-0.00005	-0.00121	
11	1.0000	0.1428157	0.0776163	0.1428	0.0776	4.8130	11.0023	2.2859	-0.00053	-0.00231	
12	1.0002	0.1428442	0.0776318	0.1428	0.0776	4.8140	11.0045	2.2859	-0.00149	-0.00451	
...	...	...	...	...	...	...	...	...	...	...	
...	...	...	...	...	...	...	...	...	...	...	
49	1.0039	0.1433727	0.0779190	0.1434	0.0779	4.8116	11.0027	2.2867	0.00092	-0.00269	
50	1.0040	0.1433869	0.0779268	0.1434	0.0779	4.8121	11.0038	2.2867	0.00044	-0.00378	

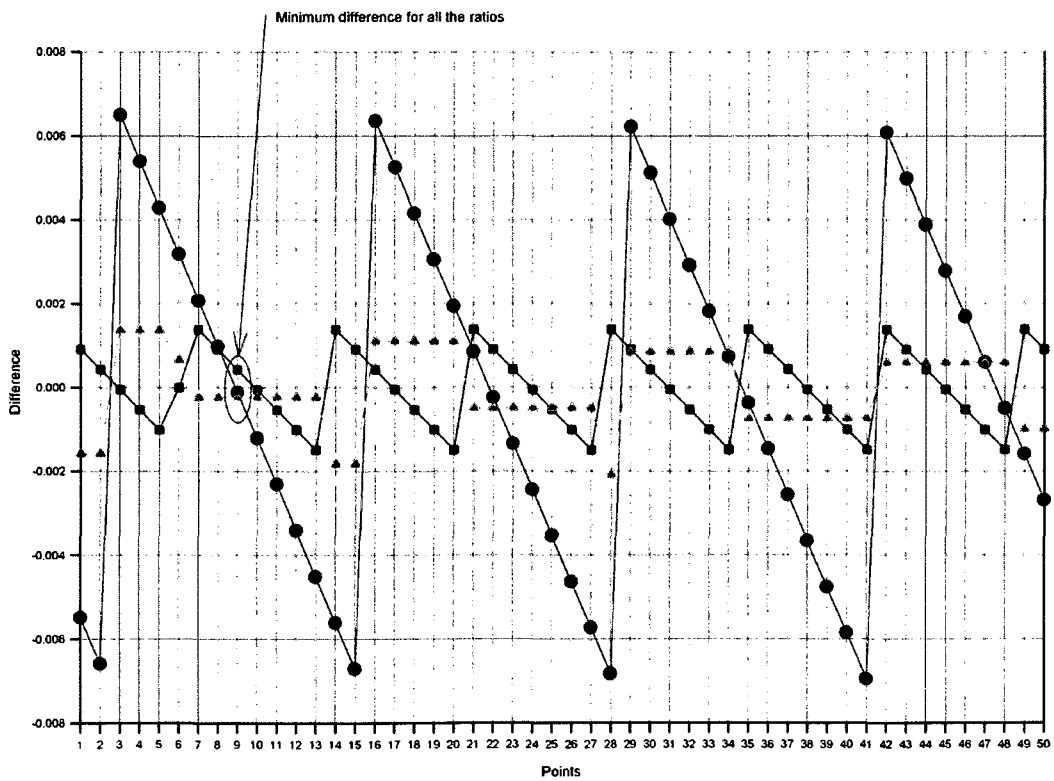

Figure (3-1) Last column of table (3-1) is plotted to visualize the difference between the calculated and measured weights. The blue squares are Zn/Sc differences, the red circles are Zn/Fe differences, and the green triangles are the Sc/Fe differences.

number nine in table (3-1), i.e. 0.9998 g, 0.1428 g, and 0.0776 g for Zn, Sc, and Fe, respectively.

3.2.2.2) Arc melting

The arc melting setup (figure (3-2)) is constructed of (a) a copper hearth as the base, (b) a sample chamber, (c) an arc needle, (d) a high voltage power supply, and (e) a rotary vacuum pump with an exchange argon gas tank. The first four components are water cooled. The water-cooled copper hearth has two cylindrical shaped grooves. The small groove is eight mm in diameter, and the bigger groove is 15 mm in diameter.

For a given sample, and after weighing the elements carefully to their nominal values, the pure elements are put together in the big groove. A pure titanium ball, typically about five mm in diameter, is also placed into the smaller groove. Then, the sample chamber is tightly closed. Afterward, the air in the sample chamber is pumped out using a rotary pump to a typical pressure value of 10^{-2} Torr. Next, the sample chamber is filled with argon gas. Pumping out the sample chamber and filling it with argon gas is repeated at least three times to ensure a humidity-free and oxygen-free environment in the chamber.

Once the sample chamber has a pure argon gas environment, a pressure of about 900 Torr of argon gas is set in it. At this stage, an outlet valve of the sample chamber is slightly opened to achieve an argon gas flow. The outlet of the sample chamber is completely immersed inside water to prevent air from exchanging with the out-going argon gas. Once these steps are completed, the setup is ready for the melting procedure.

In the melting process, the power supply is turned on and the arc needle is brought close to the discharge tip to start the arc. Next, the arc is guided towards the pure titanium

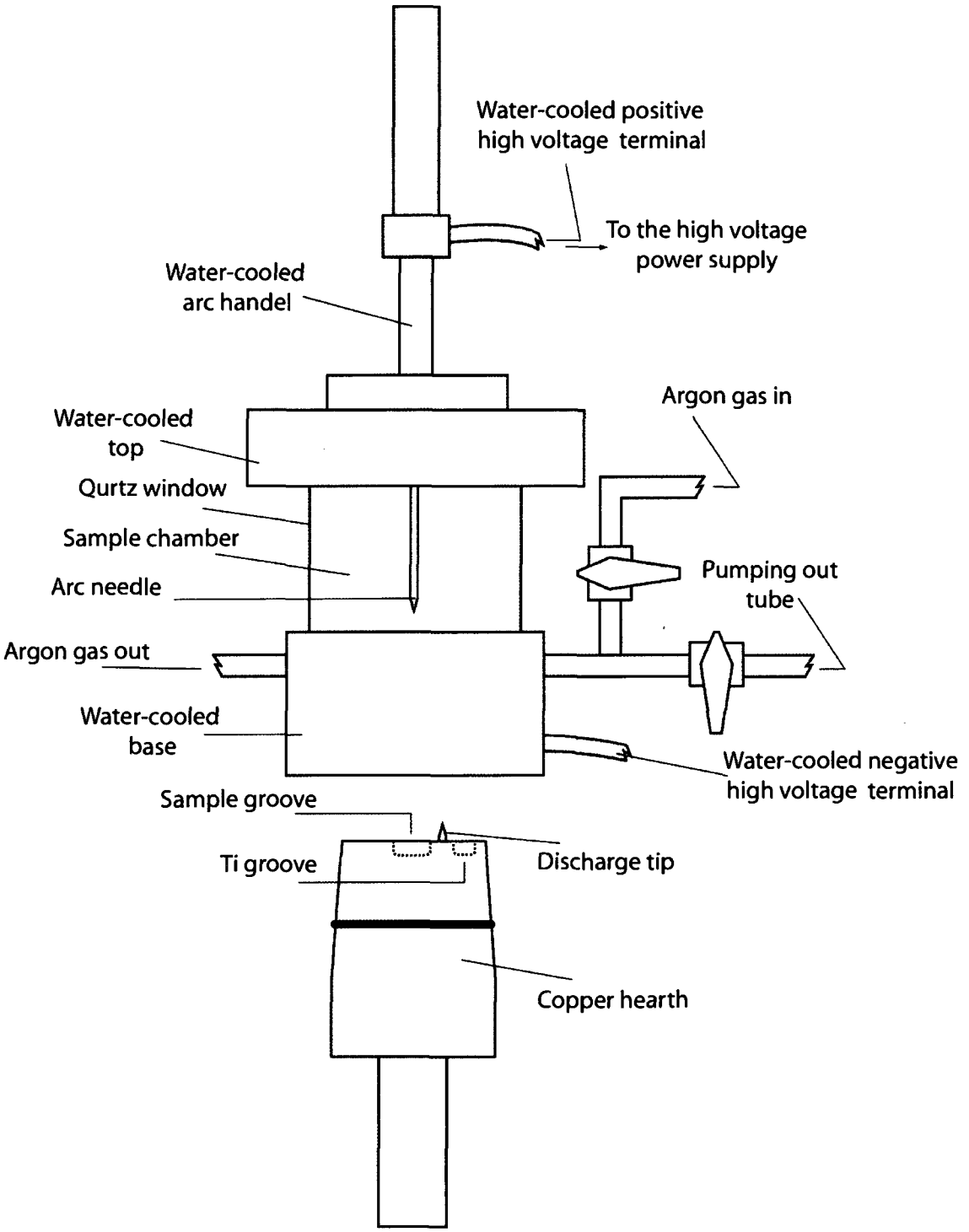

Figure (3-2) The arc melting setup.

ball to melt it. The benefit of melting Ti is to absorb any remaining molecules of oxygen. Immediately afterward, the arc needle is pointed to the pure metals to melt them. A circular motion of the arc needle is desired to distribute the heat and to ensure the mixing of the different molten metals. Once the separated pieces of the pure metals are melted together, the power supply is turned off. The alloy piece is then flipped over and the whole process is repeated again to ensure proper mixing of the metals. This process is repeated at least three times. The weight loss after repeating such process three times should not exceed 1 wt %. The sample can be visually examined by breaking it into two pieces to see whether texture is homogenous.

Although the arc melting is a useful method to produce alloys, it has some disadvantages. For example, when the melting temperatures of the sample elements have large differences, this method is not successful. An example for that is gadolinium and indium which have a melting point of 1312 °C and 156°C, respectively. In this case, some of indium will evaporate before gadolinium melts. In such process a substantial amount of indium can be lost. Also, if one of the elements has a high vapor pressure, for example zinc, then this method is not appropriate. Zinc vapor pressure can be as high as 31 atm at approximately 1400 °C [108]. This pressure is destructive to the simple structure of the arc melting setup.

3.2.2.3) Radio frequency melting

The radio frequency melting (RFM) setups, horizontal and vertical, are essential tools in the sample preparation. A typical RFM setup consists of a) a radio frequency generator unit, b) an induction coil, and c) a sample chamber. All the RFM setup parts are water cooled.

3.2.2.3.1) Radio frequency generator

In the radio frequency generator unit the necessary radio-frequency power is generated. The horizontal and the vertical units have maximum output power of 1 kW and 5 kW, respectively. The generated frequency can vary from 5 to 30 kHz.

3.2.2.3.2) Induction coil

The electrical coil design requires some important considerations. First, the electrical impedance of the coil has to match the electrical impedance of the radio-frequency generator output. Second, the induction coil inner diameter must be as small as possible. Using a smaller diameter leads to higher heat-to-power efficiency because the induction field is applied to a smaller volume. However, there must be a trade off because the coil has to be wide enough to accommodate the sample chamber. Third, the cooling of the induction coil is important to avoid melting the coil during the process. This is done by constructing the induction coil from a tube of non-magnetic metal with a good thermal conductivity, such as copper. The cold water must circulate through the tube during the process of heating.

When the power supply sends an alternating current through the induction coil, an alternating magnetic field is generated. As a result, an eddy current is produced inside the sample. The eddy current produces heat inside the sample because of the electrical resistance of the sample. In this research, the heat produced by the vertical setup is sufficient to melt all the metals and even to make a lot of them to boil. In the process of heating, the skin depth or penetration depth [109] of a metal in air is dependent on the frequency applied and the electrical resistivity of the metal. The skin depth, D, can be calculated as [109]:

$$D = \sqrt{\frac{\rho}{\pi f \mu}}, \tag{3-1}$$

where ρ is the electrical resistivity, f is the radio frequency, and μ is permeability. Applying the above equation to tantalum tubes used in the research, results in a minimum skin depth of 1.1 to 2.6 cm for the frequencies of 30 to 5 kHz, respectively. This means that the tantalum tubes and the elements inside the tantalum tubes are directly heated by the induced eddy current.

3.2.2.3.3) The sample chamber

The horizontal sample chamber shown in figure (3-3) consists of a) a water-cooled copper base and b) a vacuum-tight quartz container. The copper base has a dent of spherical shape of one centimeter width and one centimeter depth.

The vertical sample chamber shown in figure (3-4) is constructed completely out of quartz. The sample chamber is simply a quartz tube which is fused into a larger quartz tube. The larger quartz tube has two openings to allow water to circulate and cool the sample chamber. The sample container is put directly into the sample chamber. The air in the sample chamber can be evacuated and an exchange gas can be put in.

3.2.2.3.4) The melting process

In the horizontal setup, the pure pieces of the metals are put in the dent. The copper base is inserted into the quartz container and then fastened. The air is pumped out using a rotary pump and replaced by argon gas several times. The position of the induction coil is then adjusted to be around the metal pieces. Then the cooled water starts to circulate in the

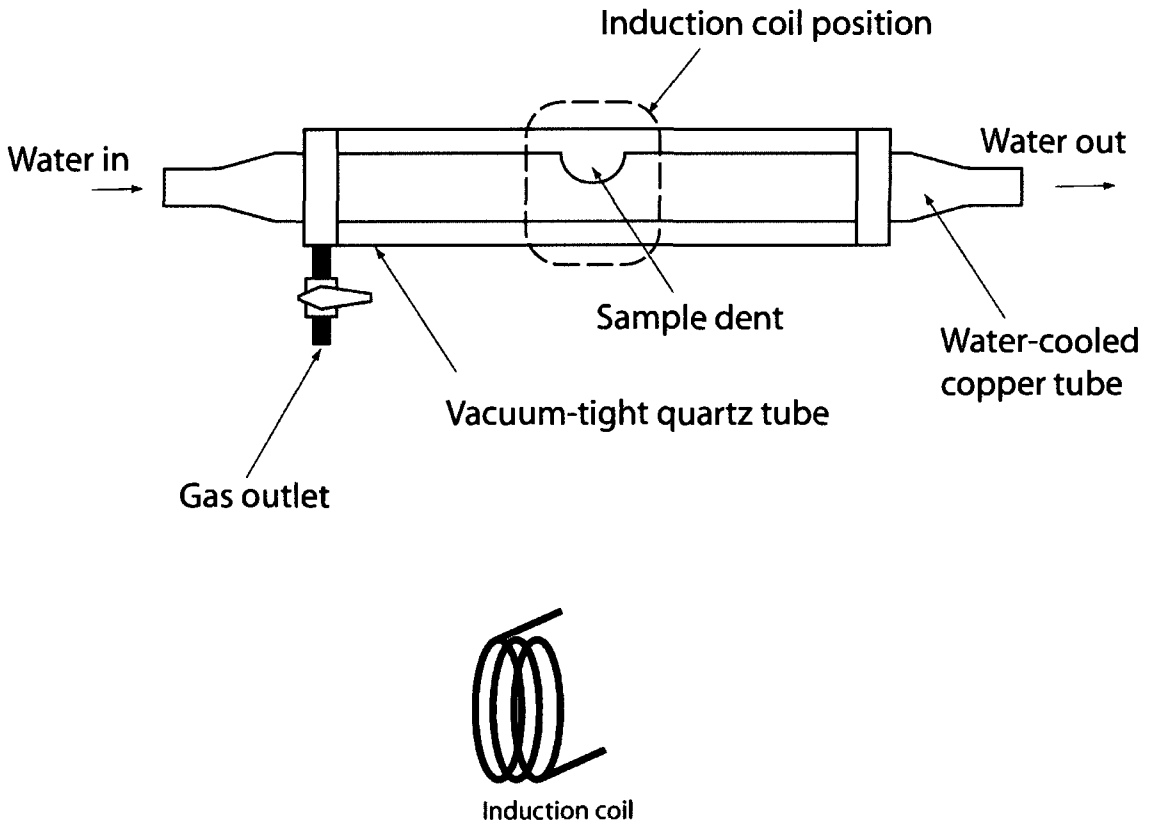

Figure (3-3) The horizontal RF sample chamber.

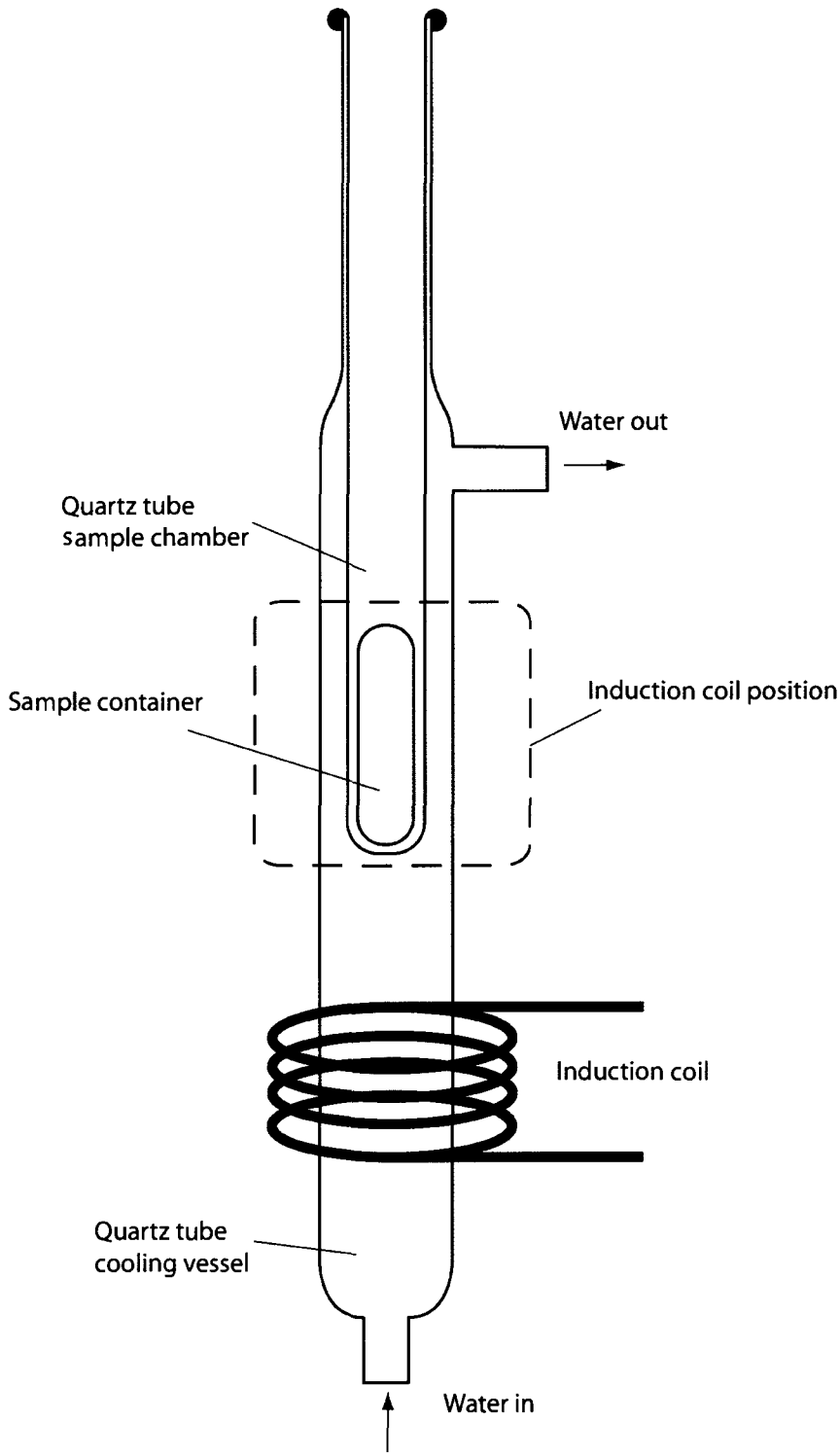

Figure (3-4) The vertical RF sample chamber.

system. Next, the frequency generator power is turned on. Gradually the output power is increased until the metal pieces start to melt. Once all the metal pieces are melted the radio frequency generator is turned off. In most cases the metals melt together to form one new piece. This piece is taken out and flipped upside down. Then, the whole process is repeated three or four times to make sure that the sample is homogeneous.

In the vertical setup, the pure pieces of metals are sealed in a tantalum tube. The tantalum tube is put inside the sample chamber and the sample chamber is evacuated using a rotary pump. Argon gas is used as an exchange gas. The position of the induction coil is then adjusted to be around the tantalum tube. The chilled water is forced to circulate into the different water-cooled parts of the system. Next, the frequency generator is turned on and the output power is gradually increased to the required value. During the heating process the tantalum tube is moved vertically up and down to make sure that the pieces inside are well melted and well mixed. Also this moving insures that there is no condensation on the upper portion inside the tantalum tube.

3.2.2.4) Furnace melting.

Another method to melt or anneal the samples is to use an electrical furnace. The electrical furnace used in this research is a three zone furnace. The three heating zones of the furnace are independently controlled. The first and the third zone controllers are coupled to the center zone thermocouple allowing a longer uniform temperature in the center zone. The operating temperature for the center zone of the furnace is 400–1400 ^{o}C. It has a uniform heated flat zone of about 35 cm in length with a temperature variance of $\pm$0.5 ^{o}C. The temperature stability for long run operation is $\pm$0.25 ^{o}C. It is ideal for annealing different

samples. Before melting or annealing a sample, some necessary pre-steps have to be taken into consideration. First, a proper container material has to be chosen based on the melting temperature of the sample and on the reactivity of the elements with the container material. Tantalum, molybdenum, tungsten, and stainless steel are the most used materials. Second, because some sample container materials, for example tantalum, react with air at high temperatures, they have to be kept in an inert environment during the melting or annealing process. This can be achieved by sealing the sample container in an inert environment of argon gas inside a quartz tube.

3.2.2.4.1) Sample container preparation.

A sample container can be a simple small shoe-box like made out from tantalum or molybdenum foil or can be a tantalum tube which can be completely sealed after putting the metal pieces inside. Tantalum and molybdenum were chosen to be the sample container materials because they do not react easily with most metals. Also, they have very high melting temperatures close to 3000°C. The molybdenum and the tantalum foils are 0.127 mm thick and 99.95% pure. The box and the box-cover have the dimensions of 7 mm x 6 mm x 30 mm. Figure (3-5) illustrates the different steps of making such a container from the original sheet. The method used to make the shoe-box sample container is a simple type of origami art.

The tantalum tube is 30 mm high, 8 mm wide, and 0.6 mm wall thick. The tube material is 99% pure. The base and the cap are machined from a tantalum rod of the same purity. The process of sealing the tantalum tube consists of two steps. First, the base is welded to the tube in an argon atmosphere. Second, the sample metal pieces are placed into

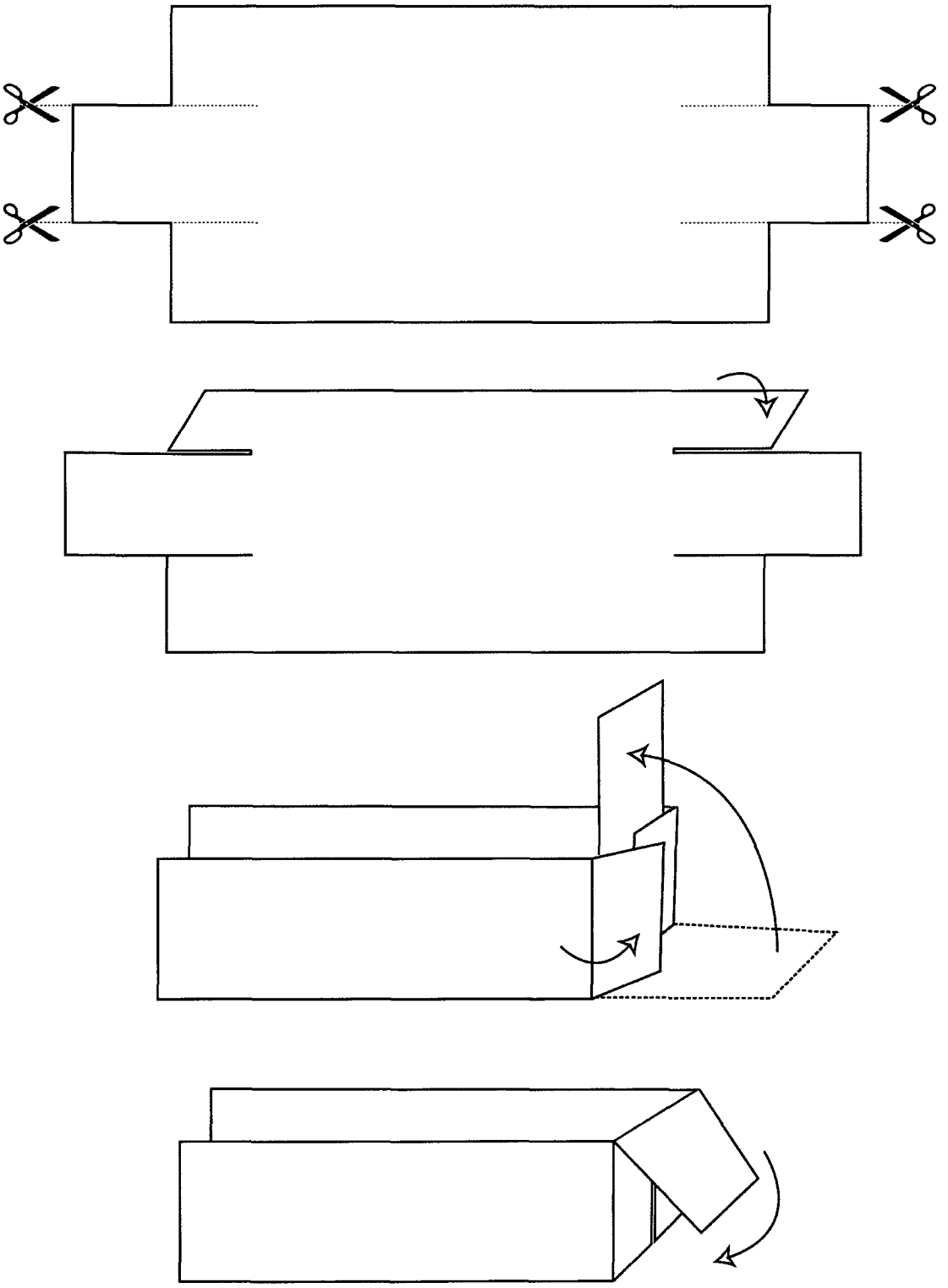

Figure (3-5) Steps to prepare the sample container from a sheet of metal.

the tantalum tube and then the cap is welded in an argon atmosphere. The welding procedure was similar to that described in section 3.2.2.2. The same arc melting setup that was described in section 3.2.2.2, with a minor change, was used to perform the welding. The water-cooled copper hearth is replaced by a specially designed hearth shown in figure (3-6). The purpose of this design is to absorb the excess heat during the welding process of the base or the cap to the tube.

3.2.2.4.2) Quartz tube sealing.

In this research, some prepared alloys contain elements that are sensitive to air such as calcium, gadolinium, and scandium. Also, tantalum which is the sample container material will start to react with air above 600 °C. Due to this, an inert environment is needed to prevent unwanted oxidization during the melting or annealing process. This is achieved by sealing the sample container in a quartz tube filled with some inert gas such as helium or argon. The quartz tube has an outside diameter of 11 mm and a wall thickness of 2 mm. The piece length of quartz tube needed to perform one seal operation is about 30 cm. The steps of sealing the sample container inside the quartz tube are illustrated in figure (3-7). The quartz tube produced from this process can have lengths as short as 4–5 cm. This is important so that the sample can be mounted vertically inside the horizontal electrical furnace.

3.2.2.5) Ribbon preparation.

Ribbons can be formed by a known technique called melt spinning, as shown in figure (3-8) [110]. This technique is used to achieve very high cooling rates in the process of

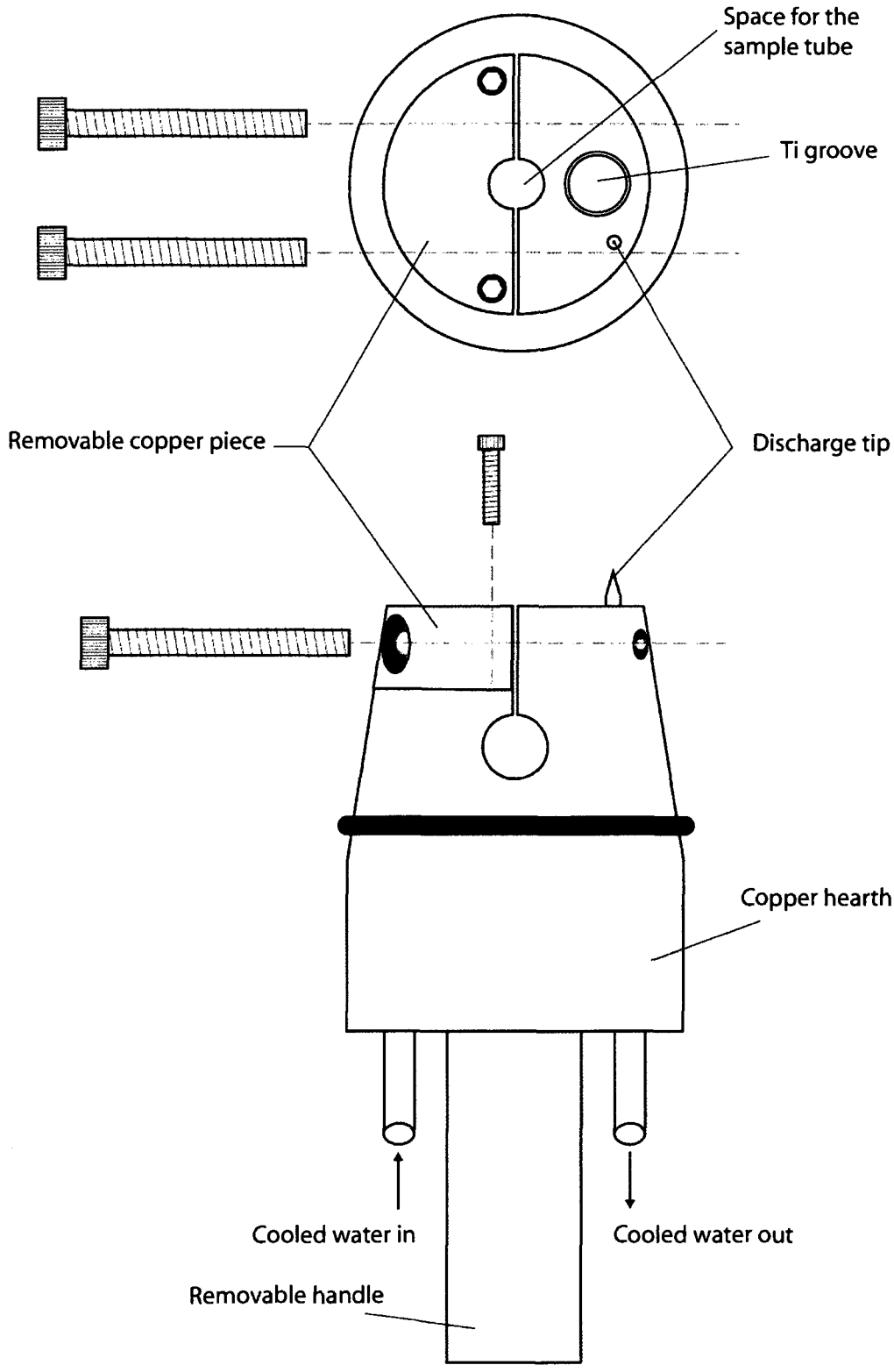

Figure (3-6) The modified water-cooled copper hearth.

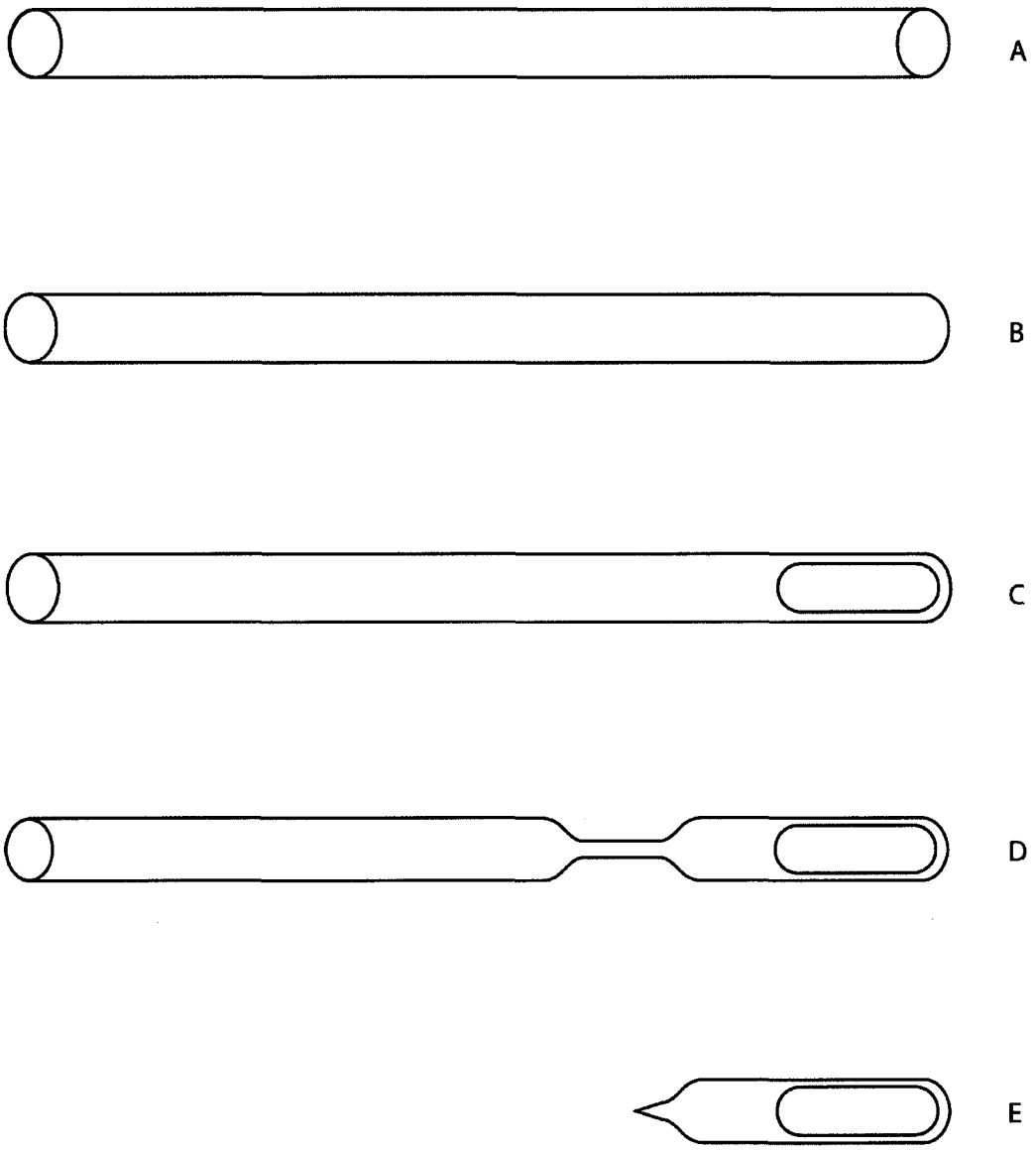

Figure(3-7)The steps for sealing the sample.First, as shown in (B), the quartz tube is sealed from one end. Then the sample container is inserted in it, as shown in (C). Next, in an area in the quartz tube that is close enough to the sample container, a small-diameter neck of the order of 2–3 cm long and 3–4 mm thick with a tiny opening is prepared, as shown in (D). The neck is necessary to make the final sealing process easier. Once the neck is prepared, the quartz tube is evacuated to high vacuum of the order of 10^{-5} Torr for about an hour. Then the quartz tube is filled with argon gas with a pressure of 300 Torr and the neck is heated and sealed (E).

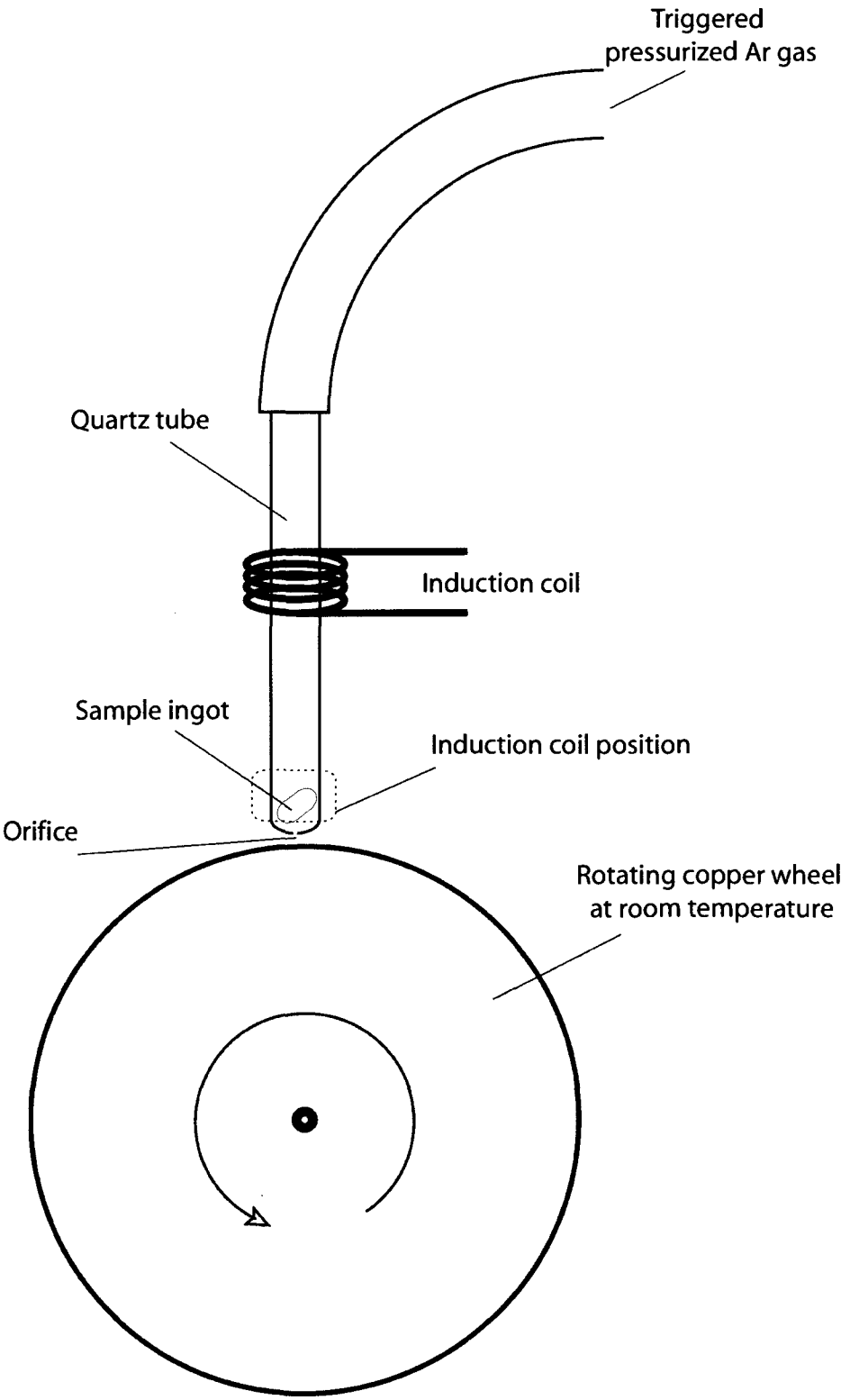

Figure (3-8) The melt spinning technique.

producing metallic ribbons. It is usually used to produce amorphous ribbons of metallic alloys. In this research it was used to produce the metastable icosahedral quasicrystal $Gd_{50}Ag_{36}In_{14}$.

First, an ingot of $Gd_{50}Ag_{36}In_{14}$ crystalline material is prepared using the arc melting procedure described in section 3.2.2.2. Then, this alloy is melted using the horizontal RFM described in section 3.2.2.3.4. Next, the molten ingot is pressured by argon gas through a 0.7 mm orifice in a quartz tube. The molten ingot immediately hits a surface of a rotating copper wheel. The copper wheel ambient temperature is about 20°C, and its tangential velocity is about 50 m/s. The molten ingot solidifies at a rate close to 10^6 K/s. The produced ribbons were shiny and fragile with the dimensions of about 1.0 cm long, 2mm wide, and 20 μm thick.

3.3) Experimental setups.

3.3.1) Introduction.

Several experimental setups have been employed to investigate the physical properties of the samples. They are: powder x-ray diffraction, dc magnetometry, ac magnetometry, and two low-temperature Mössbauer spectroscopy setups, ^{57}Fe and ^{155}Gd. In the following sections, for each setup a brief description, a summary of the technical specifications, and some experimental accuracy limitations are described.

3.3.2) Powder X-ray diffraction

3.3.2.1) X-ray diffractometer

A PANanalytical X'Pert scanning diffractometer was used to measure the x-ray

diffraction (XRD) spectra. The diffractometer is cooled by water. It uses the Bragg–Brentano geometry, as shown in figure (3-9). XRD measurements were carried out at room temperature using Cu Kα radiation. A Kevex PSi2 Peltier-cooled solid-state Si detector was used to eliminate the Kβ line. In order to avoid the deviation from intensity linearity of the solid-state Si detector, its parameters and the parameters of the diffractometer were chosen in such a way as to limit the count rate from the most intense Bragg peaks to less than 9000 counts/s [111].The goniometer has the angular accuracy of $\pm$ 0.01 degrees and the angular reproducibility of $\pm$ 0.0002 degrees. Although the angular accuracy of the goniometer is high, there are other factors, such as instrumental aberration and specimen displacement, that need to be corrected [112, 113]. Corrections to the 2θ angles using a fourth-order polynomial calibration curve were made [114]. The calibration curve was obtained from a separate scan of the specimen mixed with about 10 wt% of a Si standard [115].

Sample preparation for the x-ray scan is an important part of the process. Small pieces from the sample under investigation are chosen. Then, the pieces are grounded evenly using a well-cleaned mortar until a fine and homogenous powder is produced. The fine powder is put on a well-cleaned Si sample holder and then two or three drops of methanol is added to the powder. Next, the Si sample holder is horizontally moved in a circular motion to spread the mixture on the surface. The mixture is left to dry for about 15 minutes, and then is ready for use.

Another way to prepare the sample is to spread a thin layer of Vaseline on the surface of the Si sample holder. Next, the powder is sprinkled evenly on the Si sample holder. Then the Si sample holder is flipped upside down to remove the powder which did not stick to the Vaseline. These steps are repeated until the face of the Si sample holder is

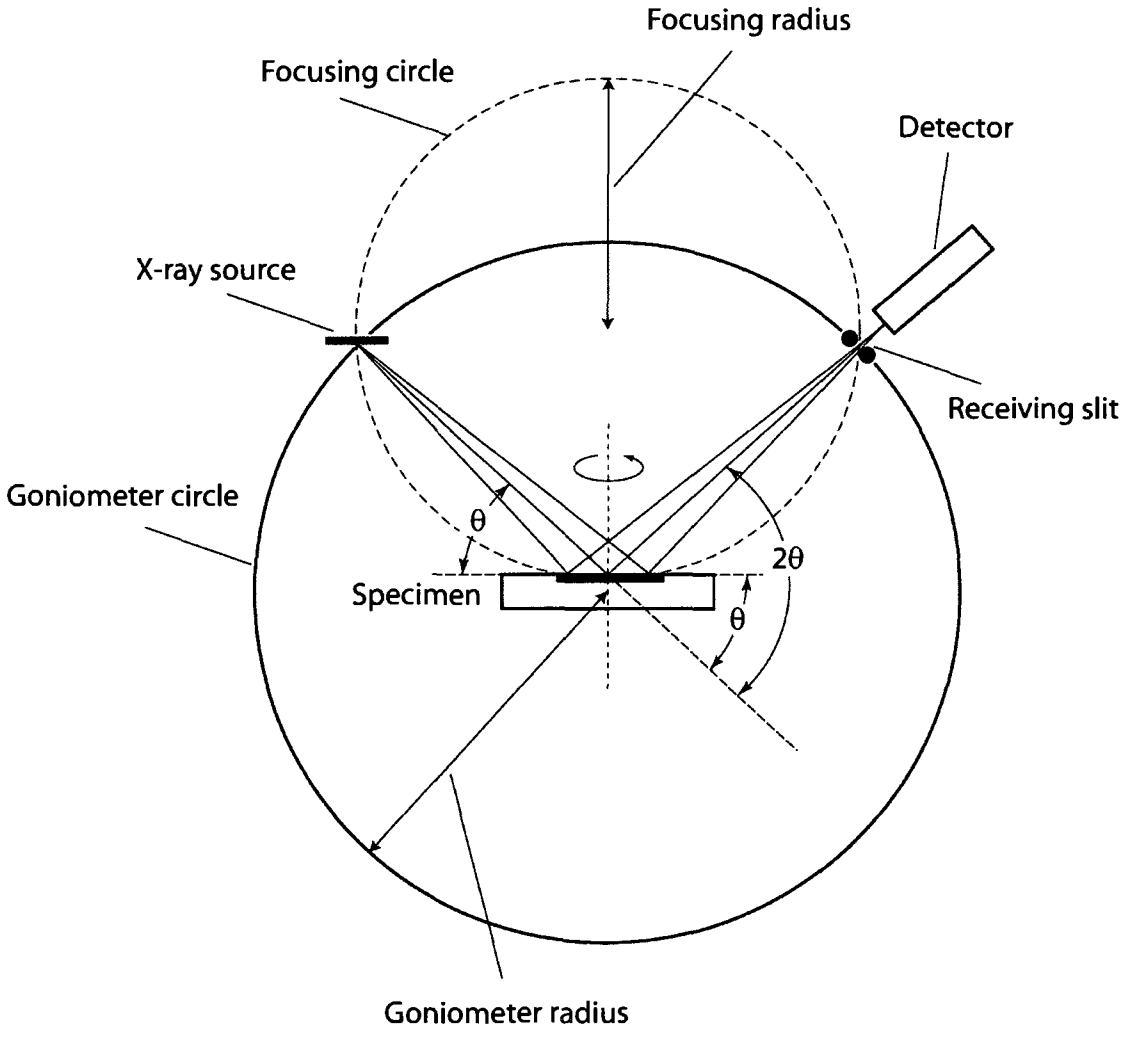

Figure (3-9) The Bragg-Brentano geometry diffractometer [112].

covered completely with the sample powder. An advantage of this method is to reduce the preferred orientation in the sample powder. A disadvantage is that the sample powder is permanently contaminated with the Vaseline. The range of the x-ray 2θ angle in this research in most cases was from 5^{o} to 90^{o}. The step size was 0.01^{o} and the collection time varied from one second to 10 seconds per step.

3.3.2.2) Rietveld analysis

Rietveld analysis or Rietveld method is a whole-pattern-fitting structure refinement analysis. It is named after its inventor Hugo Rietveld. The Rietveld analysis is computationally intensive and requires several minutes to execute one run. There are several computer programs that use Rietveld analysis, like GSAS Rietveld, Fullprof Rietveld, and X'Pert HighScore Plus, the last one was used in this research. The Rietveld algorithm of the X'Pert HighScore Plus software is based on the source code of the DBW3.2 software from Wiles & Young [116].

The results can be accurate within 1% error without the need for a standard material [117]. What is needed, for each crystalline phase in the sample, is detailed crystal structure information including space group, atom positions coordinates, lattice parameters, axes angles, and site-occupancies. Also, the background, the profile asymmetry, the specimen displacement, the specimen absorption, and the instrumental profile information are needed [117].

When the analysis is started the program generates the crystal structure peaks with peak intensities and peak profiles based on all the information provided to it. Then, the least-squares refinement is performed by the program between the total measured powder

diffraction pattern and the total calculated pattern. An important process during the refinement calculations is the feedback loop after each iteration. In the feedback loop, the program sends back an improved knowledge about the refined parameters and peak positions, intensities and profiles. The process is then repeated until the best fit between the total measured powder diffraction pattern and the total calculated pattern is reached.

The least-square refinement equation is [112, 117]:

$$S_y = \sum_i w_i (y_i - y_{ci})^2, \tag{3-2}$$

where S_y is the least-square refinement residual, w_i is the reciprocal of y_i, y_i is the measured intensity, y_{ci} is the calculated intensity, and the sum is overall the data points. The target of the Rietveld analysis is to minimize S_y using all the provided information. A special care has to be taken when preparing an x-ray sample for Rietveld analysis. Recommendations mentioned in the previous section for sample preparation must be followed. Some mistakes like inhomogeneous grain size, severe preferred orientation, or curved surface cannot be corrected with the algorithm [117, 118].

3.3.3) Mössbauer spectroscopy

Mössbauer spectroscopy is a well-established, multipurpose technique which can provide magnetic, chemical, structural, and time-dependent properties information of most solid materials [119]. A typical Mössbauer spectrometer consists of transducer, source, absorber, detector and necessary supporting electronics (figure (3-10)). The most frequently isotope used in Mössbauer spectroscopy is ^{57}Fe isotope. The technique is based on the Mössbauer effect. Rudolph Mössbauer first observed the effect of the recoilless gamma ray emission and absorption in 1957 [120]. In the following sections, a brief description of the

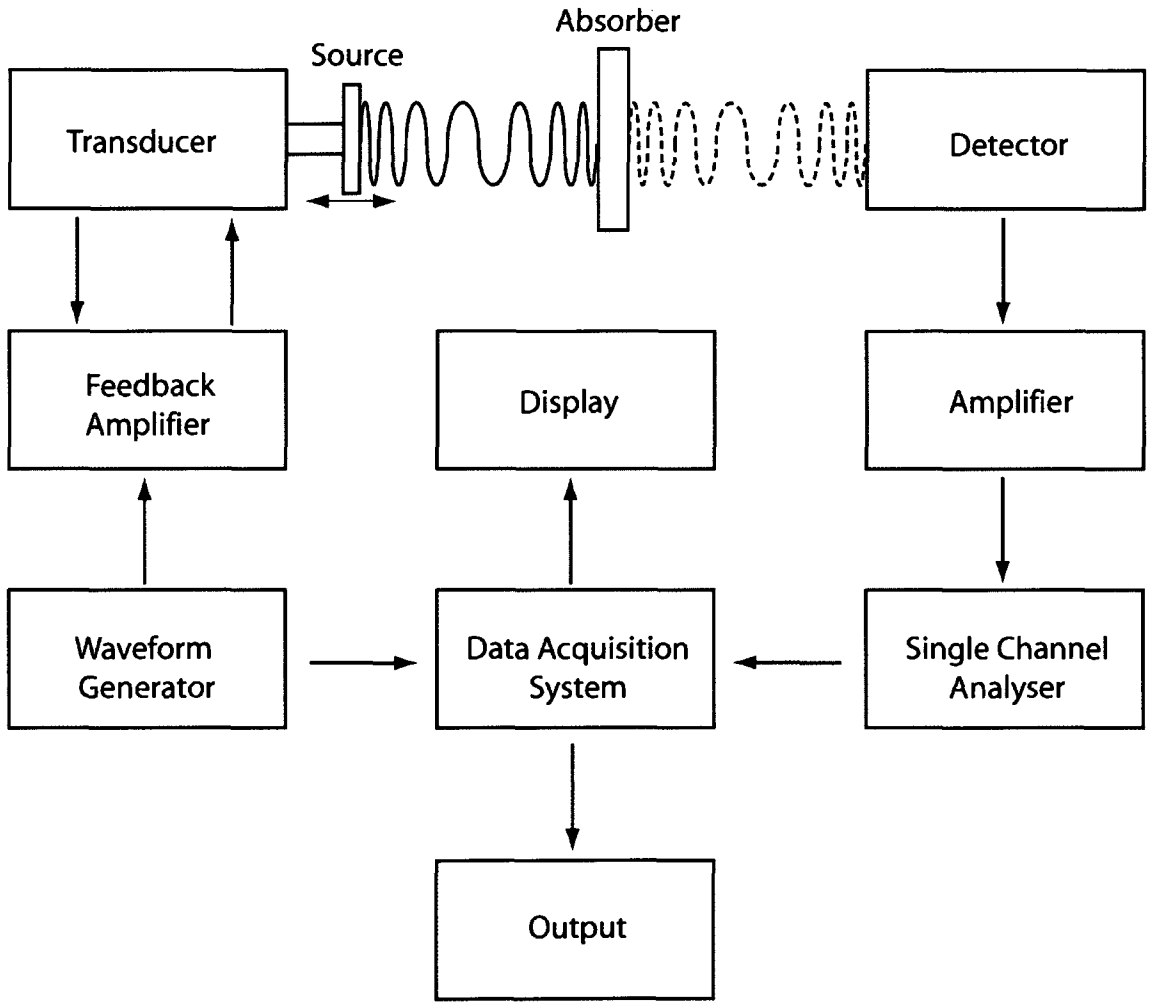

Figure (3-10) A typical Mössbauer spectrometer block diagram.

Mössbauer effect will be presented.

3.3.3.1) Mössbauer effect theory.

There are two conditions for the Mössbauer effect to take place. The first one is the occurrence of the recoilless emission and absorption, and the second, is the occurrence of resonance emission and absorption. In normal emission or absorption of gamma rays, due to the conservation of momentum, part of the momentum of the gamma photon is transferred to the nucleus that emitted or absorbed the photon. As a result, part of the energy of the photon emitted or absorbed is lost due to that. The loss is [121]:

$$E_R = \frac{E_\gamma^2}{2Mc^2}, \tag{3-4}$$

where E_γ is the gamma energy, M is the mass of the nucleus, and c is the speed of light. Equation (3-4) describes the nucleus-recoil situation in a free nucleus. When the emitting or absorbing nucleus belongs to an atom that is part of a solid, the effective mass of the nucleus becomes so large to the extent that E_R becomes zero. This is the recoilless emission or absorption situation.

Even if the first condition is satisfied, the Mössbauer effect may still not occur. When the chemical environment of the absorber nucleus is different than that of the emitter nucleus, a slight shift in the energy levels can be observed. This shift, which is called the hyperfine interaction, is due to the interaction of the absorber nucleus with the dissimilar surrounding atoms and electrons of that of the emitter nucleus' environment. Although this hyperfine interaction can be of the order of 10^{-8} eV, it can destroy the Mössbauer effect if the resonance condition is not met. To increase the resonance between the absorber and the emitter nuclei one needs to slightly change the energy of the emitted gamma photon. This is

done by means of adding a Doppler shift to the speed of the emitted photon. The source is moved back and forth in a small velocity range. For example, for ^{57}Fe, ^{151}Eu, and ^{169}Tm, the velocity ranges needed to record the full hyperfine pattern are $\pm$10, $\pm$50, and $\pm$700 mm/s, respectively [119]. The hyperfine interactions can be divided into three main interactions: the isomer shift, the quadrupole splitting, and the magnetic splitting.

3.3.3.1.1) Isomer shift

When the two chemical environments of the source and the absorber are exactly the same, the absorption of the gamma photons will occur at the 0 mm/s speed. However, when the two chemical environments are different, the electron densities at the nuclear sites in the source and the absorber atoms will be different. This difference will need a slight change in the energy (velocity) of the gamma photons to be absorbed. As a result the Mössbauer spectrum will be shifted, as shown in figure (3-11), to some positive or negative shift in velocity. Different ion charge states will result in different isomer shifts. The isomer shift can be calculated from the following equation [122, 125]:

$$\delta = \left[\frac{Ze^2R^2c}{5\varepsilon_0 E_\gamma}\right]\cdot\left[\rho_A - \rho_S\right]\cdot\left[\frac{\Delta R}{R}\right], \qquad (3\text{-}5)$$

where Z is the atomic number, e is the electron charge, R is the effective nuclear radius, c is the velocity of light, E_γ is the energy of the Mössbauer gamma ray, the ρ_A and ρ_S terms are the total electron densities at the nucleus for the absorber and the source, respectively, and $\Delta R = R_{excited} - R_{ground}$. The shift for ^{57}Fe isotope, for example, is negative because $R_{excited}$ is smaller than R_{ground}, while for ^{119}Sn isotope it is the reverse [122].

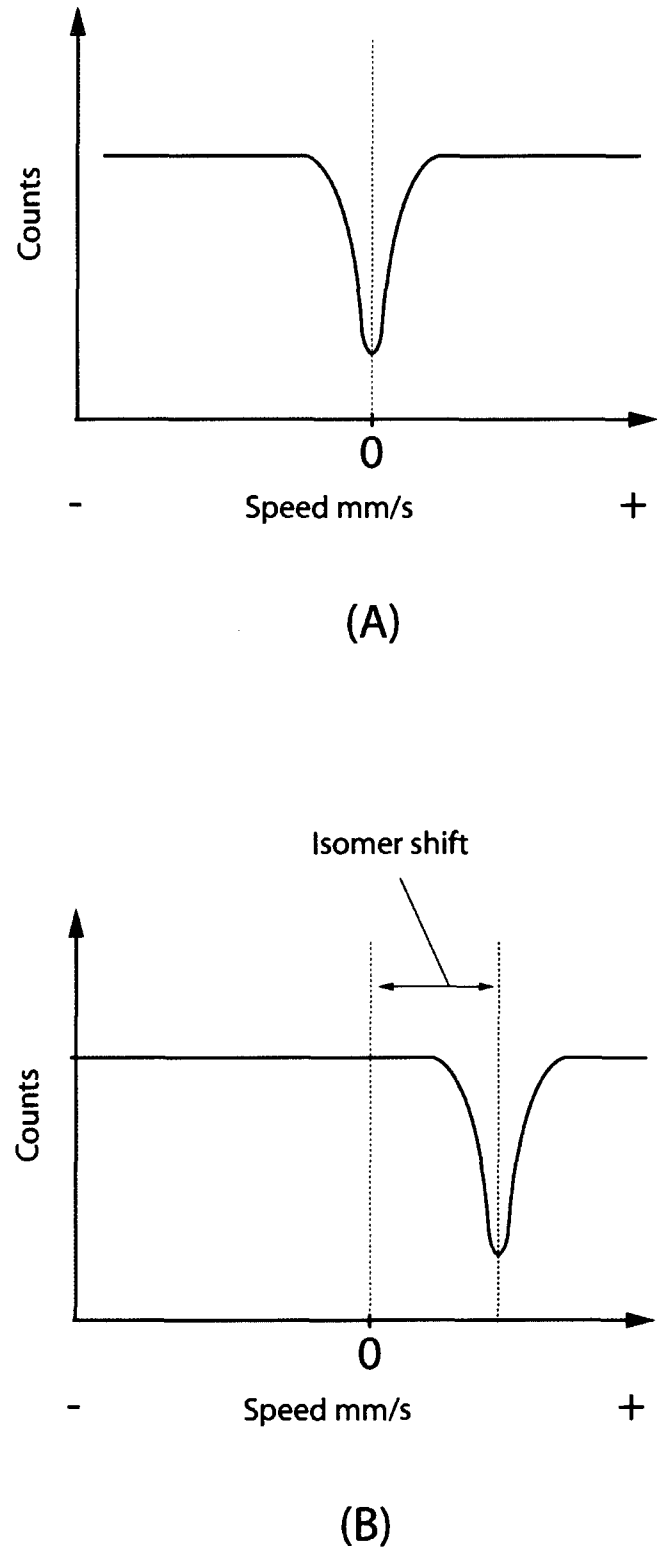

Figure (3-11) The zero shift (A) and the isomer shift (B) [122].

3.3.3.1.2) Quadrupole splitting

If a nucleus has a non spherical charge distribution, i.e. the angular momentum quantum number I is larger than 1/2, then the nucleus will have an electric nuclear quadrupole moment. If an asymmetric electronic charge distribution also exists, then it will result in a split in the nuclear energy into sublevels of the eigenvalues [122–125]:

$$E_Q = \frac{eQV_{zz}}{4I(2I-1)} \cdot \left[3m_I^2 - I(I+1)\right] \cdot \sqrt{\left(1+\frac{\eta^2}{3}\right)}, \tag{3-6}$$

where eQ is the nuclear electric quadrupole moment, V_{zz} is the principal component of the diagonalized electric field gradient (EFG) tensor, $\eta = \frac{V_{xx} - V_{yy}}{V_{zz}}$, and m_I is the nuclear magnetic spin quantum number with values m_I= -I, -I+1,...I-1,I.

For example, ^{57}Fe isotope has an excited state of I=3/2. This state will split into m_I=±1/2 and m_I=±3/2. The ground state with I=1/2 will not split. In the case that the EFG tensor is axially symmetric which means that $\eta = 0$, this will lead into two spectrum lines or a doublet, as shown in figure (3-12). The splitting due to the quadrupole interaction, ΔE_Q, can be calculated from equation (3-6) as [122–125]:

$$\Delta E_Q = E_Q\left(\pm\frac{3}{2}\right) - E_Q\left(\pm\frac{1}{2}\right) = \frac{eQV_{zz}}{2}, \tag{3-7}$$

where $E_Q\left(\pm\frac{3}{2}\right) = \frac{3}{12}eQV_{zz}$ and $E_Q\left(\pm\frac{1}{2}\right) = -\frac{3}{12}eQV_{zz}$.

3.3.3.1.2) Magnetic splitting

When the spin quantum number I of a nucleus is larger than zero, the nucleus will have a magnetic dipole moment μ [122–125]:

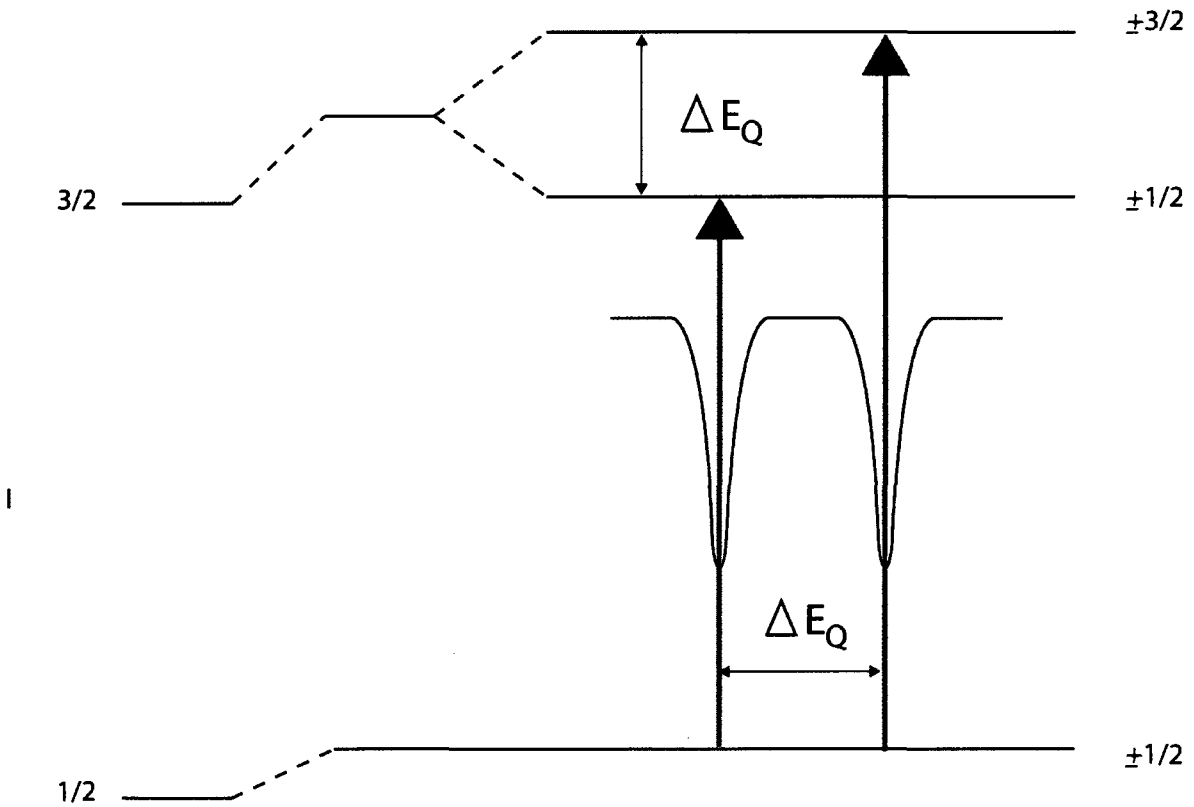

Figure (3-12) The quadrupole splitting for ^{57}Fe nucleus with spin I=3/2 in the excited state [122].

$$\mu = g_N \mu_B I \,, \tag{3-8}$$

where g_N is the nuclear Landé splitting factor and μ_B is the nuclear magneton defined as $\mu_B = \frac{e\hbar}{2Mc}$, and M is the nucleus mass. This magnetic dipole moment in the presence of a magnetic field H at the site of a nucleus will split the nuclear state into $(2I+1)$ sublevels with the eigenvalues of [122–125]:

$$E_m = -\frac{\mu H m_I}{I} = -g_N \mu_B H m_I \tag{3-9}$$

For ^{57}Fe isotope, the ground state splits into two sublevels. The excited state splits into four sublevels, as in figure (3-13). There are eight transitions possible but only six are allowed due to the selection rule $\Delta m = 0, \pm 1$.

3.3.3.2) ^{57}Fe Mössbauer spectroscopy setup

In the ^{57}Fe Mössbauer spectroscopy setup, a ^{57}Co(Rh) source is used. The source mainly emits 14.4 keV γ–ray. A sine wave drives the transducer which moves the source. The spectrometer is calibrated using a 6.35×10^{-6} m α-Fe foil with a surface density of 107×10^{-3} mg ^{57}Fe/cm^2 [126], and the spectra are folded. The spectrometer setup is capable of reaching temperatures as low as 1.9 K by means of pumping out helium gas from the liquid helium chamber. The absorber is made of powder material of the sample, which is pressed into a pellet inside a metallic container to guarantee a homogeneous temperature over the whole sample. The metallic container is made of a copper ring and 0.008 mm thick aluminum walls. The resolution of the spectrometer can be determined by measuring the full line width at half maximum of the inner pair of the α-Fe Zeeman pattern. A typical value of this resolution is about 0.2244(40) mm/s [127].

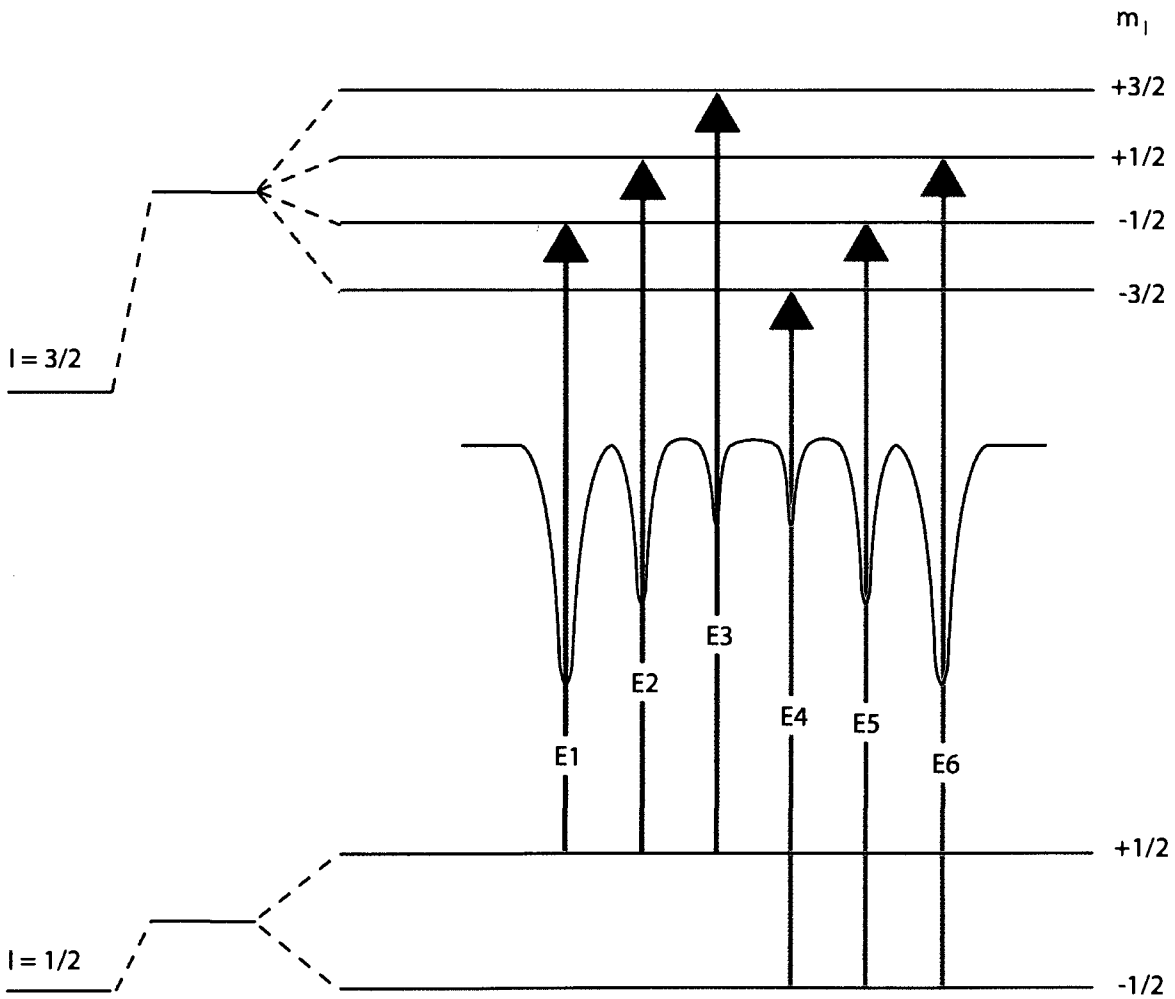

Figure (3-13) For ^{57}Fe the ground state split into two sublevels. The excited state split into 4 sublevels. There are eight transitions possible but only six are allowed due to the selection rule [122].

3.3.3.3) ^{155}Gd Mössbauer spectroscopy setup.

In the ^{155}Gd Mössbauer spectroscopy setup a ^{155}Eu(SmPd3) source is used. The source mainly emits 86.5 keV and 105.3 keV γ–ray. A sine wave drives the transducer which moves the source. A Michelson interferometer is used to calibrate the spectrometer [128], and the spectra are folded. The source and the absorber are kept at the same temperature. The absorber is made of powder material of the sample, which is pressed into a pellet inside a metallic container to guarantee a homogeneous temperature over the whole sample. The detector is a 2.5 cm crystal NaI(Tl) scintillation detector. The detector is covered with a 0.6 mm Pb sheet to remove the 105.3 keV γ–ray. The spectrometer setup is capable of reaching temperatures as low as 1.5 K by means of pumping out helium gas from the liquid helium chamber. The superconducting magnet of the setup can produce magnetic fields as high as seven Tesla.

3.3.4) dc magnetometry

The success of the Magnetic Property Measurement System (MPMS) as a device, capable of measuring very small values of magnetic fields, is due to the Superconducting Quantum Interference Device (SQUID). The SQUID can measure small magnetic fields of the order of 10^{-15} T [129]. The inner components of the MPMS can be seen in figure (3-14). The absolute sensitivity of the MPMS is 1×10^{-8} emu [130]. The nature of the solenoid-type winding of the superconducting magnet results in a magnetic field that depends on the position inside the magnet coil. As a result, the sample is exposed to a magnetic field variations as it travels through the SQUID coils. These variations can range from 0.001% for one cm scan length to 6% for eight cm scan length [131]. The superconducting magnet can

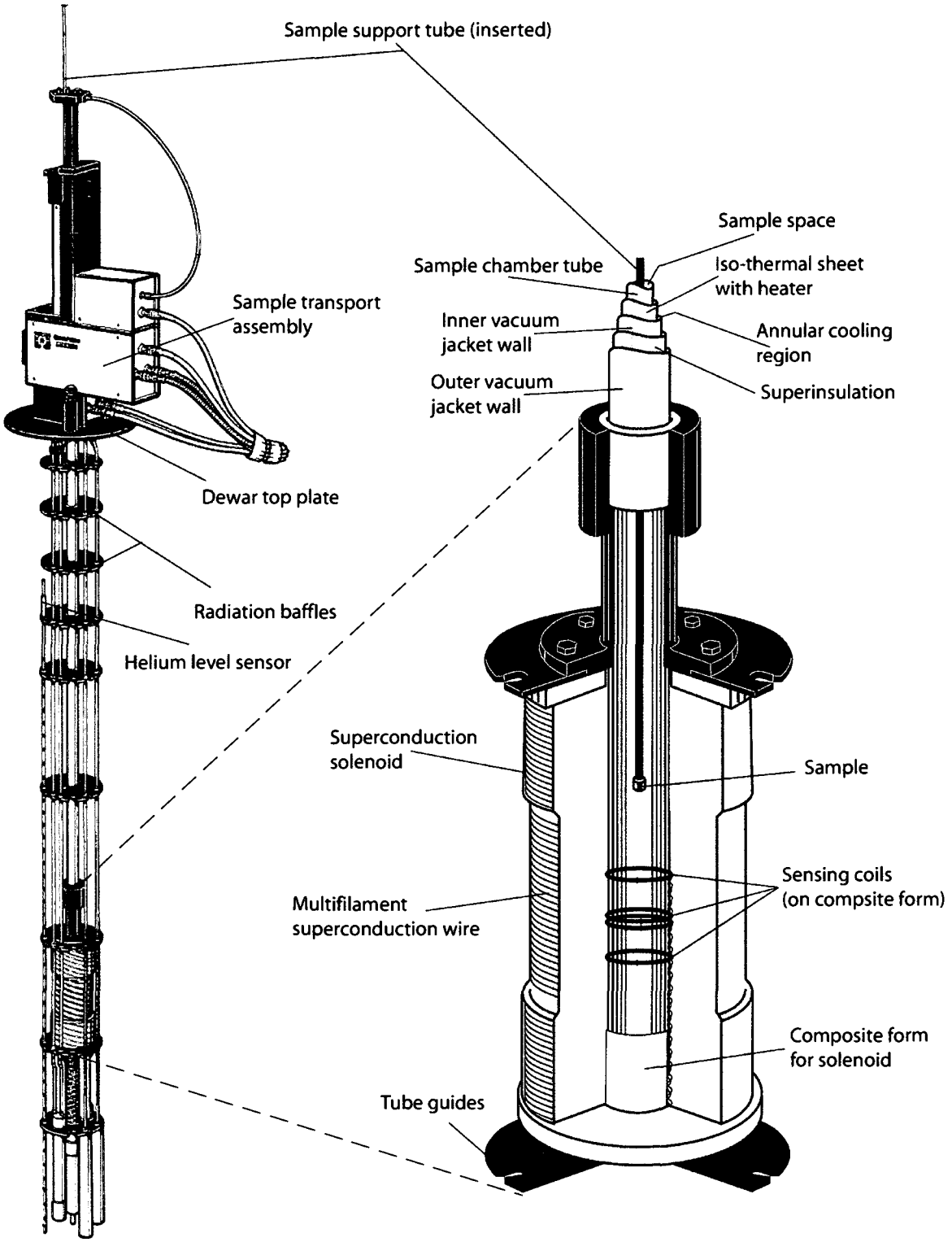

Figure (3-14) The inner components of the MPMS [130].

produce a dc magnetic field up to five Tesla. The absolute magnetic gram susceptibility values of the MPMS were calibrated using a standard Pd sample each time the superconducting magnet was cooled from room temperature. The calibration is necessary to make sure that the absolute values are correct. The measured values were compared with the standard values provided by Quantum Design [132].

One can think of a SQUID as a transducer which converts the change in magnetic field flux into voltage. A simple SQUID consists of two superconducting identical semi-circles joined together with Josephson junctions, as in figure (3-15) [129]. A Josephson junction is simply a thin layer of insulator between two superconducting rings. When a bias critical current is applied to the SQUID, Cooper electron pairs are tunneled through the Josephson junctions. As a result a constant current will flow through the circuit. Any applied magnetic field to the ring will result into a phase difference between the Cooper pairs crossing the junction which will affect the critical current of the SQUID. If the applied magnetic field is increasing or decreasing then the critical current will oscillate between a minimum and maximum value.

In dc magnetometry, the sample is put in a constant magnetic field and the magnetic moment of the sample is measured. The measurement produces dc magnetization curve, *M(H)*, versus temperature. Before measuring the dc magnetization of a sample, the position of the sample needs to be adjusted to be in the center of the pickup SQUID coils. After the sample is inserted inside the MPMS, the sample is physically moved, by means of a step motor, through the pickup SQUID coils. The magnetic moment of the moving sample will generate an output voltage in the pickup coils which is proportional to the sample magnetic moment. Then, based on the output voltage profile, the position of the sample is adjusted

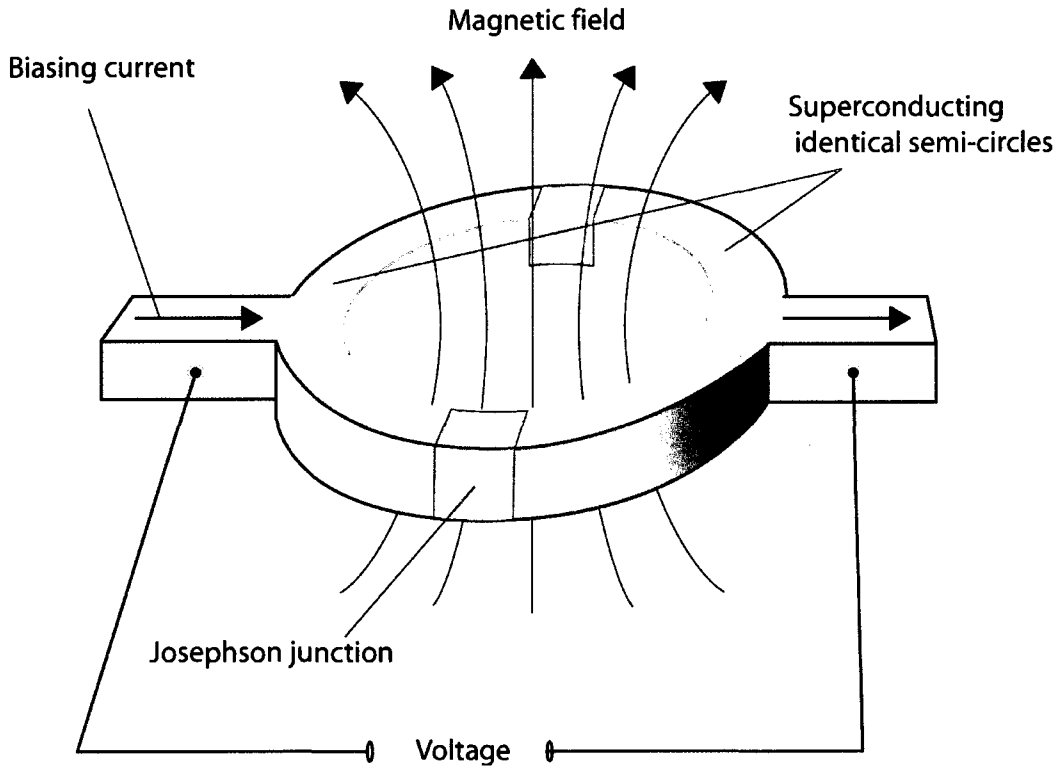

Figure (3-15) A simple SQUID consists of two super conducting identical semi-circles joined together with Josephson junctions [129].

until the maximum induced output voltage occurs at the center of the pickup coils. Usually the measured magnetic gram susceptibility values are uncertain to less than ±1%. The magnetic gram susceptibility of the samples was measured with the MPMS at various fields in the temperature range 2–300 K.

3.3.5) ac magnetometry

A Quantum Design physical property measurement system (PPMS) was used to perform the ac magnetometry measurements. In ac magnetic measurements, a small alternating magnetic field, or ac magnetic field, is applied to the sample while the sample is kept stationary. The ac magnetic field can be applied by itself or together with a dc magnetic field. The PPMS is capable to generate ac magnetic fields up to ±10 Oe in a frequency range of 10 Hz to 10 kHz. The PPMS has one ac drive coil set, that produces the ac magnetic field, and two sets of detection coils all made out of copper. The detection coils, which are separated by several centimeters, are counterwound and connected in series. This configuration helps to isolate the sample's signal from background signals. In each center of the detection coil a single-turn calibration coil exist, which is connected in series with the other calibration coil. Moreover, the ac drive coil is connected in series with counterwound compensation coil so they receive the same excitation signal. This configuration results in a uniform ac magnetic field within the measuring volume and a zero ac magnetic field elsewhere. The ac drive coil, the compensation coil, calibration coils, and the detection coils are fixed to the PPMS insert as shown in figure (3-16) [133].

In ac susceptibility measurement, the detection coils do not measure the sample's magnetic moment directly, instead they measure the sample's magnetic moment response.

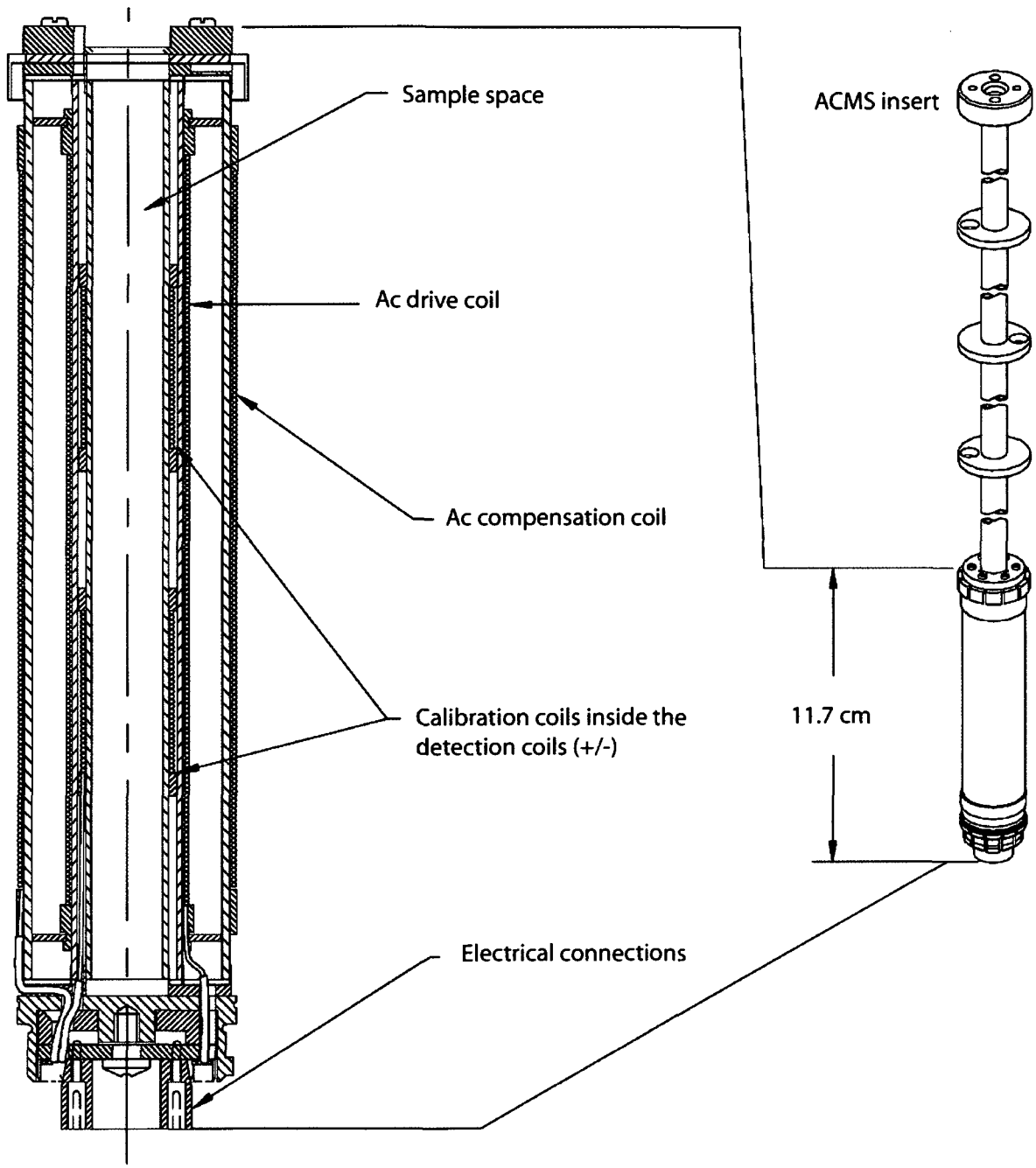

Figure (3-16) The PPMS insert and the coil set [133].

The measured amplitude is the change in the sample's magnetic moment *dM*. Ac susceptibility is defined as $\chi_{ac} = dM/dH$ (dH is amplitude of the alternating field) which is the local slope of the sample's dc magnetization curve *M(H)*. The sample's magnetic moment response contains information about both magnitude χ_{ac} and phase φ which is relative to the drive signal. The ac susceptibility measurement produces real component, χ', and imaginary component, χ'', related by [134]:

$$\chi' = \chi_{ac} \cos\varphi \quad and \quad \chi'' = \chi_{ac} \sin\varphi, \quad or \quad \chi_{ac} = \chi' + i\chi''. \tag{3-10}$$

The ac magnetic susceptibility data were collected between 2 and 30 K in a 1 Oe ac magnetic field and zero external magnetic field for frequencies varying from 20 Hz to 10 kHz.

4) ICOSAHEDRAL QUASICRYSTAL $Ag_{50}In_{36}Gd_{14}$

4.1) Introduction

Recently, new metastable icosahedral (i) QCs were discovered in the $Ag_{50}In_{36}R_{14}$ (R = rare earth) system [135]. These QCs are formed by replacing all of Cd in the binary i $YbCd_{5.7}$ QC [136] with Ag and In, and Yb with other R elements. It is thus expected that the crystal structure of the i $Ag_{50}In_{36}R_{14}$ QCs must be similar to that of the i $YbCd_{5.7}$ QC. Very recently, the crystal structure of the i $YbCd_{5.7}$ QC has been solved [137]. It is based on three building units (rhombic triacontahedra linked with acute and obtuse rhombohedra) arranged quasiperiodically with unique atomic decorations. One would expect that R atoms are located at the Yb sites (on the vertices of the icosahedron and inside the acute rhombohedron) and the Ag and In atoms are distributed among the Cd sites.

The new i $Ag_{50}In_{36}Gd_{14}$ QC is chosen for several reasons. First, it is expected to possess well localized and sizeable 4f magnetic moments on the Gd atoms and perhaps exhibit long-range magnetic order. Second, it has the exact chemical composition of the 1/1 approximant $Ag_{50}In_{36}Gd_{14}$. It is an ideal case to study the magnetic properties differences between the i QC and the 1/1 approximant. Moreover, Mössbauer spectroscopy study can be performed using the ^{155}Gd Mössbauer spectroscopy setup described in section (3.3.3.3).

4.2) Experimental procedure

An ingot of nominal composition $Ag_{50}In_{36}Gd_{14}$ was prepared by melting constituent elements in an induction furnace on water-cooled Cu boat under an Ar atmosphere. Purities of the starting elements were 99.999%, 99.999%, and 99.998% for Ag, In, and Gd,

respectively. The melting was repeated four times, in each case after turning the ingot. The total weight loss after the melting was 1.5%. The ingot was then melt spun in an Ar atmosphere by ejecting molten alloy through a 0.7 mm orifice in a quartz tube onto a surface of a copper wheel rotating with a tangential velocity of 47 m/s. The resulting ribbons were about 1.0 cm long and 20 μm thick.

4.3) Results and discussion

4.3.1) Structural characterization

The XRD pattern of the studied sample measured in the 2θ range 5–100° (figure (4-1)) shows the presence of 19 i Bragg peaks, the weaker of which were not observed earlier [135] in the patterns obtained with a scintillation/proportional counter. Four weak Bragg

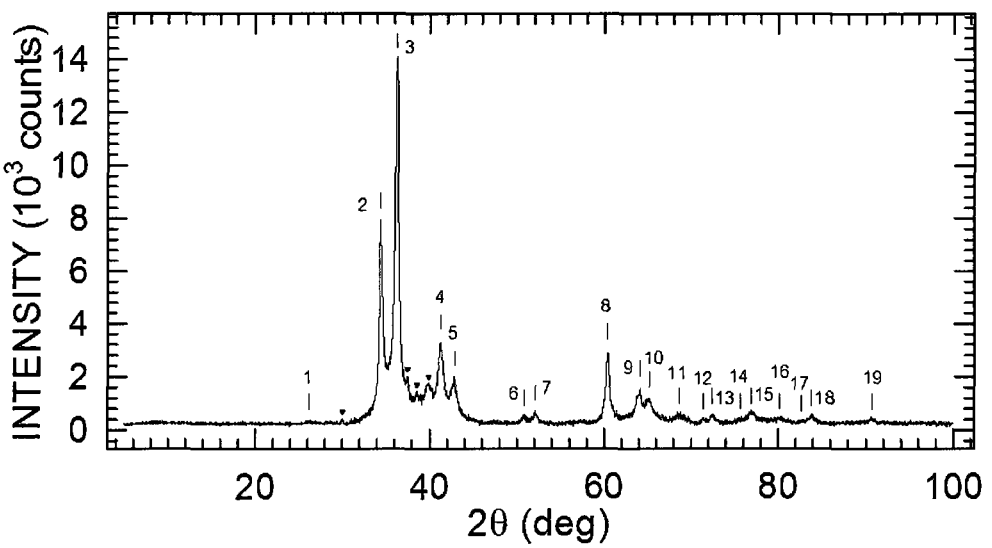

Figure (4-1) The XRD spectrum of an $Ag_{50}In_{36}Gd_{14}$ alloy at 298 K. The vertical lines labelled with integers above all detected i Bragg peaks correspond to the positions calculated for the Cu $K\alpha_1$ radiation, as explained in the text. The position, full width at half maximum, and relative intensity of each detected i peak are given in table 1 together with the corresponding index. The symbol ▾ indicates the peak positions corresponding to an unidentified second phase.

all the detected i Bragg peaks corresponding to Cu $K\alpha_1$ radiation (the value of its wavelength λ is 1.5405981 Å [138]) in terms of the angle $2\theta_1$ and the corresponding wave number $Q_{exp} = 4\pi\sin\theta_1/\lambda$, as well as their relative intensities and full widths at half maximum Γ_Q, were determined from the profile fitting using the procedure described by Schreiner and Jenkins [139]. These parameters corresponding to 19 detected i peaks, whose positions are indicated by vertical lines in figure (4-1), are presented in table (4-1). This table contains also the theoretical positions Q_{cal} which were calculated by taking the position of the second most intense i peak as the reference. Since there are several schemes employed to index the i peaks, we present in table (4-1) the indices that correspond to the most frequently used schemes [140-142].

There is a good agreement between the observed Q_{exp} and the theoretical Q_{cal} positions of the i Bragg peaks (figure (4-1) and table (4-1)). The absence of Bragg peaks that correspond to half-integer indices confirm that the i $Ag_{50}In_{36}Gd_{14}$ QC has a simple icosahedral (SI) six-dimensional Bravais lattice characteristic for i alloys that cannot be produced as thermodynamically stable. The value of the six-dimensional hypercubic lattice constant calculated from the value Q_{exp} that corresponds to the (18,29) i peak is 7.805(2) Å. The widths Γ_Q of the i peaks is significantly larger than the instrumental resolution (about 0.006 $Å^{-1}$) of the XRD spectrometer. This broadening, as well as the small shift of Q_{exp} from their ideal positions Q_{cal}, indicates the presence of some structural/chemical disorder in the i $Ag_{50}In_{36}Gd_{14}$ QC.

Table (4-1) Positions in terms of $2\theta_1$ (in degrees) corresponding to Cu $K\alpha_1$ radiation and Q_{exp} (in $Å^{-1}$), full width at half maximum Γ_Q (in $Å^{-1}$), and relative intensity INT normalized to 100.0 of all detected icosahedral Bragg peaks, which are labeled with consecutive integers in column 1, as obtained from the fit [139]. The integers correspond to the vertical lines in figure 1. Q_{cal} (in $Å^{-1}$) is the calculated Q value by taking the position of the second line with the $I1$ index 18/29 as the reference line. $I1$ and $I2$ are the indices (N/M) and (h/h',k/k',l/l') based on the indexing scheme of Cahn *et al* [140], whereas $I3$ and $I4$ are the indices corresponding, respectively, to the indexing schemes of Elser [141] and Bancel *et al* [142].

Label	$2\theta_1$	Q_{exp}	Q_{cal}	Γ_Q	INT	$I1$	$I2$	$I3$	$I4$
1	26.146	1.845	1.842	0.025	0.5	12/16	022200	211000	$31\bar{1}\bar{1}\bar{1}1$
2	34.388	2.411	2.411	0.024	44.0	18/29	122300	211111	100000
3	36.229	2.536	2.535	0.027	100.0	20/32	002400	221001	110000
4	41.230	2.872	2.876	0.034	22.4	26/41	013400	222100	111101
5	42.832	2.978	2.980	0.037	11.3	28/44	222400	311111	210001
6	50.831	3.501	3.499	0.036	3.5	38/61	233400	322101	111000
7	52.104	3.582	3.585	0.039	4.4	40/64	242400	322111	111100
8	60.376	4.102	4.102	0.031	23.9	52/84	004600	332002	101000
9	64.008	4.323	4.321	0.040	13.3	58/93	233600	333101	210000
10	65.169	4.393	4.391	0.043	10.1	60/96	224600	422211	$210\bar{1}00$
11	68.637	4.599	4.596	0.069	6.9	66/105	104700	432002	$2111\bar{1}1$
12	71.426	4.761	4.758	0.034	1.7	70/113	124700	432112	110010
13	72.485	4.822	4.822	0.034	3.9	72/116	244600	433101	200000
14	75.698	5.005	5.009	0.052	2.7	78/125	344601	433201	211001
15	76.916	5.073	5.071	0.037	3.8	80/128	004800	442002	220000
16	80.149	5.251	5.249	0.085	3.5	86/137	364500	443101	310001
17	82.674	5.388	5.392	0.016	0.4	90/145	015800	522222	111110
18	83.815	5.448	5.448	0.041	4.1	92/148	115801	443102	211000
19	90.709	5.803	5.801	0.028	1.8	104/168	464600	533212	111010

4.3.2) Magnetic measurements

4.3.2.1) dc magnetic susceptibility

The magnetic susceptibility χ of the i $Ag_{50}In_{36}Gd_{14}$ QC measured in an applied magnetic field of 30 Oe between 2.0 and 300 K is shown in figure (4-2)(a). The sample was zero-field cooled to the lowest temperature and the measurement was performed while warming the sample up to 300 K. The $\chi(T)$ curve exhibits a definite peak at 4.20(5) K indicating magnetic ordering. The $\chi(T)$ data above 50 K could be fitted to a modified Curie-Weiss law:

$$\chi = \chi_0 + \frac{C}{T - \theta_p}, \tag{4-1}$$

where χ_0 is the temperature independent magnetic susceptibility, C is the Curie constant, and θ_p is the paramagnetic Curie temperature. The Curie constant can be expressed as $C = \frac{N\mu_{eff}^2}{3k}$, where N is the concentration of magnetic atoms per unit mass and μ_{eff} is the effective magnetic moment. Figure (4-2)(b) shows the inverse magnetic susceptibility corrected for the contribution χ_0, $(\chi - \chi_0)^{-1}$ versus temperature; the validity of the Curie-Weiss law is evident. The values of χ_0, C, and θ_p obtained from the fit are, respectively, 8.57(10) × 10^{-6} emu g^{-1}, 9.91(3) × 10^{-3} emu K g^{-1}, and −37.1(2) K. This value of C corresponds to μ_{eff} of 8.15(1) μ_B per Gd atom.

For a free Gd^{3+} ion (electronic ground state $^8S_{7/2}$), the theoretical value of $\mu_{eff}^{th} = g\mu_B\sqrt{J(J+1)}$ is 7.94 μ_B [50]. Although the experimental value μ_{eff} = 8.15(1) μ_B does not agree within the experimental error with the theoretical value of 7.94 μ_B, yet they can be

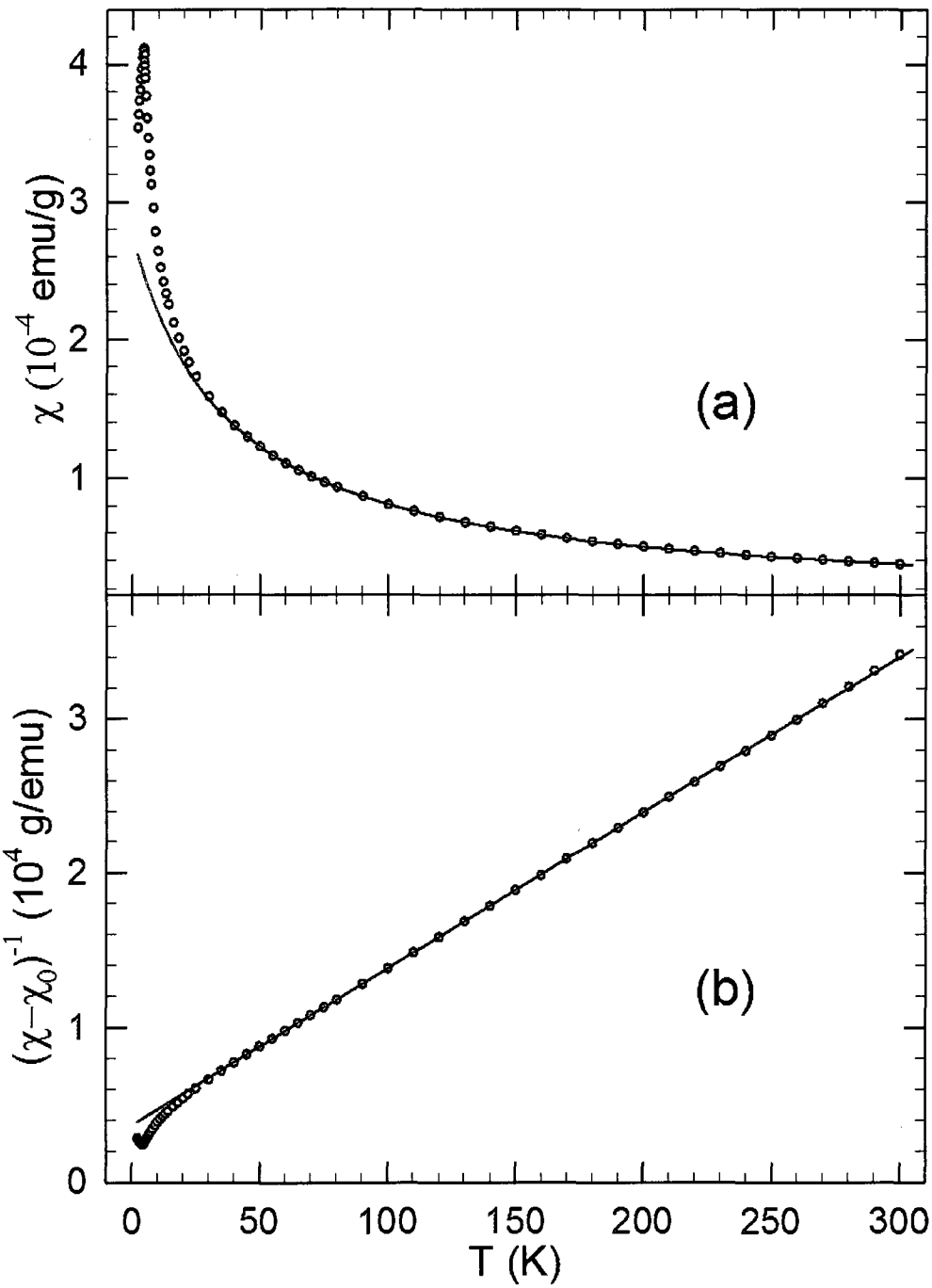

Figure (4-2)(a) The temperature dependence of the magnetic susceptibility of the icosahedral $Ag_{50}In_{36}Gd_{14}$ quasicrystal, measured in an external magnetic field of 30 Oe. The solid line is the fit to equation (4-1) in the temperature range 50 – 300 K, as explained in the text. (b) The inverse magnetic susceptibility corrected for the contribution χ_0, $(\chi - \chi_0)^{-1}$ versus temperature T of the icosahedral $Ag_{50}In_{36}Gd_{14}$ quasicrystal. The solid line is the fit to equation (4-1).

considered close for the following reasons. First, the theoretical value is based on the assumption that the Gd^{3+} ions are free and do not belong to a crystal. The value of μ_{eff} always varies depending on the environment surrounding the Gd atoms. The closest theoretical value known for the Gd atoms within a crystalline structure is $\mu_{eff} = 8.0\ \mu_B$ [50]. Second, the relative error between the measured value and the theoretical value is ~ 2.6% which can be considered small. Therefore, we can conclude that the magnetic moment is localized on the Gd^{3+} ions and that, as expected, Ag and In atoms carry no magnetic moment. The negative value of θ_p indicates the predominantly antiferromagnetic interaction between the Gd^{3+} spins.

To determine the nature of the magnetic transition at 4.20 K, we measured the temperature dependence of the ZFC and field-cooled (FC) magnetic susceptibility around 4.2 K in an applied magnetic field of 30 Oe (figure (4-3)). The occurrence of a bifurcation between the ZFC and FC data at the freezing temperature $T_f = 4.25(5)$ K is evident. Above T_f both ZFC and FC data are identical. Such a behaviour of the ZFC and FC susceptibility data is characteristic of a spin glass [51]. The i $Ag_{50}In_{36}Gd_{14}$ QC is thus a spin glass with a freezing temperature $T_f = 4.25(5)$ K.

The occurrence of a spin-glass behaviour requires both randomness and frustration [51, 143, 144]. The frustration parameter f, defined as $f = -\theta_p/T_f$ [145], is an empirical measure of frustration. Its value for the i $Ag_{50}In_{36}Gd_{14}$ QC is 8.7(1), which indicates that the studied QC belongs to a category of strongly geometrically frustrated magnets [145].

There are two other Gd-containing i alloys, $Zn_{50}Mg_{42}Gd_8$ with face-centered icosahedral (FCI) structure [146] and $Cd_{50}Mg_{40}Gd_{10}$ with SI structure [147], which are also spin glasses. The values of θ_p and T_f for these i alloys are, respectively, −38 K, 5.5 K and

–37.8(1.0) K, 4.3(1) K. These are very similar to the values of –37.1(2) K, 4.25(5) K found here for the i $Ag_{50}In_{36}Gd_{14}$ QC with SI structure. It would thus appear that SI and FCI Gd-containing i alloys have very similar bulk magnetic properties.

All three known Gd-containing ternary i alloys, $Zn_{50}Mg_{42}Gd_8$ [146], $Cd_{50}Mg_{40}Gd_{10}$ [147], and $Ag_{50}In_{36}Gd_{14}$ studied here, exhibit no long-range magnetic order and are spin glasses. Is then the spin-glass state inherent to the quasicrystalline structure of these alloys or does it result from structural/chemical disorder present in them? $Zn_{50}Mg_{42}Gd_8$ and $Cd_{50}Mg_{40}Gd_{10}$ QCs are thermodynamically stable whereas the $Ag_{50}In_{36}Gd_{14}$ QC is metastable. The fact that the spin-glass state occurs both in thermodynamically stable and metastable i QCs seems to exclude the structural disorder as the main reason for its occurrence. These three Gd-containing ternary i QCs possess some chemical disorder which may lead to the development of the spin-glass state. The fact that the thermodynamically

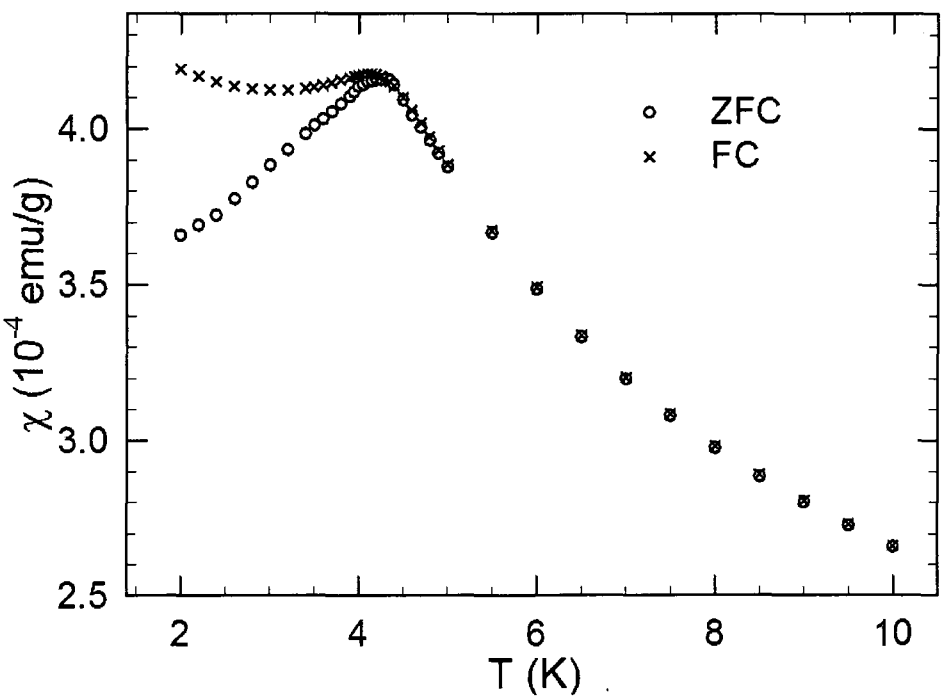

Figure (4-3) The temperature dependence of the zero-field (ZFC) and field-cooled (FC) magnetic susceptibility of the icosahedral $Ag_{50}In_{36}Gd_{14}$ quasicrystal, measured in an external magnetic field of 30 Oe.

stable binary i QC $YbCd_{5.7}$ with no chemical disorder is not a spin glass [148] seems to support this suggestion.

4.3.2.2) ac magnetic susceptibility

Figure (4-4) shows the temperature dependence of the in-phase component χ' and the out-of-phase component χ'' of the ac magnetic susceptibility for different frequencies between 20 Hz and 10 kHz. As the magnitude of χ'' is typically a few % of the value of χ' in spin glasses [51], this leads to a reduced signal-to-noise ratio in the χ'' data. Both χ' and χ'' curves show maxima whose amplitudes and positions depend on the frequency f of the applied ac magnetic field. With increasing frequency, the peak positions are shifted to higher temperatures, the peak intensity of $\chi'(T)$ is suppressed, and the peak intensity of $\chi''(T)$ is increased. These features are typical for canonical spin glasses [51]. There is a sharp peak in $\chi'(T)$ which can be used to define T_f. Below the maximum, the magnitude of χ' is frequency dependent, but it becomes independent of frequency at temperatures just above T_f. This behaviour is qualitatively similar to that of canonical spin glasses [142]. The out-of-phase component χ'' is vanishing above T_f, but is nonzero for temperatures just below T_f, which implies dissipation not only at the freezing transition but also for temperatures below it, a common feature of spin glasses [51].

The temperature (T_f) of the maximum in $\chi'(T)$ (figure (4-4)(a)) was determined from a curve fitting procedure where the variation $\chi'(T)$ near T_f was assumed to be a Gaussian function. The frequency dependence of T_f is shown in figure (4-5). A quantitative measure of the change of the freezing temperature with frequency in spin glasses is represented by the relative change in T_f per decade change in f [51] defined as:

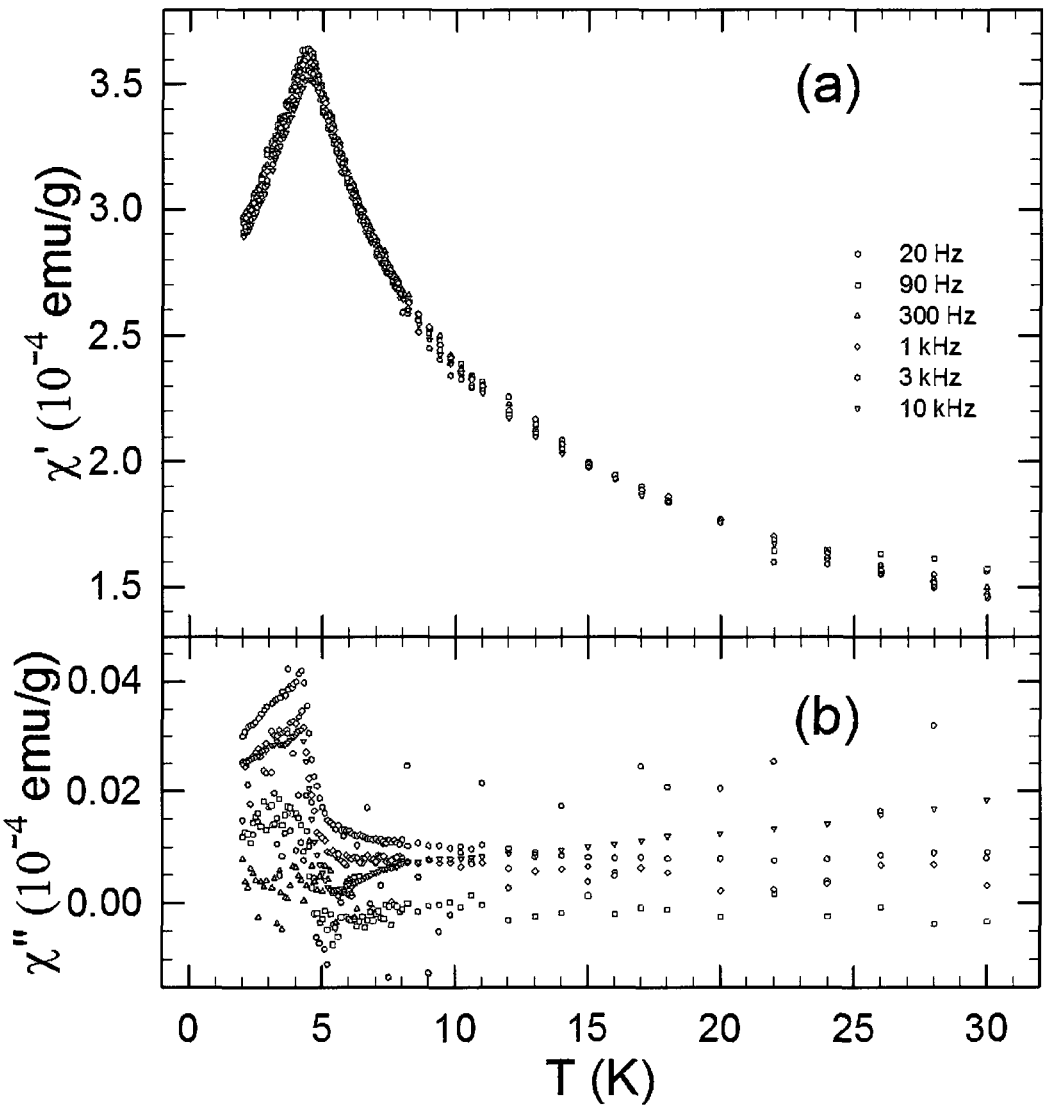

Figure (4-4) The temperature dependence of the in-phase magnetic susceptibility χ' (a) and out-of-phase magnetic susceptibility χ'' (b) measured for different applied frequencies from 20 Hz to 10 kHz for the icosahedral $Ag_{50}In_{36}Gd_{14}$ quasicrystal.

$$K = \frac{\Delta T_f}{T_f \Delta \log f}. \tag{4-2}$$

From a linear fit of the data in figure (4-5), and using the average value of $T_f = 4.42$ K for the range of frequencies used, one finds that $K = 0.010(2)$. This value is larger than

that found for such canonical spin glasses as $Cu_{1-x}Mn_x$ (K = 0.005), $Au_{1-x}Mn_x$ (K = 0.0045), $Ag_{1-x}Mn_x$ (K = 0.006), but comparable to that of other canonical spin glasses, $Au_{1-x}Fe_x$ (K = 0.010) and $Pd_{1-x}Mn_{13}$ (K = 0.013) [51]. We note that the value of K reported for another i $Tb_9Mg_{34}Zn_{57}$ QC is 0.049 [149].

There are essentially two different possible interpretations of the spin-glass freezing process. The first one assumes the existence of spin clusters and, in this case, the freezing is a nonequilibrium phenomenon [150]. The second interpretation assumes the existence of a true equilibrium phase transition at a finite temperature [151].

For magnetically interacting clusters, the frequency dependence of T_f is described by the phenomenological Vogel-Fulcher law [51, 150]

$$f = f_0 \exp[-E_a / k_B(T_f - T_0)], \tag{4-3}$$

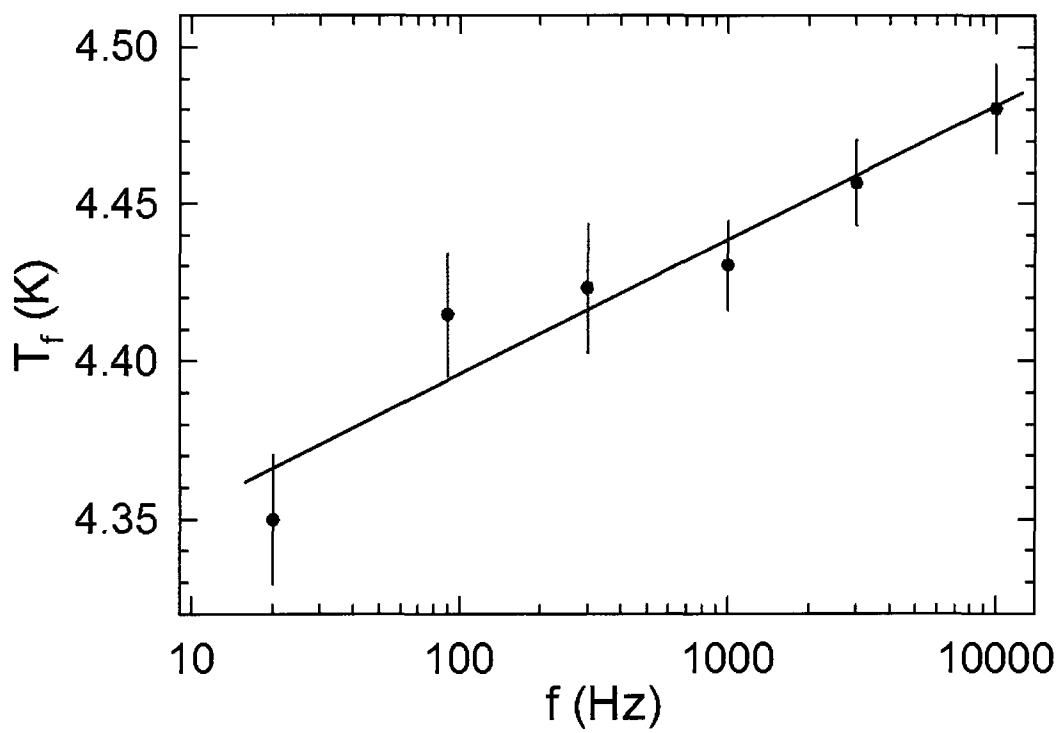

Figure (4-5) The frequency dependence of the freezing temperature T_f for the icosahedral $Ag_{50}In_{36}Gd_{14}$ quasicrystal. The solid line is the best linear fit to the T_f data.

where f_0 is a characteristic frequency, E_a is the activation energy, k_B is the Boltzmann constant, and T_0 is the Vogel-Fulcher temperature which is a measure of the interaction strengths between clusters in the spin glass [152]. Equation (4-3) implies a linear dependence of $1/(T_f - T_0)$ with $\log(f)$. The best fit of the $T_f(f)$ data to equation (4-3) (figure (4-6)), assuming $f_0 = 1 \times 10^{13}$ Hz typically observed for spin glasses [150], yields E_a/k_B = 9.09(38) K, and T_0 = 4.04(2) K. Similarly to what was found for other spin-glass systems [150], $E_a/k_B > T_0$. The values of E_a/k_B and T_0 are in general agreement with similar parameters reported

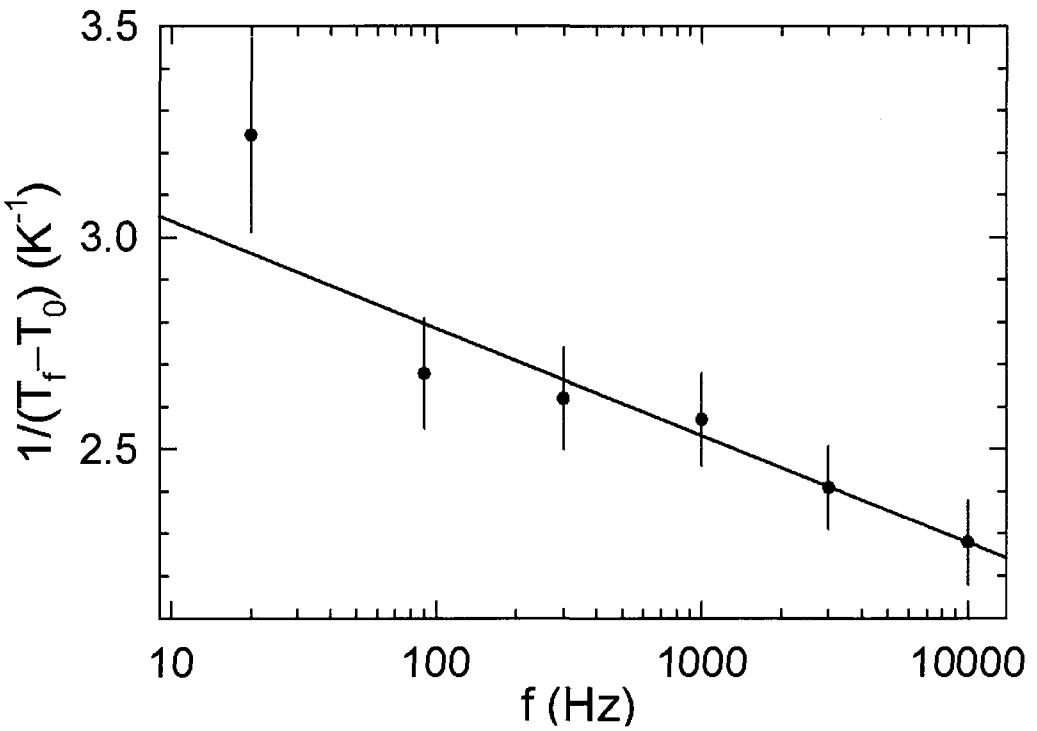

Figure (4-6) The frequency dependence of the freezing temperature T_f for the icosahedral $Ag_{50}In_{36}Gd_{14}$ quasicrystal. The solid line is the best fit to equation (4-3).

for other spin glasses [51, 149, 150].

In the second interpretation of the spin freezing phenomenon, the characteristic relaxation time $\tau = 1/f$ of magnetic moments will show a critical slowing down when

approaching T_f from above, characterized by a power law $\tau \propto \xi^z$, where ξ is the correlation length and z is the dynamic scaling exponent [153]. The correlation length ξ itself is related to the reduced temperature $t = (T_f - T_c)/T_c$, where T_c is the phase-transition temperature, by the critical correlation-length exponent ν as $\xi \propto t^{-\nu}$ [153]. Therefore, the temperature dependence of f obeys the power-law divergence [51, 153]

$$f = f_0 \left(\frac{T_f - T_c}{T_c} \right)^{z\nu}, \tag{4-4}$$

where f_0 is the microscopic relaxation frequency. The best fit of the $T_f(f)$ data to equation (4-4) (figure (4-7)), assuming $f_0 = 1 \times 10^{13}$ Hz typically observed for spin glasses [150], gives $T_c = 4.35(3)$ K and $z\nu = 5.97(10)$. The obtained value of $z\nu$ falls in the range 4–12 of $z\nu$ values found for many different spin glasses [51, 154].

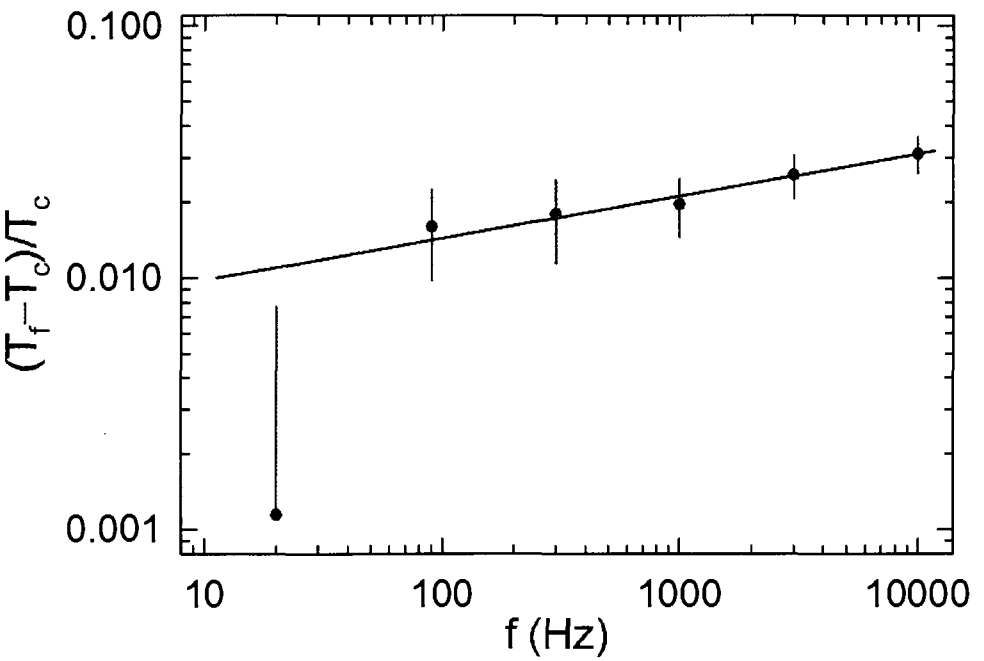

Figure (4-7) The frequency dependence of the freezing temperature T_f for the icosahedral $Ag_{50}In_{36}Gd_{14}$ quasicrystal. The solid line is the best fit to equation (4-4).

4.3.3) Mössbauer spectroscopy

The Mössbauer spectra were analyzed by means of a least-squares fitting procedure which entailed calculations of the positions and relative intensities of the absorption lines by numerical diagonalization of the full hyperfine interaction Hamiltonian. In the principal axis system of the electric field gradient (EFG) tensor, the Hamiltonian can be written as [155]:

$$\hat{H} = g\mu_B H_{hf}\left[\hat{I}_z\cos\theta + \frac{1}{2}\left(\hat{I}_+ e^{-i\phi} + \hat{I}_- e^{i\phi}\right)\sin\theta\right] + \frac{eQV_{zz}}{4I(2I-1)}\left[3\hat{I}_z^2 - I(I+1) + \frac{\eta}{2}\left(\hat{I}_+^2 + \hat{I}_-^2\right)\right], \quad (4\text{-}5)$$

where g is a nuclear g-factor of a nuclear state, μ_B is the nuclear Bohr magneton, H_{hf} is the hyperfine magnetic field at a nuclear site, Q is the quadrupole moment of a nuclear state, I is the nuclear spin, V_{zz} is the z component of the EFG tensor, η is the asymmetry parameter defined as $\eta = \left|\left(V_{xx} - V_{yy}\right)/V_{zz}\right|$ (if the principal axes are chosen such that $|V_{xx}| < |V_{yy}| < |V_{zz}|$, then $0 \le \eta \le 1$), θ is the angle between the direction of H_{hf} and the V_{zz}-axis, φ is the angle between the V_{xx}-axis and the projection of H_{hf} onto the xy plane, and the $\hat{I}_z$, $\hat{I}_+$, and $\hat{I}_-$ operators have their usual meaning. During the fitting procedure, the g factor and the quadrupole moment ratios for ^{155}Gd (I_g = 3/2, I_{ex} = 5/2) were constrained to, respectively, g_{ex}/g_g = 1.235 and Q_{ex}/Q_g = 0.087 [139]. The interference ξ factor for the E1 transition of 86.5-keV in ^{155}Gd was fixed to the value of 0.0520 which was derived from the fit of the ^{155}Gd Mössbauer spectrum of $GdFe_2$ at 4.2 K [156].

The resonance line shape of the Mössbauer spectra was described by a transmission integral formula [157]. In addition to the hyperfine parameters, only the absorber Debye-Waller factor f_a and the absorber linewidth Γ_a were fitted as independent parameters. The

source linewidth Γ_s = 0.334 mm/s and the background-corrected Debye-Waller factor of the source f_s^* [50], which were derived from the fit of the ^{151}Gd Mössbauer spectrum of $GdFe_2$ at 4.2 K [156], were used. The ^{155}Eu($SmPd_3$) source at 1.5 K emits a broadened emission line; from the fit of the ^{151}Gd Mössbauer spectrum of $GdFe_2$ at 1.5 K we found that Γ_s = 0.708 mm/s [156]. The surface density of the Mössbauer absorber of the i $Ag_{50}In_{36}Gd_{14}$ alloy was 304 mg cm^{-2}.

Figure (4-8)(a) shows a ^{151}Gd Mössbauer spectrum of the i $Ag_{50}In_{36}Gd_{14}$ QC at 10.4 K, i.e., well above T_f. This spectrum exhibits a substantial electric quadrupole hyperfine interaction. For ^{155}Gd nuclei, the quadrupole moment of the excited nuclear state with spin

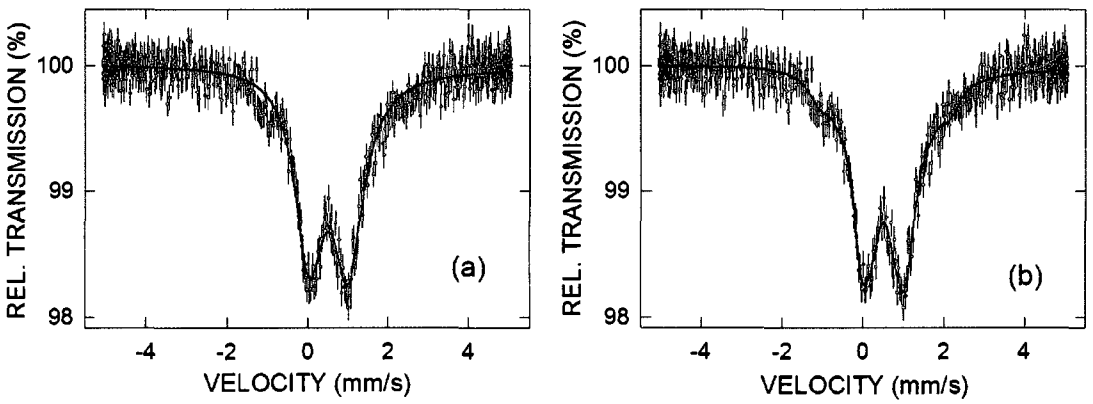

Figure (4-8) The ^{155}Gd Mössbauer spectrum of the icosahedral $Ag_{50}In_{36}Gd_{14}$ at 10.4 K fitted (solid line) with (a) one quadrupole pattern and (b) a distribution of quadrupole patterns. The zero-velocity scale is relative to the source.

I_{ex} = 5/2, Q_{ex} = 0.12 b [155], is significantly smaller than that of the ground nuclear state with spin I_g = 3/2, Q_g = 1.30 b [158]. This causes that the quadrupole splitting of the excited nuclear state, which is sensitive to the sign of V_{zz} and the magnitude of η, is smaller than the natural linewidth Γ_{nat} = 0.250 mm/s. Consequently, only the absolute value of the effective quadrupole splitting parameter $\Delta_g^{eff} = eQ_g|V_{zz}|\sqrt{1+\eta^2/3}$ can be derived from a Mössbauer spectrum of a sample in the paramagnetic state [159]. The parameters derived from the fit

(χ^2 = 1.10) of the 10.6 K Mössbauer spectrum (figure (4-8)(a)) are: the isomer shift (relative to the ^{155}Eu(SmPd$_3$) source) δ = 0.513(8) mm/s, Δ_g^{eff} = 2.030(27) mm/s, f_a = 9.9(2)%, and Γ_a = 0.508(23) mm/s. Although a relatively good fit was obtained, the value of Γ_a is unphysically large. This large value of Γ_a indicates the presence of a distribution of Δ_g^{eff}. In a QC, variations of the local coordination from site to site are expected to give rise to a distribution of the parameters V_{zz} and η [160]. The distribution of Δ_g^{eff} was simulated by fitting the 10.6 K Mössbauer spectrum with six component quadrupole patterns with Δ_g^{eff} values extending from 0.0 to 1.5 mm/s; the absorber linewidth was fixed to the value of Γ_{nat} and the same values of δ and f_a were assumed for all components. The parameters deduced from the fit assuming a distribution of Δ_g^{eff} (figure (4-8)(b)), δ, the average Δ_g^{eff}, $\overline{\Delta}_g^{eff}$, and f_a are given in table (4-2). The ^{151}Gd Mössbauer spectra of the i $Ag_{50}In_{36}Gd_{14}$ QC at 5.9 K and 5.3 K (figure (4-9)) display the presence of a distribution of Δ_g^{eff} and were fitted in the same way as the corresponding spectrum of the i $Ag_{50}In_{36}Gd_{14}$ QC at 10.6 K; the parameters derived from the fits are given in table (4-2).

The ^{151}Gd Mössbauer spectrum of the i $Ag_{50}In_{36}Gd_{14}$ QC at 4.4 K, i.e., slightly above T_f, clearly shows (figure (4-9)) the presence of a combined electric quadrupole and magnetic dipole hyperfine interactions. It was analyzed by assuming a distribution of the quadrupole splitting constant $\Delta_g = eQ_gV_{zz}$ and the same value of H_{hf} was used for all component patterns; the value of θ was fixed to 0.0° in the fit. The negative value of the average Δ_g, $\overline{\Delta}_g = eQ_g\overline{V}_{zz}$, obtained from the fit (table (4-2)) clearly establishes that the V_{zz} component of the EFG tensor at the Gd sites in the i $Ag_{50}In_{36}Gd_{14}$ QC is negative. The complete set of the

EFG tensor parameters at the Gd sites in the i $Ag_{50}In_{36}Gd_{14}$ QC determined experimentally here is: $\overline{V}_{zz} = -4.91(10) \times 10^{21}$ V cm^{-2} and $\eta = 1.00(20)$. The ^{151}Gd Mössbauer spectrum of the i $Ag_{50}In_{36}Gd_{14}$ QC at 1.5 K (figure (4-9)) was fitted in the same way as the

Table (4-2) Hyperfine interaction parameters derived from the fits to the ^{151}Gd Mössbauer spectra of the icosahedral $Ag_{50}In_{36}Gd_{14}$ at various temperatures.

T (K)	δ (mm s^{-1})	$\overline{\Delta}_g^{eff}$ or $\overline{\Delta}_g$ (mm s^{-1})	η	H_{hf} (kOe)	f_a (%)	χ^2
10.4	0.511(7)	2.498(37)			9.9(1)	0.99
5.9	0.522(7)	2.541(51)			10.0(1)	1.06
5.3	0.512(8)	2.385(87)			10.0(1)	1.19
4.4	0.501(9)	–2.212(45)	1.00(20)	69.8(7.5)	10.1(2)	1.04
1.5	0.516(16)	–2.426(95)	0.84(24)	119.6(11.2)	10.5(2)	1.10

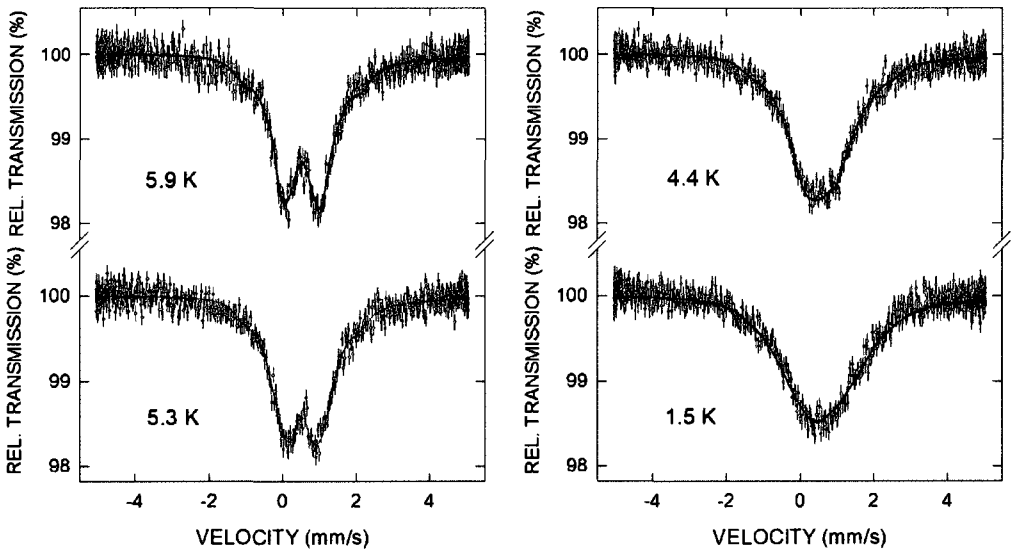

Figure (4-9) ^{155}Gd Mössbauer spectra of the icosahedral $Ag_{50}In_{36}Gd_{14}$ at various temperatures. Solid lines are fits, as described in the text. The zero-velocity scale is relative to the source.

corresponding spectrum at 4.4 K; the parameters derived from the fit are given in table (4-2).

The studied i $Ag_{50}In_{36}Gd_{14}$ QC is formed [135] by replacing all of Cd in the binary i $YbCd_{5.7}$ QC [136] with Ag and In, and Yb with Gd. It is thus expected that the crystal structure of the i $Ag_{50}In_{36}Gd_{14}$ QC must be similar to that of the i $YbCd_{5.7}$ QC. The crystal

structure of the i $YbCd_{5.7}$ QC has been recently solved [137]. One would expect that Gd atoms are located at the Yb sites (on the vertices of the icosahedron and inside the acute rhombohedron) and the Ag and In atoms are distributed among the Cd sites. Clearly, the existence of the multiplicity of Gd sites observed here is compatible with this structural model. The complete set of the EFG tensor parameters at the Gd sites in the i $Ag_{50}In_{36}Gd_{14}$ QC determined experimentally here could be compared with the corresponding parameters obtained from *ab initio* calculations of the EFGs for a possible structural model for the i $Ag_{50}In_{36}Gd_{14}$ QC, similarly as has been done for the i Al-Cu-Fe QC [161]. This could lead to the solution of the structure of the i $Ag_{50}In_{36}Gd_{14}$ QC.

In terms of the Debye approximation of the lattice vibrations, the absorber Debye-Waller factor f_a is expressed [125, 162] by the Debye temperature, Θ_D, as:

$$f_a(T) = \exp\left\{-\frac{3}{4}\frac{E_\gamma^2}{Mc^2 k_B \Theta_D}\left[1+\left(\frac{T}{\Theta_D}\right)^2 \int_0^{\Theta_D/T} \frac{x\,dx}{e^x - 1}\right]\right\}, \qquad (4\text{-}6)$$

where E_γ is the energy of the Mössbauer transition, M is the mass of the Mössbauer nucleus, and c is the speed of light. The analysis of the values of f_a given in table (4-2) via equation (4-6) yields Θ_D = 199(2) K. This is the lowest value among the known ternary i QCs. This value compares well with the anomalously low value of Θ_D (in the range 138–145 K) for the i $Yb_{5.7}Cd$ QC [148, 163–166].

The freezing temperature determined by the Mössbauer effect, T_f^m, is defined as a temperature at which the magnetic dipole hyperfine interaction sets in. The presence of the magnetic dipole hyperfine interaction in the Mössbauer spectrum of the i $Ag_{50}In_{36}Gd_{14}$ QC at 4.4 K, and its absence in the Mössbauer spectrum at 5.3 K, shows that T_f^m lies between

4.4 and 5.3 K. Clearly, T_f^m is larger than T_f. The systematically higher values of T_f^m than T_f have been observed for many spin-glass systems [51, 167–172]. The inequality $T_f^m > T_f$ results from a time window of an experimental technique used to determine the freezing temperature: as the time window decreases, the freezing temperature increases [51, 167–172].

4.3.4) Conclusions

A newly discovered icosahedral quasicrystal $Ag_{50}In_{36}Gd_{14}$ has been studied with x-ray diffraction, dc and ac magnetic susceptibility, and ^{155}Gd Mössbauer spectroscopy. The studied quasicrystal has a simple six-dimensional Bravais lattice with the six-dimensional hypercubic lattice constant of 7.805(2) Å. The observed broadening of the diffraction Bragg peaks reflects the presence of the topological/chemical disorder. The temperature dependence of the magnetic susceptibility follows the Curie-Weiss law with the effective magnetic moment of 8.15(1) μ_B per Gd atom and the paramagnetic Curie temperature of –37.1(2) K. Based on dc magnetization measurements, no evidence is found for a transition to a ground state with a long-range magnetic order in the temperature range between 2 and 300 K. The studied quasicrystal is a spin glass with a freezing temperature of 4.25(5) K. This is further confirmed by the analysis of the frequency dependence of T_f using the Vogel-Fulcher law and the dynamic scaling behaviour near T_f. The presence of the distribution of the electric quadrupole splitting in the Mössbauer spectra indicates the existence of a multiplicity of Gd sites. The values of the principal component of the electric field gradient tensor and the asymmetry parameter at these sites are, respectively, $-4.91(10) \times 10^{21}$ V cm^{-2} and η = 1.00(20). The Debye temperature of the studied quasicrystal is 199(2) K. The

hyperfine magnetic field sets in at the temperature higher than the freezing temperature.

5) ICOSAHEDRAL QUASICRYSTAL $Zn_{77}Fe_7Sc_{16}$

5.1) Introduction

Recently, new thermodynamically stable i QCs were discovered in the Zn-TM-Sc (TM = transition metal) system [173]. These QCs are formed by replacing some of Zn in the binary 1/1 approximant Zn_6Sc [174] with TM. As the 1/1 approximant Cd_6Yb of the thermodynamically stable binary i $YbCd_{5.7}$ QC is isostructural with Zn_6Sc, it is expected that the structure of the i Zn-TM-Sc QCs must be similar to that of the i $YbCd_{5.7}$ QC. One would expect that Sc and TM atoms are distributed among the Yb sites (on the vertices of the icosahedron and inside the acute rhombohedron) and the Zn atoms are located at the Cd sites.

The novel i $Zn_{77}Fe_7Sc_{16}$ QC is chosen because it contains Fe. Having Fe atoms in such a sample has two main advantages: first, the Fe atoms can possibly carry a sizeable 3d magnetic moment [175, 176] and perhaps exhibit long-range magnetic order; second, an ^{57}Fe Mössbauer spectroscopy study can be performed. Section (3.3.3.2) describes the ^{57}Fe Mössbauer spectroscopy setup.

5.2) Experimental procedure

Starting elements of Zn shots (purity, 99.999%), Fe foil (purity 99.99%) and Sc chunks (purity, 99.9%) were used as received; Fe element was enriched to 95.4% in a ^{57}Fe isotope. Appropriate amounts of these elements corresponding to the composition $Zn_{77}Fe_7Sc_{16}$ were weighed (±0.1 mg) and weld-sealed under an argon atmosphere into a tantalum container. The container was in turn held within an evacuated SiO_2 jacket to avoid

its air oxidation. The mixture was melted at 1000 °C for 2 h, followed by annealing at 700 °C for 120 h.

The ^{57}Fe Mössbauer spectroscopy (MS) measurements in the temperature range 1.9–289.4 K were conducted using a standard Mössbauer spectrometer operating in a sine mode and a source of ^{57}Co(Rh) at room temperature. The spectrometer was calibrated with a 6.35-μm-thick α-Fe foil [126], and the spectra were folded. The full linewidth at half maximum of the inner pair of the α-Fe Zeeman pattern was 0.210(2) mm/s and this value can be regarded as the resolution of the Mössbauer spectrometer. The Mössbauer absorber consisted of a mixture of pulverized material and boron nitride, which were pressed into a pellet that was put into an Al disc container of thickness of 0.008 mm to ensure a uniform temperature over the whole absorber. The surface densities of the Mössbauer absorbers of the i $Zn_{77}Fe_7Sc_{16}$ QC were 1.10 and 1.21 mg ^{57}Fe cm^{-2} for measurements below and above 4.2 K, respectively.

5.3) Results and discussion

5.3.1) Structural characterization

The XRD pattern of the studied sample measured in the 2θ range 5–90° (figure (5-1)) shows the presence of 39 i Bragg peaks. Bragg peaks of very small intensity due to an unidentified second phase are also observed (figure (5-1)). The positions of all the detected i Bragg peaks corresponding to Cu Kα_1 radiation (the value of its wavelength λ is 1.5405981 Å [138]) in terms of the angle $2\theta_i$ and the corresponding wave number $Q_{exp} = 4\pi \sin\theta_i / \lambda$, as well as their relative intensities and full widths at half maximum Γ_Q, were determined from the profile fitting using the procedure described by Schreiner and Jenkins [139]. These

parameters corresponding to 39 detected i peaks, whose positions are indicated by vertical lines in figure (5-1), are presented in table (5-1). This table contains also the theoretical positions Q_{cal} which were calculated by taking the position of the second most intense i peak as the reference. Since there are several schemes employed to index the i peaks, we present in table (5-1) the indices that correspond to the most frequently used schemes [140–142].

The form of indices of the observed i Bragg peaks (table (5-1)) shows that the i $Zn_{77}Fe_7Sc_{16}$ QC has a primitive six-dimensional Bravais lattice. There is a good agreement between the observed Q_{exp} and the theoretical Q_{cal} positions of the i Bragg peaks (figure (5-1)) and table (5-1)). The value of the six-dimensional hypercubic lattice constant calculated from the value Q_{exp} that corresponds to the (18,29) i peak is 7.087(1) Å. The width Γ_Q of most of the i peaks is very narrow: for example, Γ_Q = 0.009 $Å^{-1}$ corresponding to the (52, 52.1/84) i Bragg peak (table (5-1)) is nearly equal to that of the (400) Bragg peak of the Si standard (0.008 $Å^{-1}$) measured with the same x-ray diffractometer. This is indicative of a high degree of structural order of the studied QC.

5.3.2) Magnetic measurements

5.3.2.1) dc magnetic susceptibility

The magnetic susceptibility χ of the i $Zn_{77}Fe_7Sc_{16}$ QC measured in an applied magnetic field of 50 Oe between 2.0 and 300 K is shown in figure (5-2)(a). The sample was zero-field cooled (ZFC) to 2.0 K and the measurement was performed while warming the sample up to 300 K. The $\chi(T)$ curve exhibits a definite peak at 7.74(4) K indicating magnetic ordering. The $\chi(T)$ data above 40 K could be fitted to a modified Curie-Weiss law

$$\chi = \chi_0 + \frac{C}{T-\theta_p}, \tag{5-1}$$

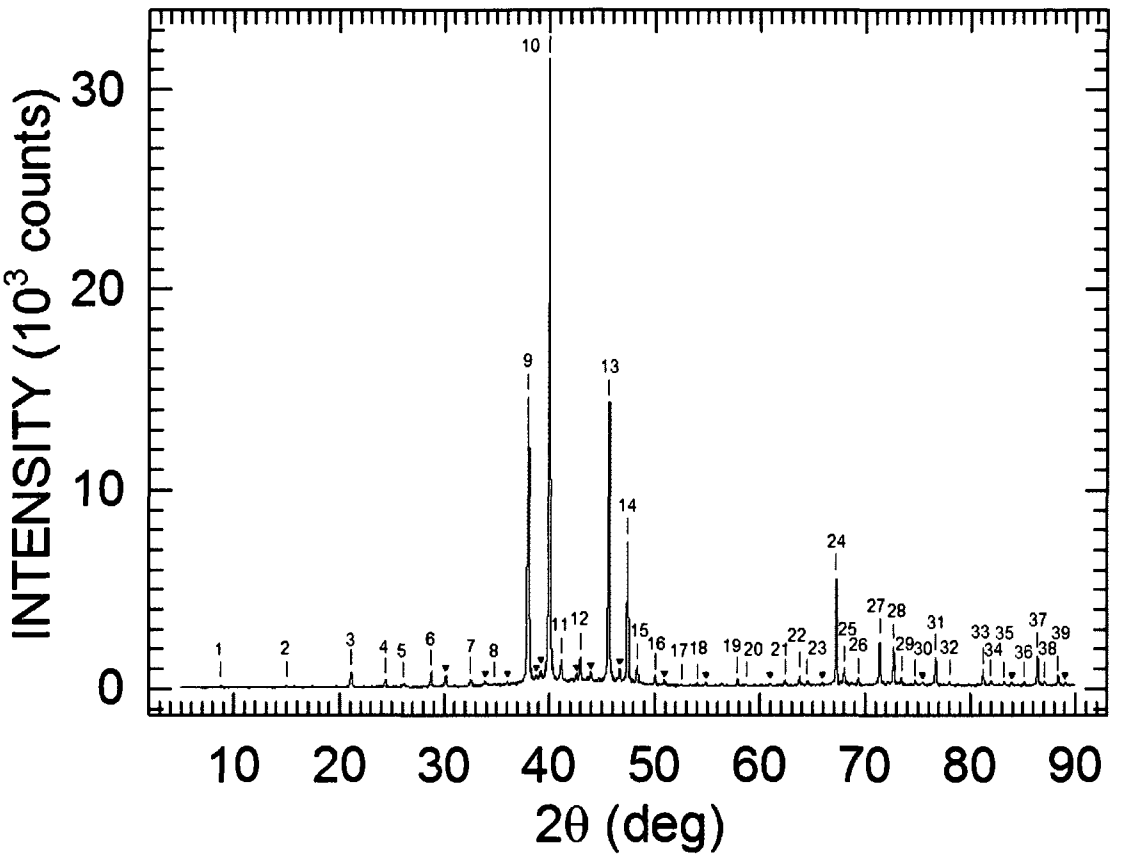

Figure (5-1) The XRD spectrum of the $Zn_{77}Fe_7Sc_{16}$ quasicrystal at 298 K corrected for the $CuK\alpha_2$ lines. The vertical lines labeled with integers above all detected i Bragg peaks correspond to the positions calculated for the Cu $K\alpha_1$ radiation, as explained in the text. The position, full width at half maximum, and relative intensity of each detected i peak are given in table (5-1) together with the corresponding index. The symbol ▼ indicates the peak positions corresponding to an unidentified second phase.

where χ_0 is the temperature independent magnetic susceptibility, C is the Curie constant, and θ_p is the paramagnetic Curie temperature. The Curie constant can be expressed as $= \frac{N\mu_{eff}^2}{3k_B}$, where N is the concentration of magnetic atoms per unit mass, μ_{eff} is the effective magnetic moment, and k_B is the Boltzmann constant. Figure (5-2)(b) shows the inverse magnetic susceptibility corrected for the contribution χ_0, $(\chi - \chi_0)^{-1}$ versus temperature; the validity of the modified Curie-Weiss law is evident. The values of χ_0, C, and θ_p obtained from the fit

Table (5-1) Positions in terms of $2\theta_1$ (in degrees) corresponding to Cu $K\alpha_1$ radiation and Q_{exp} (in $Å^{-1}$), full width at half maximum Γ_Q (in $Å^{-1}$), and relative area A normalized to 100.0 of all detected icosahedral Bragg peaks. Q_{cal} (in $Å^{-1}$) is the calculated Q value by taking the position of the ninth line with the *I*1 index 18/29 as the reference line. *I*1 and *I*2 are the indices (N/M) and (h/h',k/k',l/l') based on the indexing scheme of Cahn *et al* [140], whereas *I*3 and *I*4 are the indices corresponding, respectively, to the indexing schemes of Elser [141] and Bancel *et al* [142].

Label	$2\theta_1$	Q_{exp}	Q_{cal}	Γ_Q	A	*I*1	*I*2	*I*3	*I*4
1	8.791	0.625	0.627	0.016	0.1	2/1	011000	100000	$21\bar{1}\bar{1}\bar{1}1$
2	15.002	1.065	1.067	0.011	0.3	4/4	000200	110000	$2200\bar{1}1$
3	21.098	1.493	1.495	0.014	3.0	6/9	011200	111000	110001
4	24.401	1.724	1.726	0.011	1.2	8/12	002200	111100	$1110\bar{1}0$
5	26.108	1.842	1.836	0.017	0.9	10/13	122100	111110	$2210\bar{2}0$
6	28.791	2.028	2.029	0.008	1.9	12/16	022200	211000	$31\bar{1}\bar{1}\bar{1}1$
7	32.547	2.286	2.283	0.015	1.5	14/21	102300	211100	$2100\bar{1}1$
8	34.792	2.439	2.441	0.007	0.2	16/24	222200	211110	$210\bar{1}\bar{1}1$
9	38.002	2.656	2.656	0.014	51.5	18/29	122300	211111	100000
10	40.017	2.791	2.792	0.012	100.0	20/32	002400	221001	110000
11	41.145	2.866	2.862	0.015	5.0	22/33	012410	221101	$2210\bar{1}1$
12	42.970	2.988	2.989	0.010	3.7	24/36	022400	222000	$2211\bar{1}1$
13	45.677	3.166	3.167	0.011	43.6	26/41	013400	222100	111101
14	47.473	3.283	3.283	0.008	5.7	28/44	222400	311111	210001
15	48.368	3.342	3.342	0.009	2.6	30/45	102500	321001	$3200\bar{1}1$
16	50.041	3.450	3.452	0.010	1.3	32/48	004400	321101	$320\bar{1}\bar{1}1$
17	52.564	3.612	3.607	0.015	0.3	34/53	122500	321111	220001
18	54.057	3.707	3.709	0.008	0.3	36/56	013510	322100	$2210\bar{1}0$
19	57.878	3.947	3.949	0.009	0.8	40/64	242400	322111	111100
20	58.713	3.999	3.999	0.014	0.3	42/65	104500	322200	$310\bar{1}\bar{1}1$
21	62.383	4.224	4.222	0.010	1.0	46/73	013600	332001	$2110\bar{1}0$
22	63.765	4.308	4.310	0.009	1.3	48/76	233510	332101	$2110\bar{1}1$
23	64.520	4.354	4.355	0.010	0.7	50/77	213600	332111	320002
24	67.248	4.517	4.518	0.009	12.0	52/84	004600	332002	101000
25	67.994	4.561	4.562	0.011	2.4	54/85	253400	422111	221101
26	69.361	4.641	4.642	0.007	0.6	56/88	024600	333100	$3100\bar{1}1$
27	71.375	4.758	4.759	0.010	7.5	58/93	233600	333101	210000
28	72.718	4.836	4.837	0.008	5.4	60/96	224600	422211	$210\bar{1}00$
29	73.430	4.876	4.877	0.009	0.9	62/97	015600	432101	$320\bar{1}\bar{1}0$
30	74.755	4.952	4.953	0.006	0.2	64/100	253510	432111	$3210\bar{1}1$
31	76.706	5.061	5.062	0.009	4.0	66/105	104700	432002	$2111\bar{1}1$
32	78.010	5.134	5.135	0.005	0.2	68/108	114710	432102	221001
33	81.243	5.311	5.312	0.008	1.7	72/116	244600	433101	200000
34	81.953	5.349	5.348	0.009	0.6	74/117	235600	433111	$2220\bar{1}0$
35	83.229	5.417	5.418	0.007	0.4	76/120	015710	433200	320001
36	85.128	5.517	5.518	0.010	0.5	78/125	344601	433201	211001
37	86.399	5.584	5.585	0.007	3.2	80/128	004800	442002	220000
38	87.055	5.618	5.620	0.007	0.2	82/129	144700	442102	$3211\bar{1}1$
39	88.367	5.685	5.686	0.008	1.3	84/132	024800	522221	$320\bar{1}02$

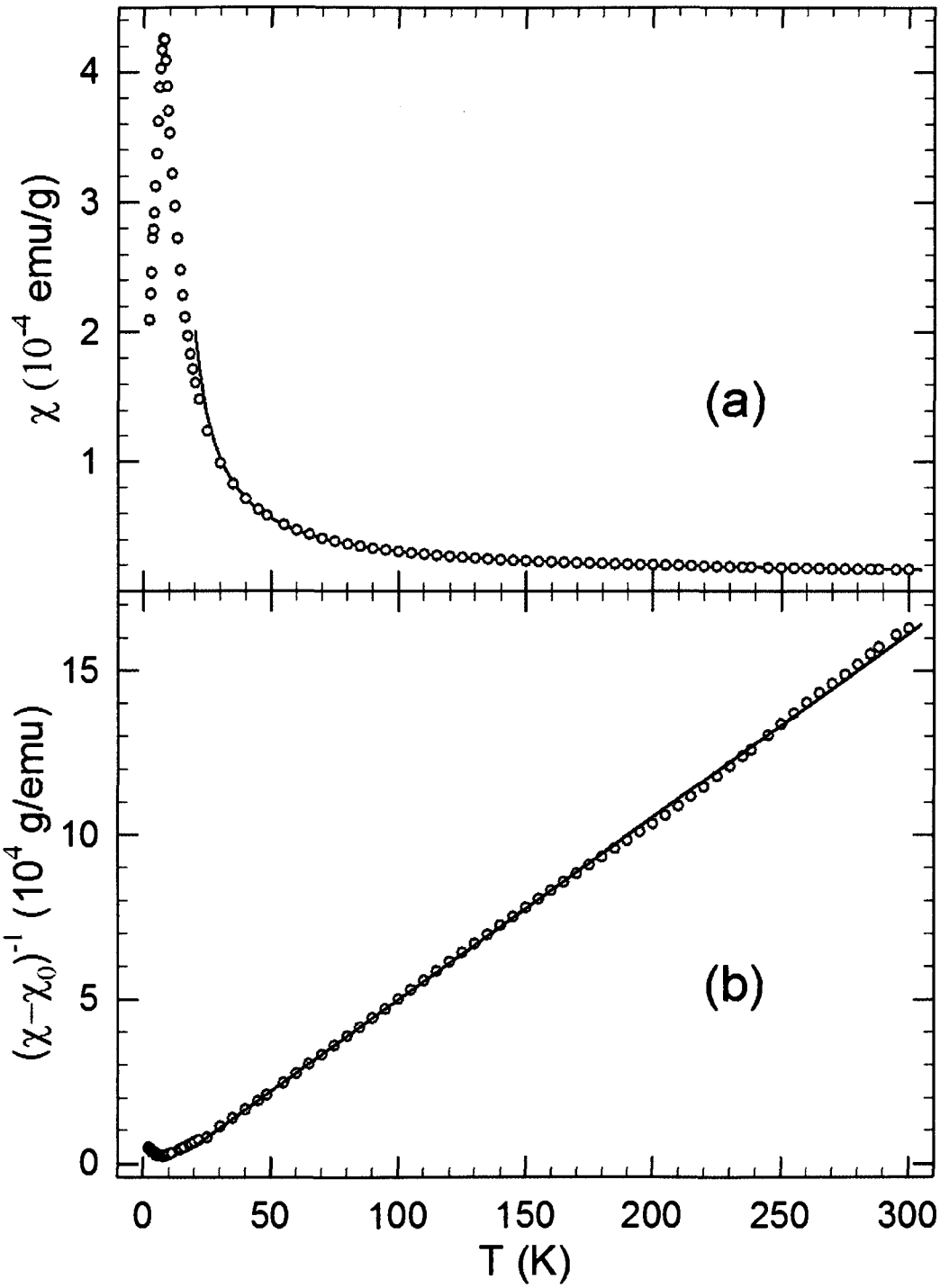

Figure(5-2)(a) The temperature dependence of the magnetic susceptibility of the icosahedral $Zn_{77}Fe_7Sc_{16}$ quasicrystal, measured in an external magnetic field of 50 Oe. The solid line is the fit to equation(5-1) in the temperature range 40 – 300 K, as explained in the text. (b) The inverse magnetic susceptibility corrected for the contribution χ_0, $(\chi - \chi_0)^{-1}$ versus temperature T of the icosahedral $Zn_{77}Fe_7Sc_{16}$ quasicrystal. The solid line is the fit to equation (5-1).

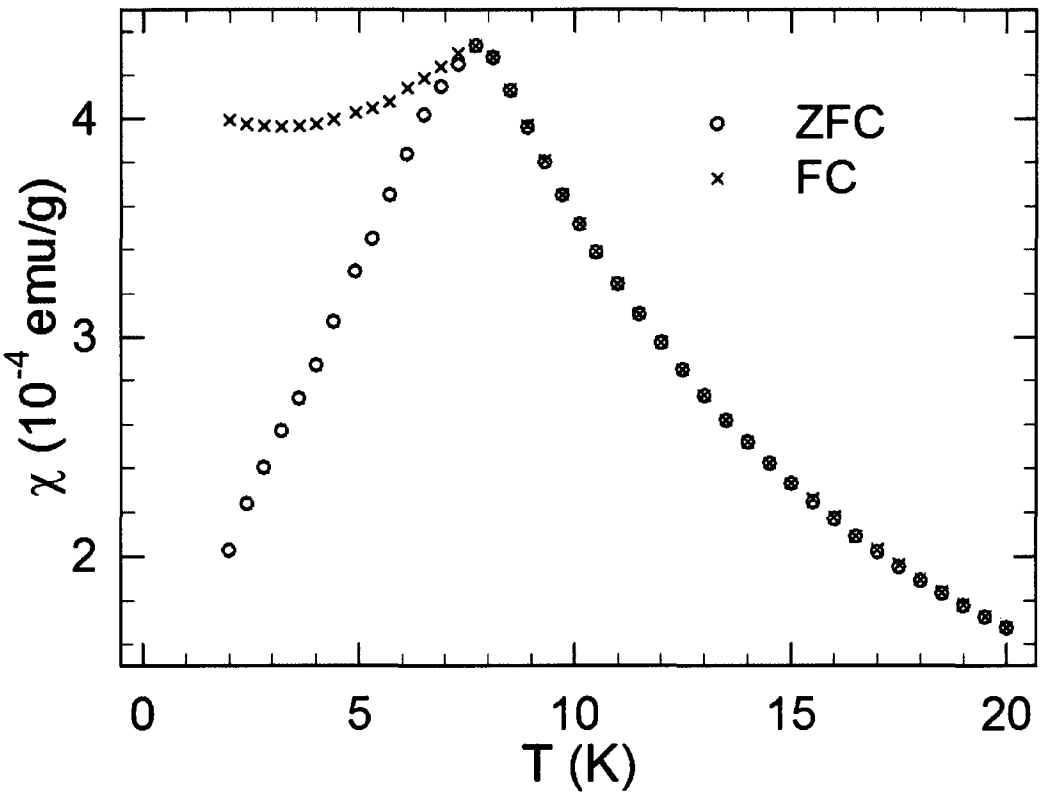

Figure(5-3)The temperature dependence of the zero-field-cooled (ZFC) and field-cooled (FC) magnetic susceptibility of the icosahedral $Zn_{77}Fe_7Sc_{16}$ quasicrystal, measured in an external magnetic field of 50 Oe.

are, respectively, $1.07(1) \times 10^{-5}$ emu/g, $1.80(1) \times 10^{-3}$ emu·K g^{-1}, and 10.6(2) K. This value of C corresponds to μ_{eff} of 3.55(1) μ_B per Fe atom.

The positive value of θ_p indicates the predominantly ferromagnetic interaction between the Fe atoms. The magnetic moment of 3.55 μ_B per Fe atom is the highest ever reported for a stable QC containing a TM element [29, 175, 176]. Recent electronic structure calculations [177] for a cubic approximant of the i $Zn_{77}Fe_7Sc_{16}$ QC predict the magnetic moment per Fe atom in the range 1.2–2.4 μ_B.

To determine the nature of the magnetic transition at 7.74 K, we measured the temperature dependence of the ZFC and field-cooled (FC) magnetic susceptibility around

8.0 K in an applied magnetic field of 50 Oe (figure (5-3)). The occurrence of a bifurcation between the ZFC and FC data at the freezing temperature T_f = 7.75(2) K is evident. Above T_f both ZFC and FC data are identical. Such a behaviour of the ZFC and FC susceptibility data is characteristic of a spin glass [51]. The i $Zn_{77}Fe_7Sc_{16}$ QC is thus a spin glass with a freezing temperature T_f = 7.75(2) K.

5.3.2.2) Relaxation effects in the dc magnetization

An ageing phenomenon, which was discovered by Lundgren *et al* in 1983 [178], is an inherent characteristic of a spin-glass system. The measurement of ageing effects in spin glasses is carried out either via the ZFC magnetization decay measurement or the complementary thermoremanent magnetization (TRM) decay measurement [51]. The first involves cooling the sample in zero magnetic field from above T_f to the measuring temperature T_m below T_f, allowing the sample to stay at T_m a certain waiting time t_w, and then applying a small magnetic field and recording the change of magnetization with time. The second utilizes cooling the sample in a small magnetic field from above T_f to T_m below T_f, keeping the sample at T_m for time t_w, and then rapidly removing the magnetic field and recording the change of magnetization with time. The dependence of the magnetization decays on t_w is called ageing.

Figure (5-4) shows the ZFC magnetization decays at T_m = 4.8 K = 0.62T_f and in 20 Oe for different waiting times. It is clear from the figure that the measured ZFC magnetization strongly depends on t_w: the longer the t_w, the slower the decay of the ZFC magnetization. The system becomes "stiffer" for larger waiting times. This confirms the existence of aging processes in the i $Zn_{77}Fe_7Sc_{16}$ QC. The observed dependence of the ZFC

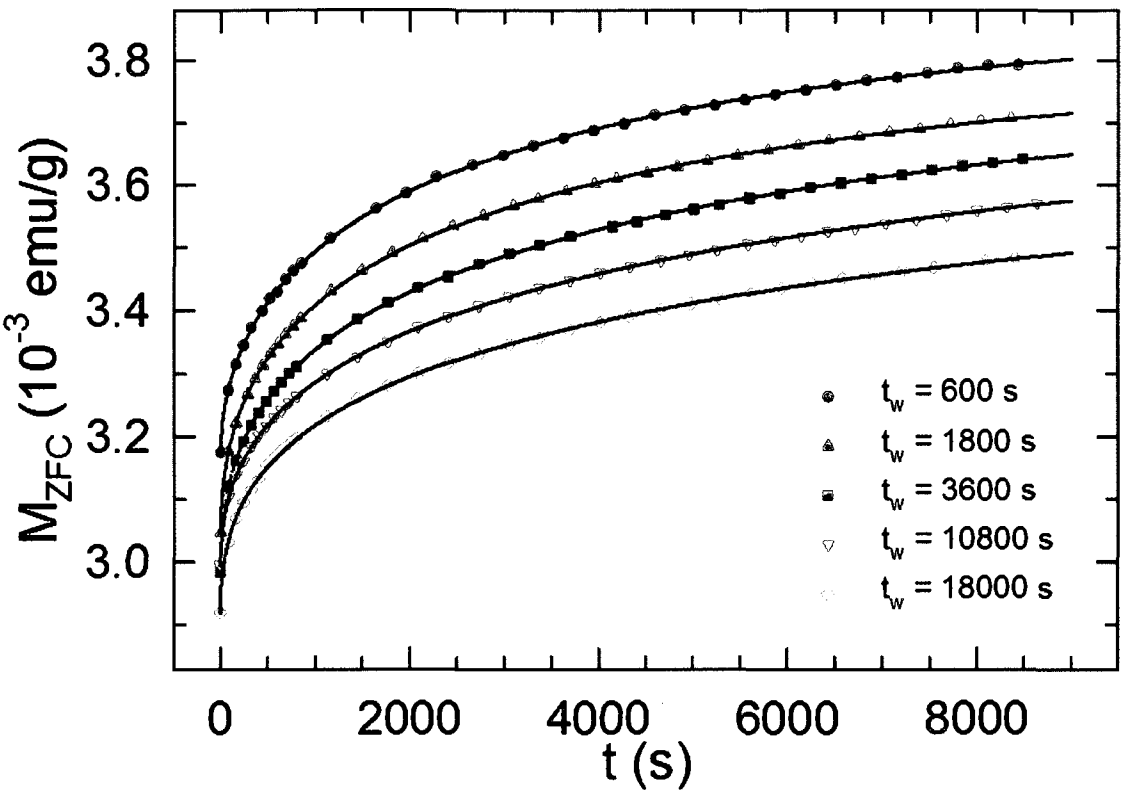

Figure (5-4) The time dependence the ZFC magnetization for an applied magnetic field of 20 Oe at 4.8 K for different waiting times t_w of the icosahedral $Zn_{77}Fe_7Sc_{16}$ quasicrystal. The solid lines are the fits to equation (5-2).

magnetization on t_w is the same as that observed for canonical spin glasses [51].

Among the various functional forms that have been proposed to describe the magnetization decay, one of the most successful in describing the data is a stretched exponential of the form

$$M(t) = M_0 - M_r \exp\left[-\left(\frac{t}{\tau_r}\right)^{1-n}\right], \qquad (5\text{-}2)$$

where M_0 relates to an intrinsic ferromagnetic component, M_r is a glassy component, τ_r is the characteristic time constant, and n is the stretched exponential exponent [88, 179, 95]. The time constant τ_r and the exponent n are related to the relaxation rate of the spin glass. The data could be well fitted to equation (5-2) as evidenced by the solid lines in figure (5-4). The

values of the fitted parameters are listed in table (5-2). To within experimental error, n and M_r are independent of t_w, whereas τ_r increases with t_w. The independence of n and M_r on t_w was observed for canonical spin glasses [88, 95, 179, 180].

The ageing phenomenon in the i $Zn_{77}Fe_7Sc_{16}$ QC was also studied by the TRM decay measurements. Figure (5-5) shows the TRM decays for different waiting times at a cooling field of 50 Oe and at T_m = 4.8 K = $0.62T_f$ and T_m = 6.0 K = $0.77T_f$. The following observations follow from the data (figure (5-5)): (1) the TRM decreases substantially as T_f is approached; (2) the larger the t_w, the larger the TRM; (3) the time decay of the TRM slows down as t_w increases. These three dependencies are precisely the same as those observed for canonical spin glasses [88, 95, 179, 182] and can be explained within the context of an ultrametric organization of the metastable states in a spin glass [181, 182].

The ultrametric topology of the metastable states was predicted by Parisi via replica-symmetry solution [74, 183] of the Sherrington-Kirkpatrick infinite-range spin-glass model [68]. A pure state α of a spin glass is characterized by the thermal average magnetization at a site i, m_i^α. An overlap function between two states α and β is $q^{\alpha\beta} = N^{-1}\sum_{i=1}^{N} m_i^\alpha m_i^\beta$, where N is the total number of spins, which are assumed here to be of Ising type. The self-overlap $q_{\alpha\alpha}$ is the Edwards-Anderson order parameter q_{EA} [66] and it fulfills the relation $-q_{EA}(T) \leq q^{\alpha\beta} \leq q_{EA}(T)$. The number N_S of metastable states, or equivalently the number

Table (5-2) Results of a fit to equation (2) of ZFC magnetization decays at T = 4.8 K and H = 20 Oe for different waiting times t_w.

t_w (s)	M_0 (10^{-3} emu/g)	M_r (10^{-3} emu/g)	τ_r (10^3 s)	n
600	3.93(3)	0.76(8)	3.08(2)	0.467(95)
1800	3.87(3)	0.83(5)	3.14(2)	0.519(43)
3600	3.90(3)	0.92(4)	5.08(8)	0.555(23)
10800	3.87(4)	0.88(4)	7.53(11)	0.550(23)
18000	3.80(5)	0.88(4)	7.84(12)	0.576(27)

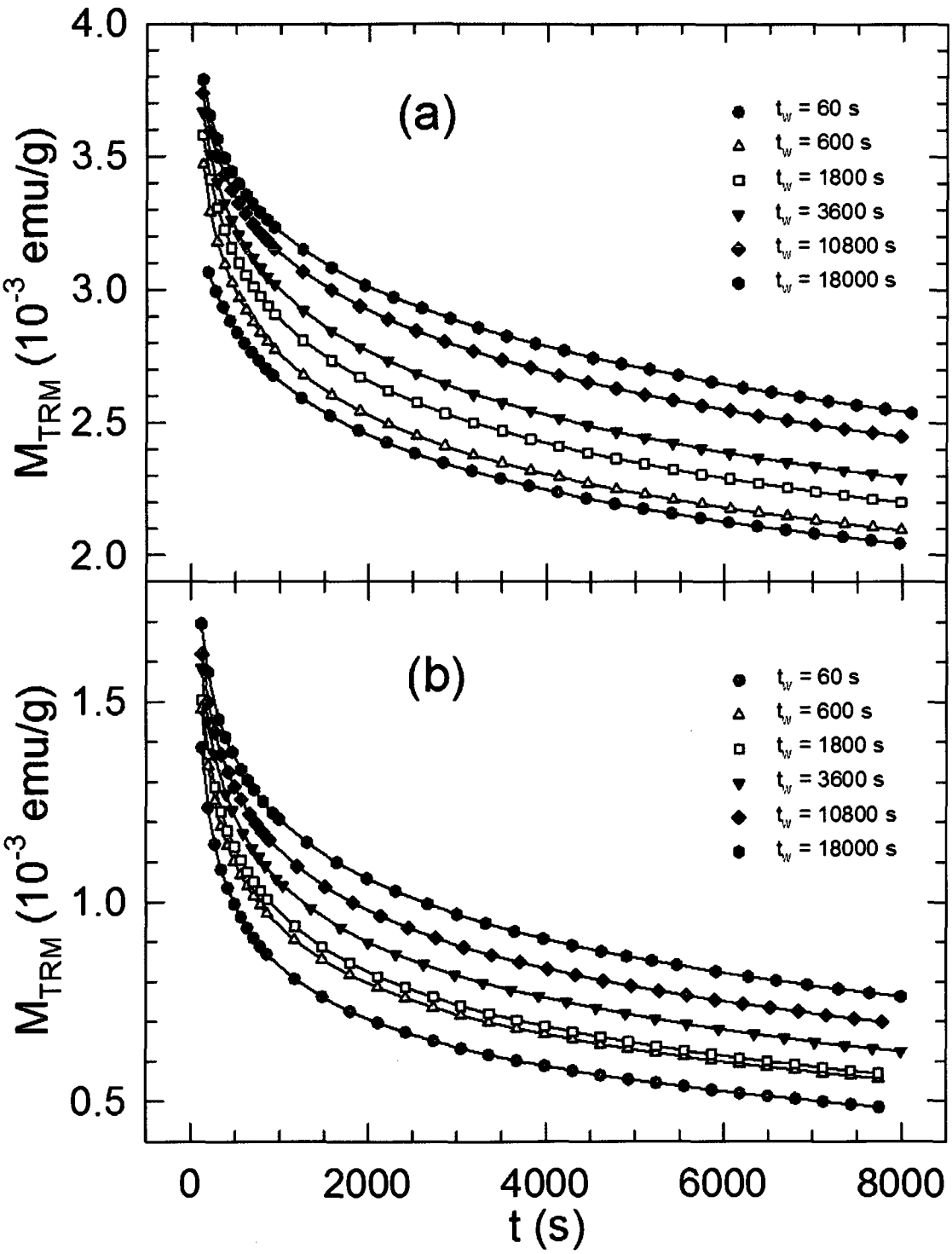

Figure (5-5) The TRM time decays at H = 50 Oe for the different waiting times t_w at (a) 4.8 K and (b) 6.0 K of the icosahedral $Zn_{77}Fe_7Sc_{16}$ quasicrystal. The solid lines are guides for the eye.

of relative minima of the free energy, is equal to the number of solutions to the Thouless-Anderson-Palmer equations [70]. Close to T_f, N_S increases exponentially with T [184] as $N_S = \exp[(8/81)N(1 - T/T_f)^6]$. As a result, the complexity of the free-energy landscape in configuration space increases dramatically with decreasing T. It was shown [183, 185] that the structure of the organization of the metastable states obeys a property called ultrametricity: for any three states α, β, and γ having mutual overlaps $q^{\alpha\beta}$, $q^{\alpha\gamma}$, and $q^{\beta\gamma}$, at least two of the overlaps are equal and the third is larger than or equal to the other two. This property can be represented as a hierarchical tree-like organization of the states [186] (figure (2-17)). As the temperature is lowered from, say, T_1 to T_2 ($T_2 < T_1 < T_f$), a given metastable state α at T_1 gives 'birth' to N_α new states at T_2.

The three dependencies of the TRM observed here for the studied i $Zn_{77}Fe_7Sc_{16}$ QC and for canonical spin glasses can be explained [181, 182] within the framework of the ultrametric organization of the metastable states (figure (2-17)). When the spin system is cooled to T_m in the magnetic field H, it explores during the waiting time t_w different metastable states in the phase space by jumping over the energy barriers. Assuming that the jumps occur via a thermally activated process, the part of the phase space explored is characterized by the highest surmounted energy barrier Δ_{max} that depends on T_m and t_w and is given by $\Delta_{max}(T_m, t_w) = T_m \ln(\frac{t_w}{\tau})$, where τ is a macroscopic attempt time. At the end of the waiting time t_w, the magnetic field is reduced from H to zero, and the TRM decay is measured. Here, two closely related processes take place. First, a new set of metastable states with zero magnetization replaces the set of the metastable states with magnetization M_{FC} as the ground state. Second, this results in a 'tilt' in the free-energy surface which rapidly empties those occupied states with M_{FC} with energy barriers less than or equal to the

change in Zeeman energy, HM_{FC}. This accounts for the rapid change of the magnetization (so-called reversible part) upon cutting the magnetic field H to zero. For longer times, the diffusion process from occupied states with M_{FC} with energy barriers larger than HM_{FC} to the states with zero magnetization occurs. This leads to the slow decay of the so-called irreversible part of the magnetization (TRM). For longer waiting times, the weight of the populated FC phase space bounded by energy barriers larger than the change in Zeeman energy increases, and consequently, the magnitude of the TRM should increase. Moreover, because of a larger fraction of states surrounded by higher energy barriers for longer waiting time, it takes a longer time for the system to leave these states and decay towards the 'sink' among low-barrier heights which have been overcome by HM_{FC}. This explains why the decay of the TRM is slower for longer waiting times.

The existence of the ultrametrically organized phase space in a spin glass can be also evidenced by studying the TRM decay as a function of the cooling field H, which should be in the low-field region where the ZFC and FC magnetizations differ substantially [182]. The decay of the TRM for $t_w = 3600$ s at $T_m = 0.62T_f$ and $T_m = 6.0$ K $= 0.77T_f$ as a function of the cooling field H is shown in figure (5-6). It is clear from figure (5-6) that the magnitude of the TRM increases with increasing cooling field. The TRM dependence on H observed here is exactly *opposite* to that observed for a canonical spin glass where the TRM decreases with increasing H. The decrease of the TRM with H is expected for the ultrametrically organized phase space in a spin glass [182]: the larger the cooling field H, the smaller the region of populated states bounded by barriers of height $\Delta(t_w) > HM_{FC}$, so that a smaller TRM remains after $H \rightarrow 0$. We thus have to conclude that the observed increase of the TRM with H in the i $Zn_{77}Fe_7Sc_{16}$ QC is inconsistent with the ultrametrically organized phase space. This result

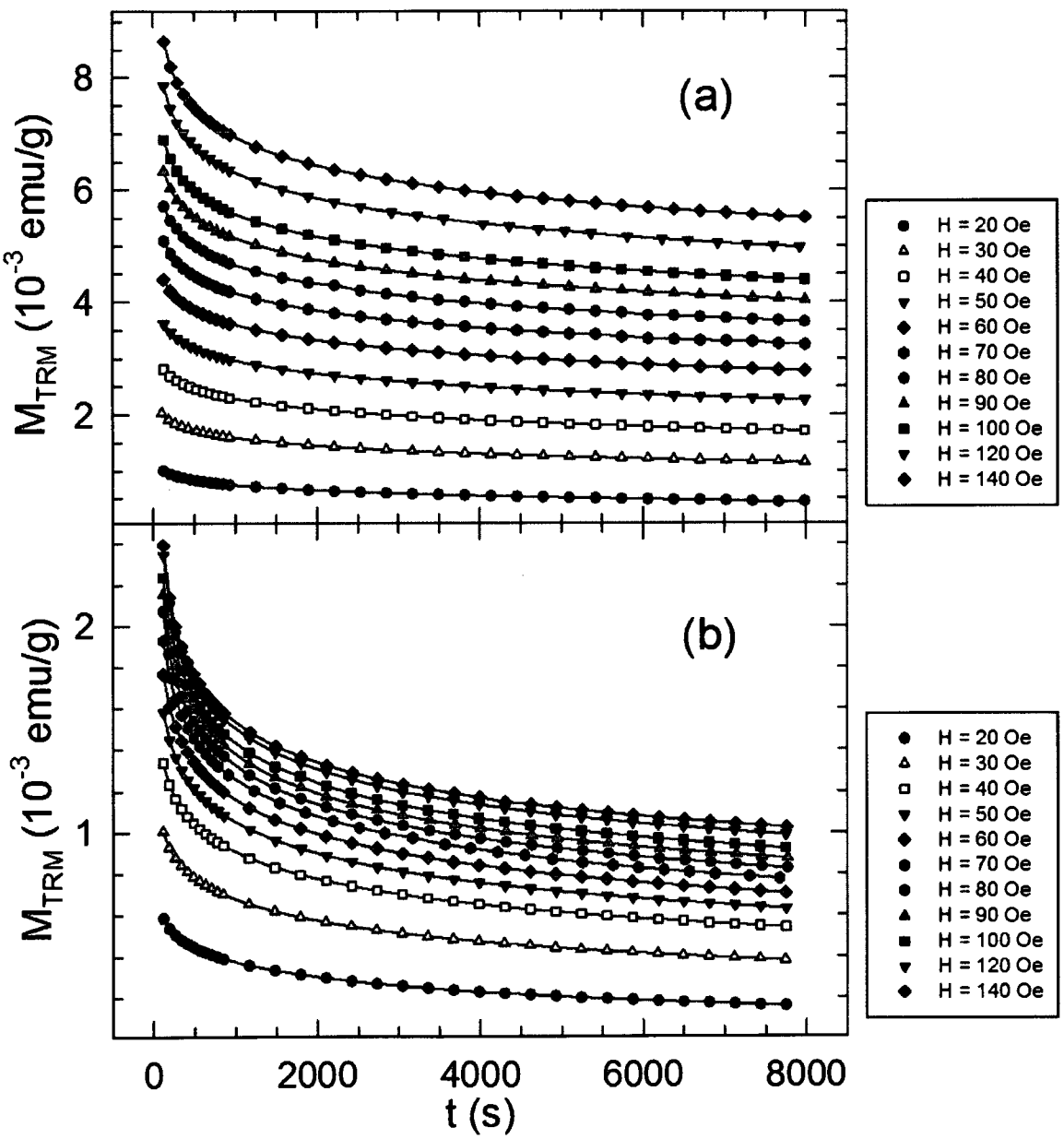

Figure (5-6) The TRM time decays for t_w = 3600 s at (a) 4.8 K and (b) 6.0 K for different cooling fields H of the icosahedral $Zn_{77}Fe_7Sc_{16}$ quasicrystal. The solid lines are guides for the eye.

contradicts the spin-glass nature of the ground state in the i $Zn_{77}Fe_7Sc_{16}$ QC in the sense of a canonical spin glass.

5.3.2.3) ac magnetic susceptibility

The in-phase component χ' and the out-of-phase component χ'' of the ac magnetic susceptibility for i $Zn_{77}Fe_7Sc_{16}$ QC, measured in the temperature range from 2 to 30 K and for selected frequencies between 20 Hz and 10 kHz, are shown in figures (5-8)(a) and (5-8)(b), respectively. Both χ' and χ'' curves show maxima whose amplitudes and positions depend on the frequency f of the applied ac magnetic field. There is a sharp peak in χ' which can be used to define T_f. $\chi'(T)$ attains a maximum at T_f that shifts towards higher temperatures with higher frequencies, which is typical for conventional spin glasses [51]. Below the maximum, the magnitude of χ' is frequency dependent, but it becomes independent of frequency at temperatures just above T_f. This behaviour is qualitatively similar to that of conventional spin glasses [51]. The out-of-phase component χ'' is vanishing above T_f, but is nonzero for temperatures just below T_f, which implies dissipation not only at the freezing transition but also for temperatures below it, a common feature of spin glasses [51].

The frequency dependence of T_f, which was determined from the curve fitting for the maximum of the data in figure (5-7)(a), is shown in figure (5-8). A quantitative measure of the change of the freezing temperature with frequency in spin glasses is represented by the relative change in T_f per decade change in f [51] defined as

$$K = \frac{\Delta T_f}{T_f \Delta \log f}. \tag{5-3}$$

From a linear fit of the data in figure (5-8), and using the average value of T_f = 8.08 K for

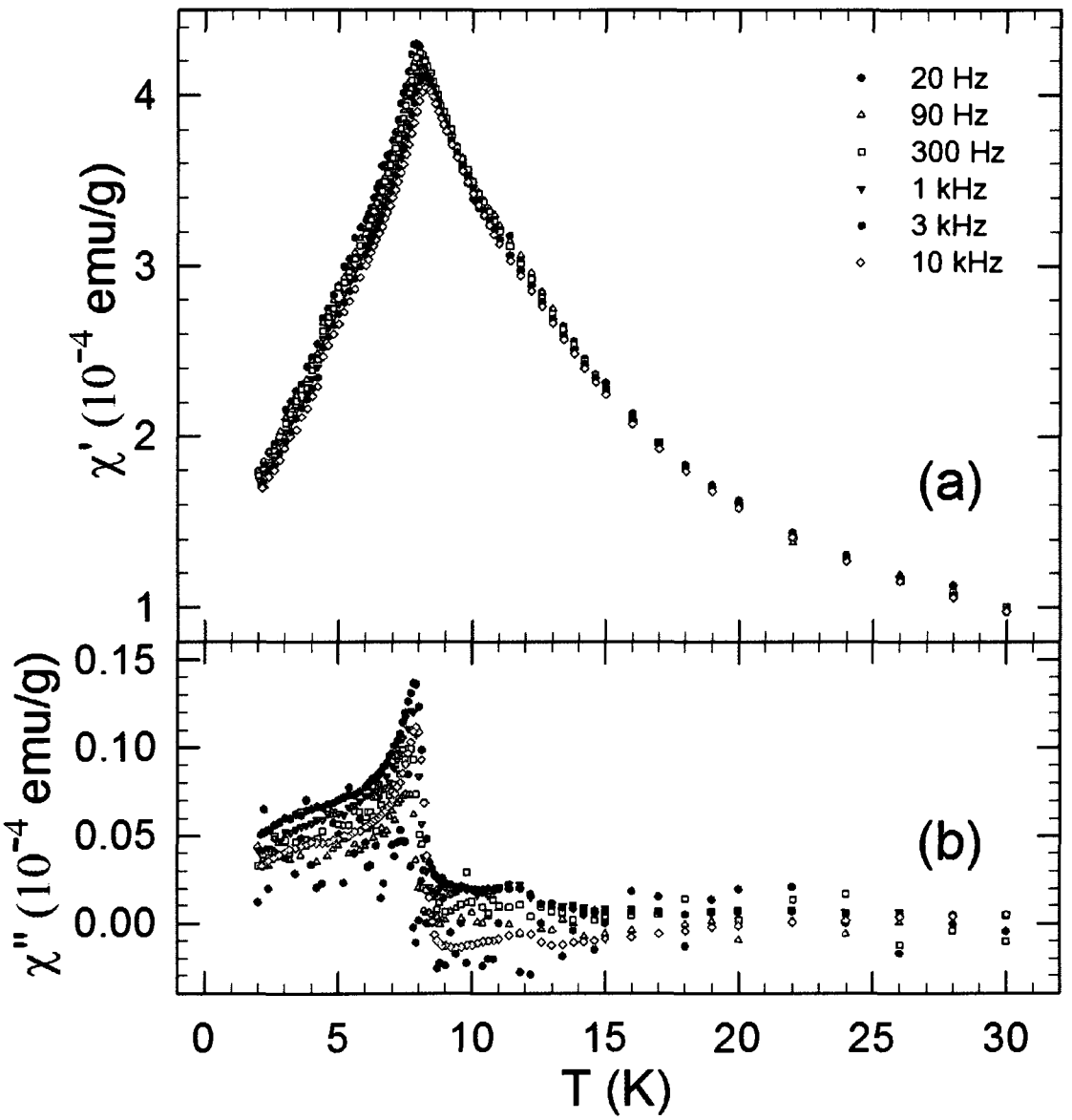

Figure (5-7) The temperature dependence of the in-phase magnetic susceptibility χ' (a) and out-of-phase magnetic susceptibility χ'' (b) measured for different applied frequencies from 20 Hz to 10 kHz for the icosahedral $Zn_{77}Fe_7Sc_{16}$ quasicrystal.

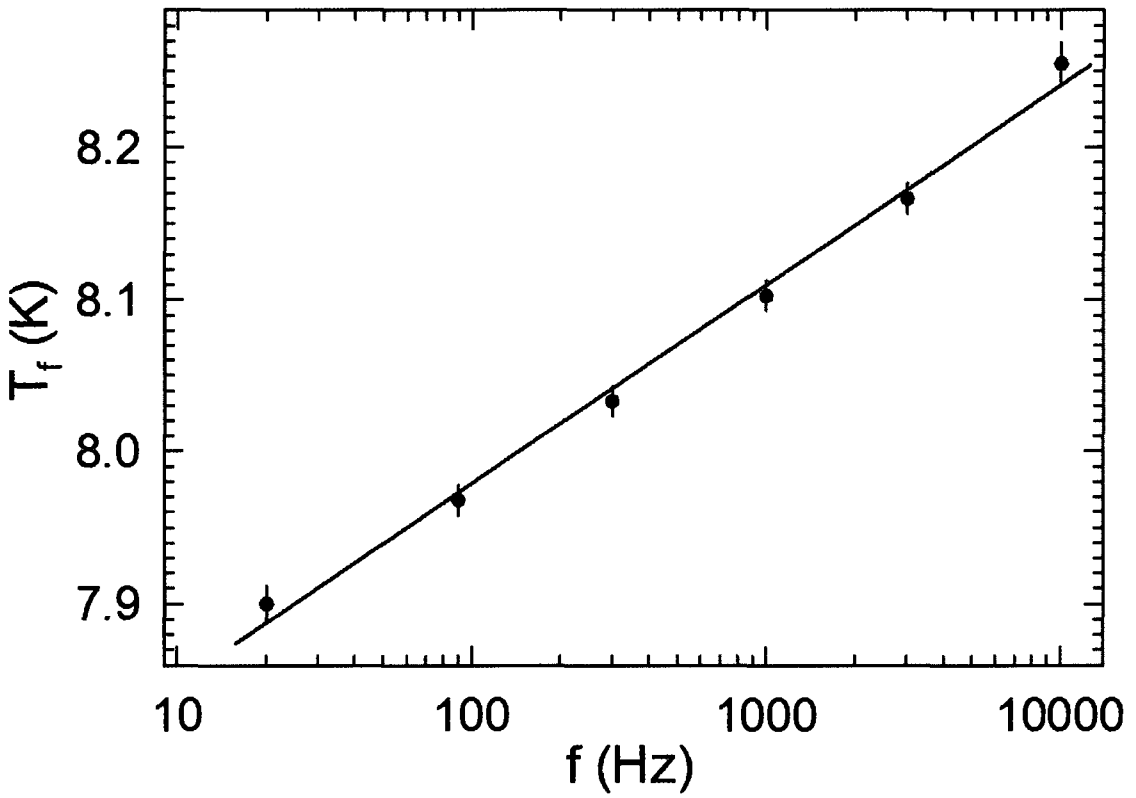

Figure (5-8) The frequency dependence of the freezing temperature T_f for the icosahedral $Zn_{77}Fe_7Sc_{16}$ quasicrystal. The solid line is the best linear fit to the T_f data.

the range of frequencies used, we find that $K = 0.016(1)$. This value is a factor of 3 greater than that observed for the canonical $Cu_{1-x}Mn_x$ spin glass but comparable to that of several other canonical spin glasses [51]. We note that the value of K reported for another i $Tb_9Mg_{34}Zn_{57}$ QC is 0.049 [149].

There are basically two different interpretations of the spin freezing phenomenon in spin glasses [51]: one is the cluster model in which the system is considered as a set of interacting superparamagnetic clusters and the other is the model which assumes the occurrence of a true phase transition. The frequency dependence of T_f in spin glasses is described within the cluster model by the phenomenological Vogel-Fulcher law [51, 150]

$$f = f_0 \exp[-E_a/k_B(T_f - T_0)], \tag{5-4}$$

where f_0 is a characteristic frequency, E_a is the activation energy, k_B is the Boltzmann constant, and T_0 is the Vogel-Fulcher temperature which is a measure of the interaction strengths between clusters in the spin glass [152]. Equation (5-4) implies a linear dependence of $1/(T_f - T_0)$ with $\log(f)$. The best fit of the $T_f(f)$ data to equation (5-4) (figure (5-9)) yields $f_0 = 7.20(22)\times10^{11}$ Hz, $E_a/k_B = 25.1(2.6)$ K, and $T_0 = 6.87(47)$ K. Similarly to what was observed for other spin glasses [150], $T_0 < E_a/k_B$. The values of f_0, E_a/k_B, and T_0 obtained for i $Zn_{77}Fe_7Sc_{16}$ QC are in general agreement with similar parameters reported for other spin-glass systems [51, 149, 150].

The frequency-dependent maximum in χ' indicates the freezing temperature T_f where the maximum relaxation time, τ, of the system is equal to the characteristic time $1/f$ set by

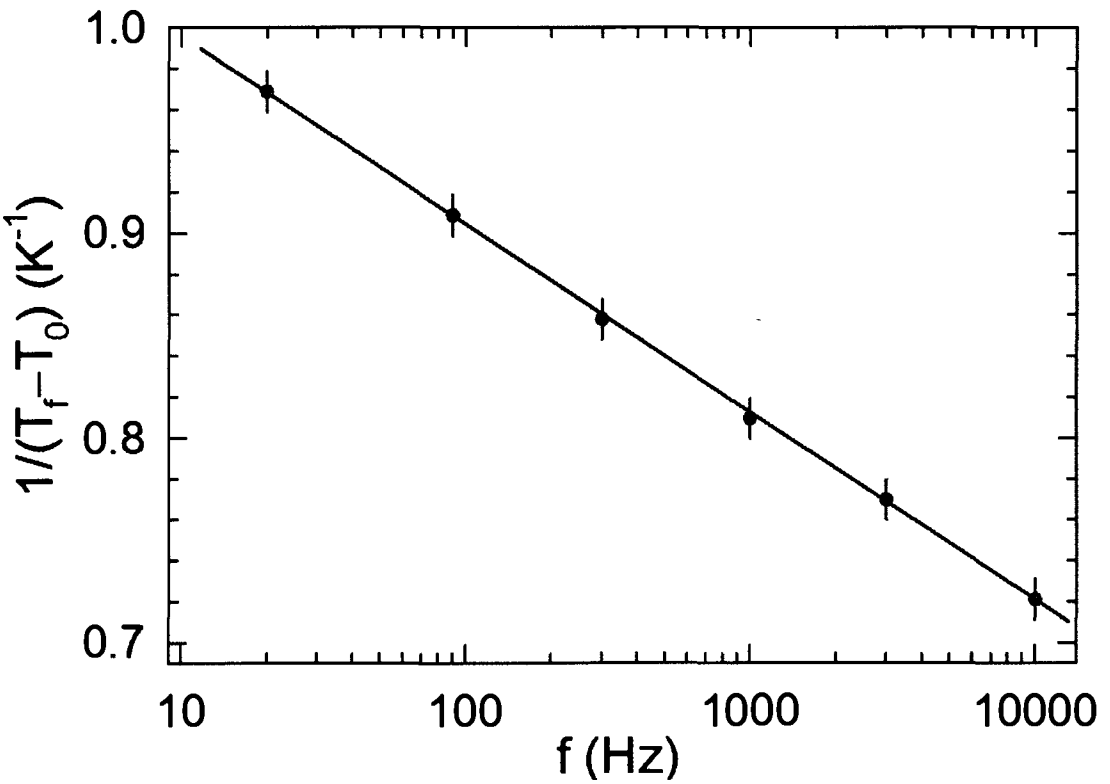

Figure (5-9) The frequency dependence of the freezing temperature T_f for the icosahedral $Zn_{77}Fe_7Sc_{16}$ quasicrystal. The solid line is the best fit to equation (5-4).

the frequency of the ac-susceptibility measurement. The scaling theory near a phase transition at T_c predicts that the temperature dependence of τ obeys the power-law divergence [51, 153]

$$\tau = \tau_0 \left(\frac{T_f - T_c}{T_c}\right)^{-zv} \qquad T_f > T_c, \tag{5-5}$$

where τ_0 is the microscopic relaxation time, z is the dynamic exponent relating the correlation length ξ and τ as $\tau \propto \xi^z$, and v is the critical exponent for the correlation length $\xi \propto \left(\frac{T_f}{T_c} - 1\right)^{-v}$. The best fit of the $T_f(f)$ data to equation (5-5) (figure (5-10)) gives τ_0 = 1.47(32)×10^{-12} s, T_c = 7.72(8) K, and zv = 6.77(1.14). The derived values of τ_0 and zv are similar to those for the canonical $Cu_{1-x}Mn_x$ spin glass [51, 154].

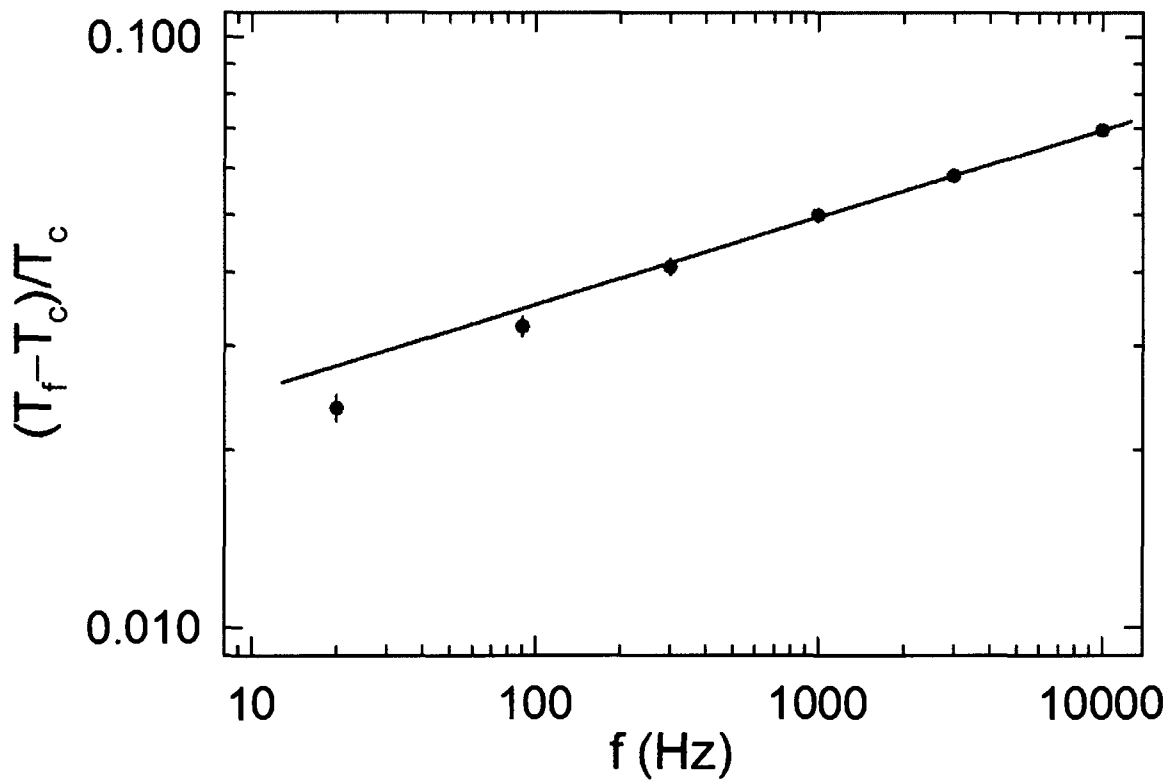

Figure (5-10) The frequency dependence of the freezing temperature T_f for the icosahedral $Zn_{77}Fe_7Sc_{16}$ quasicrystal. The solid line is the best fit to equation (5-5).

5.3.3) Mössbauer spectroscopy

The Mössbauer spectra of the i $Zn_{77}Fe_7Sc_{16}$ QC recorded at temperatures at which no magnetic dipole hyperfine interaction [125, 162] is present are shown in figure (5-11). All the spectra consist of a broadened doublet which results from the distribution of the quadrupole splittings, $P(\Delta)$ [160]. A quadrupole splitting

$$\Delta = \frac{1}{2} eQ|V_{zz}|\sqrt{1+\eta^2/3}, \tag{5-6}$$

where e is the proton charge and Q is the electric quadrupole moment of the ^{57}Fe nucleus.

The asymmetry parameter $\eta = \left|(V_{xx} - V_{yy})/V_{zz}\right|$, $(0 \leq \eta \leq 1)$, where V_{xx}, V_{yy}, and V_{zz} are the eigenvalues of the electric field gradient (EFG) tensor in order of increasing magnitude [125, 162]. The distribution $P(\Delta)$ is the consequence of the distributions of the EFG and of the asymmetry parameter. The Mössbauer spectra in figure (5-11) were fitted with the Voigt-based quadrupole distribution method of Rancourt and Ping [187]. To account for a small asymmetry of the spectra, a linear coupling between the centre shift, δ, and Δ for the elementary Lorentzian doublets was assumed. The best fits of the Mössbauer spectra in figure (5-11) could be obtained with the probability quadrupole splitting distribution functions $P(\Delta)$ shown in figure (5-12).

The determined distributions $P(\Delta)$ (figure (5-12)) have clearly a bimodal character. This is in contrast to the unimodal distribution $P(\Delta)$ observed for the thermodynamically stable i $Al_{62.5}Cu_{24.5}Fe_{13}$ QC [188]. The bimodal character of $P(\Delta)$ may be indicative of the presence of two classes of Fe sites in the structure of the i $Zn_{77}Fe_7Sc_{16}$ QC. The lack of *ab initio* calculations of the distribution of the EFG in the i $Zn_{77}Fe_7Sc_{16}$ QC inhibits a comparison of the experimentally determined $P(\Delta)$ with theory. Such calculations are very desirable since the experimentally determined shape of $P(\Delta)$ could be directly used to

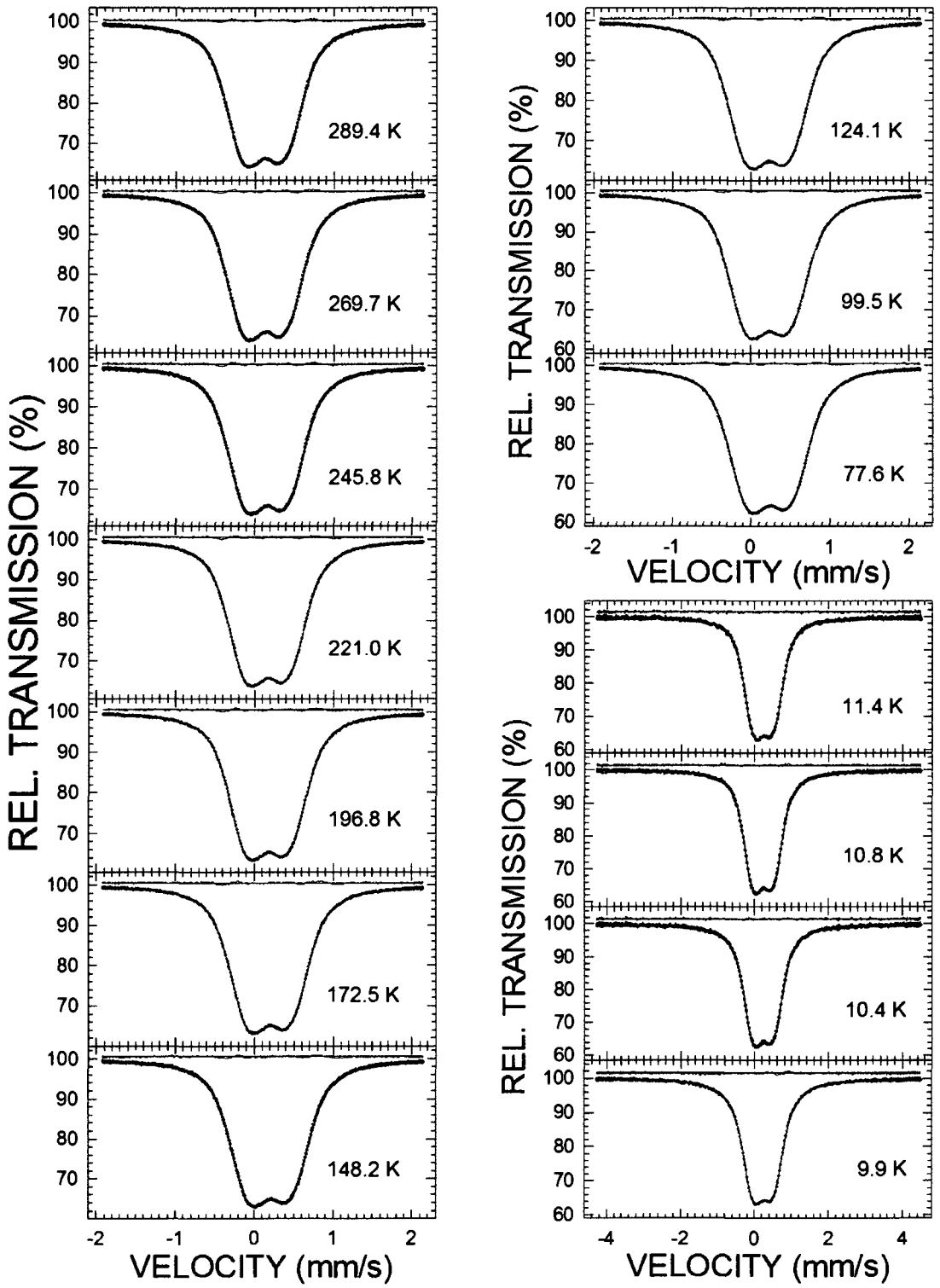

Figure (5-11) The ^{57}Fe Mössbauer spectra of the icosahedral $Zn_{77}Fe_7Sc_{16}$ quasicrystal obtained at the indicated temperatures fitted (solid lines) with the quadrupole splitting distributions $P(\Delta)$ shown in figure (5-12). The residuals are shown above each spectrum. The zero-velocity origin is relative to α-Fe at room temperature.

determine which of the possible structural models of the i $Zn_{77}Fe_7Sc_{16}$ QC is the most appropriate.

The average value of the quadrupole splitting, $\bar{\Delta}$, at a given temperature was calculated from the $P(\Delta)$ distribution at that temperature (figure (5-12)). One can note a small increase of $\bar{\Delta}$ with decreasing temperature (figure (5-13)). The temperature dependence of $\bar{\Delta}$ could be fitted well (figure (5-13)) to the empirical equation

$$\bar{\Delta}(T) = \bar{\Delta}(0)\left(1 - BT^{3/2}\right), \qquad (5\text{-}7)$$

where $\bar{\Delta}(0)$ is the value of $\bar{\Delta}$ at 0 K and B is a constant. Such a $T^{3/2}$ temperature dependence has been observed in many metallic noncubic crystalline alloys [189], in some metallic amorphous alloys [190–194], and recently in QCs [188, 193–196] over temperature ranges from a few K to the melting point. This seemingly universal $T^{3/2}$ dependence is not well understood. Its origin seems to be associated with a strong temperature dependence of mean-square lattice displacements and, to a lesser extent, with the temperature dependence of lattice expansion [197–199]. The values of $\bar{\Delta}(0)$ and B determined from the fit for the i $Zn_{77}Fe_7Sc_{16}$ QC are, respectively, 0.527(1) mm/s and 8.87(44) × 10^{-6} $K^{-3/2}$. The value of B is similar to that found for other metallic amorphous alloys and QCs [190–196].

The Mössbauer spectra of the i $Zn_{77}Fe_7Sc_{16}$ QC measured at temperatures at which the magnetic dipole hyperfine interaction [125, 162] is present are shown in figure (5-14). They were fitted with the Voigt-based hyperfine magnetic field, H_{hf}, distribution method of Rancourt and Ping [187]. A linear coupling between δ and H_{hf}, and the quadrupole shift [125, 162], ε, and H_{hf}, for the elementary sextets was assumed. The best fits of the Mössbauer spectra in figure (5-14) were obtained with the hyperfine magnetic field probability distribution functions $P(H_{hf})$ shown in figure (5-15).

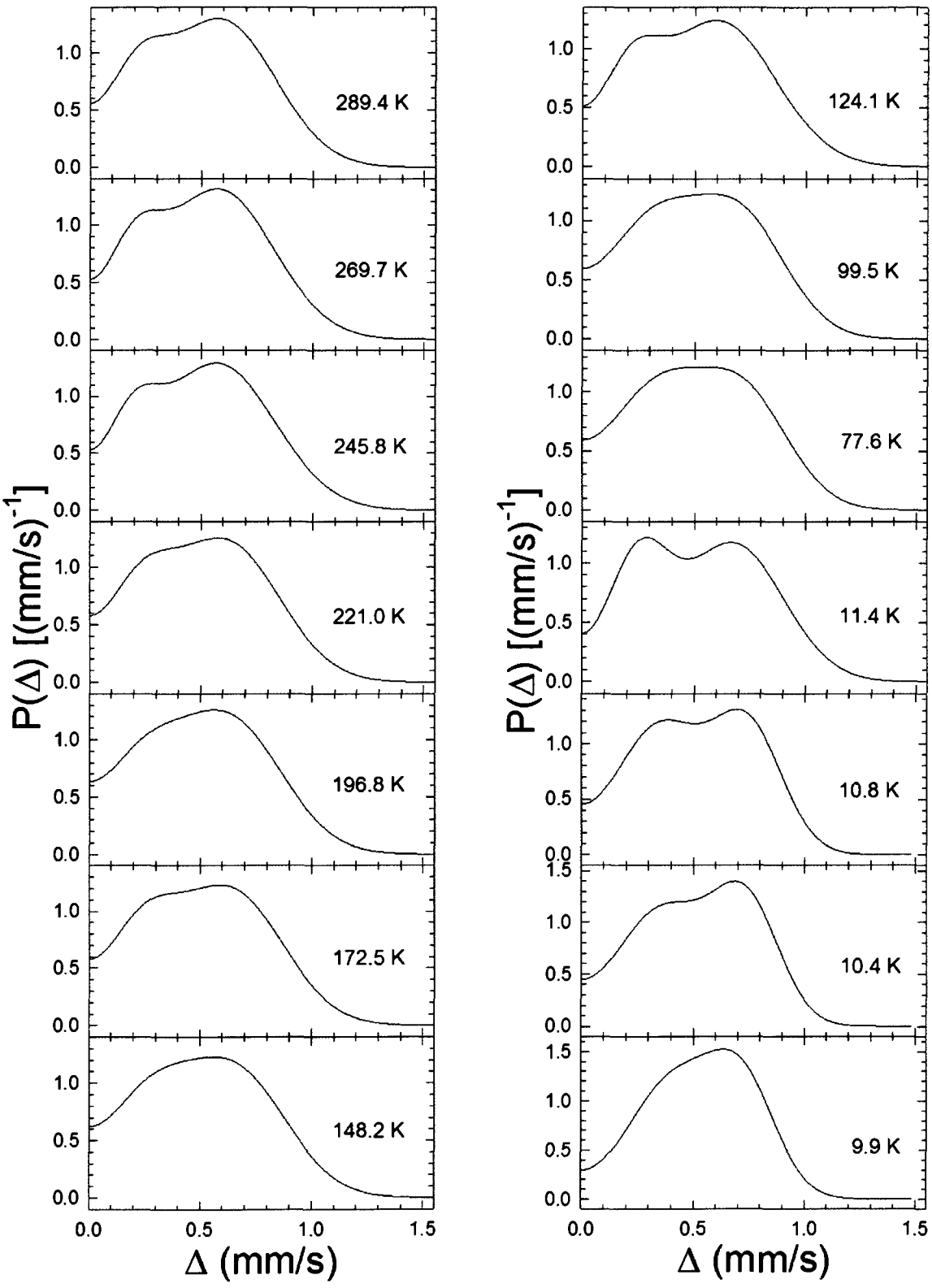

Figure (5-12) The quadrupole splitting distributions $P(\Delta)$ which fit the best the ^{57}Fe Mössbauer spectra in figure (5-11).

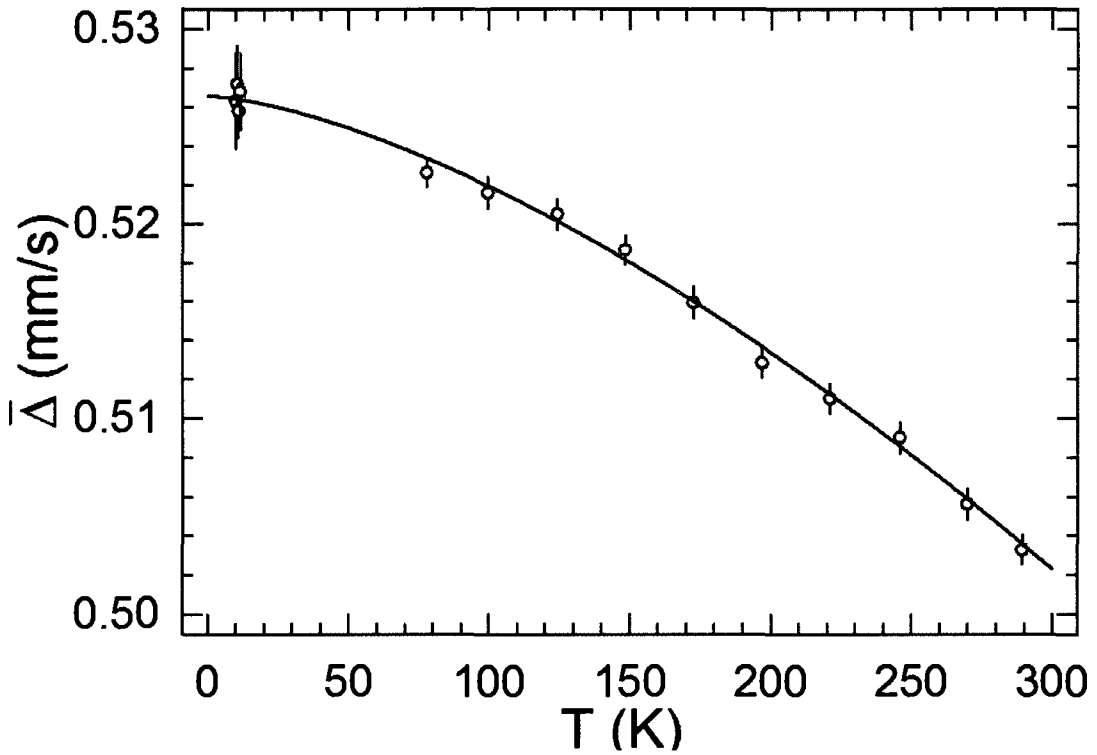

Figure (5-13) The temperature dependence of the average quadrupole splitting of the icosahedral icosahedral $Zn_{77}Fe_7Sc_{16}$ quasicrystal. The solid line is the fit to equation (5-7).

Similarly to the case of the $P(\Delta)$ distributions, the $P(H_{hf})$ distributions are also bimodal (figure (5-15)). This is suggestive of two classes of Fe sites in the structure of the i $Zn_{77}Fe_7Sc_{16}$ QC. The average value of the hyperfine magnetic field, $\overline{H}_{hf}$, at a given temperature was calculated from the $P(H_{hf})$ distribution at that temperature (figure (5-15)). The temperature dependence of $\overline{H}_{hf}$ is presented in figure (5-16). The temperature at which $\overline{H}_{hf}$ vanishes, that was estimated from the extrapolation of the $\overline{H}_{hf}(T)$ data in figure (5-16), is 9.87(5) K. If one defines the freezing temperature of a spin glass determined from the Mössbauer effect, T_f^m, as the temperature at which the magnetic dipole hyperfine interaction disappears, then T_f^m = 9.87(5) K. Clearly, T_f^m is significantly larger than the freezing temperature T_f = 7.75(2) K determined from the dc magnetic susceptibility data. The systematically higher values of T_f^m than T_f have been observed for many other spin-

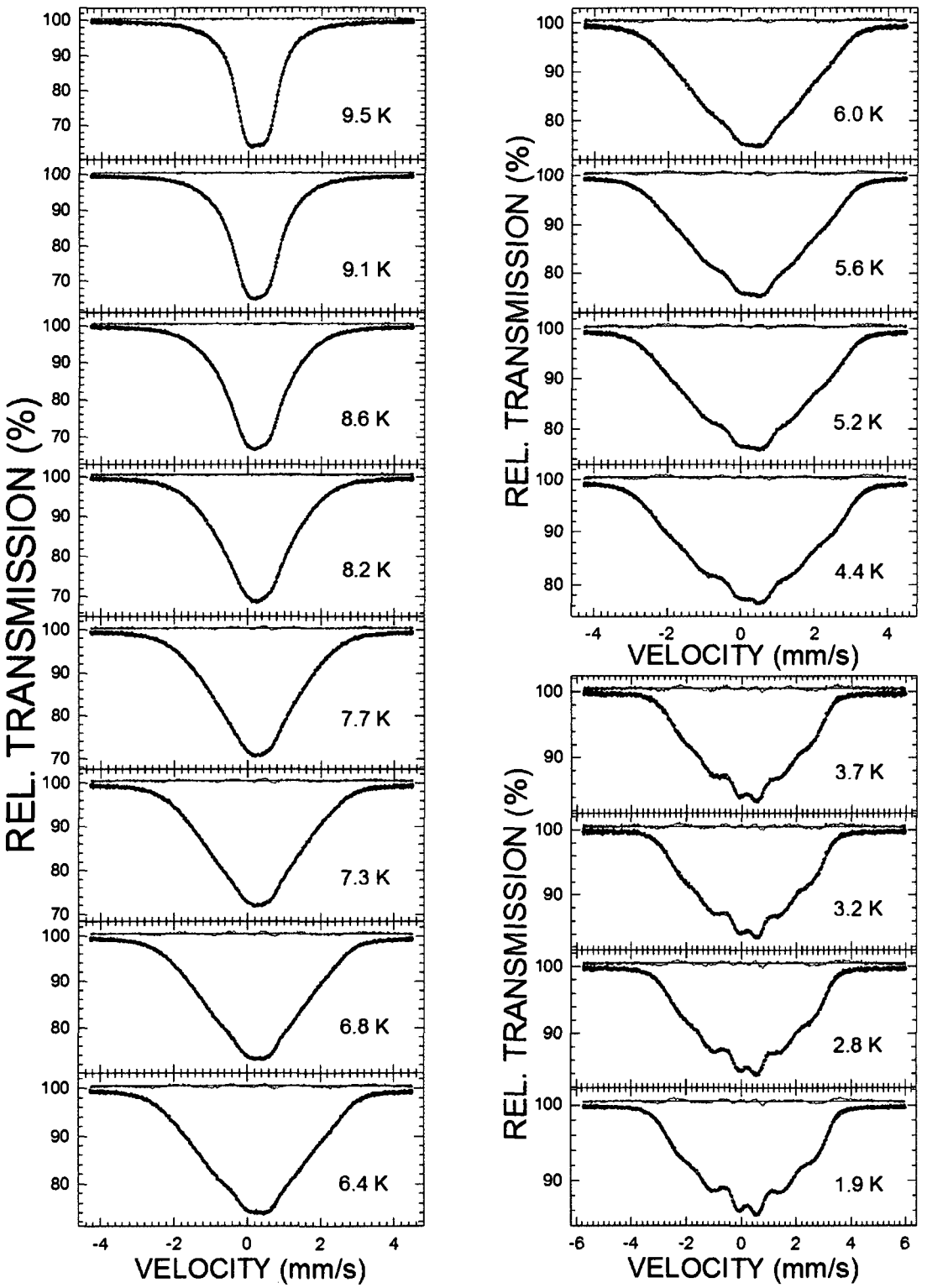

Figure (5-14) The ^{57}Fe Mössbauer spectra of the icosahedral $Zn_{77}Fe_7Sc_{16}$ quasicrystal obtained at the indicated temperatures fitted (solid lines) with the hyperfine magnetic field distributions $P(H_{hf})$ shown in figure (5-15). The residuals are shown above each spectrum. The zero-velocity origin is relative to α-Fe at room temperature.

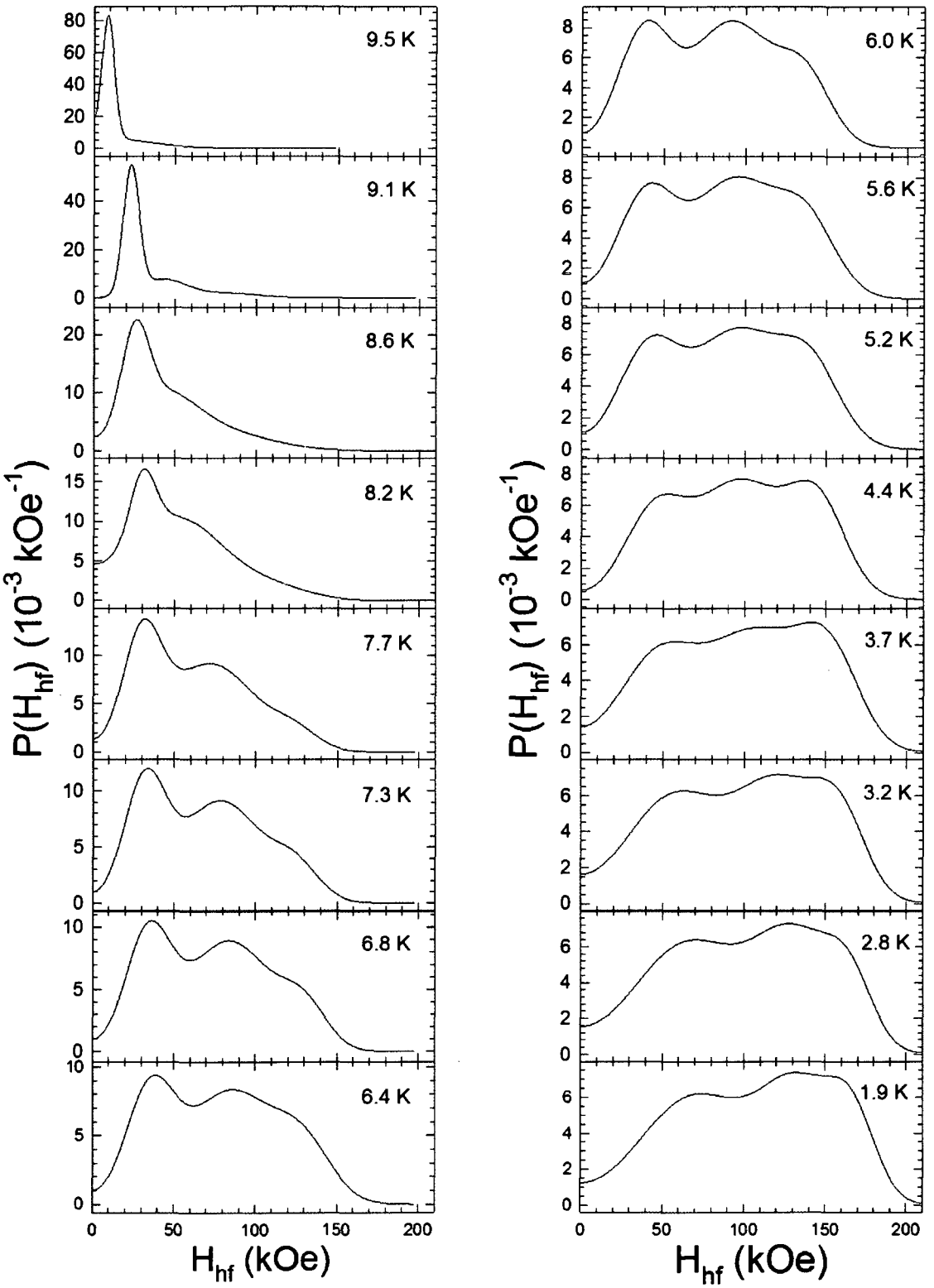

Figure (5-15) The hyperfine magnetic field distributions $P(H_{hf})$ which fit the best the ^{57}Fe Mössbauer spectra in figure (5-14).

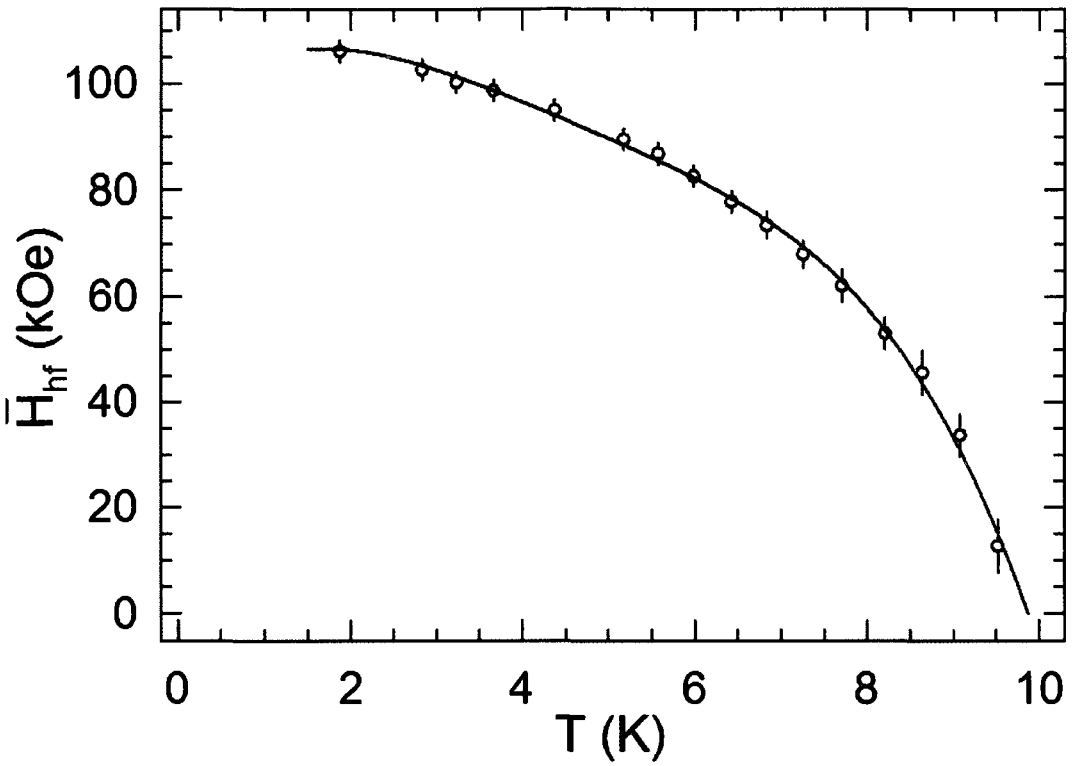

Figure (5-16) The temperature dependence of the average hyperfine magnetic field of the icosahedral $Zn_{77}Fe_7Sc_{16}$ quasicrystal. The solid line is a guide for the eye.

glass systems [51, 167–172]. The inequality $T_f^m > T_f$ results from a time window τ_{exp} of an experimental technique used to determine the freezing temperature. For MS, τ_{exp} is given by the Larmor precession time τ_L of the nuclear magnetic moment in the hyperfine magnetic field. In the case studied here, $\tau_L = 1.2 \times 10^{-7}$ s (f_L = 8.4 MHz) for $\bar{H}_{hf}$ = 106.2 kOe at 1.9 K. With a wide distribution of the relaxation times τ of fluctuating spin clusters in a spin glass [51, 167–172, 200], those clusters fluctuating with τ larger than τ_{exp} of a given experimental technique will appear frozen and will be discerned at a higher temperature than by the experimental technique characterised by a smaller τ_{exp}. Thus, one expects to observe an increase of T_f with decreasing τ_{exp}, which is indeed universally observed in spin glasses [51, 167–172].

The average centre shift at temperature T, $\bar{\delta}(T)$, determined from the fits of the

spectra in figures (5-12) and (5-15) is given by

$$\bar{\delta}(T) = \delta_0 + \delta_{\mathrm{SOD}}(T)\,, \tag{5-8}$$

where δ_0 is the intrinsic isomer shift and $\delta_{\mathrm{SOD}}(T)$ is the second-order Doppler (SOD) shift which depends on lattice vibrations of the Fe atoms [125, 162]. In terms of the Debye approximation of the lattice vibrations, $\delta_{\mathrm{SOD}}(T)$ is expressed [125, 162] by the Debye temperature, Θ_{D}, as

$$\delta_{\mathrm{SOD}}(T) = -\frac{9}{2}\frac{k_B T}{Mc}\left(\frac{T}{\Theta_D}\right)^3 \int_0^{\Theta_D/T} \frac{x^3 dx}{e^x - 1}\,, \tag{5-9}$$

where M is the mass of the Mössbauer nucleus and c is the speed of light. By fitting the experimental data $\bar{\delta}(T)$ (figure (5-17)) to equation (5-8), the quantities δ_0 and Θ_{D} were found to be, respectively, 0.226(1) mm/s and 443(8) K. The value of Θ_{D} found here is comparable to the values of Θ_D found for other i QCs [188, 193–196].

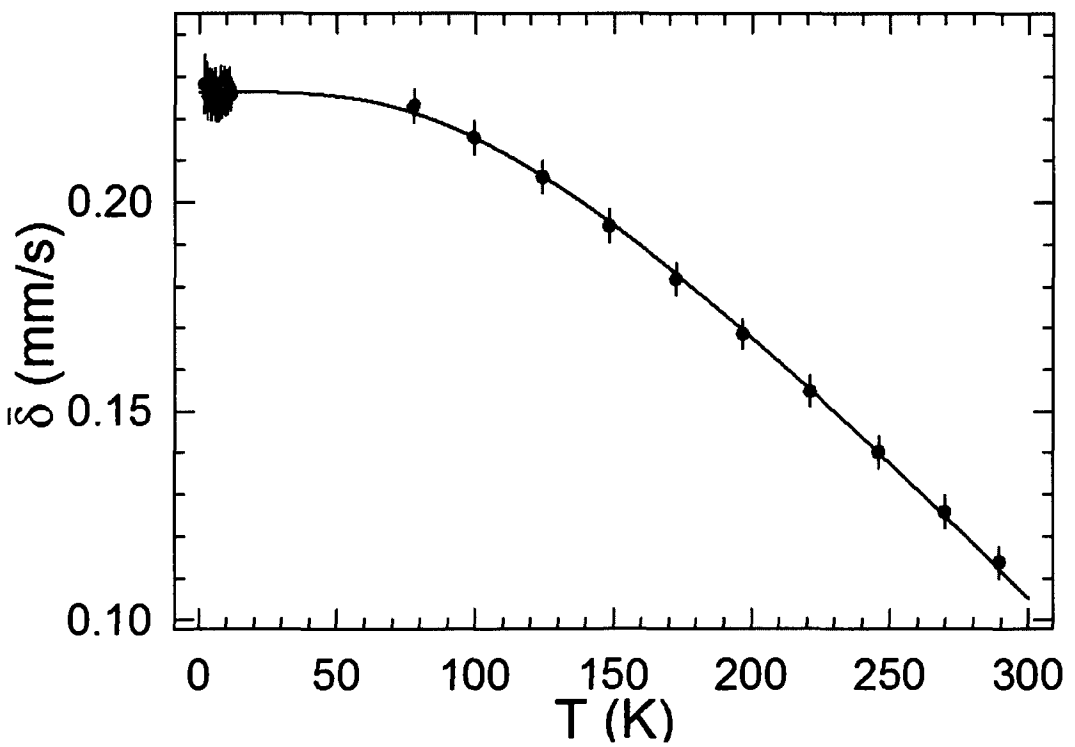

Figure (5-17) The temperature dependence of the average center shift of the icosahedral $Zn_{77}Fe_7Sc_{16}$ quasicrystal. The solid line is the fit to equation (5-8), as explained in the text.

5.3.4) Conclusions

A new thermodynamically stable icosahedral quasicrystal $Zn_{77}Fe_7Sc_{16}$ has been studied with x-ray diffraction, dc and ac susceptibility, and ^{57}Fe Mössbauer spectroscopy. It has a primitive six-dimensional Bravais lattice at room temperature with the six-dimensional hypercubic lattice constant of 7.087(1) Å. Based on dc magnetization measurements, no evidence is found for a transition to a ground state with a long-range magnetic order in the temperature range between 2 and 300 K. The temperature dependence of the dc magnetic susceptibility follows the modified Curie-Weiss law with the paramagnetic Curie temperature of 10.6(2) K and an effective magnetic moment of 3.55(1) μ_B per Fe atom. The dc zero-field-cooled and field-cooled susceptibility data indicate that the studied quasicrystal is a spin glass with the freezing temperature T_f = 7.75(2) K. This spin-glass state of the icosahedral quasicrystal $Zn_{77}Fe_7Sc_{16}$ is further confirmed by observing ageing effects through the dc zero-field-cooled magnetization and the thermoremanent magnetization time decays, and by the analysis of the frequency dependence of T_f using the Vogel-Fulcher law and the dynamic scaling behavior near T_f. However, the observed increase of the thermoremanent magnetization with the magnetic field in the low-field regime is incompatible with the ultrametrically organized phase space of a canonical spin glass. The nature of the spin-glass state of the icosahedral quasicrystal $Zn_{77}Fe_7Sc_{16}$ is thus fundamentally different from that of a canonical spin glass. The bimodal distribution of the electric quadrupole splitting and of the hyperfine magnetic field derived from Mössbauer spectra indicates the existence of two classes of Fe sites. The average quadrupole splitting decreases with temperature as $T^{3/2}$. The hyperfine magnetic field sets in at a temperature of 9.87(5) K, which is significantly higher than T_f. The vibrations of the Fe atoms are well

described by a Debye model, with a Debye temperature of 443(8) K.

6) 1/1 APPROXIMANT $Ag_{50}In_{36}Gd_{14}$

6.1) Introduction

The discovery of the first binary icosahedral (i) quasicrystals (QCs) $YbCd_{5.7}$ and $CaCd_{5.7}$ by Tsai *et al* [136] has led to finding many ternary i QCs by total or partial replacement of Yb(Ca) and Cd with other metallic elements. In particular, by replacing Yb with rare-earth (RE) elements and Cd with Ag and In, a series of new Ag-In-RE i QCs was synthesized [201, 58]. Cubic crystalline alloys $YbCd_6$ and $CaCd_6$ are 1/1 approximants [202] to the i QCs $YbCd_{5.7}$ and $CaCd_{5.7}$, respectively [203, 204]. A similar replacement in $YbCd_6$ of Yb with RE elements and Cd with Ag and In has led to the discovery of ternary Ag-In-RE 1/1 approximants to the Ag-In-RE i QCs [58, 205]. The availability of the i and 1/1 approximant Ag-In-RE alloys of the same composition allows for a study of the influence of quasiperiodicity on physical properties of these alloys.

The recent study of the new i $Ag_{50}In_{36}Gd_{14}$ QC [206] found no evidence for a transition to a ground state with a long-range magnetic order in the temperature range 2–300 K. The i $Ag_{50}In_{36}Gd_{14}$ QC was demonstrated to be a spin glass with a freezing temperature of 4.25 K [206].

6.2) Experimental procedure

For starting elements, Ag shots (purity, 99.99%), In shots (purity, 99.999%), and Gd chunks (purity, 99.9%), were used as received. Appropriate amounts of these elements corresponding to the composition $Ag_{50}In_{36}Gd_{14}$ were weighed (±0.1 mg) and weld-sealed under an argon atmosphere into a tantalum container. The container was in turn held within

an evacuated SiO_2 jacket to avoid its air oxidation. The mixture was melted using an induction furnace.

6.3) Results and discussion

6.3.1) Structural characterization

The ternary alloy $Ag_{50}In_{36}Gd_{14}$ crystallizes in the $YbCd_6$-type crystal structure [204] with the space group $Im\bar{3}$ (No. 204). There are 24 formula units of $Ag_{50}In_{36}Gd_{14}$ per unit cell. The x-ray powder diffraction pattern of the sample studied is shown in figure (6-1). A Rietveld refinement of the x-ray powder diffraction data was performed yielding the lattice parameter a = 15.202(1) Å. The obtained atomic positions for the Ag, In, and Gd sites and their occupancies are listed in table (6-1).

The lattice constant a of a 1/1 approximant to an i QC is related to the six-dimensional hypercubic lattice constant a_{6D} of the i QC via the relation $a = \sqrt{\frac{2}{2+\tau}}(1+\tau)a_{6D}$, where τ is the golden mean [$\tau = (1+\sqrt{5})/2$] [40]. From the value of a_{6D} = 7.805(2) Å for the i $Ag_{50}In_{36}Gd_{14}$ QC [206], one would expect that a = 15.192(4) Å, which is in a good agreement with the value of 15.202(1) Å obtained from a Rietveld refinement knowing that both the i $Ag_{50}In_{36}Gd_{14}$ QC and the 1/1 $Ag_{50}In_{36}Gd_{14}$ approximant do not have perfect structures.

6.3.2) Magnetic measurements

6.3.2.1) dc magnetic susceptibility

The temperature dependence of the magnetic susceptibility χ of the i $Ag_{50}In_{36}Gd_{14}$

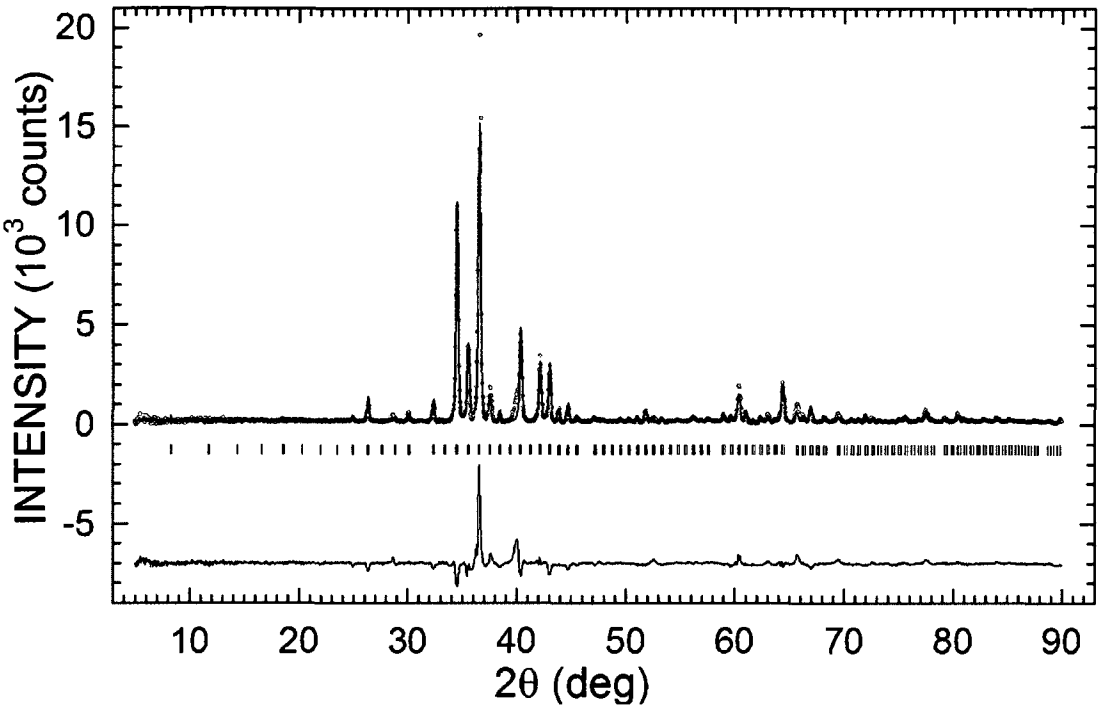

Figure (6-1) The x-ray diffraction spectrum of an $Ag_{50}In_{36}Gd_{14}$ alloy at 298 K. The experimental data are denoted by open circles, while the line through the circles represents the results of the Rietveld refinement. The vertical bars represent the Bragg peak positions corresponding to the $Ag_{50}In_{36}Gd_{14}$ phase. The lower solid line represents the difference curve between experimental and calculated spectra.

Table (6-1) Atomic positions for the $Ag_{50}In_{36}Gd_{14}$ alloy obtained through Rietveld analysis.

Atom	Site	Point symmetry	*x*	*y*	*z*	Occupancy
Ag1	24g	*m*..	0	0.0815(3)	0.0800(3)	0.207(8)
Ag2	24g	*m*..	0	0.09136(5)	0.23902()7	0.5814(5)
Ag3	16f	.3.	0.16056(4)	0.16056(4)	0.16056(4)	0.5814(5)
Ag4	48h	1	0.20018(3)	0.34058(3)	0.11665(3)	0.5814(5)
Ag5	12d	*mm*2..	0.40611(7)	0	0	0.5814(5)
Ag6	24g	*m*..	0	0.34535(4)	0.40387(4)	0.5814(5)
Ag7	12e	*mm*2..	0.18975(6)	$\frac{1}{2}$	0	0.5814(5)
In1	24g	*m*..	0	0.0815(3)	0.0800(3)	0.149(8)
In2	24g	*m*..	0	0.09136(5)	0.23902()7	0.4186(5)
In3	16f	.3.	0.16056(4)	0.16056(4)	0.16056(4)	0.4186(5)
In4	48h	1	0.20018(3)	0.34058(3)	0.11665(3)	0.4186(5)
In5	12d	*mm*2..	0.40611(7)	0	0	0.4186(5)
In6	24g	*m*..	0	0.34535(4)	0.40387(4)	0.4186(5)
In7	12e	*mm*2..	0.18975(6)	$\frac{1}{2}$	0	0.4186(5)
Gd	24g	*m*..	0	0.29904(3)	0.18751(3)	1

alloy measured in an applied magnetic field of 50 Oe is shown in figure (6-2)(a). The sample was field-cooled to 2.0 K and the measurement was performed while warming the sample up to 300 K. The $\chi(T)$ curve exhibits a definite peak at 3.6(1) K indicating magnetic ordering. The $\chi(T)$ data above 70 K could be fitted to a modified Curie-Weiss law:

$$\chi = \chi_0 + \frac{C}{T - \theta_p}, \tag{6-2}$$

where χ_0 is the temperature independent magnetic susceptibility, C is the Curie constant, and θ_p is the paramagnetic Curie temperature. The Curie constant can be expressed as $C = \frac{N\mu_{eff}^2}{3k_B}$, where N is the concentration of magnetic atoms per unit mass, μ_{eff} is the effective magnetic moment, and k_B is the Boltzmann constant. Figure (6-2)(b) shows the inverse magnetic susceptibility corrected for the contribution of χ_0, $(\chi - \chi_0)^{-1}$ versus temperature; the validity of the Curie-Weiss law is evident. The values of χ_0, C, and θ_p obtained from the fit are, respectively, 8.94(48) × 10^{-6} emu g^{-1}, 8.71(20) × 10^{-3} emu K g^{-1}, and –55.9(2) K. This value of C corresponds to μ_{eff} of 7.64(9) μ_B per Gd atom.

The same argument used in chapter (4) to compare the experimental and the theoretical values of the μ_{eff} applies here. The experimental value μ_{eff} = 7.64(9) μ_B can be considered close to the theoretical value of 7.94 μ_B [50] which confirms that the magnetic moment is localized on the Gd^{3+} ions and that, as expected, Ag and In atoms carry no magnetic moment. The negative value of θ_p indicates the predominantly antiferromagnetic interaction between the Gd^{3+} spins.

To determine the nature of the magnetic transition at 3.6 K, we measured the temperature dependence of the zero-field-cooled (ZFC) and field-cooled (FC) magnetic

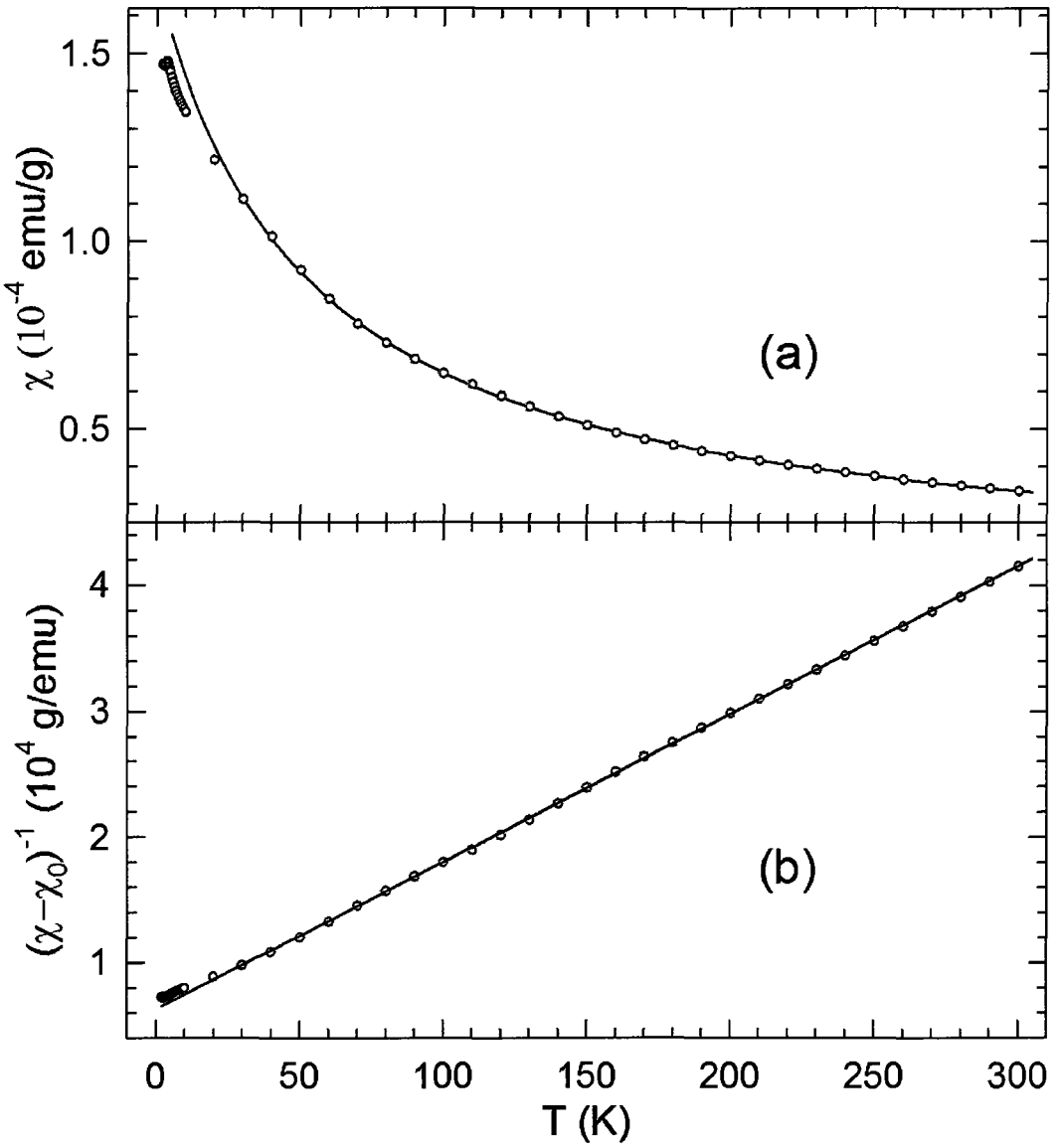

Figure (6-2)(a) The temperature dependence of the magnetic susceptibility of the $Ag_{50}In_{36}Gd_{14}$ alloy measured in an external magnetic field of 50 Oe. The solid line is the fit to equation (6-1) in the temperature range 70–300 K, as explained in the text. (b) The inverse magnetic susceptibility corrected for the contribution χ_0, $(\chi-\chi_0)^{-1}$ versus temperature T of the $Ag_{50}In_{36}Gd_{14}$ alloy. The solid line is the fit to equation (6-2).

susceptibility between 2 and 10 K in an applied magnetic field of 50 Oe (figure (6-3)). The occurrence of a bifurcation between the ZFC and FC data at the freezing temperature T_f = 3.6(1) K is evident. Above T_f both ZFC and FC data are essentially identical. Such a behaviour of the ZFC and FC susceptibility data is characteristic of a spin glass [51]. The $Ag_{50}In_{36}Gd_{14}$ alloy is thus a spin glass with a freezing temperature T_f = 3.6(1) K.

The occurrence of a spin-glass behaviour requires both randomness and frustration [51, 143, 144]. The frustration parameter f, defined as $f = -\theta_p/T_f$ [145], is an empirical measure of frustration. Its values for the $Ag_{50}In_{36}Gd_{14}$ alloy is 15.5(1.1). The value of f for the i $Ag_{50}In_{36}Gd_{14}$ QC is 8.7 [206]. This indicates that the studied alloy belongs to a category of strongly geometrically frustrated magnets [145].

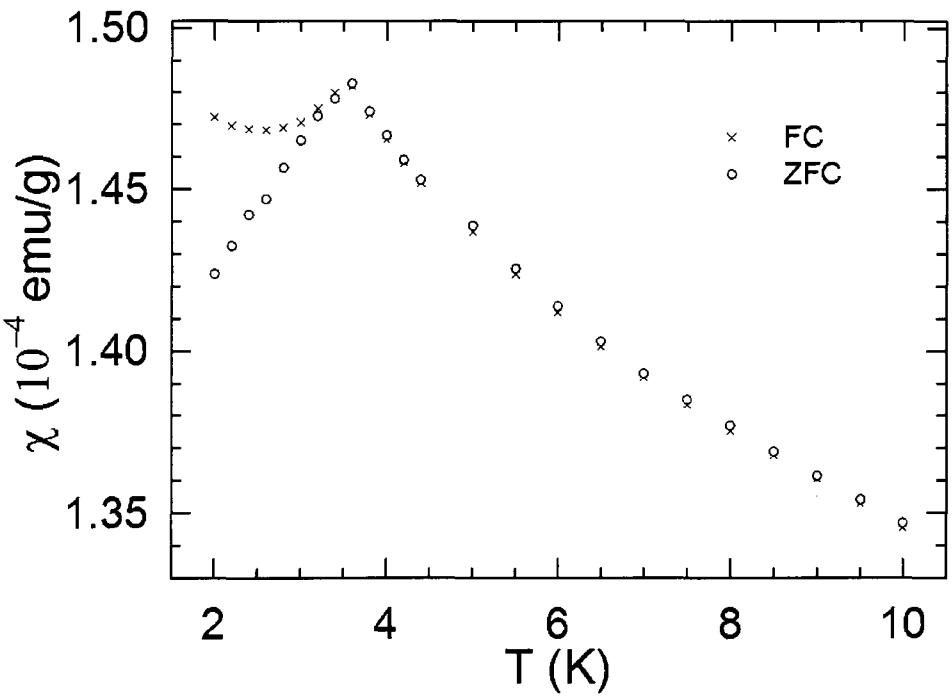

Figure (6-3) The temperature dependence of the zero-field-cooled (ZFC) and field-cooled (FC) magnetic susceptibility of the $Ag_{50}In_{36}Gd_{14}$ alloy measured in an external magnetic field of 50 Oe.

6.3.2.2) ac magnetic susceptibility

Figure (6-4) shows a temperature dependence the in-phase component χ' of the ac magnetic susceptibility of the i $Ag_{50}In_{36}Gd_{14}$ alloy for selected frequencies between 300 and 10 kHz. The $\chi'(T)$ curve shows two maxima: one at ~3.6 K and the other at ~2.4 K. The maximum at ~3.6 K is similar to that observed in the dc $\chi(T)$ data (figure (6-3)). The amplitudes and positions of these two maxima depend on the frequency f of the applied ac magnetic field. The position of the maximum in the $\chi'(T)$ curve is used to define T_f. It thus appears that the spin freezing in the spin glass $Ag_{50}In_{36}Gd_{14}$ is a two-stage process: it starts at $T_{f_1} \approx 3.6$ K and is completed at $T_{f_2} \approx 2.4$ K.

The out-of-phase component χ'' of the ac magnetic susceptibility of the $Ag_{50}In_{36}Gd_{14}$ alloy measured in the temperature range 2–20 K for selected frequencies between 300 and

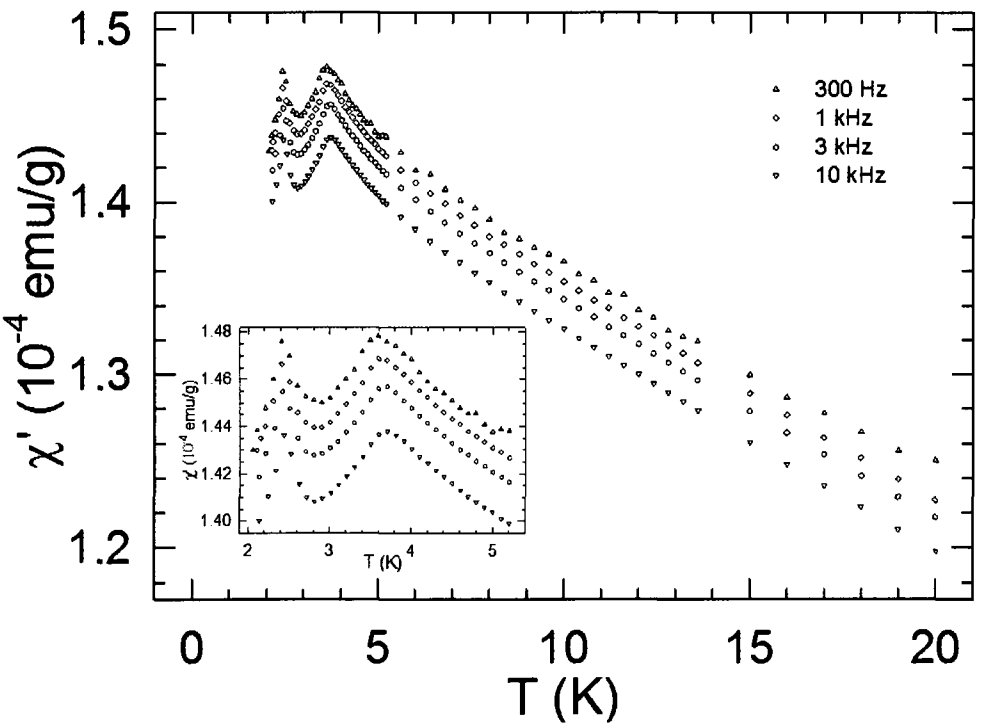

Figure (6-4) The temperature dependence of the in-phase magnetic susceptibility χ' measured for different frequencies from 300 Hz to 10 kHz for the $Ag_{50}In_{36}Gd_{14}$ alloy. The inset shows a magnification of the low-temperature region.

10 kHz is shown in figure (6-5). One can clearly observe a sudden increase of χ'' above its background near T_{f_1} and a sudden decrease of χ'' back to its background value near T_{f_2}.

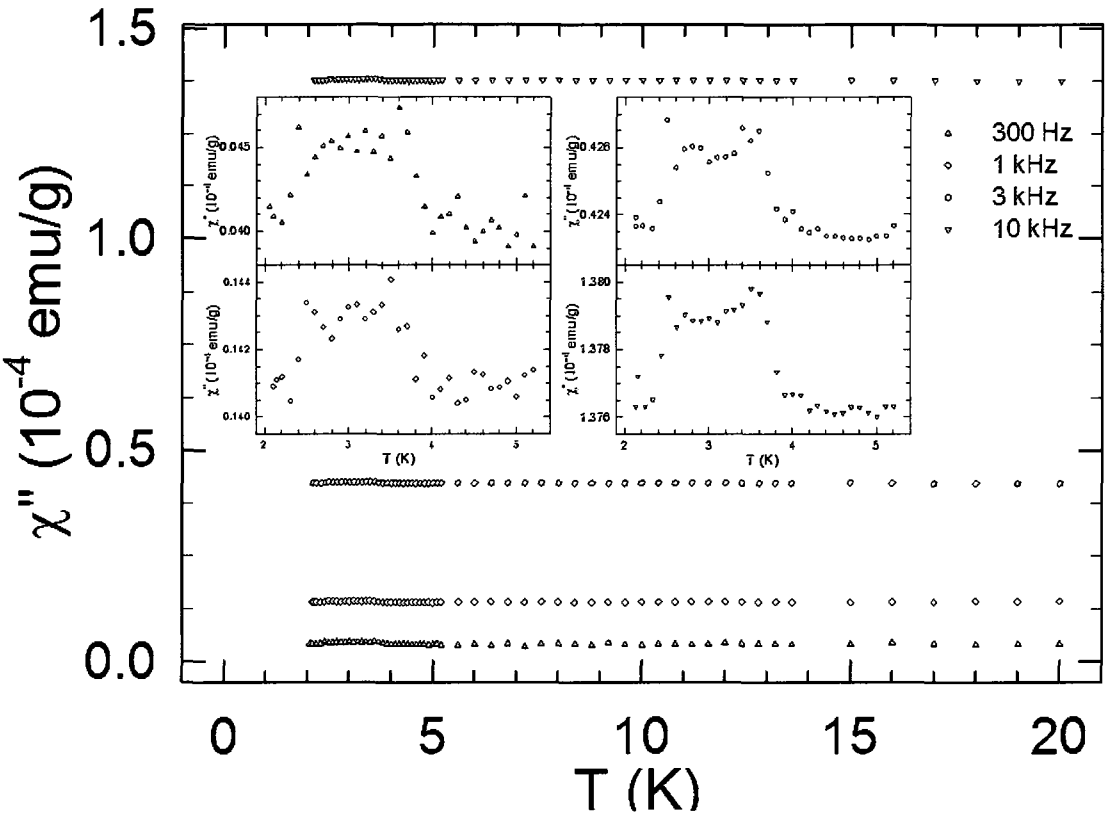

Figure (6-5) The temperature dependence of the out-of-phase magnetic susceptibility χ'' measured for different frequencies from 300 Hz to 10 kHz for the $Ag_{50}In_{36}Gd_{14}$ alloy. The insets show a magnification of the low-temperature region.

The temperatures T_{f_1} and T_{f_2} of the maxima in χ' (figure (6-4)) were determined using a curve fitting procedure. The frequency dependence of T_{f_1} and T_{f_2} is shown in figure (6-6). A quantitative measure of the change of the freezing temperature with frequency is represented by the relative change in T_f per decade change in f, defined as:

$$K = \frac{\Delta T_f}{T_f \Delta \log f}. \qquad (6\text{-}3)$$

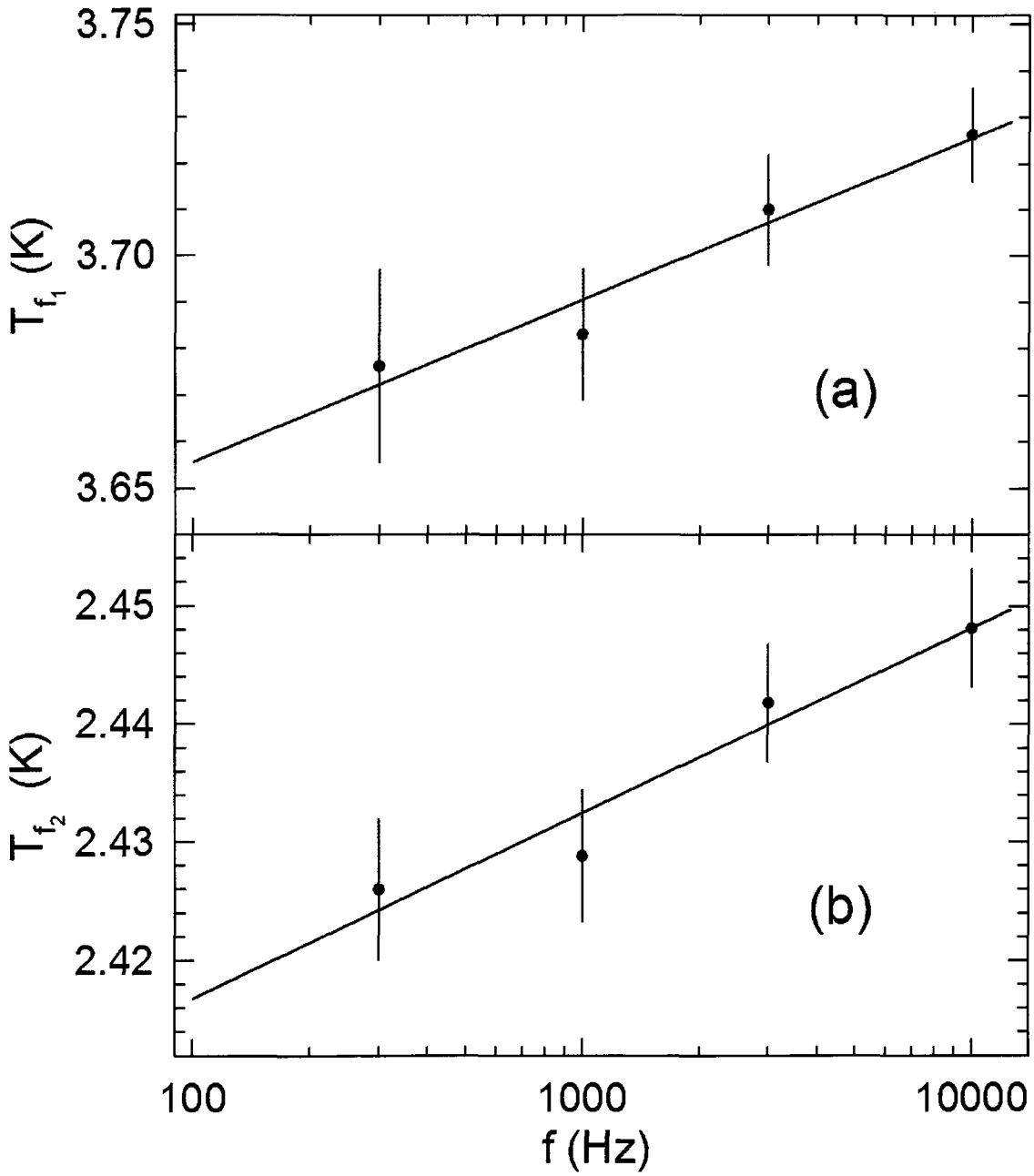

Figure (6-6) The frequency dependence of the freezing temperatures (a) T_{f_1} and (b) T_{f_2} for the $Ag_{50}In_{36}Gd_{14}$ alloy. The solid lines are the best linear fits to the data.

From a linear fit of the data in figure (6-6), and using the average values of T_{f_1} = 3.70 K and T_{f_2} = 2.44 K for the range of frequency used, we find that $K_1 = 9.4(1.5) \times 10^{-3}$ and $K_2 = 6.4(1.1) \times 10^{-3}$. These values are of the same order of magnitude as those of the canonical spin glasses [51], and similar to the value of 0.010(2) found for the i $Ag_{50}In_{36}Gd_{14}$ QC in chapter (4).

There are mainly two different interpretations of the phenomenon of spin freezing in spin glasses [154]. The first is a cluster model in which a system is considered as a set of interacting clusters. The other model assumes the existence of a true equilibrium phase transition. In the framework of the cluster model, the frequency dependence of T_f is described by a phenomenological Vogel-Fulcher law [51, 150]:

$$f = f_0 \exp[-E_a / k_B(T_f - T_0)], \tag{6-4}$$

where f_0 is a characteristic frequency, E_a is the activation energy, and T_0 is the Vogel-Fulcher temperature which is a measure of the interaction strength between clusters in a spin glass [152]. Equation (6-4) implies a linear dependence of $1/(T_f - T_0)$ with $\log(f)$. The best fit of the $T_{f_1}(f)$ and $T_{f_2}(f)$ data (figure (6-7)) to equation (6-4), assuming $f_0 = 10^{13}$ Hz which is typical for a spin glass [150], yields E_a^1 / k_B = 6.60(79) K, T_0^1 = 3.41(4) and E_a^2 / k_B = 2.56(41) K, T_0^2 = 2.32(2) K, respectively. Similarly to what was observed for other spin glasses [150], the derived parameters fulfill the inequality $E_a/k_B > T_0$.

The scaling theory predicts that when approaching the phase transition temperature T_c from above, the relaxation time $\tau = 1/f$ of individual spin clusters will show a critical slowing down, characterized by a power law $\tau \propto \xi^z$, where ξ is the correlation length and z is the dynamic exponent [153]. The correlation length itself is expected to diverge at T_c according

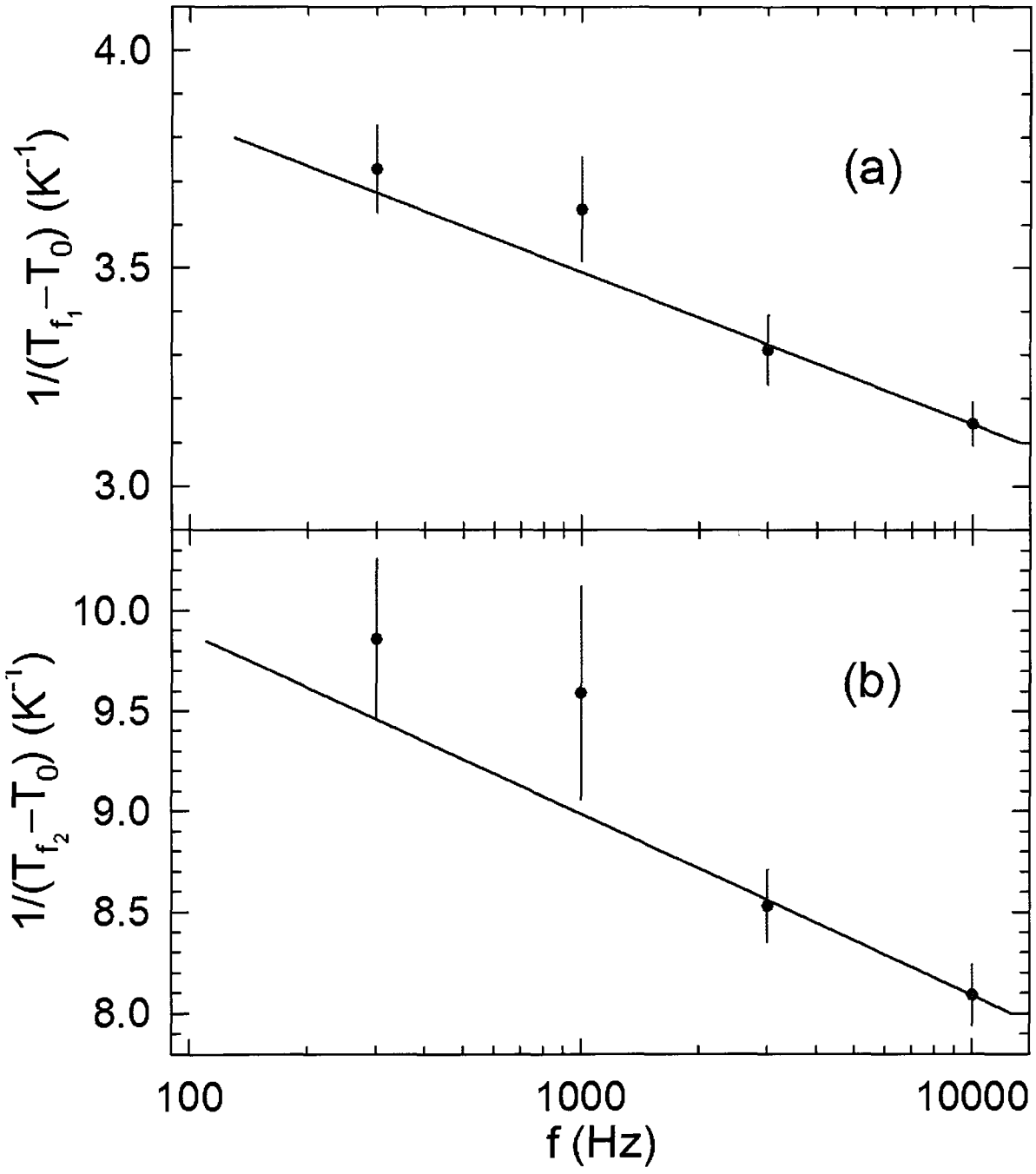

Figure (6-7) The frequency dependence of the freezing temperatures (a) T_{f_1} and (b) T_{f_2} for the $Ag_{50}In_{36}Gd_{14}$ alloy. The solid line is the best fit to equation (6-4).

to $\xi \propto \left(\frac{T_f - T_c}{T_c}\right)^{-\nu}$, where ν is the critical exponent for the correlation length. Therefore, near T_c the temperature dependence of f is expected to obey the power-divergence [51, 153]:

$$f = f_0\left(\frac{T_f - T_c}{T_c}\right)^{z\nu}, \quad T_f > T_c \tag{6-5}$$

where f_0 is a characteristic frequency. The best fit of the $T_{f_1}(f)$ and $T_{f_2}(f)$ data (figure (6-8)) to equation (6-4), assuming $f_0 = 10^{13}$ Hz which is typical for a spin glass [154], gives T_c^1 = 3.63(2) K, $(z\nu)_1$ = 5.64(30) and T_c^2 = 2.42(1) K, $(z\nu)_2$ = 4.70(25). The determined values of $z\nu$ fall into the range 4–12 found for the different spin glasses [51].

The presence of two distinct features in the $\chi'(T)$ and $\chi''(T)$ is perhaps the most interesting aspect of the spin-freezing phenomenon in the 1/1 approximant to the i $Ag_{50}In_{36}Gd_{14}$ QC. In virtually all known spin glasses, the spin freezing is a one-stage process [51]. It appears that the spin freezing in the $Ag_{50}In_{36}Gd_{14}$ alloy is most likely occurring in two stages: at ~3.6 K spins develop short range correlations but they continue to fluctuate at low frequencies, and then long-range freezing is achieved upon further cooling to below ~2.4 K. We are aware of only two spin-glass systems in which the spin freezing occurs in two stages: $Gd_3Ga_5O_{12}$ [207] and $Dy_{2-x}Y_xTi_2O_7$ [208].

It has been argued that quasiperiodicity leads naturally to geometrical frustration, and consequently QCs cannot develop long-range magnetic order but become spin glasses. All presently known QCs exhibit no long-rage magnetic order and many of them are spin glasses. The i $Ag_{50}In_{36}Gd_{14}$ QC is a spin glass [14]. The fact that its 1/1 approximant of the same composition and of high structural quality is also a spin glass indicates that quasiperiodicity does not necessarily precludes the development of a long-range magnetic

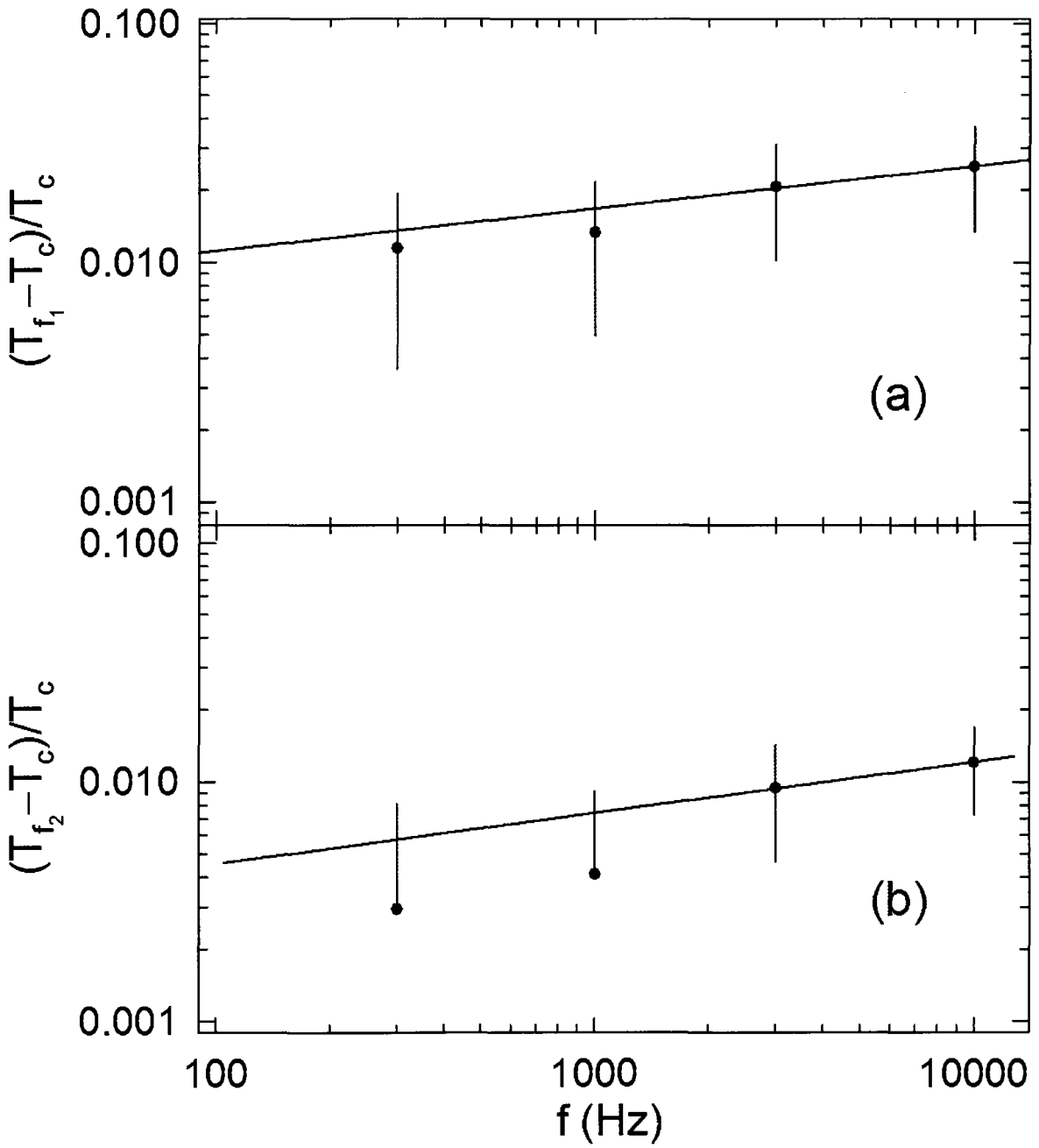

Figure (6-8) The frequency dependence of the freezing temperatures (a) T_{f_1} and (b) T_{f_2} for the $Ag_{50}In_{36}Gd_{14}$ alloy. The solid line is the best fit to equation (6-5).

order.

6.3.3) Mössbauer spectroscopy

Figure (6-9) shows a ^{151}Gd Mössbauer spectrum of the $Ag_{50}In_{36}Gd_{14}$ measured at 4.6 K, i.e., in the paramagnetic region above T_{f_1}. The Gd^{3+} ions are located at the site with the point symmetry *m*.. (table (6-1)) which ensures a non-zero EFG at the Gd^{3+} site, and hence a non-zero electric quadrupole hyperfine interaction. The Mössbauer spectrum in figure (6-9) exhibits indeed the presence of a substantial electric quadrupole hyperfine interaction and the absence of the magnetic dipole hyperfine interaction. The absence of the magnetic dipole hyperfine interaction in the Mössbauer spectrum in figure (6-9) proves that at 4.6 K the Gd spins are not in a frozen state. The parameters derived from the fit (χ^2 = 1.11) of the 4.6 K Mössbauer spectrum (figure (6-9)) are: the isomer shift (relative to the ^{155}Eu($SmPd_3$) source)

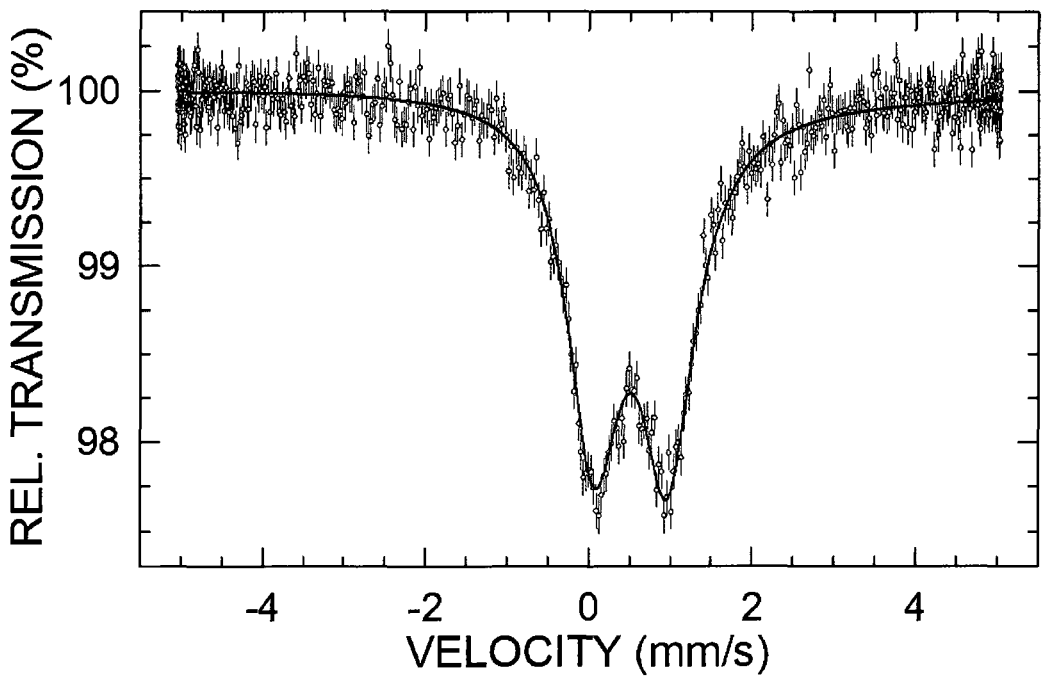

Figure (6-9) The ^{155}Gd Mössbauer spectrum of the $Ag_{50}In_{36}Gd_{14}$ alloy at 4.6 K fitted (solid line) with an electric quadrupole hyperfine interaction. The zero-velocity origin is relative to the source.

δ = 0.506(6) mm/s, Δ_g^{eff} = 1.897(19) mm/s, f_a = 10.3(1)%, and Γ_a = 0.424(16) mm/s. The value of δ confirms the trivalent state of Gd in the $Ag_{50}In_{36}Gd_{14}$ alloy [159]. The value of Δ_g^{eff} is close to that for the i $Ag_{50}In_{36}Gd_{14}$ QC [206], which indicates the strong similarity of the local atomic structure around the Gd atoms in the 1/1 approximant and the i $Ag_{50}In_{36}Gd_{14}$ QC. The surface density of the Mössbauer absorber of the $Ag_{50}In_{36}Gd_{14}$ alloy was 356 mg cm^{-2}.

In terms of the Debye approximation of the lattice vibrations, the absorber Debye-Waller factor f_a is expressed [17] by the Debye temperature, Θ_D, as in equation (4-6). The value of f_a = 10.3(1)% derived from the fit of the Mössbauer spectrum (figure (6-9)) via equation (4-6) yields Θ_D = 199(1) K which is the same for i $Ag_{50}In_{36}Gd_{14}$ QC studied in chapter (4) . This low value of Θ_D compares well with the value of 145.2 K for the 1/1 approximant $YbCd_6$ derived from the specific heat [209].

The ^{151}Gd Mössbauer spectrum of the $Ag_{50}In_{36}Gd_{14}$ alloy at 1.5 K, i.e., below T_{f_2}, clearly shows (figure (6-10)) the presence of a combined magnetic dipole and electric quadrupole hyperfine interactions. The presence of the magnetic dipole hyperfine interaction in the Mössbauer spectrum in figure (6-10) proves that at 1.5 K the Gd spins are frozen. The Mössbauer spectrum in figure (6-10) was fitted by fixing the value of Γ_a to 0.424 mm/s obtained from the fit of the 4.6 K Mössbauer spectrum, and the value of θ to 0.0°. The parameters derived from the fit (χ^2 = 1.06) of the 1.5 K Mössbauer spectrum (figure (6-10)) are: δ = 0.483(18) mm/s, H_{hf} = 137.3(11.8) kOe, the quadrupole splitting constant Δ_g = eQ_gV_{zz} = –1.899(29) mm/s (V_{zz} = –4.21(6) × 10^{21} V cm^{-2}), η = 0.0(2), and f_a = 10.4(1)%. A substantial value of H_{hf} indicates a considerable magnetic moment of Gd atoms.

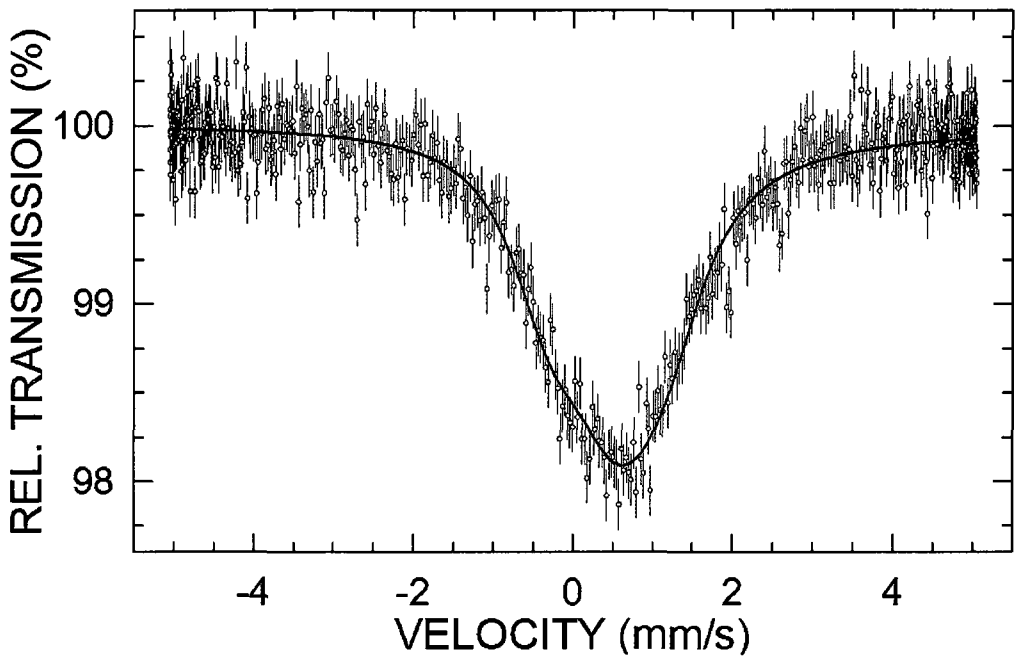

Figure (6-10) ^{155}Gd Mössbauer spectrum of the $Ag_{50}In_{36}Gd_{14}$ at 1.5 K fitted (solid line) with a combined magnetic dipole and electric quadrupole hyperfine interactions. The zero-velocity origin is relative to the source.

6.3.4) Conclusions

A newly discovered ternary alloy $Ag_{50}In_{36}Gd_{14}$ has been studied by means of x-ray diffraction, dc and ac magnetic susceptibility, and ^{151}Gd Mössbauer spectroscopy. The studied alloy has the cubic $YbCd_6$-type structure (space group $Im\bar{3}$) with the lattice parameter a = 15.202(1) Å. The $Ag_{50}In_{36}Gd_{14}$ alloy is shown to be a 1/1 approximant to the icosahedral quasicrystal $Ag_{50}In_{36}Gd_{14}$. Based on dc magnetization measurements, no evidence is found for a transition to a ground state with long range magnetic order in the temperature range 2–300 K. The temperature dependence of the dc magnetic susceptibility follows the modified Curie-Weiss law with the paramagnetic Curie temperature of −55.9(2) K and an effective magnetic moment of 7.64(9) μ_B per Gd atom. The studied alloy is a spin glass. The unusual spin freezing process occurs in two stages: at ~3.6 K spins develop short range correlations but they continue to fluctuate at low frequencies, and then long-range

freezing is achieved upon further cooling to below ~2.4 K. The frequency dependence of the freezing temperatures is equally well accounted for by the Vogel-Fulcher law and the power law. The presence of the magnetic dipole hyperfine interaction in the ^{151}Gd Mössbauer spectrum at 1.5 K and its absence in the spectrum at 4.6 K proves that the Gd spins are, respectively frozen and fluctuating at these temperatures. The Debye temperature of the $Ag_{50}In_{36}Gd_{14}$ alloy is 199(1) K.

7) CONCLUSIONS

The recently discovered icosahedral quasicrystals $Ag_{50}In_{36}Gd_{14}$ and $Zn_{77}Fe_7Sc_{16}$, and a 1/1 approximant $Ag_{50}In_{36}Gd_{14}$, have been synthesized. Their structural and magnetic properties have been investigated with x-ray diffraction, dc and ac magnetic susceptibility, and ^{155}Gd and ^{57}Fe Mössbauer effect techniques.

The icosahedral quasicrystal $Ag_{50}In_{36}Gd_{14}$ has a simple six-dimensional Bravais lattice with the six-dimensional hypercubic lattice constant of 7.805(2) Å. The temperature dependence of the dc magnetic susceptibility is shown to follow the modified Curie-Weiss law with the effective magnetic moment of 8.15(1) μ_B per Gd atom and the paramagnetic Curie temperature of −37.1(2) K. No evidence is found for a transition to a ground state with a long-range magnetic order in the temperature range 2–300 K. The icosahedral quasicrystal $Ag_{50}In_{36}Gd_{14}$ is shown to be a spin glass with a spin freezing temperature of 4.25(5) K. The frequency dependence of the freezing temperature determined from the ac susceptibility data is well described by the Vogel-Fulcher law and the power law. The presence of the distribution of the electric quadrupole splitting in the ^{155}Gd Mössbauer spectra is evidence for the existence of the multiplicity of Gd sites. The hyperfine magnetic field sets in at the temperature higher than the spin freezing temperature. The Debye temperature of the icosahedral quasicrystal $Ag_{50}In_{36}Gd_{14}$ is 199(2) K.

The icosahedral quasicrystal $Zn_{77}Fe_7Sc_{16}$ crystallizes in a simple six-dimensional Bravais lattice with the six-dimensional hypercubic lattice constant of 7.087(1) Å. The dependence of the dc magnetic susceptibility on temperature follows the modified Curie-Weiss law with the effective magnetic moment of 3.55(1) μ_B per Fe atom and the

paramagnetic Curie temperature of 10.6(2) K. No long-range magnetic order in the temperature range 2–300 K is found in the icosahedral quasicrystal $Zn_{77}Fe_7Sc_{16}$. This quasicrystal is found to be a spin glass with a spin freezing temperature of 7.75(2) K. The dependence of the freezing temperature determined from the ac susceptibility data on frequency is shown to be well described by the Vogel-Fulcher law and the power law. However, the observed increase of the thermoremanent magnetization with the magnetic field is found to be incompatible with the ultrametrically organized phase space of a canonical spin glass. It is concluded that the nature of the spin-glass state in the icosahedral quasicrystal $Zn_{77}Fe_7Sc_{16}$ is fundamentally different from that of a canonical spin glass. The presence of the bimodal distribution of the electric quadrupole splitting and of the hyperfine magnetic field derived from the ^{57}Fe Mössbauer spectra is indicative for the existence of two classes of Fe sites. The hyperfine magnetic field sets in at the temperature higher than the spin freezing temperature. The Debye temperature of the icosahedral quasicrystal $Zn_{77}Fe_7Sc_{16}$ is 443(8) K.

The ternary alloy $Ag_{50}In_{36}Gd_{14}$ crystallizes in the space group $Im\bar{3}$ with the lattice parameter of 15.202(1) Å. It is shown to be a 1/1 approximant to the icosahedral quasicrystal $Ag_{50}In_{36}Gd_{14}$. Magnetization measurements show no evidence for the existence of a long-range magnetic order in the temperature range 2–300 K. The temperature dependence of the dc magnetic susceptibility follows the modified Curie-Weiss law with the effective magnetic moment of 7.64(9) μ_B per Gd atom and the paramagnetic Curie temperature of –55.9(2) K. The approximant $Ag_{50}In_{36}Gd_{14}$ is shown to be an unusual spin glass with two spin freezing temperatures. The spin freezing is a two-stage process: at ~3.6 K spin develop short-range correlations but continue to fluctuate at low frequencies, and then long-range freezing is

achieved upon further cooling to below ~2.4 K. The frequency dependence of the two freezing temperatures can be accounted for by the Vogel-Fulcher law and the power law. The Debye temperature of the 1/1 approximant $Ag_{50}In_{36}Gd_{14}$ is found to be 199(1) K.

Although the i $Ag_{50}In_{36}Gd_{14}$ QC and the 1/1 approximant $Ag_{50}In_{36}Gd_{14}$ have the same chemical composition, it is clear that they differ in their bulk magnetic properties. This is a proof that quasiperiodicity indeed is responsible for these differences. Table (7-1) shows a comparison between some physical quantities obtained from different measurements of the i $Ag_{50}In_{36}Gd_{14}$ and the 1/1 approximant $Ag_{50}In_{36}Gd_{14}$.

Table (7-1) Comparison between experimental values obtained of the two different structures of $Ag_{50}In_{36}Gd_{14}$ alloy.

$Ag_{50}In_{36}Gd_{14}$	T_f (K)	θp (K)	f	μ_{eff} (μ_B)	K	θ_D (K)
i QC	4.25(5)	-37.1(2)	8.7(1)	8.15(1)	0.010(2)	199(1)
1/1 Approximant	3.6(1) and 2.4	-55.9(2)	15.5(1.1)	7.64(9)	0.094(1.5) and 0.064(1.1)	199(2)

The most exciting finding of this thesis is the discovery that the nature of the spin-glass state in the icosahedral quasicrystal $Zn_{77}Fe_7Sc_{16}$ is fundamentally different from the nature of a canonical spin glass which is described in terms of the ultrametric phase space. Dolinsek *et al* [210–213] reported similar phenomena in two icosahedral quasicrystals Tb-Mg-Zn and Tb-Mg-Cd. They claimed that the icosahedral quasicrystals are rather a mix of a spin glass and a superparamagnet. However, I think that the physics behind this new observation is fundamentally different and yet to be understood. An obvious question that arises is whether the nature of the spin-glass state in all other quasicrystals is also different from that of a canonical spin glass. This can be investigated by studying the field dependence of the thermoremanent magnetization decays. Future research should then involve such studies for other quasicrystals exhibiting a spin-glass behavior.

Refrences:

[1] Shechtman D, Blech I, Gratis D and Cahn J W 1984 *Phys. Rev. Lett.* **53** 1951

[2] Suck J-B, Schreiber M and Häussler P (ed) 2002 *Quasicrystals, an Introduction to Structure, Physical Properties, and Applications* (Berlin: Springer)

[3] Stadnik Z M (ed) 1999 *Physical Properties of Quasicrystals* (Berlin: Springer)

[4] Lifshitz R 1995 *Proc.* 5th *Int. Conf. Quasicrystals* ed. C Janot and E Mosseri (Singapore: World Scientific) p 43

[5] Lifshitz R 1998 *Phys. Rev. Lett.* **80** 2717

[6] Lifshitz R 2000 *Mater. Sci. Eng.* A **294–296** 508

[7] Lifshitz R and Mandel S E-D 2004 *Acta Crystallogr.* A **60** 167

[8] Godrèche C, Luck J M and Orland H 1986 *J. Stat. Phys.* **45** 777

[9] Bhattacharjee S M, Ho J-S and Johnson J A Y 1987 *J. Phys. A-Math. Gen.* **20** 4439

[10] Okabe Y and Niizeki K 1988 *J. Phys. Soc. Japan* **57** 16

[11] Duneau M, Dunlop F, Jagannathan A and Oguey C 1991 *Mod. Phys.* B **5** 1895

[12] Matsuo S, Ishimasa T and Nakano H 2000 *Mater. Sci. Eng.* A **294–296** 633

[13] Matsuo S, Ishimasa T and Nakano H 2002 *J. Magn. Magn. Mater.* **246** 223

[14] Matsuo S, Nakano H, Motomura S, and Ishimasa T 2005 *J. Phys. Soc. Japan* **74** 1036

[15] Matsuo S, Motomura S and Ishimasa T 2007 *Phil. Mag.* **87** 51

[16] Ledue D, Teillet J, Carnet J and Dujardin J 1993 *J. Non-Cryst. Solids* **153–154** 403

[17] Reid R W, Bose K and Mitrović B 1998 *J. Phys.: Condens. Matter* **10** 2303

[18] Hermission J 2000 *J. Phys. A-Math. Gen.* **33** 57

[19] Wessel S, Jagannathan A and Hass S 2003 *Phys. Rev. Lett.* **90** 177205

[20] Vedmedenko E Y, Oepen H P and Kirschner J 2003 *Phys. Rev. Lett.* **90** 137203

[21] Jagannathan A 2004 *Phys. Rev. Lett.* **92** 047202

[22] Vedmedenko E Y, Grimm U and Wiesendanger R 2004 *Phys. Rev. Lett.* **93** 076407

[23] Jagannathan A 2005 *Phys. Rev.* B **71** 115101

[24] Vedmedenko E Y 2004 *Ferroelectrics* **305** 129

[25] Vedmedenko E Y, Grimm U and Wiesendanger R 2006 *Phil. Mag.* **86** 733

[26] Jagannathan A and Schultz H J 1997 *Phys. Rev.* B **55** 8045

[27] Hida K 2001 *Phys. Rev. Lett.* **86** 1331

[28] Stadnik Z M, Stroink G, Ma H and Williams G 1989 *Phys. Rev.* B **39** 9797

[29] Fukamichi K 1999 in *Physical Properties of Quasicrystals* ed Z M Stadnik (Berlin: Springer) p 295

[30] Charrier B and Ouladdiaf B and Schmitt D 1997 *Phys. Rev. Lett.* **78** 4637

[31] Sato T J, Takakura H, Tsai A P and Shibata K 1998 *Phys. Rev. Lett.* **81** 2364

[32] Noakes D R, Kalvius G M, Wäppling R, Stronach C E, White Jr. M F, Saito H and [16] Fukamichi K 1998 *Phys. Lett.* A **238** 197

[33] Islam Z, Fisher I R, Zarestky J, Canfield P C, Stassis C and Goldman A I 1998 *Phys. Rev.* B **57** R11047

[34] Sato T J, Takakura H, Tsai A P, Shibata K, Ohoyama K and Andersen K H 2000 *Phys. Rev.* B **61** 476

[35] Sato T J, Takakura H, Tsai A P, Ohoyama K, Shibata K and Andersen K H 2000 *Mater. Sci. Eng.* A **294–296** 481

[36] Sato T J, Takakura H, Guo J, Tsai A P and Ohoyama K 2002 *J. Alloy. Compd.* **342** 365

[37] Sato T J 2005 *Acta Crystallogr.* A **61** 39

[38] Sato T J, Takakura H, Tsai A P and Shibata K 2006 *Phys. Rev.* B **73** 054417

[39] Fisher I R, Cheon K O, Panchula A F, and Canfield P C 1999 *Phys. Rev. B* **59** 308 .

[40] Goldman A I and Kelton K F 1993 *Rev. Mod. Phys.* **65** 213

[41] Steurer W 2004 *Z. Kristallogr.* **219** 391

[42] Janot C, Dubois J-M, and de Boissieu M 1989 *Am. J. Phys.* **57** 972

[43] Lu P J and Steinhardt P J 2007 *Science (www.sciencemag.org)* **315** 1106

[44] Photographer Grata di Silenzio `http://www.flickr.com`

[45] Photographer Aleksey Golyko `http://www.flickr.com`

[46] Penrose R 1979*Math. Intelligencer* **2** 32

[47] Elser V 1985 *Phys. Rev.* B **32** 4892

[48] Buschow K H J and de Boer F R 2004 *Physics of Magnetism and Magnetic Materials*, (New York: Kluwer Academic Publishers)

[49] Kittel C 2005 *Introduction to Solid State Physics* (New York: John Wiley & Sons, Inc.)

[50] Ashcroft N W and Mermin N D 1976 *Solid State Physics* (New York: Thomson Learning, Inc.)

[51] Mydosh J A 1993 *Spin Glasses: an Experimental Introduction* (London: Taylor and Francis)

[52] Vincent E 2007 *Lect. Notes Phys.* **716** 7–60

[53] Mydosh J A 1978 *J. Magn. Magn. Mater.* **7** 237

[54] Binder K and Young A P 1986 *Rev. Mod. Phys.* **58** 4

[55] Mulder C A M, van Duyneveldt A J, and Mydosh J A 1981 *Phys. Rev.* B **23** 1384

[56] Stadnik Z M, Al-Qadi K, and Wang P 2007 *J. Phys. Condens. Matter* **19** 326208

[57] Ishimasa T, Kaneko Y, and Kaneko H 2004 *J. Non-Cryst Solids* **334&335** 1

[58] Iwano S, Nishimoto K, Tamura R, and Takeuchi S 2006 *Philos. Mag.* B **86** 435

[59] Abe E and Tsai A-P 2004 *J. Non-Cryst. Solids* **334&335** 190

[60] Tamura R, Edagawa K, Muro Y, Suzuki K, Ichihara M, Isobe M, and Ueda Y 2004 *J. Non-Cryst Solids* **334&335** 173

[61] Ryan D H, Saleema N M, Gagnon R, and van Lierop J 2001 *J. Phys. Condens. Matter.* **13** 10159

[62] Kuo Y K and Lai J R 2004 *J. Appl. Phys.* **95** 1900

[63] Okada J T, Watanabe Y, Nanao S, Tamura R, Takeuchi S, Yokoyama Y, Hiraoka N, Itou M, and Sakurai Y 2003 *Phys. Rev.* B **68** 132204

[64] Gomez C P and Lidin S 2003 *Phys. Rev.* B **68** 024203

[65] Jiang J Z, Gerward L, and Olsen J S 2001 *Appl. Phys. Lett.***79** 2538

[66] Edwards S F and Anderson P W 1975 *J. Phys.* F *Met. Phys.* **5** 965

[67] Fischer K H 1975 *Phys. Rev. Lett.* **34** 1438

[68] Kirkpatrick S and Sherrington D 1978 *Phys. Rev.* B **17** 4384

[69] de Almeida J R L and Thouless D J 1978 *J. Phys. A: Math. Gen.* **11** 983

[70] Thouless D J, Anderson P W, and Palmer R G 1977 *Philos. Mag.* B **35** 593

[71] Parisi G 1979 *Phys. Rev. Lett.* **43** 1754

[72] Parisi G 1980 *J. Phys. A: Math. Gen.* **13** 1101

[73] Parisi G 1980 *J. Phys. A: Math. Gen.* **13** 1887

[74] Parisi G 1983 *Phys. Rev. Lett.* **50** 1946

[75] Dotsenko V S 1985 *J. Phys.* C **18** 6023

[76] Rammal R, Toulouse G, and Virasoro M A 1986 *Rev. Mod. Phys.* **58** 765

[77] Newman C M and Stein D L 1996 *Phys. Rev. Lett.* **76** 515

[78] Newman C M and Stein D L 1998 *Phys. Rev.* E **57** 1356

[79] Newman C M and Stein D L 2003 *Phys. Rev. Lett.* **91** 197205-1

[80] Malozemoff A P and Barnes S E 1983 *Phys. Rev. Lett.* **51** 1704

[81] Barbara B and Malozemoff A P 1983 *J. Less-Common Met.* **94** 45

[82] Huse D A and Fisher D S 1991 *J Phys. Paris* I **1** 621

[83] McMillan W L 1985 *Phys. Rev.* B **31** 430

[84] Smith D A 1975 *J Phys.* F **5** 2148

[85] Abrikosov A A 1978 *J Low Temp. Phys.* **33** 505

[86] Stauffer D 1979 *Phys. Rep.* **54** 1

[87] Chowdhury D and Bhattacharjee J K 1984 *Phys. Lett.* A **104** 100

[88] Chamberlin R V, Mozurkewich G and Orbach R 1984 *Phys. Rev. Lett.* **52** 867

[89] Bontemps N, Rajchenback J, Chamberlin R V, and Orbach R 1984 *Phys. Rev.* B **30** 6514

[90] Malozemoff A P and Barbara B 1985 J Appl *Phys.* **57** 3410

[91] Ayadi M, Ferr´e J, Mauger A, and Triboulet R 1986 *Phys. Rev. Lett.* **57** 1165

[92] Lundgren L, Nordblad P, and Svedlindh P 1986 *Phys. Rev.* B **34** 8164

[93] Fisher D S and Huse D A 1986 *Phys. Rev. Lett.* **56** 1601

[94] Continentino M A and Malozemoff A P 1986 *Phys. Rev.* B **34** 471

[95] Continentino M A and Malozemoff A P 1986 *Phys. Rev.* B **33** 3591

[96] Malozemoff A P and Pytte E 1986 *Phys. Rev.* B **34** 6579

[97] Bray A J and Moore M A 1987 *Phys. Rev. Lett.* **58** 57

[98] Bray A J and Moore M A 1987 *Phys. Rev.* B **31** 631

[99] Carre E, Puech L, Prejean J J, Beauvillain P, and Renard J P in Heidelberg Colloquium on Glassy Dynamics 1987 *Lect. Notes. Phys.* edited by J L van Hemmen and I Morgnestern Springer-Verlag Berlin p 75

[100] Fisher D S and Huse D A 1988 *Phys. Rev.* B **38** 373

[101] Fisher D S and Huse D A 1988 *Phys. Rev.* B **38** 386

[102] Continentino M A and de Oliveira S M 1988 *Phys. Rev.* B **37** 5877

[103] Ocio M, Hammann J M, and Vincent E 1990 *J Magn Magn Mater* **90-91** 329

[104] Singh R R P and Huse D A 1991 *J. Appl. Phys.* **69** 5225

[105] Grannan E R and Hetzel R E 1991 *Phys. Rev. Lett.* **67** 907

[106] Glauber R J 1963 *J. Math. Phys.* **4** 294

[107] Sompolinsky H 1981 *Phys. Rev. Lett.* **47** 935

[108] Klimova A M, Ananichev V A, Arif M, and Blinov L N 2005 *Glass Physics and Chemistry* **31** 760

[109] D. G. Fink and D. Christiansen, *Electronics Engineers' Handbook*, McGraw-Hill, New York, 1989

[110] R. Zallen, *The Physics of Amorphous Solids*, Wiley, New York, 1983

[111] Bish D L and Chipera S J 1989 *Powder Diffract.* **4** 137

[112] R. Jenkins and R.L. Snyder, *Introduction to X-ray Powder Diffractometry*, John Wiley and Sons, New York 1996

[113] Langford J I and LouNr D 1996 *Rep. Prog. Phys.* **59** 131

[114] Wong-Ng W and Hubbard C R 1987 *Powder Diffr.* **2** 242

[115] *Standard Reference Material 640c, Silicon Powder Line Position and Line Shape Standard for X-ray Diffraction 2000* (US: Natl. Inst. Stand. Techn)

[116] X'Pert HighScore Plus manual *2007*

[117] R.A. Young (ed.), *The Rietveld Method*, Oxford University Press, Oxford 1993

[118] McCusker L B, Von Dreele R B, Cox D E, Louër D and Scardi P, 1999 *J. Appl. Cryst.* **32** 36

[119] *Mössbauer Spectroscopy and Its Applications*, International Atomic Energy Agency, Vienna, 1972

[120] Mössbauer R L 1958 *Z. Physik.* **151** 124

[121] Mössbauer R L 1961 Nobel Lecture http://nobelprize.org (Recoilless Nuclear Resonance Absorption of Gamma Radiation)

[122] U. Gonser (ed.), *Mössbauer Spectroscopy,* Springer-Verlag, New York, 1975

[123] A. G. Maddock, *Mössbauer Spectroscopy Principles and Applications of the Techniques,* Horwood Publishing, Chichester, 1997

[124] G. J. Long (ed.) and F. Grandjean, *Mössbauer Spectroscopy Applied to Magnetism and Materials Science II,* Plenum Press, New York, 1996

[125] N.N. Greenwood and T.C. Gibb, *Mössbauer Spectroscopy*, Chapman and Hall, London, 1971

[126] Cali J P (ed) 1971 *Certificate of Calibration, Iron Foil Mössbauer Standard,* NBS Circular no 1541 (Washington, DC: US Govt Printing Office)

[127] Stadnik Z M and Zhang G 2005 *J. Phys.: Condens. Matter* **17** 6599

[128] Otterloo B F, Stadnik Z M and Swolfs A E M 1983 *Rev. Sci. Instrum.* **54** 1575

[129] Clarke J 1994 *Scientific American* **271** #2 46

[130] Quantum Design, *MPMS Application Note 1014-822,* http://www.qdusa.com/resources

[131] Quantum Design, *MPMS Application Note 1014-204*, http://www.qdusa.com/resources

[132] Quantum Design, *Palladium Reference Samples,* http://www.qdusa.com/resources

[133] Quantum Design, *Physical Property Measurement System AC Measurement System (ACMS) Option User's Manual*, Part Number 1084-100 C-1, http://www.qdusa.com/resources

[134] Quantum Design, *Introduction to AC Susceptibility,* http://www.qdusa.com/resources

[135] Iwano S, Nishimoto H, Tamura R and Takeuchi S 2006 *Phil. Mag.* **86** 435

[136] Tsai A P, Guo J Q, Abe E, Takakura H, and Sato T J 2000 *Nature* **408** 537

Guo J Q, Abe E and Tsai A P 2000 *Phys. Rev.*B **62** R14605

[137] Takakura H, Gómez C P, Yamamoto A, de Boissieu M, and Tsai A P 2007 *Nat. Mater.* **6** 58

[138] Jenkins R and Schreiner W N 1989 *Powder Diffr.* **4** 74

[139] Schreiner W N and Jenkins R 1983 *Adv. X-ray Anal.* **26** 141

[140] Cahn J W, Shechtman D and Gratias D 1986 *J. Mater.Res.* **1** 13

[141] Elser V 1986 *Acta Crystallogr.* A **42** 36

[142] Bancel P A, Heiney P A, Stephens P W, Goldman A I and Horn P M 1985 *Phys. Rev. Lett.* **54** 2422

[143] Toulouse G 1977 *Commun. Phys.* **2** 116

[144] Binder K and Young A P 1986 *Rev. Mod.* Phys. **58** 801

[145] Ramirez A P 2001 *Handbook of Magnetic Materials* vol 13, ed K H J Buschow (Amsterdam: Elsevier) p 423

[146] Hattori Y, Niikura A, Tsai A P, Inoue A, Masumoto T, Fukamichi K, Aruga-Katori H and Goto T 1995 *J. Phys.: Condens. Matter* **7** 2313

[147] Sebastian S E, Huie T, Fisher I R, Dennis K W and Kramer M J 2004 *Phil. Mag.* **84** 1029

[148] Dhar S K, Palenzona A, Manfrinetti P, and Pattalwar S M 2002 *J. Phys.: Condens. Matter* **14** 517

[149] Fisher I R, Cheon K O, Panchula A F, Canfield P C, Chernikov M, Ott H R and Dennis

K 1999 *Phys. Rev.* B **59**, 3081

[150] Tholence J L 1980 *Solid State Commun.* **35** 113

[151] Edwards S F and Anderson P W 1975 *J. Phys. F: Met. Phys.* **5** 965

[152] Shtrikman S and Wohlfarth E P 1981 *Phys. Lett.* A **85** 467

[153] Hohenberg P C and Halperin B I 1977 *Rev. Mod. Phys.* **49** 435

[154] Souletie J and Tholence J L 1985 *Phys. Rev.* B **32** 516

[155] Armon H, Bauminger E R and Ofer S 1973 Phys. Lett. B 43 380

[156] Stadnik Z M and Żukrowski J, 2005 unpublished results

[157] Margulies S and Ehrman J R 1961 *Nucl. Instrum. Meth.* **12** 131

Shenoy G K, Friedt J M, Maletta H and Ruby S L 1974 *Mössbauer Effect Methodology* vol 10, ed I J Gruverman, C W Seidel and D K Dieterly (New York: Plenum) p 277

[158] Tanaka Y, Laubacher D B, Steffen R M, Shera E B, Wohlfahrt H D and Hoehn M V 1982 *Phys. Lett.* B **108** 8

[159] Czjzek G 1993 *Mössbauer Spectroscopy Applied to Magnetism and Materials Science* vol. 1, ed G J Long and F Grandjean (New York: Plenum) p 373

[160] Stadnik Z M 1996 *Mössbauer Spectroscopy Applied to Magnetism and Materials Science* vol. 2, ed G J Long and F Grandjean (New York: Plenum) p 125

[161] Zijlstra E S, Kortus J, Krajčí M, Stadnik Z M and Bose S K 2004 *Phys. Rev.* B **69** 094206

[162] Gütlich P, Link R, and Trautwein A 1978 Mössbauer Spectroscopy and Transition Metal Chemistry (Berlin: Springer)

[163] Tamura R, Murao Y, Takeuchi S, Tokiwa K, Watanabe T, Sato T J and Tsai A P 2001 *Japan. J. Appl. Phys.* **40** L912

[164] Pope A L, Tritt T M, Gagnon R, and Strom-Olsen J 2001 *Appl. Phys. Lett.* **79** 2345

[165] Tamura R, Murao Y, Kishino S, Takeuchi S, Tokiwa K, and Watanabe T 2004 *J. Mater. Sci. Eng.* A **375–377** 1002

[166] Kramer M J, Lograsso T A and Sordelet D J 2005 *Phil. Mag. Lett.* **85** 151

[167] Murani A P 1977 *J. Magn. Magn. Mater.* **5** 95

[168] Murani A P 1981 *J. Magn. Magn. Mater.* **22** 271

[169] Wagner H G and Gonser U 1983 *J. Magn. Magn. Mater.* **31-34** 1343

[170] Meyer C, Hartmann-Boutron F, Gros Y and Campbell I A 1985 *J. Magn. Magn. Mater.* **46** 254

[171] Aruga H, Tokoro T and Ito A 1988 *J. Phys. Soc. Japan* **57** 261

[172] Bogner J, Reissner M, Steiner W and Dubiel S M 1998 *J. Phys.: Condens. Matter* **10** 9849

[173] Lin Q and Corbett J D 2003 *Phil. Mag. Lett.* **83** 755

Maezawa R, Kashimoto S and Ishimasa T 2004 *Phil. Mag. Lett.* **84** 215

[174] Lin Q and Corbett J D 2004 *Inorg.Chem.* **43** 1912

[175] Kashimoto S, Motomura S, Maezawa R, Matsuo S and Ishimasa T 2004 *Jpn. J. Appl. Phys.* B **43** L526

[176] Kashimoto S, Motomura S, Francoual S, Matsuo S and Ishimasa T 2006 *Philos. Mag.* **86** 725

[177] Ishii Y, Nozawa K and Fujiwara T 2006 *Philos. Mag.* **86** 693

[178] Lundgren L, Svedlindh P, Nordblad P, and Beckman O 1983 *Phys. Rev. Lett.* **51** 911

[179] Hoogerbeets R, Luo Wei-Li and Orbach R 1985 *Phys. Rev. Lett.* **55** 111

[180] Chamberlin R V 1984 *Phys. Rev.* B **30** 5393

[181] Ledermann M, Orbach R, Hammann J M, Ocio M and Vincent E 1991 *Phys. Rev.* B **44** 7403

[182] Chu D, Kenning G G and Orbach R 1995 *Pilos. Mag.* B **71** 479

[183] Mézard M, Parisi G, Sourlas N, Toulouse G and Virasoro M 1984 *J. Phys.* (Paris) **45** 843

[184] Bray A J and Moore M A 1980 *J. Phys.* C **13** L469

[185] Mézard M and Virasoro M A 1985 *J. Phys.* (Paris) **46** 1293

[186] Dotsenko V S 1985 *J. Phys.* C **18** 6023

[187] Rancourt D G and Ping J Y 1991 *Nucl. Instrum. Meth. Phys. Res.* B **58** 85

[188] Stadnik Z M, Takeuchi T, Tanaka N and Mizutani U 2003 *J. Phys.: Condens. Matter* **15** 6365

[189] Kaufmann E N and Vianden R J 1979 *Rev. Mod. Phys.* **51** 161 and references therein.

[190] Deppe P and Rosenberg M 1983 *Hyperfine Interact.* **15–16** 735

[191] Kopcewicz M, Kopcewicz M and Gonser U 1987 *J. Magn. Magn. Mater.* **66** 79

[192] Mao M, Ryan D H and Altounian Z 1994 Hyperfine Interact. **92** 2163

[193] Stadnik Z M, Saida J and Inoue A 2001 *Ferroelectrics* **250** 297

[194] Stadnik Z M, Rapp Ö, Srinivas V, Saida J and Inoue A 2002 *J. Phys.: Condens. Matter* **14** 6883

[195] Brand R A, Voss J and Calvayrac Y, 2000 *Mater. Sci. Eng.* A **294–296** 666

[196] Stadnik Z M and Zhang G 2006 *J. Phys.: Condens. Matter* **17** 6599

[197] Jena P 1976 *Phys. Rev. Lett.* **36** 418

[198] Nishiyama K, Dimmling F, Kornrumph Th and Riegel D 1976 *Phys. Rev. Lett.* **37** 357

[199] Christiansen J, Heubes P, Keitel R, Klinger W, Loeffler W, Sandner W, Witthuhn W 1976 *Z. Phys.* B **24** 177

[200] Lundgren L, Svedlindh P and Beckman O 1982 *J.* Phys.: Met. Phys. F **12** 2663

[201] Guo J Q and Tsai A P 2002 *Phil. Mag. Lett.* **82** 349

[202] Elser V and Henley C L 1985 *Phys. Rev. Lett.* **55** 2883

[203] Takakura H, Guo J Q and Tsai A P 2002 *Phil. Mag. Lett.* **81** 411

[204] Gómez C P and Lidin S 2000 *Phys. Rev.*B **68** 024203

[205] Ruan J F, Kuo K H, Guo J Q and Tsai A P 2004 *J. Alloys Comp.* **370** L23

[206] Stadnik Z M, Al-Qadi K and Wang P 2007 *J. Phys.: Condens. Matter* **19** 326208

[207] Schiffer P, Ramirez A P, Huse D A, Gammel P L, Yaron U, Bishop D J and Valentino A J 1995 *Phys. Rev. Lett.* **74** 2379

[208] Snyder J, Slusky J S, Cava R J and Schiffer P 2002 *Phys. Rev.* B **66** 064432

[209] Dhar S K, Palenzona A, Manfrinetti P and Pattalwar S M 2002 *J. Phys.: Condens. Matter* **13** 517

[210] Dolinsek J, Jaglicic Z, Chernikov M A, Fisher I R and Canfield P C 2001 *Phys. Rev.* B **64** 224209

[211] Dolinsek J, Jaglicic Z, Sato T J, Guo J Q and Tsai A P 2003 *J. Phys.: Condens. Matter* **15** 7981

[212] Jaglicic Z, Dolinsek J and Trontelj Z 2004 *J. Magn. Magn. Mater.* **272–276** 597

[213] Jaglicic Z, Dolinsek J, Trontelj Z and Martinez-Agudo J M 2004 *Mater. Sci. Eng.* A **375–377** 998